Dissertation
submitted to the
Combined Faculty of Mathematics, Engineering and Natural Sciences
of Heidelberg University, Germany
for the degree of
Doctor of Natural Sciences

Put forward by
M.Sc. Lindamulage Malinda Shiram de Silva

Born in: Sri Jayawardenapura Kotte, Sri Lanka
Oral examination: 29-11-2023

SiPM-on-Tile Modules for the CMS High Granularity Calorimeter

Referees: Priv.-Doz. Dr. Felix Sefkow

Prof. Dr. Norbert Herrmann

”I, a universe of atoms. An atom in the universe”

- Richard Feynman

Abstract

For the HL-LHC phase, the calorimeter end-cap of the CMS detector will be upgraded with a High Granularity Calorimeter (HGCAL) with increased transverse and longitudinal granularity to cope with the expected pileup and radiation. In regions where radiation levels allow, the hadronic calorimeter will use scintillator tiles coupled to silicon photomultipliers (SiPM-on-tiles) as active materials. The HGCAL Tilemodule is the basic detector module of this region and can hold up to 144 SiPM-on-tile channels and two readout electronic chips (HGCROCs). Performances of various SiPM-on-tiles, including different SiPM sizes, tile sizes, scintillator materials, production technologies and irradiated SiPMs, were quantified at beam tests using 3 GeV electron beams at DESY-II. Further tests were conducted in temperature-controlled chambers to quantify the relationship between noise and leakage current passing through irradiated SiPMs on Tilemodules. The results from these tests were used in a model to obtain estimates of the signal-to-noise ratio (SNR) at the detector's end-of-life. Based on the estimates, changes to the final scintillator layout are proposed to obtain SNR>3 throughout the detector, including using smaller scintillator tiles in the frontmost layers and increasing the use of SiPMs with $3 \times 3\,\mathrm{mm}^2$ active area in the detector.

Zusammenfassung

Für die HL-LHC-Phase wird die Kalorimeter-Endkappe des CMS-Detektors durch das High Granularity Calorimeter (HGCAL) mit erhöhter transversaler und longitudinaler Granularität aufgerüstet, um dem erwarteten Pileup und der Strahlung standzuhalten. Als aktives Material wird in den hadronischen Kalorimeterbereichen, in denen die Strahlenbelastung dies erlaubt, Szintillator Kacheln verwendet, die direkt mit Silizium-Photomultipliern (SiPM-on-tiles) gekoppelt sind. Das grundlegende Detektormodul dieser Region ist das HGCAL Tilemodul. Es kann bis zu 144 SiPM-on-tile-Kanäle und zwei Auslesechips (HGCROCs) aufnehmen. Das Verhalten verschiedener SiPM-on-tiles, einschließlich verschiedener SiPM-Größen, Kachelgrößen, Szintillatormaterialien, Produktionstechnologien und bestrahlter SiPMs, wurden in Strahl Tests mit 3 GeV-Elektronenstrahlen bei DESY-II quantifiziert. Weitere Tests wurden in einer Klima-Kammer durchgeführt, um die Beziehung zwischen Rauschen und Leckstrom, der durch bestrahlte SiPMs auf Tilemodulen fließt, zu quantifizieren. Die Ergebnisse dieser Tests wurden in einem Modell verwendet, um Abschätzungen für das Signal-Rausch-Verhältnis (SNR) am Ende der Lebensdauer des Detektors zu erhalten. Auf der Grundlage dieser Schätzungen werden Änderungen am Szintillator-Layout vorgeschlagen, um ein SNR>3 im gesamten Detektor zu erreichen. Diese Änderungen umfassen die Verwendung kleinerer Szintillator-Kacheln in den vordersten Lagen und die verstärkte Verwendung von SiPMs mit $3 \times 3\,\mathrm{mm}^2$ aktiver Fläche im Detektor.

Contents

Abstract v

Zusammenfassung v

Contents vii

1 Introduction 1

2 Theoretical Overview 5

- 2.1 Standard Model of Particle Physics . . . 5
  - 2.1.1 The Fundamental Forces in the Standard Model . . . 6
  - 2.1.2 Fermions in the Standard Model . . . 7
  - 2.1.3 Shortcomings of the Standard Model . . . 7
- 2.2 Introduction to Collider Physics . . . 8
  - 2.2.1 Anatomy of a Particle Collision . . . 8
  - 2.2.2 Physics Potential in the End-Cap Region of CMS . . . 11
    - 2.2.2.1 Vector-Boson Fusion (VBF) . . . 11
    - 2.2.2.2 Quark-Gluon Discrimination . . . 12
    - 2.2.2.3 Supersymmetry (SUSY) and Beyond the Standard Model (BSM) Particle Searches . . . 12
- 2.3 Introduction to Calorimetry . . . 12
  - 2.3.1 Particle Interactions with Matter in Calorimeters . . . 13
    - 2.3.1.1 Interactions of Electrons and Photons in Matter . . . 13
    - 2.3.1.2 Interactions of Heavy Charged Particles . . . 15
    - 2.3.1.3 Interactions of Hadrons . . . 17
  - 2.3.2 Energy Loss in Thin Layers . . . 18
  - 2.3.3 Introduction to Calorimeters . . . 19
    - 2.3.3.1 Energy Measurement and Response of Calorimeters . . . 19
    - 2.3.3.2 Energy Resolution in Calorimeters . . . 20
    - 2.3.3.3 Types of Calorimeters . . . 21
- 2.4 Calorimeter Technologies Relevant for HGCAL Scintillator Section . . . 22
  - 2.4.1 Plastic Scintillators . . . 22
    - 2.4.1.1 Plastic Scintillator Material and Production Techniques . . . 23
    - 2.4.1.2 Radiation Effects on Plastic Scintillators . . . 24
  - 2.4.2 Silicon Photomultipliers . . . 25
    - 2.4.2.1 Breakdown Voltage, Bias Voltage and Over-Voltage . . . 27
    - 2.4.2.2 SiPM gain . . . 27
    - 2.4.2.3 Photon Detection Efficiency of the SiPM . . . 28
    - 2.4.2.4 Noise in SiPMs . . . 29

2.4.2.5 SiPM Pitch Size . . . 32
2.4.2.6 Linearity and Dynamic Range of the SiPM . . . 32
2.4.2.7 Radiation Effects in SiPMs . . . 33
2.4.2.8 Determination of SiPM Breakdown Voltage . . . 33
2.5 SiPM-on-Tile Technology . . . 35
2.5.1 Light Yield of the SiPM-on-Tile . . . 35

3 Phase II Upgrade of the CMS High Granularity End-Cap Calorimeter (HGCAL) 37
3.1 High Luminosity Upgrade of the Large Hadron Collider . . . 37
3.2 Introduction to the HGCAL Upgrade . . . 39
3.3 The Scintillator Section of the CMS HGCAL . . . 40
3.3.1 SiPM-on-Tile Sensors . . . 41
3.3.2 HGCAL Tilemodules and Layout . . . 41
3.3.3 Front-End Electronics . . . 44
3.4 HGCROC: Front-End Read Out Chip for the HGCAL . . . 45
3.4.1 The Analogue Front-End . . . 46
3.4.2 The Mixed-Signal Block (Latency Manager) . . . 48
3.4.3 The Digital Block . . . 48
3.4.4 L1 Trigger and Signal Sampling . . . 49
3.5 Data Acquisition Systems used for Testing . . . 50
3.5.1 The KCU105 DAQ System . . . 50
3.5.2 The TB-Tester DAQ System . . . 51
3.6 HGCAL Tilemodule Prototypes (Tileboards) . . . 52
3.6.1 Tileboard Version 1 : TBv1 . . . 53
3.6.2 Tileboard Version 2 : TBv2 . . . 54
3.6.3 Tileboard Version 3 : TBv3 . . . 56
3.6.4 Mini-Tileboard : MiniTB . . . 58
3.7 Signal-to-Noise Based Requirements for HGCAL Scintillator Section at End-of-Life . . . 59

4 Quantifying the Start of Life Performance of SiPM-on-Tiles on HGCAL Tilemodule Prototypes 61
4.1 Overview of Devices under Test . . . 61
4.2 Beam Tests with SiPM-on-Tiles . . . 62
4.2.1 Test Setup . . . 64
4.2.1.1 Over-Voltage Supply . . . 65
4.2.2 Data Analysis Method using a Template Fit for KCU105 DAQ . . . 67
4.2.2.1 Verification using Time-of-Arrival . . . 68
4.2.3 Data Analysis Method using Trigger Timestamps of TB-Tester DAQ . 70
4.2.3.1 Verification of TrigTime using Time-of-Arrival (TOA) . . . 72
4.2.4 Reproducibility of MIP Maxima using the Two Analysis Methods . . . 73
4.3 SiPM Gain Determination . . . 73
4.3.1 Methodology . . . 74
4.3.2 Gain Measurement Strategy . . . 75
4.3.2.1 Differential Non-Linearity Correction . . . 75
4.3.2.2 Optimal LED Intensity for Different SiPMs . . . 77
4.3.2.3 Sampling the Peak of the Pulse . . . 77
4.3.2.4 SiPM Gain Uncertainties . . . 79

4.3.2.5 Linearity of the Gain at Lower SiPM Over-Voltages 79
4.3.3 Gain Dependence on SiPM Size 81
4.3.3.1 Gain Measurement from 3 × 3 mm² SiPMs 81
4.4 Determination of Light Yields 83
4.4.1 Light Yield Correction for Over-Voltage and Temperature 83
4.4.2 Uncertainty of Light Yield Measurements 86
4.4.3 Reproducibility of Light Yield for Different Conveyor Gains 88
4.4.4 Reproducibility of Light Yields for Different Tile Board Generations . 89
4.5 Comparison of Light Yields for Different SiPM-on-Tile Configurations 90
4.5.1 Effect of SiPM Size on Light Yield 91
4.5.2 Effect of Over-Voltage on Light Yield 92
4.5.3 Effect of Scintillator Material on Light Yield 92
4.6 Reproducibility of Light Yields with Muon Beam at SPS Facility, CERN . . . 94
4.6.1 Test Setup 94
4.6.2 Results and Discussion 94
4.7 Reproducibility of Light Yields with Strontium-90 Source 96
4.7.1 Results and Discussion 97
4.8 Latest Tile Studies using ^{90}Sr Setup 98

5 Investigation of the Performance of Irradiated SiPMs on Tilemodule Prototypes 99
5.1 Determination of the Breakdown Voltages of Irradiated HGCAL SiPMs 100
5.1.1 Difference between Breakdown Voltage Definitions 100
5.1.2 Methodology and Test Setup 101
5.1.3 Results 101
5.1.4 Discussion 104
5.2 MIP Response of Irradiated SiPMs 106
5.2.1 Methodology and Test Setup 107
5.2.2 MIP Adjustment due to noise 109
5.2.3 Results and Discussion 110
5.3 Impact of Pedestal Noise on Irradiated SiPMs 112
5.4 MIP Efficiency vs. Noise Occupancy Measurement 113
5.4.1 Methodology and Test Setup 113
5.4.2 Results and Discussion 115

6 Study of Current and Noise from SiPMs on Tilemodule Prototypes 117
6.1 Noise vs. Leakage Current Relationship between Irradiated SiPMs 117
6.1.1 Measurement by Variation of Temperature 117
6.1.1.1 Methodology and Test Setup 118
6.1.1.2 Re-scaling of the SiPM Noise to the Photo-Electron Scale . . 120
6.1.1.3 Results and Discussion 121
6.1.2 Measurement by Variation of LED Intensity 122
6.1.2.1 Methodology and Test Setup 123
6.1.2.2 Results and Discussion 123
6.2 Noise vs. Current Relationship for Different HGCROC Generations 124
6.2.1 Results and Discussion 124
6.3 Noise vs. Current Relationship for Different Non-Irradiated SiPMs 126
6.3.1 Results and Discussion 126

6.4 SiPM Noise Extrapolation to High Luminosity LHC (HL-LHC) End-of-Life Conditions . . . 129

7 Signal-to-Noise Ratio Extrapolations of the HGCAL Scintillator Section 131
7.1 Mathematical Model . . . 131
7.1.1 SiPM-on-tile Positions . . . 132
7.1.2 Neutron Fluence and Absorbed Dose . . . 134
7.1.3 Light Yields . . . 135
7.1.4 SiPM Noise . . . 137
7.1.5 Scintillator Tile Performance Degradation with Irradiation . . . 138
7.1.6 Signal-to-Noise Ratio . . . 139
7.1.7 Layout . . . 140
7.2 Signal-to-Noise Ratio For HGCAL Default Configuration . . . 141
7.3 Evaluating Strategies to Improve SNR . . . 143
7.3.1 Layout Scenario 1 . . . 144
7.3.2 Layout Scenario 2 . . . 144
7.3.3 Discussion of Layout 1 and Layout 2 . . . 145
7.3.4 Layout Scenario 3 . . . 147
7.3.5 Over-Voltage Optimisation . . . 150
7.3.6 Layout Scenario 4 . . . 153
7.4 Optimised, Realistic Final Layout and Configuration for Maximal SNR . . . 157

8 Conclusions and Outlook 159

A Determination of the Pedestal Mean Dependance on Leakage Current 163
A.1 Methodology and Setup . . . 163
A.2 Results and Discussion . . . 164
A.3 Breakdown Voltage Determination using Pedestal Mean . . . 164
A.3.1 Methodology and Setup . . . 165
A.3.2 Results and Discussion . . . 165

Bibliography 169

List of Figures 177

List of Tables 191

Acronyms 193

Acknowledgements 195

Chapter 1

Introduction

Particle physics is a captivating field of study that seeks to uncover the fundamental building blocks of matter and the forces that govern their interactions. The development of a theoretical framework to encapsulate all fundamental particles and their interactions began in the mid-1900s and culminated with the creation of the Standard Model of particle physics.

The Standard Model is a theoretical framework based on quantum field theory, which describes the interactions between different fundamental particles. The Standard Model stands on the theoretical knowledge and scientific brilliance of thousands of great minds such as Max Planck, Erwin Schrödinger, Paul Dirac, Murray Gell-Mann, Richard Feynman, Steven Weinberg, Abdus Salam, François Englert and Peter Higgs.

Verification through experiments is vital for the development of the Standard Model. Therefore, developing detector technologies is essential for identifying particles and their interactions. Particle detector experiments have come a long way in the past century. The earliest particle detectors used cathode ray tubes and are credited for discovering electrons (J.J. Thompson [1]) and x-rays (Wilhelm Röntgen [2]). Photographic film or scintillation screens were later used to record the passage of particles and aided the discovery of spontaneous radioactivity by Henri Becquerel [3]. Cloud chambers [4] used condensed vapours, bubble chambers [5] used superheated liquids, and spark chambers used a gas that produces a spark to track particles.

As time passed, the detectors increased in complexity, with most experiments now comprising multiple detectors to measure different properties of particles. For instance, the CMS experiment at the LHC consists of silicon pixel and strip detectors to observe tracks of charged particles; an electromagnetic calorimeter (ECAL) made of $PbWO_4$ crystals coupled to avalanche photo-diodes (APDs) and a hadronic calorimeter (HCAL) made of steel plates and scintillator tiles coupled to APDs to measure the energy of the particles; and a muon tracker system made of drift tubes (DTs), cathode strip chambers (CSCs) and resistive plate chambers (RPCs) to track muons and measure their momentum.

Today's most powerful particle collider experiment is the LHC situated 100 m beneath France and Switzerland. Since 2009, this 27 km long tunnel collides protons with protons at a centre-of-mass energy of up to 13.6 TeV at four interaction points. These interaction points host four large experiments: ATLAS, CMS, LHCb, and ALICE. The most outstanding achievement in the LHC era was the discovery of the Higgs boson in 2012 by the ATLAS and CMS collaborations [6, 7]. The Higgs particle was the last remaining particle predicted by the Standard Model to be observed. Peter Higgs and François Englert won the Nobel Prize in physics in 2013 for this discovery.

However, LHC has not been able to discover any other particle predicted by supersymmetry or any other beyond the standard model (BSM) physics phenomenon. To galvanise the effort to find new physics, the LHC will undergo a major upgrade potentially starting in 2029 [8]. Labelled the high luminosity upgrade of the LHC or HL-LHC for short, this upgrade is proposed to increase the rate of particle collisions to increase the frequency of rare interaction processes occurring by a factor close to ten in comparison to the current LHC [9].

However, the increased interaction rates also come with multiple challenges. The more significant interaction rates will increase the number of collisions per bunch crossing (pileup). As most collisions are standard processes, it is vital to disentangle rare events from common events to measure their properties. Similarly, the increased collision frequency also results in more significant radiation levels and, therefore, more damage to the detectors. This is especially true in the forward direction of the detectors. As a result, many of the detector components will be replaced with radiation-hard components capable of mitigating the expected pileup. One such detector that will be replaced is the end-cap calorimeter of the CMS detector.

The end-cap calorimeter will replace the existing calorimeter with an electromagnetic calorimeter comprising silicon sensors as active readout components and a hadronic calorimeter equipped with silicon sensors and scintillator tiles readout using silicon photomultipliers (SiPMs). Labelled as the High Granularity Calorimeter (HGCAL), this 5D imaging calorimeter will be tracking particle showers developing in the three spatial coordinates and measuring energy deposition and the time of arrival [10]. The high granularity and the timing information can be used to associate the track information from the tracking detector to the calorimeter for all events and select the most interesting event, mitigating pileup. The high radiation tolerance of the silicon sensors will also allow their operation even after acquiring a 1 MeV equivalent neutron fluence of $1 \times 10^{16}\,\mathrm{n_{eq}/cm^2}$ in the entire runtime.

The HGCAL is also motivated by key physics searches in the forward direction. One such search is the reactions initiated by Vector Boson Fusion (VBF). VBF begins with the interaction of two vector bosons produced by two incoming quarks in the proton beams. The vector bosons may fuse to produce particles such as Higgs bosons, while the two interacting quarks are deflected by a slight angle, producing quark-induced jets in the forward region where the HGCAL will lie. Identifying such events will allow for more precise measurements of the properties of such events and test the limits of the Standard Model.

The area that is covered by the scintillator tiles and associated SiPMs was chosen using projections of the expected 1 MeV equivalent neutron fluence expected at the end of life of the detector (or after collecting an integrated luminosity of $3000\,\mathrm{fb^{-1}}$) [10]. Areas which will receive a neutron fluence less than $5 \times 10^{13}\,\mathrm{n_{eq}/cm^2}$ will use scintillator tiles and SiPMs. Due to geometric reasons, the scintillator tiles in the end-cap are trapezoidal and will increase in size radially from $4\,\mathrm{cm^2}$ to $32\,\mathrm{cm^2}$ in area. A SiPM will sit underneath the centre of each scintillator tile, capturing the scintillation light produced by the scintillator and producing the electronic signal. The coupling of the scintillator and SiPM in this method is known as the SiPM-on-tile technology.

The SiPM-on-tile technology was initially developed for the Analog Hadronic Calorimeter (AHCAL) prototype [11] by the CALICE collaboration. It was developed for e^+e^- colliders like the proposed International Linear Collider (ILC) to be built in Japan. Adapting the technology developed for the ILC to the requirements set for HGCAL is no easy task. The calorimeters at the

ILC will operate at a much lower radiation environment than the HGCAL. Due to considerably smaller radiation damage, the SiPMs, scintillators and onboard electronics do not need to be particularly radiation-hard. Commercial sensors can be used without modifications to the detector. With the HGCAL, the SiPMs, the onboard LED system and electronics must be radiation-hard to withstand the expected high radiation levels.

ILC also operates using ”power-pulsing” for data readout. A bunch train consisting of roughly 2800 bunches spaced by about 300 ns will cross each other at the interaction point lasting for about 1 ms. Bunch trains occur once every 200 ms. The readout chip will save the analogue signals produced during the bunch train period in its internal buffer. During the 199 ms between bunch trains, the readout chip will digitise the signal and send the information to the back-end, where it is analysed. Therefore, depending on how many events occurred during the bunch train, the readout electronics can be switched off when it is not in use [12]. This is impossible at the LHC as proton bunches cross every 25 ns. Therefore, a continuous readout and data transfer to the back-end is required for HGCAL operation.

Since the detector components are off or idle most of the time, they do not heat up as much as they would under continuous readout. Furthermore, they can be operated at room temperature as radiation does not limit them. Therefore, no active cooling is necessary in the context of the ILC [12]. With the LHC, active cooling is required to cool down the detector to a temperature of $-30\,^{\circ}\mathrm{C}$ such that the effects of radiation damage are reduced.

The HGCAL will use a custom-made readout ASIC designed for the silicon sensors and SiPM-on-tiles. Known as the High Granularity Calorimeter Read-Out Chip (HGCROC) [13, 14], this readout ASIC can read out analogue signals from up to 72 SiPM-on-tile channels simultaneously at the LHC bunch crossing frequency, convert the signals into digital values and transfer them along four trigger and two data links at a rate of 1.28 Gbps.

The basic detector module used in the scintillator region is the Tilemodule. Most Tilemodules hold up to 64 SiPM-on-tiles and are read out using a single HGCROC. In Tilemodules containing more than 72 SiPM-on-tiles, two HGCROCs will be used.

This thesis studies the properties of SiPM-on-tiles on Tilemodules readout using the HGCROC chips produced in the context of the CMS HGCAL upgrade. Chapter 2 introduces particle physics, calorimetry and the SiPM-on-tile technology. Chapter 3 introduces the HGCAL upgrade in much more detail, including a description of the sensors, Tilemodules, readout electronics produced for the upgrade and DAQ systems used for testing.

The measurement of the SiPM-on-tile signals via the electronics on the Tilemodule prototypes for non-irradiated SiPMs is discussed extensively in chapter 4. Extensive studies were performed to test the performance of SiPM-on-tiles under different configurations of SiPMs, scintillators and HGCROC parameters. Chapter 5 uses the methods developed in chapter 4 to successfully read out signals from irradiated SiPMs on the Tilemodule prototypes. Most of the work done for these two chapters comes from beam tests conducted primarily at the DESY-II test beam facility [15]. Chapter 5 also investigates the impact of SiPM noise on the SiPM signals due to irradiation. In chapter 6, the relationship between the noise of irradiated SiPMs and their leakage current is investigated.

Based on the performance of non-irradiated SiPM-on-tiles measured in chapter 4, noise measured from irradiated SiPMs in chapter 6 and performances of irradiated HGCAL scintillators [16], a model predicting the signal-to-noise ratio (SNR) at the end of life was further developed in chapter 7. This chapter also discusses the mitigation strategies needed to improve the SNR at the end of life and proposes several layouts. Chapter 8 will summarise this thesis and include a few conclusions and an outlook.

Chapter 2

Theoretical Overview

This chapter establishes the physics motivation and experimental foundation for the research presented in this thesis. It begins by introducing the Standard Model of particle physics and then the basic concepts of calorimetry.

2.1 Standard Model of Particle Physics

The Standard Model of particle physics gives the most up-to-date theoretical framework, which uses quantum field theory to describe interactions between fundamental particles. This model classifies twelve spin-half particles, known as fermions, along with the gauge bosons that mediate their interactions through three fundamental forces. Additionally, the Higgs field, coupled with its associated Higgs boson, plays a pivotal role in providing mass to these particles. Figure 2.1 shows the particles classified in the Standard Model alongside the force carriers.

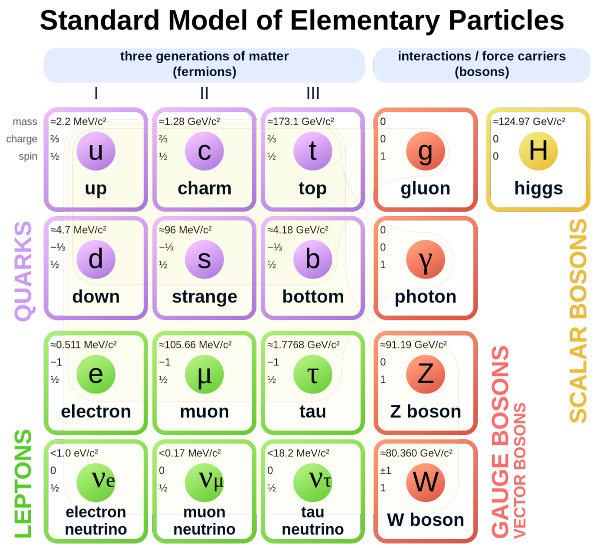
Standard Model of Elementary Particles
three generations of matter (fermions)
interactions / force carriers (bosons)
I
II
III
mass
charge
spin
≈2.2 MeV/c²
⅔
½
u
up
≈1.28 GeV/c²
⅔
½
c
charm
≈173.1 GeV/c²
⅔
½
t
top
0
0
1
g
gluon
≈124.97 GeV/c²
0
0
H
higgs
≈4.7 MeV/c²
−⅓
½
d
down
≈96 MeV/c²
−⅓
½
s
strange
≈4.18 GeV/c²
−⅓
½
b
bottom
0
0
1
γ
photon
≈0.511 MeV/c²
−1
½
e
electron
≈105.66 MeV/c²
−1
½
μ
muon
≈1.7768 GeV/c²
−1
½
τ
tau
≈91.19 GeV/c²
0
1
Z
Z boson
<1.0 eV/c²
0
½
νe
electron neutrino
<0.17 MeV/c²
0
½
νμ
muon neutrino
<18.2 MeV/c²
0
½
ντ
tau neutrino
≈80.360 GeV/c²
±1
1
W
W boson
QUARKS
LEPTONS
GAUGE BOSONS
VECTOR BOSONS
SCALAR BOSONS

Figure 2.1: Elementary particles in Standard Model of particle physics [17]

In the passing years, all fundamental particles in the Standard Model were discovered. The Higgs boson became the final particle to be discovered when it was observed in 2012 by ATLAS and CMS detectors at the Large Hadron Collider (LHC) at CERN [6, 7]. With its discovery, the Standard Model was completed.

2.1.1 The Fundamental Forces in the Standard Model

The Standard Model describes three of the four fundamental forces in the universe: the strong, electromagnetic, and weak forces. They are mediated by integer spin force-carrier particles known as gauge bosons.

The strong force is the strongest among the three forces described in the Standard Model. Based on the coupling constants of the strong (α_s), electromagnetic (α_{em}) and weak (α_w) interactions, the strong force is 3×10^6 times stronger than the weak force and 137 times stronger than the electromagnetic force at an energy of $\sim$ 1 GeV.

Strong interactions take place between colour-charged particles governed by the laws of Quantum Chromodynamics (QCD). Only six of the twelve fundamental fermions (see section 2.1.2) carry a colour charge (i.e. red, blue or green) and, therefore, can interact via the strong force. These fermions are known as quarks. The strong force binds quarks together to form composite particles known as Hadrons and is mediated by gluons (g). As gluons themselves contain a colour charge, gluons can self-interact. The first direct observation of gluons came from the experiments at the PETRA collider in DESY, Hamburg, in 1979 [18].

The electromagnetic force is responsible, among others, for the interactions between electrically charged particles. This force is mediated by massless photons (γ). The interactions between electrically charged particles and the electromagnetic field are governed by the laws of Quantum Electrodynamics (QED).

The weak force is the weakest among the forces described in the Standard Model. These interactions are responsible for the decay of subatomic particles, changing the flavour of the fermion. The electrically charged W bosons ($W^\pm$) and neutral Z^0 bosons mediate the weak force. Particles carrying a weak isospin can interact via the W boson. The electroweak theory, which describes weak interactions, is a theory which combines the electromagnetic force and the weak nuclear force into a unified framework, treating them as different aspects of a single electroweak force.

The first indirect evidence for the existence of the W bosons came with the observation of charged current interactions of neutrinos at the Gargamelle bubble chamber experiment at CERN [19]. The first observations of W and Z bosons came in 1983 thanks to the UA1 and UA2 experiments at CERN's Proton-Antiproton Collider ($Sp\bar{p}S$).

The gauge bosons of the weak force are massive particles, unlike the massless photon and gluon. This mass is acquired through interactions with the Higgs field, also a vital component of the Electroweak Theory. The Higgs field gives rise to the Higgs boson (H). This scalar particle (zero-spin) generates the masses of the $W^\pm$ and neutral Z^0 bosons and of the electrically charged fermions via Yukawa couplings [20].

Unifying the electromagnetic and weak forces into a single electroweak force represents a significant achievement in theoretical physics. The Electroweak Theory, together with quantum chromodynamics (QCD) for the strong nuclear force, forms the foundation of the Standard Model, providing a comprehensive understanding of the fundamental particles and their interactions.

2.1.2 Fermions in the Standard Model

Fermions are half-integer spin particles described by Fermi-Dirac statistics and follow the Pauli exclusion principle. Fundamental fermions are spin-half particles which can be further categorised as quarks and leptons.

Quarks are spin-half fermions that contain a colour charge and, therefore, can interact via the strong force. There are six quarks, namely up (u), down (d), charm (c), strange (s), top (t), and bottom (b). Each of these quarks also has an anti-quark with the charge reversed. The u, c, and t quarks have an electric charge of +2/3, while the d, s, and b quarks have a charge of -1/3.

As the strong force does not weaken with distance, quarks exist solely in bound states known as hadrons. The quarks are bound such that the colour charge is neutral. A bound state containing a quark-anti-quark pair is known as a meson, while a bound state containing a combination of three quarks and antiquarks is known as a baryon. Quarks are asymptotically free, meaning the coupling strength reduces at very high energies. Hence, at collider experiments such as at the LHC at CERN, quarks from different protons can interact during a collision.

Leptons are fundamental particles that do not carry a colour charge and do not interact via the strong force. As a result, leptons can exist in unbound states. There are six leptons, namely electron (e), muon (μ), tau (τ), electron-neutrino (ν_e), muon-neutrino (ν_μ), tau-neutrino (ν_τ). The electron, muon and tau carry an electrical charge of minus one, while the neutrinos are neutral. Each of the leptons also has an anti-lepton whose charges are reversed. Since neutrinos are charge neutral, neutrons have been the subject of many experiments to find if they are their own anti-particles (Majorana particles) [21].

Standard Model fermions can be categorised into three generations in incrementing mass order as shown in fig. 2.1. The quark pair in the same generation form a weak isospin pair. Since particles of higher masses can decay into first-generation particles, most ordinary matter we interact with consists of only first-generation particles such as protons (containing two u-quarks and a d-quark), neutrons (containing two d-quarks and an u-quark) and electrons.

2.1.3 Shortcomings of the Standard Model

The Standard Model has been instrumental in explaining various experimental observations and has successfully predicted numerous phenomena. However, despite its remarkable success, several outstanding questions and avenues for exploration within particle physics remain. These include:

- **Gravity:** Based on the gravitational constant and weak (Fermi) interaction constants, gravity is 10^{34} times smaller than the weak force. Due to the extremely weak nature of gravity in comparison to other fundamental forces, gravity is not incorporated into the Standard Model. As a result, quantum mechanics and the general theory of relativity remain incompatible.
- **Dark Matter and Dark Energy:** Matter described in the Standard Model accounts for only 5 % of the universe. Observations from the motion of galaxies and the cosmic

microwave background indicate the existence of dark matter. At the same time, the universe's accelerating expansion is attributed to the mysterious dark energy.

- **Matter-Antimatter Asymmetry:** Though the Standard Model does have leeway for an asymmetry in matter and antimatter in the universe via CP-violation, the factor to which it is observed in the universe is not described by the Standard Model and remains an unanswered question.

Addressing these shortcomings requires extending the Standard Model, potentially through theories such as supersymmetry, string theory, or other yet-to-be-discovered frameworks. These shortcomings are some of the prime reasons for advocating for high-energy particle physics collider experiments such as those at the LHC.

2.2 Introduction to Collider Physics

From the first atom smasher built by Cockcroft and Walton [22] to the modern creations of CERN's Large Hadron Collider - the largest particle collider in the world, many contributions have been made in the creation and validation of the Standard Model.

The modern particle accelerators come in two variants. The first variant known as a linear accelerator (LINAC), uses alternating electric fields to accelerate particles along a straight trajectory. The accelerator will end at an interaction point where the particles in the beam will be forced to interact either with a fixed target or with another beam coming from the opposite direction. These interactions will occur within a well-crafted particle detector experiment, which allows the reconstruction of the interaction. Prime examples of famous LINACs include the Stanford Linear Accelerator Center (SLAC National Accelerator Laboratory) in the USA [23] and the proposed ILC in Japan [24].

The second variant is known as circular accelerators or synchrotrons. Synchrotrons use radio frequency cavities (RF cavities) with alternating electric fields to accelerate the particles and bending magnets to ensure that the particles travel in the pre-defined circular trajectory. Circular accelerators offer the possibility of keeping the particle bunch circling for longer durations in the synchrotron ring. With each cycle within an accelerator ring, particles are accelerated, reaching much higher energies than what is capable of a LINAC of equivalent length. Furthermore, the synchrotron can be designed to have multiple interaction points such that multiple particle detectors can be housed. Due to these advantages, synchrotrons have been the preferred technology for accelerator complexes. The most famous examples include the KEKB synchrotron (SuperKEKB) in Japan [25], the Tevetron accelerator in the USA [26], HERA and PETRA accelerators in DESY, Germany [27] and the LHC at CERN.

2.2.1 Anatomy of a Particle Collision

In circular collider experiments, two particle bunches travelling in opposite directions collide. At the LHC, the primary particles used for these collisions are protons. The bunch crossing frequency is the frequency at which two bunches meet at an interaction point. In the CMS experiment, the bunch crossing frequency is 25 ns.

Protons are composite particles consisting of two up quarks and a down quark interacting via QCD in a sea of quarks and gluons. Parton distribution functions (PDF) give the probability of finding partons (i.e. quarks and gluons) in a hadron (such as a proton) as a function of a fraction of the hadron's momentum carried by the parton.

At high-energy collisions, partons of the two colliding bunches interact based on the momentum they carry, determined by the proton PDF. If the momentum fractions of the two interacting partons are x_1 and x_2, the hard interaction occurs with energy given by:

$$E = 2E_{proton} \cdot \sqrt{x_1 \cdot x_2}, \tag{2.1}$$

where E_{proton} is the proton energy. This parton interaction will produce particles based on the laws of strong and electroweak theories governing particle physics (excluding any beyond the Standard Model physics scenarios).

If quarks and gluons are produced, they undergo a process known as hadronisation. Hadronisation is the process of hadron formation from quarks and gluons interacting in a collider. QCD dictates that quarks and gluons cannot exist in unbound states. Therefore, they combine with quarks and gluons spontaneously created in the vacuum. This can be thought of as a cascade of quarks and gluons being created from the vacuum, combing with other quarks and gluons to produce hadrons, all moving close to the direction of the initial parton. This tight cone of particles created by the hadronisation is called a jet.

Any heavy particles that have been produced may decay into lighter particles. Only the stable and relatively long-lived particles will reach the detector components. These particles include protons, neutrons, electrons, muons, pions, kaons, and displaced decays like J/ψ, B mesons. It is by observing the final states of these interactions and measuring their properties that details about the initial hard interaction are determined.

High-energy collider experiments typically combine several detector systems to measure the properties of particles, such as particle type, charge, energy and momentum. The CMS experiment at the LHC incorporates an inner tracker, electromagnetic and hadronic calorimeters and a muon system as shown in fig. 2.2[28] to determine these properties.

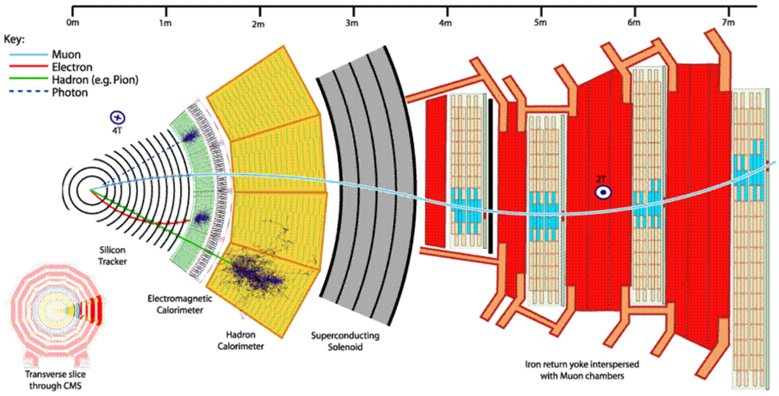

Figure 2.2: Simplified scheme of the CMS detector at CERN including the electromagnetic and hadronic calorimeters [28].

The inner tracker tracks the particle trajectories in a magnetic field through several layers of material, which aids in measuring the particle's momentum and charge. Based on the position

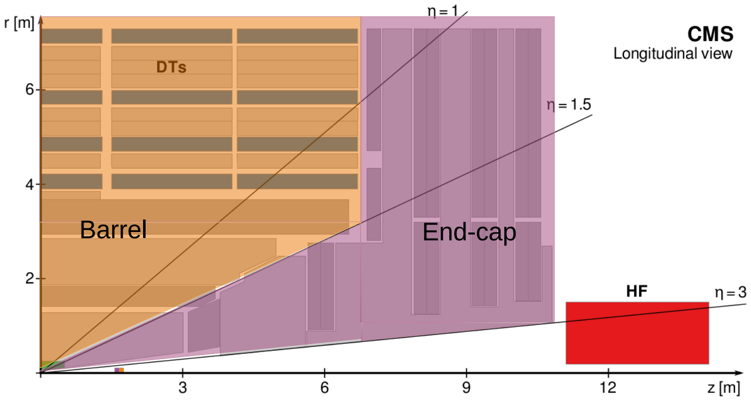

Figure 2.3: A cross-section of the CMS detector with the barrel marked in orange and end-cap region marked in purple. The red area marks the very forward calorimeter of the CMS. Taken and repurposed from [29].

information, the tracker can also determine whether the particles originated from the primary or secondary interaction points due to a particle's decay. The inner tracker is also helpful for identifying and clustering jets to obtain energy.

The calorimeters are detectors which aid in the measurement of the particle energy. This task is achieved by forcing the particles to interact with matter and produce particle showers in the calorimeter. The calorimeter is better suited to measure the energy of neutral and charged particles.

The muon tracker is typically the largest detector component and has the task of measuring the momentum of muons. Muons classified as minimum ionising particles (see section 2.3.1.2) typically travel through the entire detector without showering. Therefore, the only way muons and their energy can be determined is by using a large tracker placed in a magnetic field.

The direction from the interaction point is given via pseudorapidity (η), which is defined as:

$$\eta = -\ln(\tan(\theta/2)). \tag{2.2}$$

where θ is the angle with respect to the beam axis. Suppose a particle travels perpendicular to the beam axis, then $\eta = 0$. As the particle approaches the direction of the beam axis, then $\eta \to \pm\infty$ depending on the direction. In a typical multi-purpose detector such as the CMS detector, the region around $\eta = 0$ is called the barrel while the region around $1.0 < |\eta| < 3.0$ (depending on the detector) are the end-caps. Figure 2.3 shows a cross-section of the CMS detector with the barrel (shown in orange) and end-cap (shown in purple) regions marked. In addition, many detectors may also incorporate a very forward detector (shown in red).

In particle physics, **cross section** measures the probability of interaction between two particles. It can be mathematically viewed as the ”apparent size” of one of the particles viewed by the other and is often given in units of barns (b). A barn is equal to 1×10^{-28} m².

Luminosity ($\mathcal{L}$) is defined as the ratios of the rate of particle interactions (dN/dt) and cross section (σ). That is:

$$\mathcal{L} = \frac{1}{\sigma} \cdot \frac{dN}{dt}. \tag{2.3}$$

Luminosity quantifies the ability of a particle accelerator to produce interactions and is measured in units cm^{-2}s^{-1}.

The **integrated luminosity** ($\mathcal{L}_{int}$) integrates the luminosity over time. That is:

$$\mathcal{L}_{int} = \int \mathcal{L} \cdot dt. \tag{2.4}$$

The integrated luminosity is an important quantity measured in units b^{-1} and often describes the amount of data collected during the operation time of the detector.

2.2.2 Physics Potential in the End-Cap Region of CMS

Particle detectors in collider experiments typically surround the interaction point. The CMS detector at the LHC is one such example. The detector is cylindrical and contains a barrel region and an end-cap region.

The detector structure in the barrel region is very similar to the detector structure in the end-cap region. While the barrel region is where the primary interactions with the highest momentum occur, the barrel region placed in the forward regions of the detector sees the residuals of scattering interactions. This includes interesting physics interactions such as Vector Boson Fusion.

This thesis presents the hardware work undertaken in developing the novel end-cap calorimeter of the CMS detector, which will replace the current end-cap calorimeter. The end-cap calorimeter will sit in the area covered by $1.5 < |\eta| < 3$. Therefore, let us look at the physics potential in this region.

2.2.2.1 Vector-Boson Fusion (VBF)

Vector Boson Fusion (VBF) refers to the fusion of two vector-bosons (typically WW or ZZ) radiated from two quarks of the interacting protons. As the longitudinal momentum of the interacting protons is much larger than the transverse momentum, the quark is only mildly deflected and is still close to the beam direction. These quark jets also take most of the energy. Therefore, VBF is characterised by two high-energetic quark jets with near opposite directions in the forward direction. VBF events are typically identified by looking at the pseudorapidity difference and the invariant mass between the two jets.

VBF probes rare boson interactions at high energy scales and thus tests the limits of the electroweak theory and, in particular, Higgs-vector boson interactions. One such Higgs production mode via VBF is shown in fig. 2.4.

Upgrading the CMS end-cap with high granularity will help to reconstruct the energy, direction and timing of particles produced at small scattering angles where the particle flux and density are expected to be exceptionally high. This is crucial for the precision measurement of rare processes, testing the underlying theory, and potentially discovering new particles in the high pile-up environment of the HL LHC [10].

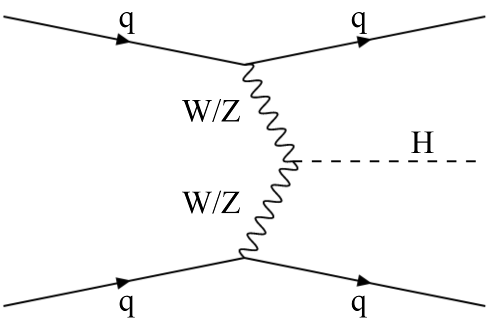

Figure 2.4: Vector Boson Fusion leading to the Higgs boson production.

2.2.2.2 Quark-Gluon Discrimination

Quarks and gluons are fundamental particles that interact through the strong force of QCD described. However, distinguishing between them can be challenging because they quickly form bound states (hadrons) and cannot be directly observed as free particles once produced.

Gluon jets are softer and more dispersed, while quark jets are highly collimated and contain fewer particles. Therefore, studies for improved discrimination power between quark and gluon jets will be possible due to the higher granularity of the end-cap calorimeter [10].

Advanced machine learning algorithms, such as graph neural networks, are good candidates to work optimally with irregular HGCAL geometry. These algorithms can learn complex patterns and correlations between various observables, helping to optimise the discrimination between quarks and gluons.

2.2.2.3 Supersymmetry (SUSY) and Beyond the Standard Model (BSM) Particle Searches

Supersymmetry (SUSY) is considered by many to be the natural extension of the Standard Model as it offers solutions to many of the shortcomings of the Standard Model. SUSY also predict a wide range of particles, which should be observable in collider experiments. However, these particles have not been observed to date. On the contrary, the HL-LHC will offer much better and more constrained searches due to its low production cross-section [10].

Similar BSM theories hypothesise long-lived particles [30] and many dark matter candidates [31]. The improved sensitivity to VBF once again helps with calculations of missing transverse momentum searches, especially if the production modes of the SUSY or other BSM particles arise via VBF [10].

2.3 Introduction to Calorimetry

The origins of calorimeters lie in thermodynamics, where they were used to measure energy in the form of heat deposition in objects. Nuclear and particle physics experiments later adapted calorimeters to measure the energy of particles through total absorption in matter. Different particles interact in different ways in calorimeters. Therefore, it is essential first to understand how particles interact with matter.

2.3.1 Particle Interactions with Matter in Calorimeters

Despite the large number of particles that exist as elementary or composite particles, only a handful reach the calorimeters. These could be heavy charged particles (p,$\pi^{\pm}$,$K^{\pm}$), neutral hadrons (n,K^0), charged leptons ($e^{\pm}$,$\mu^{\pm}$) or photons (γ). The interactions primarily depend on the particle type, momenta and charge. Particles such as $e^{\pm}$ and γ induce electromagnetic showers, while all other particles (except π^0) produce hadronic showers. The difference between electromagnetic and hadronic showers is described in the coming sections.

2.3.1.1 Interactions of Electrons and Photons in Matter

Light-charged particles such as electrons and positrons lose energy by two main processes. At lower energies (below 10 MeV in Pb), the dominant process is the inelastic scattering with atomic electrons. This produces electron-ion pairs, an effect known as ionisation. The dominant process is bremsstrahlung or ”breaking radiation” at higher energies. Bremsstrahlung is caused by relativistic particles which lose momentum due to the change of direction in the presence of an electric field. An overview of all possible losses in energy for electrons and positrons is found in fig. 2.5(a).

Energy loss in a material is often given in terms of stopping power. The stopping power of a material is the rate at which a particle loses energy as it travels through the material. That is:

$$\text{Stopping Power} = -\frac{dE}{dx} \tag{2.5}$$

where dE is the energy loss by the particle in a dx path length in the material. The stopping power depends on the particle's properties and the material, including the atomic number Z. The stopping power increases as the atomic number Z increases, making high Z materials an attractive option for absorber materials.

The energy at which the radiative stopping power equals the stopping power through ionisation is critical energy E_c [32, 33]. That is:

$$\left(\frac{dE_c}{dx}\right)_{Ionization} = \left(\frac{dE_c}{dx}\right)_{Radiative} . \tag{2.6}$$

With neutral charge and zero rest mass, photons do not directly interact with electric or magnetic fields and always travel at the speed of light. Similar to electrons, the processes by which photons interact with matter depend on the photon energies. At lower energies (below 100 keV in Pb), photons predominantly interact via the photoelectric effect. At intermediate energies (between 100 keV and 10 MeV in Pb), Compton scattering dominates. At the highest energies (above 10 MeV in Pb), a photon passing near a nucleus of an atom spontaneously generates an electron-positron pair due to electromagnetic field effects. This is known as electron-positron pair production. The probability of interaction of photons with matter is defined as cross section and is measured in barns (b). Figure 2.5(b) plots the cross sections for the different modes of photon interaction in Pb.

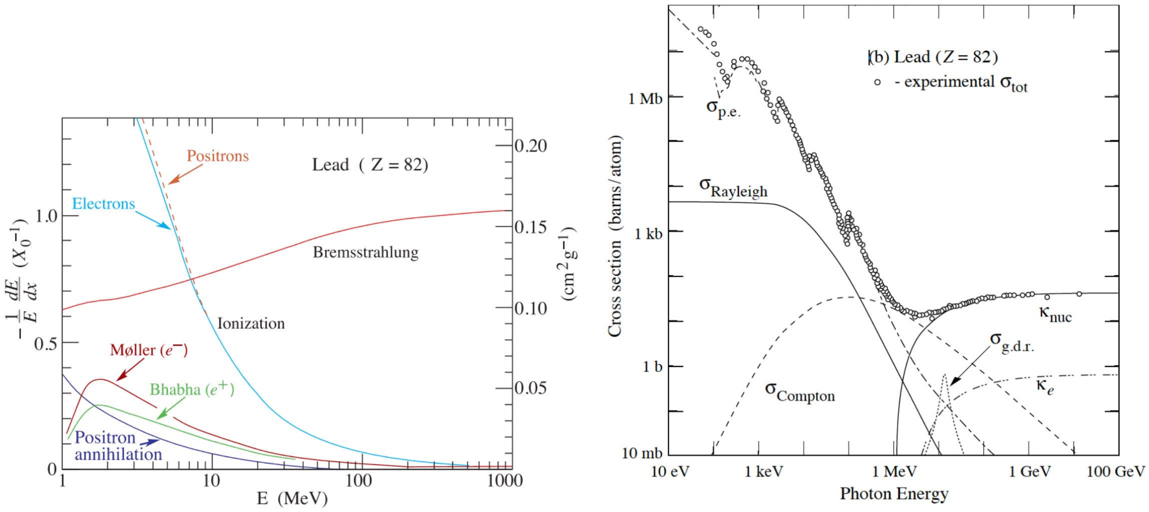

(a) (b)

Figure 2.5: (a) shows the stopping power of electrons and positrons per radiation length as a function of the particle energy. (b) shows the total photon cross sections as a function of photon energy for each type of interaction, showing the contributions of different processes. $\sigma_{\text{p.e.}}$ is the cross section for photoelectric effect, σ_{Rayleigh} for Rayleigh scattering, σ_{Compton} for Compton scattering, κ_{nuc} for pair production in nuclear field, κ_{e} for pair production in electron field and $\sigma_{\text{g.d.r.}}$ for photo-nuclear interactions. Both diagrams are for interactions in lead and taken from [33].

When high-energy photons interact with matter, they can produce electron-positron pairs. These electrons and positrons then lose their energy primarily through bremsstrahlung, which produces additional photons. These photons will once again produce electron-positron pairs, which produce more photons. This process causes a cascade of electrons, positrons and photons and is known as an electromagnetic shower (as shown in fig. 2.6). These showers end when the energy of the electrons in the cascade falls below the critical energy (E_c), and they stop radiating. The remaining electrons with energies below E_c lose the remainder of their energy through ionisation.

Radiation length (X_0) is often used to compare the stopping power of electrons and positrons in different materials. It is defined as the distance an incoming electron travels before it reduces its energy by a factor of $1/e$ due to bremsstrahlung. Similarly, the mean distance a photon travels before pair production in a material is called the mean free path (λ_{pair}). Typically X_0 and λ_{pair} are related and given by [34]:

$$X_0 = \frac{7}{9}\lambda_{pair}. \tag{2.7}$$

This equation shows that X_0 and λ_{pair} are reasonably similar in values. This means that an electron or photon will typically interact after travelling about one X_0 distance, producing a shower of secondary particles.

A simple cascade model of an electromagnetic shower can be created using this information. The model assumes that the shower starts with a single electron or photon and that the secondary particles produced by each interaction also produce showers after travelling a distance of X_0. The model then tracks the number of particles in the shower as it propagates through the material. The particle will only stop in the material without producing further showers after reaching the critical energy E_c. Under this model, the shower will contain the maximum number of particles N_{max} at location x_{max} given by:

$$x_{max} = X_0 \frac{ln\left(\frac{E_0}{E_c}\right)}{ln(2)}, \tag{2.8}$$

where E_0 is the initial energy given in electron Volts (eV).

In the case N different materials stacked one after the other are present, the radiation length is calculated according to the volume fractions:

$$X_0 = \sum_{n=0}^{N} \frac{X_i}{V_i}, \tag{2.9}$$

where X_i and V_i are the radiation lengths and volume fractions of the ith element. This is similar to the situation expected in a sampling calorimeter (see section 2.3.3).

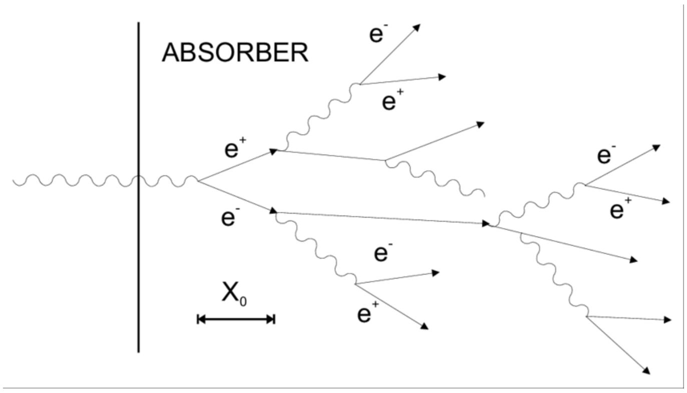

Figure 2.6: An illustration of the development of an electromagnetic shower using the simple cascade model. X_0 is the radiation length. Taken from [35].

2.3.1.2 Interactions of Heavy Charged Particles

Inelastic collisions with atomic electrons govern interactions of heavy charged particles for particles with moderately high momenta and by bremsstrahlung for highly relativistic particles. Inelastic collisions cause an energy transfer from the particle to the bound electron, resulting in ionisation. The mean rate of energy loss by moderately relativistic charged heavy particles is well described by the Bethe-Bloch equation [33] given by:

$$-\left\langle \frac{dE}{dx} \right\rangle = K z^2 \frac{Z}{A} \frac{1}{\beta^2} \left[\frac{1}{2} \ln \left(\frac{2 m_e c^2 \beta^2 \gamma^2 W_{max}}{I^2} - \beta^2 - \frac{\delta(\beta\gamma)}{2} \right) \right], \tag{2.10}$$

where:

$-\left\langle \frac{dE}{dx} \right\rangle$ = mean stopping power of the particle in material

β = ratio of relative velocity to speed of light,

γ = Lorentz factor $(1/\sqrt{1-\beta^2})$,

K = coefficient for dE/dx ($0.307\,075\,\mathrm{MeV}\cdot\mathrm{mol}^{-1}\cdot\mathrm{cm}^2$),
z = charge of particle,
A = mass number of material,
Z = atomic number of material,
m_e = electron mass,
$'\,c$ = speed of light in vacuum,
I = material average potential,
W_{max} = maximum energy transfer possible in a collision,
$\frac{\delta(\beta\gamma)}{2}$ = density factor correcting the logarithmic increase in energy loss for higher momenta.

The Bethe-Bloch equation is generally valid between $0.1 \lesssim \beta\gamma \lesssim 1000$. A plot of the energy loss as a function of particle momenta can be found in fig. 2.7. To understand these interactions better, let us divide the effects responsible for ionisation energy loss into smaller regimes depending on the particle momentum ($\beta\gamma = p/Mc$).

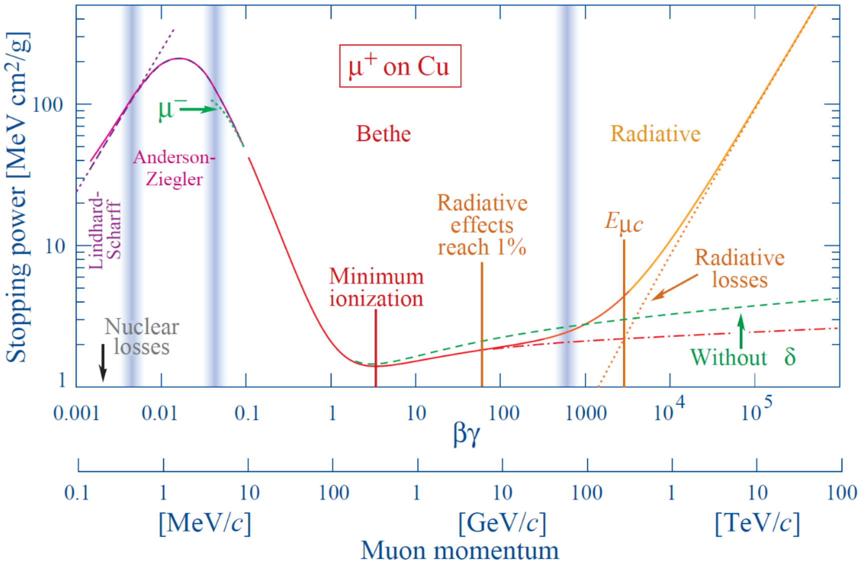

Figure 2.7: Stopping power for positive muons traversing copper as a function of the muon momentum. The solid line shows the total stopping power and the dashed lines show the different contributions, including the stopping power via inelastic collisions and bremsstrahlung. Taken from [33].

- **At lower momenta ($\beta\gamma < 3$):**$\left\langle\frac{dE}{dx}\right\rangle \propto \frac{1}{\beta^2}$ Due to the low momenta, particles have more time to interact with atomic electrons and, therefore, interact readily with the electrons.
- **At momenta $\beta\gamma \simeq 3$:** Particles at this momentum interact the least with atomic electrons, resulting in the least energy loss due to ionisation. Therefore, particles at these momenta are referred to as minimum ionizing particles (MIPs). MIPs are often used to calibrate detectors because they have a well-defined most probable energy loss.
- **At higher momenta ($3.5 < \beta\gamma < 1000$):** $\left\langle\frac{dE}{dx}\right\rangle \propto \ln(\gamma\beta)$ As the energy of a particle increases, the number of particles interacting increases due to relativistic effects. However,

the radiative effects are not that significant at these energies. This means that the energy loss due to ionisation is still the dominant factor. The increase in stopping power compared to that of MIPs is less than a factor two as the relativistic effects primarily increase the tail. Therefore, particles in these energy ranges are relatively good substitutes for MIPs.

- **At highest momenta ($\beta\gamma > 1000$):** Particle interactions are no longer dominated by inelastic scattering but rather by radiative effects such as bremsstrahlung (see section 2.3.1.1).

The energy loss through ionisation also depends on the charge of the particle, as given by:

$$\left\langle \frac{dE}{dx} \right\rangle \propto z^2. \tag{2.11}$$

Muons produced in collisions at colliders are particularly interesting in high-energy physics experiments among all charged particles because they typically have energies which classify them as MIPs. As muons have a lifetime of ~ 2.2 µs, coupled with the Lorenz boost, they can travel from the interaction point through all detector systems and exit the system before decaying and without showering. Therefore, muons are often used to calibrate particle detectors, including calorimeters.

Inelastic collisions could also occur with atomic nuclei. These often lead to nuclear spallation, which results in hadronic showers. See section 2.3.1.3 for more on hardonic showers.

2.3.1.3 Interactions of Hadrons

In addition to inelastic scattering with atomic electrons, hadrons can lose energy through inelastic scattering with nuclei in the material. The incoming hadron can strongly interact with the atomic nuclei in the material, resulting in the fragmenting of the nuclei. This is called nuclear spallation, and it results in the production of many particles, including mesons ($\pi^{\pm}$ or π^{0}), hadrons such as neutrons and heavy nuclear fragments. Particles produced in spallation can cause further spallation of other nuclei, creating a hadronic shower. The properties of hadronic showers vary depending on the primary hadron. Figure 2.8 shows the formation of such a hadronic shower.

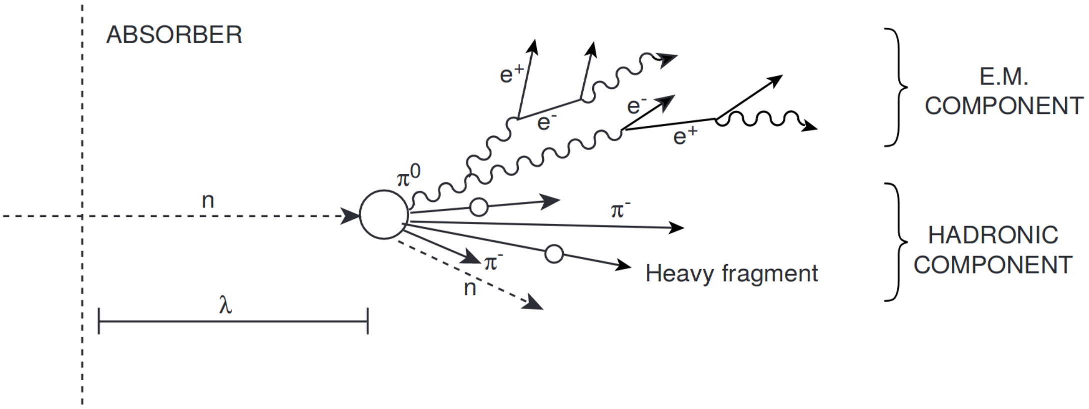

Figure 2.8: An illustration of the development of a hadronic shower. λ describes the mean distance a particle travels in a given material before undergoing inelastic interactions. Taken from [36].

The composition of hadronic showers is much more complex than electromagnetic showers. In about $2/3$ of the cases, the particles in the hadronic shower produce charged mesons like $\pi^{\pm}$, neutrons or heavy fragments. However, the spallation can also create π^0 which has a 98 % chance of producing two photons. These photons create an electromagnetic sub-shower within the hadronic shower.

Nuclear spallation can also produce neutrons. Neutrons are neutral particles and, therefore, do not undergo ionisation directly. However, neutrons can elastically or inelastically scatter with nuclei. In the case of elastic scattering, the neutron will lose energy to the nuclei, which is then excited. They will de-excite by emitting radiation. Neutrons can also inelastically scatter, producing more nuclear spallations, which lead to more hadronic showers. Neutrons may also get absorbed by the material, causing nuclear fission reactions. However, neutrons can also escape the detector due to their neutrality, leaving a deficit in the total energy reconstructed.

Production of nuclear fragments from spallation also leads to energy losses as binding energy is required to create them. Fragments left after the spallation and fission events can produce hard X-ray photons, α particles, and other light nuclei, contributing to the hadronic shower.

The length of the hadronic shower is determined by the nuclear interaction length λ, defined as the mean distance a hadronic particle travels in a given material before undergoing inelastic hadronic interactions. The nuclear interaction length λ is typically much larger than the radiation length X_0 in the same material. For an example, X_0 and λ in copper are 1.436 cm and 15.32 cm respectively [37]. Therefore, hadronic showers are typically much larger than electromagnetic showers in the same medium.

2.3.2 Energy Loss in Thin Layers

As discussed in section 2.3.1.2, the probability of interaction of particles increases as a function of Atomic number (Z) and as the thickness of the material increases. However, it is possible to decrease the energy loss in a medium by reducing Z and reducing the thickness of the material such that the thickness $r << X_0$ and $r << \lambda$.

Most particles interact minimally in thin, low Z materials such as 3 mm thick plastic scintillators. Therefore, most particles that pass through the scintillator can be considered as MIPs in this material. Most of these particles lose a fixed energy in the order of keV in the material. At the same time, infrequent high-energy-transfer collisions may cause higher energy loss of up to several GeV. This results in the iconic shape of the Landau (or Landau-Vavilov-Bischel) distribution, first described by Landau in 1944 [38]. It consists of a well-defined most probable charge deposition in the material (also known as most probable value (MPV)) and a long tail extending to high energies as shown in fig. 2.9(a).

The Bethe-Bloch formula's description of energy loss of charged particles in matter calculates the mean energy losses. At the same time, the Landau distribution describes the MPV of energy loss in the materials. The Landau-Vavilov most probable energy loss reaches a plateau for MIPs as shown in fig. 2.9(b). This means that MIPs deposit the same energy with the highest probability in thin layers, such as a 1.7 mm thin silicon or 3 mm scintillator. This makes the MPV a valuable asset in calibrating the detector. As the MPV is less sensitive to particle momentum than the mean energy loss, MPV can be used as a natural deposition scale.

Though energy depositions by charged particles follow Landau distributions, due to detector noise, shower fluctuations and the detection efficiencies of the detector, additional Gaussian smearing convoluted the distribution. Therefore, as a mathematical consequence, the energy deposition on the thin layers is modelled using a Landau function convoluted with a Gaussian. The most probable value of this convoluted function will be referred to as **MIP Maximum** in this thesis. The MIP scale that counts the number of MIPs in multiples of MIP maxima is a more realistic natural deposition scale that can be used to calibrate the detector as it considers the impact of noise in the detector.

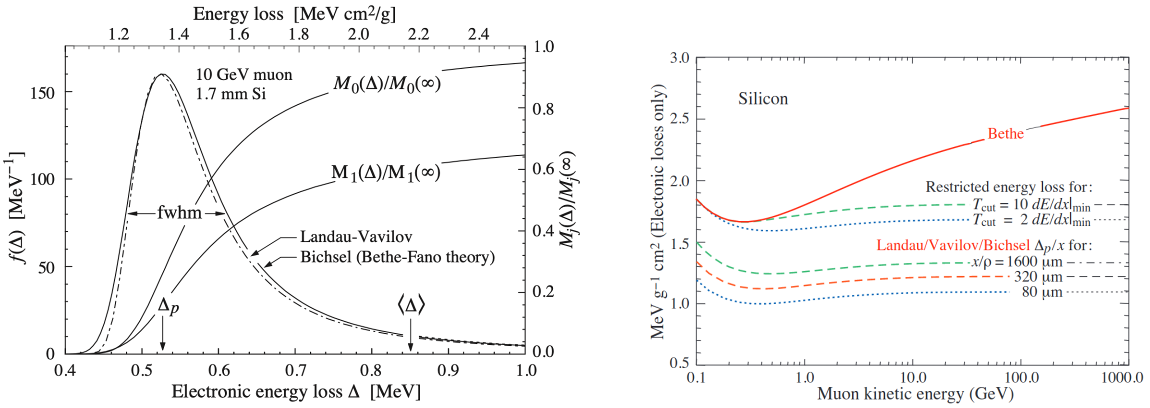

(a) (b)

Figure 2.9: (a) shows the electronic energy deposit distribution for a 10 GeV muon traversing 1.7 mm of silicon. (b) shows the mean stopping power (dE/dx) described by the Bethe-Bloch equation and the most probable energy loss described by the Landau-Vavilov-Bichsel equation (Δ_p/x) shown as a function of muon energy traversing 1.7 mm of silicon. Silicon has a similar stopping power as a 3 mm of PVT-based scintillator. Taken from [33].

2.3.3 Introduction to Calorimeters

In collider experiments, calorimeters are responsible for the measurement of particle energies. They perform this by inducing electromagnetic and hadronic showers and collecting the charge deposited by the particles in the shower in the detector. They also help with the identification of the particles during analysis.

2.3.3.1 Energy Measurement and Response of Calorimeters

Ideally, the energy of the primary particle which generates a corresponding shower is given by the sum of all charges collected by the calorimeter associated with that event. That is, if the charge collected is Q_{vis} and the energy of the primary particle is E_{prime}:

$$E_{prime} \propto Q_{vis}. \tag{2.12}$$

This principle is the basis for all calorimetric measurements, and the proportionality constant is measured using particles with known energies as primary particles and measuring the charge collected by the detector. This procedure is often called **detector calibration**. Many detectors use charge-sensitive devices such as silicon sensors or photon-sensitive devices such as photomultiplier tubes (PMTs), or SiPMs to convert the charge or photons to a signal.

The relationship between the signal produced by a calorimeter cell and the energy deposited by the particle os given by the calorimeter response. For an ideal calorimeter where all sensors produce identical signals for the same energy, independent of the incoming particles, the calorimeter has a constant response [34].

In reality, calorimeters may have varying material or sensor conditions, which results in uneven signals for the same energy deposit. One such example would be when multiple types of sensors are used with different sensitivities. In such cases, the detector must be calibrated so the calorimeter response becomes constant.

For a calorimeter which consists of thin sensors as described in section 2.3.2, a practical scale to do such calibrations is the MIP scale. Since the most probable value of the MIP (MIP maximum) is at a fixed charge deposition, one can use MIPs as primary particles travelling parallel to the sensor to measure the MIP maxima of each cell in the calorimeter, thereby providing an effective calibration factor for all cells.

The calorimeter response could also depend on the shower type. Electromagnetic showers produce electrons, positrons and photons alone. They produce detectable signals. Therefore, if non-linearities caused by the readout is neglected, the calorimeter response is linear. However, hadronic showers involve a wide variety of particles including particles such as neutrinos which does not deposit any energy in the calorimeter leaving a missing energy component. Furthermore, hadronic showers also contain electromagnetic sub-showers.

For calorimeters optimised for hadronic showers, an important parameter that is used to quantify the calorimeter response is the e/h ratio given by:

$$\frac{e}{h} = \frac{\text{Response of the Electromagnetic Component}}{\text{Response of the Hadronic Component}} \tag{2.13}$$

If the calorimeter response to purely hadronic showers (excluding the electromagnetic component) is smaller than for electromagnetic showers, the e/h ratio will be greater than 1. This indicates that energy is underestimated for hadronic showers and needs to be compensated such that e/h ratio=1.

2.3.3.2 Energy Resolution in Calorimeters

The energy resolution (σ/E) refers to the ability of a calorimeter to accurately distinguish and measure the energy of individual particles that interact with the detector. Energy resolution in calorimeters is parameterised as follows:

$$\frac{\sigma(E)}{E} \approx \frac{A}{\sqrt{E}} \oplus \frac{B}{E} \oplus C. \tag{2.14}$$

where $A/\sqrt{E}$ is called the stochastic term, B/E is known as the noise term and C is known as the constant term.

The stochastic term $A/\sqrt{E}$ is due to random fluctuations in the number of particles taking part in the shower governed by Poissonian statistics. That is, if N is the expected number of particles contributing to the signal, the standard deviation (or uncertainty) is given by $\sqrt{N}$. Therefore the uncertainty $\sigma(N)/N$ is given by $1/\sqrt{N}$. Since N is proportional to the particle's energy, this derives the stochastic term. The stochastic term is dominant at higher energies, and therefore, for high-energy experiments such as CMS, the stochastic term is often quoted as the energy resolution of the calorimeter per GeV.

The noise term B/E is caused by fluctuations in the electronic signal produced by the sensor and readout electronics. This includes fluctuations in charge conversion efficiency, charge amplification, signal shaping, etc. The noise term impacted by radioactivity and pileup. This term is typically dominant at lower energies below a few GeV energy. Therefore, the noise equivalent energy is usually required to be much smaller than 100 MeV per channel for applications in the several GeV region [39].

The constant term C depends on imperfections in the calorimeter inhomogeneities which cause variations in the calorimeter response. This could originate from irregularities in the detector geometry, imperfections in the mechanical structure, non-linearities in the readout electronics or leakage of particles from the detector. The constant term is independent of particle energy and should be limited to less than 1 % [39].

2.3.3.3 Types of Calorimeters

Typical high-energy particle collider experiments incorporate two calorimeters: an **electromagnetic calorimeter (ECAL)** and a **hadronic calorimeter (HCAL)**. The ECAL is optimised to generate electromagnetic showers and contain the shower within the calorimeter volume, while the HCAL is optimised similarly for hadronic showers. As mentioned in section 2.3.1.3, X_0 is much smaller than λ for the same material. This results in much larger HCALs than ECALs produced using the same material. This is also the reason for implementing the ECAL before the HCAL relative to the interaction point.

As mentioned in section 2.3.1.1, electromagnetic showers consist of only electrons, positrons and photons. In comparison, hadronic showers are much larger and produce many neutral particles, such as neutrons and neutrinos, which may not deposit any energy in the calorimeter. As a result, generally, ECALs have a much better energy resolution than HCALs. For an example, The ATLAS ECAL and HCAL in the barrel region has an energy resolution (stochastic term) of about $10\,\%/\sqrt{E[\mathrm{GeV}]}$ and $50\,\%/\sqrt{E[\mathrm{GeV}]}$ respectively [40, 41].

Calorimeters can also be classified into two main types based on their construction technique: **homogeneous calorimeters** and **sampling calorimeters**. Homogeneous calorimeters use a single material to create showers and convert the energy from particles into readable signals, typically via ionisation. Sampling calorimeters delegates these two functions to two different materials known as an absorber and an active medium. The absorber, a dense material, creates the shower, while the low-dense active material creates the detectable signal to measure the energy deposition by the particles.

Since the readout is only in the active medium in sampling calorimeters, all energy depositions in the absorber material are lost. Meanwhile, homogeneous calorimeters use a single material to create showers and convert the energy from particles into readable signals. As a result, homogenous calorimeters have an inherently better energy resolution than sampling calorimeters. Today's most famous example of a homogeneous ECAL is the CMS ECAL, which uses lead tungstate ($PbWO_4$) crystals. It has an energy resolution (stochastic term) of $3.6\,\%/\sqrt{E[\mathrm{GeV}]}$ [42]. In comparison, the ATLAS Liquid Argon sampling calorimeter, as stated above, measures the stochastic term to be about $10\,\%/\sqrt{E[\mathrm{GeV}]}$.

However, homogeneous materials are rare, expensive and typically less dense than absorber materials used in sampling calorimeters. Meanwhile, sampling calorimeters can be optimised to reduce the thickness of the detector. This makes homogeneous calorimeters thicker and more expensive than typical sampling calorimeters.

Despite these cost and material constraints, it is still possible to design homogeneous ECALs. However, it is practically impossible to design a homogeneous HCAL due to the cost and volume required. The CMS homogeneous ECAL and has a 23 cm thickness (or $26 \cdot X_0$) in the $\eta = 0$ direction. In numbers, $\lambda =\sim 25 \cdot X_0$ in $PbWO_4$. A typical HCAL is designed to cover $\sim 10 \cdot \lambda$. So if an HCAL was made purely from $PbWO_4$ crystals to cover a thickness of $\sim 10 \cdot \lambda$, the thickness of the HCAL will be about ten times the thickness of the ECAL, or 1000 times the ECAL volume. The cost of homogeneous calorimeter materials are several factors larger than those used in sampling calorimeters. This factor coupled to the much larger volume makes it an impractical solution for hadronic calorimeters. Therefore, sampling calorimeters are the only practical choice for hadronic calorimeters.

2.4 Calorimeter Technologies Relevant for HGCAL Scintillator Section

Among the various calorimeter technologies available, the scintillator section of the CMS end-cap calorimeter upgrade for the high-luminosity LHC upgrade uses plastic scintillators and silicon photomultipliers. This section introduces these technologies and the essential concepts to understand their functionality.

2.4.1 Plastic Scintillators

A scintillator is a material that produces scintillation photons from electron excitation. One of the most commonly used scintillator materials in particle physics experiments are plastic scintillators due to their low cost and ability to scintillate visible or near-visible photons. Compared to other scintillators, plastic scintillators are characterised by a rapid decay time of a few nanoseconds, making them ideal for fast detection [34].

When a charged particle traverses the plastic scintillator medium, the ground state electrons absorb a fraction of its kinetic energy through elastic scattering. This results in the electron excitation to higher energy levels as illustrated in fig. 2.10. Electrons at the higher energy levels (S_2, S_3) will quickly de-excite to the lowest singlet state (S_1) via internal radiation-less transitions. However, they release fluorescence photons as they de-excite down to ground level. This entire process typically happens in a few nanoseconds, and therefore, it is most often fluorescence that is detected as scintillation light in experiments.

However, some electrons may transition from higher states to the triplet T_1. These electrons will also de-excite to the ground state, emitting phosphorescence photons. Since this process takes microseconds, these photons add a delayed component to the emission spectrum of plastic scintillators.

Scintillators are coupled with photon-sensitive devices, including photomultiplier tubes (PMTs), charge-coupled devices (CCDs), or silicon photomultipliers (SiPMs) to convert the

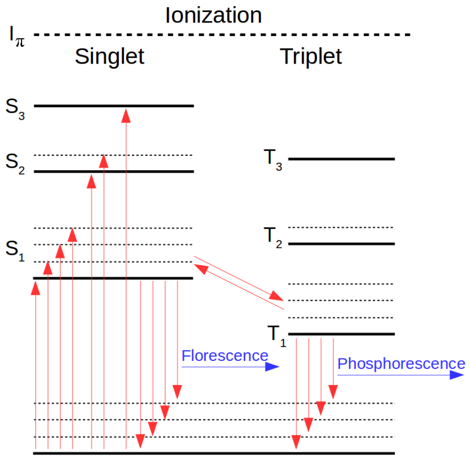

Figure 2.10: Energy levels of organic molecules. S denotes the singlet state, and T denotes the triplet states. Red arrows mark electron movements, while blue arrows mark the emitted photons. Taken from [43]

scintillation light into a detectable electrical signal successfully.

The size of the scintillator tile directly correlates to the amount of light the photon detector, such as a SiPM, can detect. Larger scintillators result in more photon losses, leading to a decrease in photon detection efficiency. However, wrapping the scintillator in a highly reflective foil can improve photon detection efficiency.

2.4.1.1 Plastic Scintillator Material and Production Techniques

Plastic scintillators are often the only practical choice if large volumes of solid scintillators are necessary. This is due to the commercial availability of plastic scintillators with a good selection of standard sizes of rods, cylinders and flat sheets, and its inexpensiveness to be manufactured in bulk [44].

The scintillator material determines the efficiency at which ionisation energy from the particle produces scintillation photons and the wavelength of these produced photons. There are two most commonly used methods of scintillator production.

The first method is known as injection moulding. This process includes injecting molten plastic into a mould, where it cools and hardens in the shape of the mould. Thermoplastics such as polystyrene are considered suitable materials for manufacturing injection-moulded scintillators due to their relatively low melting point. This thesis primarily uses injection-moulded scintillators from the Institute for High Energy Physics (IHEP), Protvino, Russia and Fermi National Laboratory (FNAL), Chicago, USA.

The second method is to use commercially produced cast sheets of plastic. These sheets are typically produced using Polyvinyl Toluene (PVT). The PVT is poured into a thin cast and made to react with a monomer. The result is a polymerised sheet of plastic scintillator. All raw materials are extensively purified before polymerisation. Once polymerised, they are machined into their final dimensions using diamond tooling [45]. The cast scintillators mentioned in this thesis were produced at Saint-Gobain S.A. in Paris, France (BC-408 and BC-412 [46]) and Eljen Technologies in Texas, USA (EJ-208 [47]). The scintillators were machined into tiles at the Institute for High Energy Physics (IHEP) in Protvino, Russia, the Institute for Scintillation Materials (ISMA) in Kharkiv, Ukraine and Northern Illinois University (NIU), Illinois, USA.

Plastics on their own are typically not good scintillator material. Primary fluors or dopants are often added to the scintillator solvent to make them scintillate. Examples of such fluors or dopants include solutes such as PBD, p-terphenyl and PBO. Secondary fluors or dopants are added to the scintillator solvent in a much smaller proportion to shift the wavelengths of the scintillation photons produced by the material. This is necessary to shift the photons' wavelengths to values to which the photosensitive devices are sensitive. POPOP is one such material added as a secondary fluor [34, 48].

Typically, PVT scintillators exhibit better scintillation light yields than polystyrene scintillators. Since cast tiles are primarily produced using PVT, cast scintillators exhibit better scintillator light yields than polystyrene-based injection-moulded tiles. However, cast scintillator sheets are also generally more expensive to purchase and come with the additional burden of needing to machine the sheets into the tile shapes needed, which often takes longer than injection-moulding. They also may require polishing once cut to improve the light output.

2.4.1.2 Radiation Effects on Plastic Scintillators

The atoms are held together via covalent bonds in the long molecules that make up the polystyrene or PVT material. Electromagnetic interactions can break these bonds, producing molecules with unpaired electrons known as radicals.

Radicals are highly chemically reactive. They can annihilate when coming into contact with another radical, bind to monomers, causing them to link together to produce polymers (polymerisation), bind polymers together (cross-linking) and break polymer links, creating shorter polymer fragments (chain scission). These interactions could lead to a decrease in scintillator transparency, producing what is known as absorption centres. Absorption centres absorb specific wavelengths of light, which may decrease the scintillator's light output over time [49, 50]. These centres could be stable, leading to the **permanent damage** of the scintillator, which does not anneal over time.

They could also be long-lived absorption centres which anneal after many days or weeks. Some absorption centers may also appear stable at low temperatures ($-30\,^{\circ}$C), only to anneal at higher temperatures ($0\,^{\circ}$C). Due to their annealing nature, the damage caused by these absorption centres is often called **temporary damage**.

Permanent damage has been extensively studied at room temperature and atmospheric oxygen levels in a detector environment. Experimental results from the current CMS end-cap calorimeter [51] have found the reduction in scintillator signal after permanent damage to follow an exponential function at doses less than about 10 Mrad as:

$$\left(\frac{L_{perm}(d)}{L_0}\right) = \exp\left(\frac{-d}{D_{perm}}\right), \tag{2.15}$$

where $L_{perm}(d)$ is the signal after irradiation due to permanent damage, L_0 is the signal before irradiation, d is the absorbed dose (energy deposited by ionising radiation in a material per unit mass) and D_{perm} is the permanent dose constant. One major finding from the CMS end-cap calorimeter was that the dose constant D_{perm} follows a power law function given by:

$$D_{perm} = A \cdot R^B, \tag{2.16}$$

where R is the dose rate the scintillator tile experiences, and A and B are constants whose value depends on the scintillator geometry, the specific scintillator used, and environmental factors such as oxygen levels and temperature. Larger values of D_{perm} indicate a greater radiation tolerance. This means that the permanent damage is larger for lower dose rates.

The CMS HGCAL will operate at $-30\,°\mathrm{C}$ in $3\,\%$ O_2 conditions. The dose rate at the HGCAL experiment will vary between $1\,\mathrm{rad/hr}$ and $30\,\mathrm{rad/hr}$ depending on the exact location in the detector. More on the HGCAL can be found in chapter 3.

Temporary damage in hypoxic and low temperature environments had been investigated in a recent study by the University of Maryland in the context of the HGCAL. Using scintillator tiles produced for the CMS HGCAL upgrade, this study showed that the effect of scintillator temporary damage is non-negligible in low-temperature environments [16].

The experiment conducted by Maryland University took place at the Goddard Space Flight Center over several weeks, at the same temperature and hypoxic levels expected at the HGCAL with the scintillators irradiated by a ^{60}Co γ-source at dose rates of $130\,\mathrm{rad/hr}$ and $30\,\mathrm{rad/hr}$ [16]. The scintillators were coupled with HDR-2 SiPMs, replicating the conditions under which the HGCAL will operate. A double-exponent function fits the fractional light remaining after temporary damage [16]. For a negligible amount of permanent damage, this is given by:

$$\left(\frac{L_{temp}(d)}{L_0}\right) = K \cdot \exp\left(\frac{-d}{D_1}\right) + (1-K)\cdot \exp\left(\frac{-d}{D_2}\right), \tag{2.17}$$

where L_0 is the number of photons produced by the scintillator before irradiation, L_{temp} is the number of photons produced after temporary damage, D_1 and D_2 are the dose constants associated with temporary damage, d is the absorption dose, K is a constant based on material properties.

Maintaining a temperature of $-30\,°\mathrm{C}$ after the removal of the source will result in the annealing of the long-lived temporary damage. However, raising the temperature level will facilitate the annealing of this temporary damage. Therefore, it is expected that the temperature of the detector is raised to $0\,°\mathrm{C}$ during the LHC year-end technical stops (YETS).

Understanding how the temporary and permanent damage can be mathematically modelled is essential to extrapolate and predict the conditions at the detector's end-of-life. More on this study and the final mathematical model used to extrapolate the tile performance can be found in chapter 7.

2.4.2 Silicon Photomultipliers

Silicon photomultipliers (SiPMs), also known as Multi-Pixel Photon Counters (MPPCs), are photo-detectors capable of detecting individual photons. SiPMs are used for similar applications as PMTs while offering all the benefits of a solid-state sensor, such as low voltage operation, insensitivity to magnetic fields, mechanical robustness and excellent uniformity. SiPMs are also cheaper, have a fast rise time in the order of picoseconds and can be as small as 1×1 mm^2 in area, making them smaller than most PMTs. These properties make SiPMs a prime candidate for photon detector systems, timing detectors and calorimeters, among many other applications requiring high integration levels [52].

A SiPM consists of many Single-Photon Avalanche Diodes (SPADs) readouts in parallel.

Each SPAD is also known as a micro-cell or pixel. Figure 2.11 shows an image of a SiPM consisting of thousands of SPADs alongside a microscopic image of one of the SPADs.

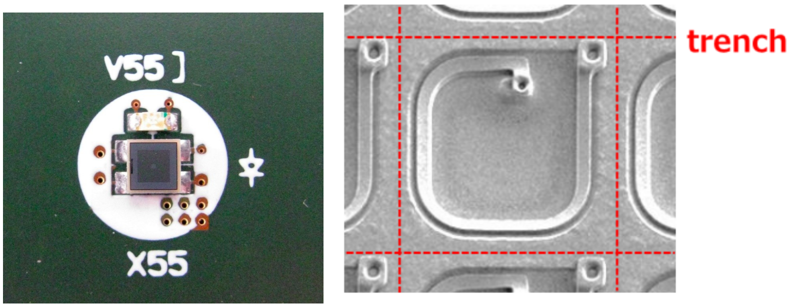

(a) (b)

Figure 2.11: (a) shows an image of Hamamatsu HDR-2 type SiPM with a 15 µm pitch while (b) shows an individual SPAD of a similar SiPM seen through a microscope taken from [53]. An optical trench separates each SPAD from the neighbouring SPADs in this generation of SiPMs.

A SPAD consists of a larger, lightly doped p-type (or n-type) layer sandwiched between a smaller, heavily doped n-type (or p-type) layer and a heavily doped p-type (or n-type) layer. This structure creates a depletion region between the p-type and n-type layers. A sketch of the SPAD structure is shown in fig. 2.12. The SPADs are connected in reverse-biased mode, with the sandwiched layers exposed to photons through a thin insulating layer. A photon that can penetrate the insulating layer enters the depletion region, which a valence electron absorbs. This absorption creates a free electron-hole pair via the photoelectric effect [54].

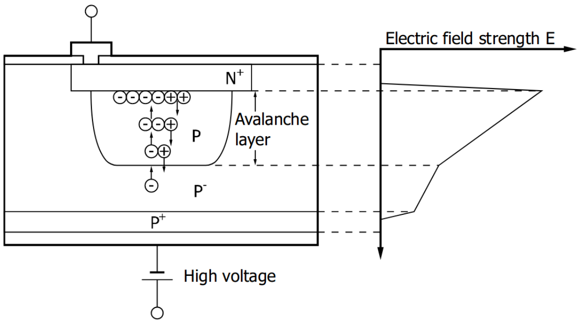

Figure 2.12: The avalanche region within a silicon SPAD alongside the strength of its electric field. Taken from [54].

SPADs consist of an avalanche region in which charge carriers are accelerated in the electric field, gain energy, and create more electron-hole pairs by secondary ionisation. This process repeats, creating even more electron-hole pairs, producing what is known as an avalanche. An avalanche will result in a current flow through the diode. The current is stopped or ”quenched” using a quenching resistor, which reduces the bias voltage (voltage supplied to the SiPM) and stops the avalanche. However, the SPAD remains saturated until the bias voltage returns to its original value. The time required for this recovery is called effective recovery time, and during this time, no further avalanches can occur in the SPAD.

The SPAD is operated in Geiger mode. That is, the amount of charge an avalanche would produce is independent of the energy of the initial photon. However, a SiPM consists of an array of such SPADs. If multiple photons create avalanches in different SPADs simultaneously, the SiPM will produce a signal whose integrated area (charge) is proportional to the number of SPADs undergoing Geiger discharges simultaneously. Therefore, the charge of the SiPM pulse produced is proportional to the number of photo-electron (p.e.) detected by the SPAD cells. If n number of micro-cells undergo avalanches, the signal will be n p.e.

Even though the charge produced in an avalanche is independent of photon energy, the detection efficiency of photons varies with the photon energy. Similar to PMTs, SiPMs are often coupled with scintillating materials. As explained in section 2.4.1.1, by changing the optical properties of the scintillators, the photon energy produced by scintillation can be shifted to the energies to which the SiPM is sensitive.

Listed are some of the most important properties of SiPMs discussed in this thesis.

2.4.2.1 Breakdown Voltage, Bias Voltage and Over-Voltage

The voltage above which avalanches can occur in a SiPM is the breakdown voltage (V_{br}). For the SiPM to function, a reverse bias voltage (also known as bias voltage V_{bias}) larger than the breakdown voltage must be supplied. The difference in voltage between V_{bias} and V_{br} is called over-voltage (V_{over}). That is:

$$V_{over} = V_{bias} - V_{br}. \tag{2.18}$$

For SiPM operation, the over-voltage must take a positive value. The avalanche produced in a SPAD cell is only stopped by the quenching resistor, which reduces the bias voltage to less than the breakdown voltage.

2.4.2.2 SiPM gain

The factor by which the charge of a single electron-hole pair created by the photoelectric effect multiplies during the avalanche is known as the gain of the SiPM. The gain is proportional to the over-voltage of the SiPM and is typically in the order of 10^6. The total charge (Q_{pix}) is given by [54]:

$$Q_{pix} = G \cdot e = C_{pix} \cdot (V_{bias} - V_{br}) = C_{pix} \cdot V_{over}. \tag{2.19}$$

where G is the gain, e is the electron charge and C_{pix} is the capacitance of a single pixel. C_{pix} depends on various properties of the SiPM, like the dimensions of the pixel or the doping profile. Since all cells are identical, ideally, the gain is the same regardless of the excited micro-cell. However, the gain may vary by a few per cent from micro-cell to micro-cell.

The gain of a SiPM can be measured using short pulses of low-intensity illumination of the SiPM. The photons produced by this source will simultaneously produce avalanches in a few pixels of the SiPM. Since the number of photons detected with each LED pulsed event differs, the charge collected by the pulses produces a multi-peaked Poisson-distributed spectrum known as a single photon spectrum (SPS). An example of such an SPS is given in fig. 2.13.

The first peak of fig. 2.13 gives the pedestal peak. This peak corresponds to the charge collected when the SiPM detects no photons. Since no signal is produced, the charge collected is the baseline charge determined by the SiPM and electronics when no signal is present. The second peak corresponds to the charge collected when the SiPM detects a single photon, while

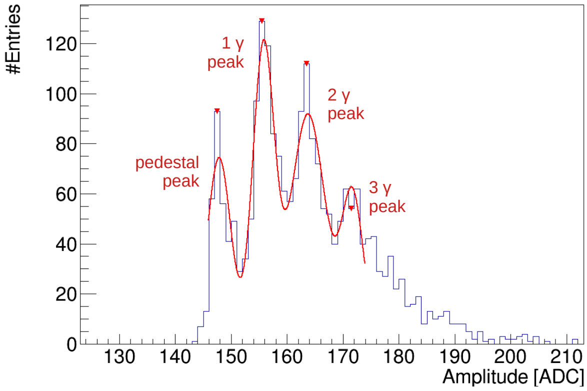

Figure 2.13: A single photon spectrum (SPS) obtained from a S14160 series SiPM produced by Hamamatsu Photonics K.K. (HPK) operated at an over-voltage of 6 V. The SiPM was on a Tilemodule prototype produced for the CMS HGCAL upgrade. The charge was obtained by sampling the signal's peak and converted using an analog-to-digital converter (ADC) to a digital value. Each peak corresponds to the number of photons detected by the SiPM.

the third and fourth peak corresponds to the charge collected when the SiPM detects two and three photons, respectively. Since the gain is defined as the charge amplification factor of a single SPAD avalanche, the gain is the distance between two consecutive photo-electron (p.e.) peaks.

2.4.2.3 Photon Detection Efficiency of the SiPM

The photon detection efficiency (PDE) is the probability of detecting a photon by a SiPM. Mathematically, PDE is the product of three factors [54].

- **SiPM fill factor:** ratio between the photosensitive area of the SiPM to the total SiPM area,
- **quantum efficiency:** efficiency at which a photon can produce an electron via photoelectric effect,
- **Geiger-mode avalanche probability:** probability of creating an avalanche from a single electron in the SPAD.

That is:

$$\text{PDE} = \text{Quantum Efficiency} \times \text{Fill Factor} \times \text{Avalanche Probability} \tag{2.20}$$

The PDE depends on the SiPM's over-voltage (V_{over}) and the wavelength (or energy) of the incoming photon. Information on the wavelengths the SiPMs are sensitive to, as well as the PDE dependence on over-voltage, is often shown in the datasheet of the SiPMs. The PDE vs. over-voltage and PDE vs. photon wavelength curves from the datasheet of the commercial HDR-2 SiPMs (S14160) produced by Hamamatsu Photonics K.K. (HPK) are given in fig. 2.14

as an example. Among the four SiPMs mentioned in this single datasheet, the S14160-1315PS SiPMs are the SiPMs that will be used in the HGCAL upgrade, but with a special radiation-hard packaging with improved thermal contact. The typical maximum PDE is between 400 nm and 500 nm wavelength.

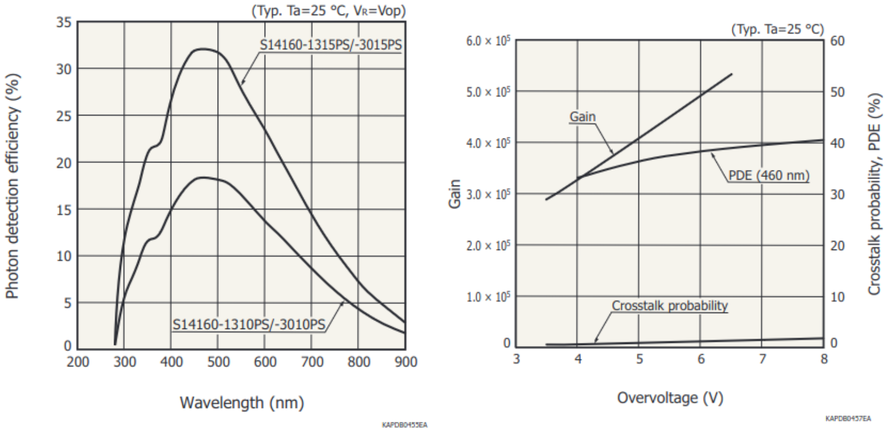

(a) (b)

Figure 2.14: Photon Detection Efficiency dependence on (a) photon wavelength and (b) over-voltage for HPK S14160-1315PS, -3015PS, 1310PS and -3010PS HDR-2 SiPMs. (b) also shows the increase in SiPM gain and crosstalk with over-voltage. Taken from [55]

The increase in gain with over-voltage is also shown in fig. 2.14 alongside the increase in crosstalk. See section 2.4.2.4 for more about sources of noise such as thermal noise, crosstalk and afterpulsing.

2.4.2.4 Noise in SiPMs

As explained previously, passing a photon through the active region of a SPAD micro-cell produces the SiPM signal as a flow of current through the SiPM. However, avalanches can occur in the SiPM cell for various reasons without detecting an externally produced photon. These are what are considered noise in SiPMs.

There are three main sources of noise in SiPMs. These are dark count, optical crosstalk and after-pulsing.

- **Dark Count:** An avalanche could occur due to the thermal excitation of an electron within the cell without the aid of photons. Such excitations are called dark counts. These avalanches will also produce a current flow through the SiPM (I_{dark}). The dark count is one of the primary sources of noise in SiPMs.

- **Optical Crosstalk:** Optical crosstalk occurs when electrons taking part in the avalanche release a photon by de-excitation. These photons can travel into neighbouring micro-cells, causing an avalanche in the micro-cell. The signals produced by these photons within the avalanche region of the neighbouring cell are indistinguishable from an externally produced photon signal.

- **After-pulses:** Electrons may be trapped in the silicon lattice's impurities during an avalanche process. These trapped electrons are released after a short delay (typically a few nanoseconds) and would cause further avalanches. These types of signals are known as after-pulses. Due to the delay in producing the avalanche, this type of noise is distinguishable from the signal.

The SiPM noise is often measured in terms of Dark Count Rate (DCR), which measures the rate of noise pulses produced per second. That is:

$$\mathrm{DCR} = \frac{N_{noise}}{\Delta t} \tag{2.21}$$

where N_{noise} is the number of avalanches produced from sources of SiPM noise in a time period of Δt. Shown in fig. 2.15 is a measurement counting the number of avalanches occurring in a SiPM in a dark environment. The trigger threshold is increased from below the pulse height of a single p.e. up to the height of a few p.e. The count reduces as the discriminator threshold increases in the form of a step function. For this particular SiPM, DCR at a threshold below 1 p.e. is measured to be around 100 kHz and is primarily dominated by the dark count. For higher thresholds, the noise is dominated by optical crosstalk.

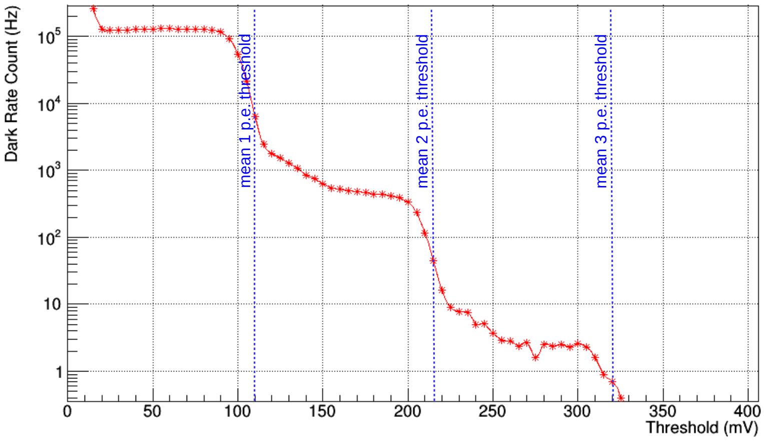

Figure 2.15: Measured dark count rate as a function of the discriminator threshold. Each blue vertical line corresponds to the mean amplitude of a SiPM signal due to the discharge of n microcells (in p.e. scale). The measurement of DCR was performed using an HPK S13360-1325PE SiPM at a V_{bias} of 55.0 V, taken from [43].

As after-pulsing or crosstalk stem from the same cell or neighbouring cell undergoing an avalanche, these noise types correlate with either the signal or the primary dark count pulse, which caused the primary avalanche. Therefore, they are sources of correlated noise. On the other hand, dark counts are due to random excitations and, therefore, are uncorrelated with the signal and follow Poissonian statistics. That is, for a system where dark count dominates noise,

$$\mathrm{Var}(N_{noise}) = \mathrm{E}(N_{noise}). \tag{2.22}$$

where $\mathrm{E}(N_{noise})$ and $\mathrm{Var}(N_{noise})$ are the expectation value (mean) and variance of the number of pixels excited in a period of Δt due to dark count, respectively. If one takes that square root of this,

$$\sigma(N_{noise}) = \sqrt{\mathrm{E}(N_{noise})}. \tag{2.23}$$

where $\sigma(N_{noise})$ is the standard deviation of the number of pixels excited due to dark count.

The SiPMs used for the HGCAL experiment have improved optical trenches, which reduces the crosstalk probability to less than 1 %. Therefore, crosstalk can be assumed to be negligible. Similarly, the SiPM signals after passing through a shaper are sampled at the peak, which reduces the probability of sampling an after-pulse to negligible amounts. This indicates that it is safe to assume negligible correlated noise sources.

The noise due to the various sources mentioned above broadens the pedestal peak. The most important factor for noise calculations in a single-photon detector application, as in the case of the SiPMs, is not the increment of N_{noise} but the fluctuations in N_{noise} around the pedestal. Therefore, for this application, the SiPM noise is defined as the standard deviation of the pedestal peak. Since the pedestal peak position is determined by $\mathrm{E}(N_{noise})$, from eq. (2.23):

$$\text{SiPM noise [p.e.]} = \sigma(N_{noise}) = \sqrt{E(N_{noise})}. \tag{2.24}$$

Since the SiPM amplifies the noise by a factor $G \cdot e$ where G is the gain of the SiPM, and e is the electron charge, the observable SiPM noise is given by:

$$\text{SiPM noise [C]} = \sigma(N_{noise}) \cdot G \cdot e = \sqrt{E(N_{noise})} \cdot G \cdot e. \tag{2.25}$$

Here, $\sigma(N_{noise}) \cdot G \cdot e$ is the width of the pedestal peak given in Coulombs. A current passing through the SiPM could indicate one of two scenarios. The first is the detection of photons, which results in a flow of photo-current (I_{photo}). The second is the leakage current flow due to SiPM noise (I_{leak}). That is:

$$I = I_{leak} + I_{photo}. \tag{2.26}$$

In a dark environment, if optical crosstalk probability and after-pulsing probability are negligibly small, the current passing through the SiPM I_{leak} can be formulated as:

$$I_{leak} = \frac{\mathrm{E}(N_{noise}) \cdot G \cdot e}{\Delta t}, \tag{2.27}$$

where $\mathrm{E}(N_{noise})$ is the mean number of cells undergoing avalanches in a period of Δt, G is the gain of the SiPM, and e is the electron charge. From eq. (2.25):

$$\text{SiPM noise [C]} = \sqrt{I_{leak}} \cdot \sqrt{G \cdot e \cdot \Delta t}. \tag{2.28}$$

This means that, in a light-tight environment, for a given over-voltage, if the SiPM gain does not change:

$$\text{SiPM noise [C]} \propto \sqrt{I_{leak}}. \tag{2.29}$$

Similarly, using eq. (2.24) and eq. (2.27), one can derive the relationship for SiPM noise in p.e. as:

$$\text{SiPM noise [p.e.]} = \sqrt{I_{leak}} \cdot \frac{\sqrt{\Delta t}}{\sqrt{G \cdot e}}, \tag{2.30}$$

which again results in eq. (2.29) for a SiPM type with the same gain.

In reality, the SiPM is read out using onboard electronics. The noise on onboard electronics could also contribute to the increase in noise of the system. That is:

$$\text{Total Noise} = \text{SiPM Noise} + \text{Electronic Noise} \tag{2.31}$$

Therefore, the total noise is derived from eq. (2.29) as:

$$\text{Total Noise} = A \times \sqrt{I_{leak}} + B \tag{2.32}$$

where A is a proportionality factor and B is a constant. A is primarily due to the SiPM noise, while B is due to the electronic noise contribution.

2.4.2.5 SiPM Pitch Size

The distance between the centres of two adjacent micro-cells is known as the pitch size or pitch for short. A smaller pitch describes a smaller micro-cell, while a larger pitch describes a larger micro-cell. Typical pitch sizes of SiPMs could range from small values such as 10 µm to more than 250 µm. The SiPMs discussed in this thesis will primarily focus on SiPMs with a pitch size of 15 µm as these SiPMs will be used in the HGCAL upgrade.

2.4.2.6 Linearity and Dynamic Range of the SiPM

The SiPM is a photo-detector optimised to detect single photons. In high illumination, the probability of multiple photons passing through the same micro-cell increases. Since the micro-cell works in Geiger mode, this results in a single avalanche despite multiple photons passing through the micro-cell. If every pixel has been fired, no further detection is possible until the SiPM recovers. In a dark environment, the noise from the SiPMs dominates.

The linearity of the SiPM is the range in which a proportionality exists between the number of photons impinging on the SiPM and the number of photons detected by the SiPM. The dynamic range is the ratio between the upper and lower limits of the linearity region [54].

The linearity exists for only a small percentage of the number of pixels firing. An experimental observation of linearity [56] is shown in fig. 2.16, which shows this phenomenon. However, it is possible to use dedicated setups with a laser system to measure the deviation from linearity for the SiPM of interest and use the curve to account for this linearity deviation.

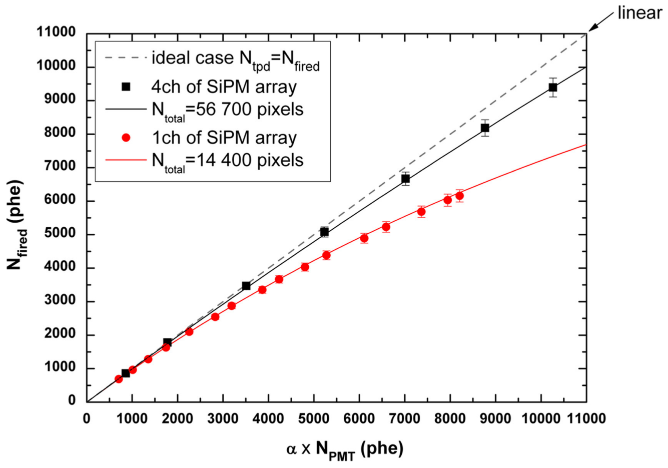

Figure 2.16: The number of single photon avalanche photo-diode cells in a SiPM fired (N_{fired}) vs. the number of photo-electrons detected by a photomultiplier tube (N_{PMT}) as observed by Grodzicka et al. [56].

The number of cells in the SiPM can also estimate the linearity. As the number of cells increases and the pitch size of the SiPM decreases, the probability of photons exciting the same micro-cell as the micro-cell decreases. This reduction in probability effectively pushes the upper bound of the linearity. Similarly, reducing the probability of noise pushes the lower bound of the linearity even lower. The combination of the two results in an increase in dynamic range.

2.4.2.7 Radiation Effects in SiPMs

Two major types of damage apply to silicon-based sensors such as SiPMs. They are bulk damage due to non-ionisation energy loss (NIEL) and surface damage due to ionisation energy loss (IEL).

Bulk damage is primarily produced by high-energy particles (protons, pions, electrons and photons) and neutrons, which can displace atoms from their lattice site, creating a vacancy in the lattice. These displaced atoms are often called primary knock-on atom (PKA). The PKA can rest at an interstitial site (interstitial defect or fixed point defect). If the kinetic energy of a PKA is sufficiently high, it can displace additional atoms, creating a cluster defect. For much higher PKA energies, multiple-cluster defects can also form. The energy threshold for the creation of a PKA is $\sim$25 eV while the thresholds for the production of cluster defects are $\sim$35 keV for neutrons and protons, and $\sim$8 MeV for electrons [57, 58].

Both point defects and clusters can severely affect the detector performance, depending on their concentration, energy level and the individual electron and hole capture cross-section. Figure 2.17 gives an overview of these processes. Defects create deep energy levels in the middle of the forbidden gap, which act as recombination/generation centres. This results in increased leakage current and dark noise in the SiPM. The high cell occupancy due to the high generation-recombination rate and limited cell recovery time causes a reduction of the PDE. Large leakage current also increases the p-n junction temperature and high power consumption. Defects can also remove dopants in the substrate, changing the doping concentration and increasing the breakdown voltage of the SiPM. Finally, such defects could also act as trapping centres, affecting the charge collection efficiency. These charge-trapping centres could be found in the bulk and the dielectric-silicon interface (SiPM entrance window) and can reduce the PDE of the SiPM [58–60].

Surface damage is primarily produced by photons with energies below 300 keV and charged particles. These particles produce charge-trapping centres on the SiPM entrance window, resulting in a leakage current flow due to IEL. Therefore, the final leakage current observed is a combination of both the leakage currents originating from surface and bulk damage sources.

2.4.2.8 Determination of SiPM Breakdown Voltage

In the most basic definition, the voltage above which avalanches could occur in SPADs is the breakdown voltage. This value can be measured in multiple ways. However, the values obtained from different measurement techniques do not necessarily agree. Two such techniques are widely discussed in this thesis. The first is the V_{br} definition based on the SiPM gain measurement, and the second is a V_{br} definition based on the relationship between current and bias voltage measurements (I-V curves) [54].

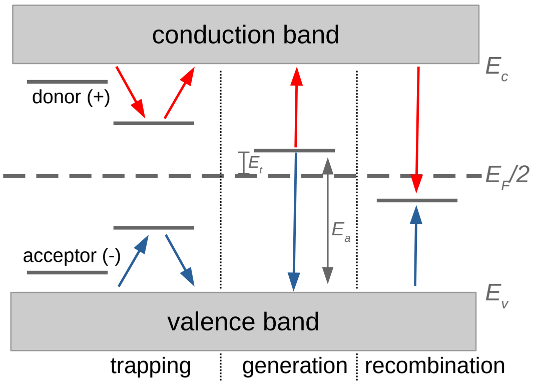

Figure 2.17: Schematic of possible band gap defects in silicon, including in SiPMs. The red lines indicate the movement of electrons and the blue ones of holes.

- **Determination using SiPM Gain (V_{br}(TO))**: As given by eq. (2.19), the SiPM gain is proportional to the difference between bias and breakdown voltages. The over-voltage gives this difference in voltages. Therefore, the SiPM gain has a linear relationship with over-voltage, and the breakdown voltage is the voltage at which the SiPM gain becomes zero. That is:

$$G \propto (V_{bias} - V_{br}), \tag{2.33}$$

  if $G = 0$, then $V_{br} = V_{bias}$. Therefore, the breakdown voltage can be determined by measuring the SiPM gain for different bias voltages and using a linear fit to extrapolate the voltage at which the SiPM gain becomes zero. Often, this is also referred to as turn-off voltage (V_{br}(TO)), and this is the default definition of breakdown voltage used in this thesis.

- **Relative Derivative Method using I-V curves (V_{br}(IV))**: I-V curves obtained from SiPM are used in several different breakdown voltage definitions. One of these definitions is the breakdown voltage defined by the relative derivative method. The relative derivative breakdown voltage is defined as the voltage where the dependence of the current on the voltage is the highest [61]. That is:

$$V_{br} = \left(\frac{1}{I} \cdot \frac{dI}{dV_{bias}}\right)_{peak}. \tag{2.34}$$

The numerical value difference between the two defined breakdown voltages solely depends on the SiPM type. HPK quotes V_{br}(TO) as breakdown voltages of the SiPMs. However, measuring V_{br}(TO) takes much more time than measuring the IV curves for a batch of SiPMs. As a result, HPK measures V_{br}(TO) and V_{br}(IV) for one SiPM in a batch of SiPMs, measures V_{br}(IV) for the rest of the SiPMs and uses the offset between the two definitions measured for the first SiPM to correct all breakdown voltages to the gain definition (V_{br}(TO)) for all individual SiPMs [54].

2.5 SiPM-on-Tile Technology

The SiPM-on-tile technology consists of a plastic scintillator tile wrapped in reflective foil on top of a SiPM. The SiPM is housed underneath a dome-shaped cavity at the centre of the scintillator, as shown in fig. 2.18(a) and fig. 2.18(b).

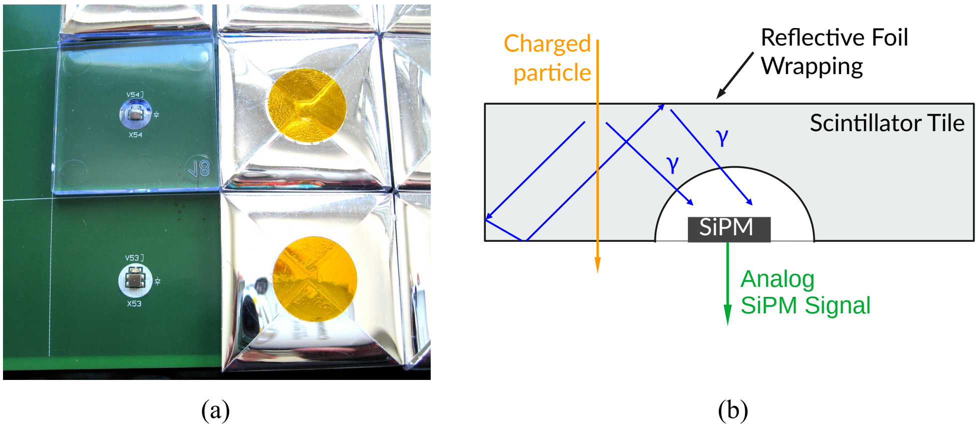

(a) (b)

Figure 2.18: SiPM-on-tiles produced for the CMS HGCAL scintillator section. (a) shows scintillator tiles with a central dimple, wrapped and unwrapped, mounted on a Tilemodule with SiPMs. (b) sketches the working principle of the SiPM-on-Tile.

A scintillator produces scintillation photons when a charged particle passes through the tile. The reflective foil wrapping reflects these photons in the SiPM placed underneath the dome-shaped cavity. Photons passing through the SPAD cells produce avalanches, producing the analogue SiPM signal. A sketch of this action is found in fig. 2.18(b).

The SiPM-on-tile technology was first introduced by the CALICE collaboration with the AHCAL prototype [11], which was developed for e^+ e^- colliders. The CMS collaboration later adapted this technology for the CMS HGCAL upgrade.

2.5.1 Light Yield of the SiPM-on-Tile

Section 2.3.2 defined how traversing charged particles lose energy in thin layers such as plastic scintillator tiles via ionisation. The particles' charge deposition in the scintillator is converted to photons detected by the SiPM pixels.

Most particles travelling through the scintillator behave like MIPs due to the thinness and low-Z nature of the scintillator. Therefore, the amplitudes of the MIPs as detected by the SiPM follow a convoluted Landau-Gaussian function as described in section 2.3.2. The maximum obtained from the fit is well-defined for MIPs due to its well-defined energy loss due to ionisation in thin materials if the MIPs travel perpendicular to the scintillator. Therefore, the most probable number of photons detected by the SiPM from a MIP traversing the scintillator tile in a perpendicular direction is defined as Light Yield.

SiPMs measure the charge deposition in Coulomb. The gain of the SiPM gives the charge measured by a single SiPM pixel discharge. Therefore, light yield can be defined mathematically as:

$$\text{Light Yield of SiPM-on-Tile [p.e.]} = \frac{\text{Most Probable Charge deposited by a MIP}}{\text{SiPM gain}}. \tag{2.35}$$

Light yield is a quantity measured in terms of the number of photons detected by the SiPM. Therefore, the unit used will also be p.e.. Light yield is a purely optical parameter independent of any electronic system used and solely depends on the SiPM, scintillator and tile wrapper properties. This makes light yield an excellent scale that can be used to calibrate the calorimeter.

Light yield is proportional to the PDE of the SiPM. That is:

$$\text{LY}\left(V_{over}\right) \propto \cdot\text{PDE}\left(V_{over}\right). \tag{2.36}$$

Multiple experiments observed that for a fixed over-voltage, the light yield (LY) is also inversely proportional to the square root of the scintillator area [62, 63]. This indicates that a better photon collection is present in smaller tiles than in larger tiles, leading to a better conversion of the energy depositions into electric signals. That is:

$$\text{LY} \propto \frac{1}{\sqrt{\text{Area of scintilator}}}. \tag{2.37}$$

For a given SiPM type with a fixed pitch size, the larger the SiPM's active area (or increased number of cells), the better the chance of detecting photons. Therefore, light yield can be given as:

$$\text{LY} \propto \frac{\text{SiPM area}}{\sqrt{\text{Area of scintilator}}}. \tag{2.38}$$

All of these light yield properties are valid if the properties of the scintillator tile, SiPM and reflective foil wrapping remain the same. In summary, the light yield can be modelled as follows:

$$\text{LY}\left(V_{over}\right) = k_1 \cdot \text{PDE}\left(V_{over}\right) \cdot \frac{\text{SiPM area}}{\sqrt{\text{Scintillator area}}}, \tag{2.39}$$

where k_1 depends on the SiPM, scintillator and foil wrapping properties.

Chapter 3

Phase II Upgrade of the CMS High Granularity End-Cap Calorimeter (HGCAL)

Since the discovery of the Higgs boson in 2012 [6, 7], many analyses have been conducted to measure its properties precisely. However, a large amount of data is required to reduce statistical uncertainties in the calculations.

By the end of 2025, the LHC is projected to collect an integrated luminosity of 450 fb^{-1} for each of the multi-purpose experiments ATLAS and CMS. The High Luminosity LHC (HL-LHC) phase will succeed the LHC phase and will aim to increase the integrated luminosity to about 3000 fb^{-1} collected during the LHC runtime.

To facilitate the conditions of HL-LHC under which the detectors will operate, the end-cap calorimeter of the CMS detector will be replaced with a 5D calorimeter known as the High Granularity Calorimeter (HGCAL). This chapter contains an overview of the HGCAL upgrade, especially the region containing scintillators and SiPMs for signal readout.

3.1 High Luminosity Upgrade of the Large Hadron Collider

The High-Luminosity LHC upgrade (HL-LHC) is a major upgrade of the LHC. In its scheduled 10-year operation of HL-LHC, the ATLAS and CMS detectors will collect an integrated luminosity of about 3000 fb^{-1}, which is close to seven times more than that collected in the scheduled 16-year operation of the LHC since 2009. The current plan of the LHC operation is shown in fig. 3.1 [8].

However, the increase in luminosity poses significant challenges for radiation tolerance and event pileup on detectors. An instantaneous luminosity of $7.5 \times 10^{34}\ \text{cm}^{-2}\text{s}^{-1}$ and an average pileup of 200 collisions/bunch crossing are foreseen at its peak. At the end of life, this results in many detectors, especially those close to the interaction point and beam pipe, accumulating a 1 MeV neutron equivalent fluence in silicon of $\sim 1 \times 10^{16}\ \text{n}_{\text{eq}}/\text{cm}^2$. As a result of being designed to work at much lower fluences, many detectors of the LHC require upgrade or replacement. For the CMS detector, this includes the following upgrades and additions:

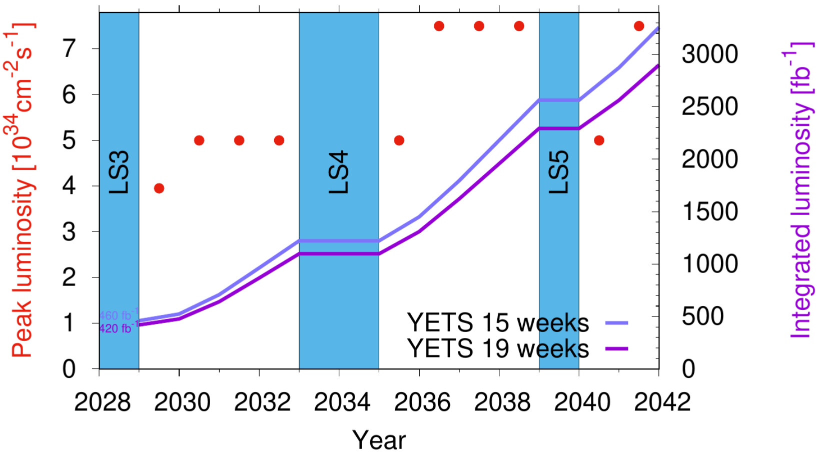

Figure 3.1: Latest luminosity estimates during the operation of the HL-LHC between 2028 and 2042 for the CMS and ATLAS experiments. The blue line depicts the expected integrated luminosity collected with 15 weeks of year-end technical stops (YETS), while the purple line depicts the expected integrated luminosity collected with 19 weeks of YETS. Taken from [8].

- **Inner Tracker: [64]**
    - replacement of the current inner tracker with new higher granularity silicon strip and pixel detectors,
    - extending the area of coverage from $|\eta| < 3$ to $|\eta| < 3.8$.
- **New MIP Timing Detector:** addition of a new MIP timing detector for high precision time reconstructions (timing resolution of 30 ps) [65],
    - with crystal plus SiPMs in the barrel region,
    - with low-gain avalanche detectors (LGAD) in the end cap.
- **Calorimeter:**
    - the upgrade of the ECAL crystal readout to allow precision timing for $e^{\pm}$ and γ at 30 GeV [66],
    - replacement of the end-cap with a new silicon and scintillator active region-based system [10].
- **Muon System: [67]**
    - the replacement of electronics associated with the drift tubes (DTs), resistive plate chambers (RPCs) and cathode strip chambers (CSCs) to facilitate the expected trigger rate of up to 750 kHz,
    - extension of the muon system coverage to $|\eta| < 3$ using new RPCs,
    - addition of new gas electron multipliers (GEMs).
- **Trigger System: [68, 69]**
    - upgrades the electronics and data acquisition systems to maintain the Level 1 (L1) Trigger, High Level Trigger (HLT) and data acquisition (DAQ) systems to work for a 750 kHz particle-flow-like selection rate.

Out of these upgrades of the CMS detector, the CMS end-cap calorimeter upgrade will be the focus of this thesis.

3.2 Introduction to the HGCAL Upgrade

As part of the HL-LHC upgrade at CERN, two new calorimeter end-caps will be installed in the CMS detector, containing a novel calorimeter with unprecedented transverse and longitudinal granularity. Therefore, this calorimeter is known as High Granularity Calorimeter (HGCAL). The high granularity and timing information allows particle shower reconstruction in five dimensions: three spatial coordinates, time and energy. The high granularity and timing information will aid in pileup rejection and allow for ”particle flow”-type energy reconstruction by associating tracks in the tracker systems to showers in the calorimeter [10].

As shown in fig. 3.2, each end-cap will consist of an Electromagnetic End-Cap Calorimeter (CE-E) composed of 13 double layers (26 layers) and 21 layers of a Hadronic End-Cap Calorimeter (CE-H). The entire CE-E section and the first eight layers of the CE-H will use silicon sensors as the active material. The last 14 layers of the CE-H will contain mixed layers of silicon sensors and scintillator-based readouts. The detector will cover a region of $1.5 < \eta < 3.0$.

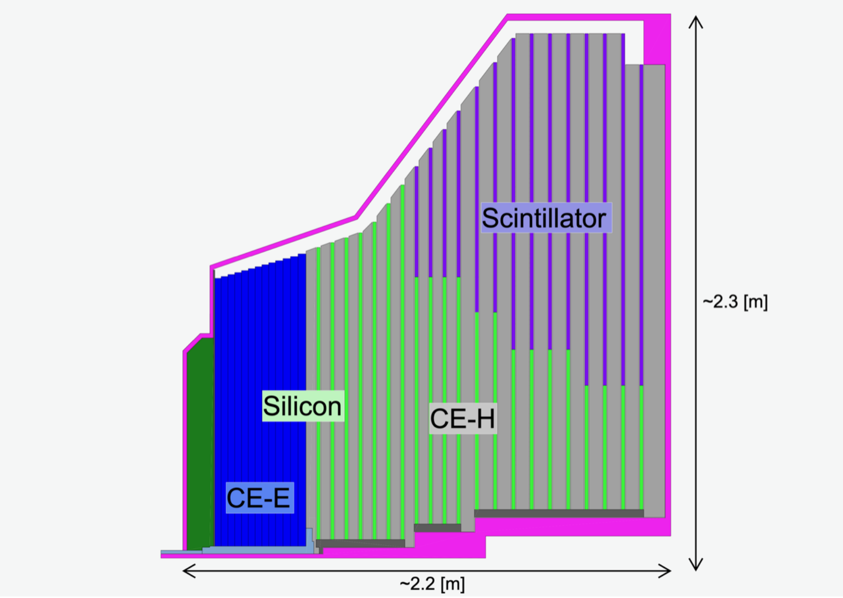

Figure 3.2: Schematic view of the CMS high granularity end-cap calorimeter. Taken from [70].

The silicon sensors will be hexagon-shaped with a cell area of $0.5\,\mathrm{cm}^2$ closer to the beam pipe for higher granularity and better particle separation. The sensors away from the beamline will have an area of about $1.1\,\mathrm{cm}^2$. The thickness of these sensors also varies as 120, 200 and 300 µm based on the expected fluence at the end of the detector lifetime. A total of six million such cells in about $620\,\mathrm{m}^2$ of silicon will cover the silicon section of the HGCAL, making it the largest silicon-based detector in the world.

The scintillator section of the HGCAL will be based on SiPM-on-tiles (see section 2.5). Each SiPM-on-tile is a single detector channel in the scintillator section of the HGCAL. Due to their relative costs compared to silicon sensors, these detectors are cost-effective while maintaining a good performance.

Figure 3.3 show the cross sectional structure of a CE-E and CE-H layer as it was in the Technical Design Report (TDR). This layout still holds true with minor changes. As shown in fig. 3.3(a), two 2.1 mm^2 thick lead plates act as the primary absorber in the CE-E. In addition, 6 mm^2 copper plates are used for cooling while the baseplate of the silicon sensors is constructed with 1.4 mm^2 Cu-W layers. These layers act as secondary absorber plates in the CE-E. CE-E will cover a range of $27.7X_0$ and 1.5λ.

In the CE-H region (see figs. 3.3(b) and 3.3(c)), 4 cm and 6 cm thick stainless steel is used as the absorber plate. Though copper plates and Cu-W baseplates are used in the CE-H, given the difference in thicknesses, their contribution to shower creation is rather small. The CE-H will cover 8.5λ in the longitudinal direction.

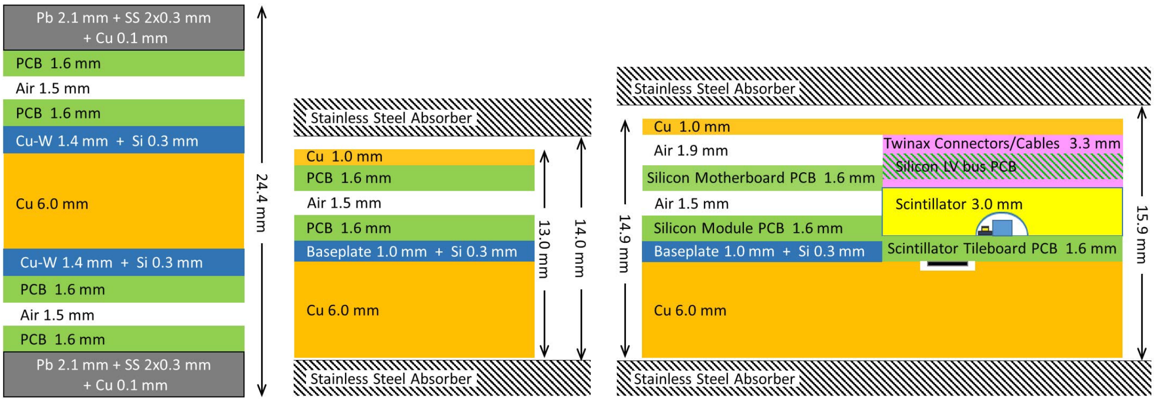
Pb 2.1 mm + SS 2x0.3 mm + Cu 0.1 mm
PCB 1.6 mm
Air 1.5 mm
PCB 1.6 mm
Cu-W 1.4 mm + Si 0.3 mm
Cu 6.0 mm
Cu-W 1.4 mm + Si 0.3 mm
PCB 1.6 mm
Air 1.5 mm
PCB 1.6 mm
Pb 2.1 mm + SS 2x0.3 mm + Cu 0.1 mm
24.4 mm
Stainless Steel Absorber
Cu 1.0 mm
PCB 1.6 mm
Air 1.5 mm
PCB 1.6 mm
Baseplate 1.0 mm + Si 0.3 mm
Cu 6.0 mm
13.0 mm
14.0 mm
Stainless Steel Absorber
Stainless Steel Absorber
Cu 1.0 mm
Air 1.9 mm
Twinax Connectors/Cables 3.3 mm
Silicon LV bus PCB
Silicon Motherboard PCB 1.6 mm
Air 1.5 mm
Scintillator 3.0 mm
Silicon Module PCB 1.6 mm
Baseplate 1.0 mm + Si 0.3 mm
Scintillator Tileboard PCB 1.6 mm
Cu 6.0 mm
14.9 mm
15.9 mm
Stainless Steel Absorber

(a) (b) (c)

Figure 3.3: Schematic cross-sections of the three different sections in the CMS end-cap: (a) the CE-E region consisting of silicon-based active layers and Pb/Cu-W/Cu absorber layers, (b) the CE-H silicon sensor section with stainless steel absorber layers, and (c) the CE-H mixed silicon/scintillator cassette with stainless steel absorber layers. Cu is used as the cooling plate. Taken from [10].

Both silicon sensor-based calorimetry and SiPM-on-tile technologies were first developed by the CALICE collaboration for the proposed International Linear Collider (ILC) to be built in Japan [11], which was then adopted by the CMS collaboration [10]. HGCAL will operate in an area where the magnetic field can reach 4 T, prohibiting the use of magnetic materials and magnetic-sensitive components. The non-magnetic nature of the SiPMs, scintillators, silicon sensors, and all other components used was a reason for using them for the HGCAL upgrade. SiPMs and scintillators are also much cheaper than silicon sensors, making them an attractive solution to limit the cost of the detector overall.

3.3 The Scintillator Section of the CMS HGCAL

As mentioned previously, the scintillator section will cover the outer area in the last 14 layers of the CE-H region. An overview of this region is described below.

3.3.1 SiPM-on-Tile Sensors

The scintillator section of the HGCAL will be based on SiPM-on-tile technology (see section 2.5). Each plastic scintillator is trapezoidal in shape and increases in area from 4 cm^2 to 32 cm^2 with increasing radial distance to the beam axis. They are wrapped in 3M Enhansed Specular Reflector (ESR) [71], which boasts a high reflectivity well above 98 %. The wrapped plastic scintillator tile will be placed on top of a SiPM such that the SiPM is housed within a circular cavity at the centre of the scintillator, referred to as the dimple. Shown in fig. 2.18(a) are a few such scintillator tiles (wrapped and unwrapped in reflective foil) placed on top of SiPMs.

The scintillator section of the HGCAL will use the novel HDR-2 SiPMs produced by HPK. This SiPM offers a higher dynamic range than its predecessors due to the improved trenches for optical insulation, reducing crosstalk and after-pulsing probabilities to less than 1 %. Additionally, this SiPM offers improved PDE compared to previous generations of SiPMs of similar size [53]. Typically, the PDE suffers if the cell size decreases due to the reduction of the fill factor. For calorimetry, dynamic range is as important as PDE. The improvement of both PDE and dynamic range simultaneously makes the novel HDR-2 SiPMs ideal for the needs of the HGCAL upgrade. Figure 2.11 shows a sketch of this device.

Though the commercially available version of these SiPMs (S14160 series [72]) are not radiation hard, HPK has produced several custom-made packaging for the HDR-2 type SiPMs over the years for the HGCAL upgrade [72, 73]. These custom-made radiation-hard packages are particularly tolerant to surface damage caused by ionisation energy loss (IEL). As a result, the leakage current due to IEL in the case of the HGCAL SiPMs is considered negligibly small. See section 2.4.2.7 for an overview of SiPM radiation damage. The breakdown voltage is at 38 V for these devices at a temperature of 25 °C. They can be used at any temperature between $-40\,^{\circ}\mathrm{C}$ to 60 °C with the breakdown voltage changing with a 37.5 $\mathrm{mV/K}$ temperature coefficient with respect to the breakdown voltage measured at 25 °C [74].

HPK has produced a variety of HDR-2 SiPMs varying in pitch size. Two main pitch sizes were considered over the years: 10 µm and 15 µm. The 15 µm devices were ultimately chosen to be used in the detector due to the better PDE and SiPM gain in comparison to the 10 µm devices.

Similarly, HDR-2 devices were also produced in several photosensitive areas, including SiPMs with $1.4 \times 1.4\,\mathrm{mm}^2$, $2 \times 2\,\mathrm{mm}^2$ and $3 \times 3\,\mathrm{mm}^2$ area. Initially, $1.4 \times 1.4\,\mathrm{mm}^2$ and $2 \times 2\,\mathrm{mm}^2$ devices were considered for the detector. However, subsequent measurements in light yields using Tilemodules discussed in this thesis resulted in the replacement of $1.4 \times 1.4\,\mathrm{mm}^2$ with $3 \times 3\,\mathrm{mm}^2$ SiPMs in the proposed detector layout.

A low-intensity LED is mounted next to each SiPM and is to calibrate the SiPM. Such calibrations are used to calculate the light yields of SiPM-on-tiles on the Tilemodules.

3.3.2 HGCAL Tilemodules and Layout

The current version of the SiPM HGCAL layout includes 42 different scintillator rings. Every pair of scintillator rings will have the same scintillator tiles to simplify the production of tiles on a large scale. Ring zero (R0) and ring one (R1) are the smallest scintillator tiles with an area of 5.3 cm^2. The largest scintillators are in ring 40 (R40) and ring 41 (R41) and have an area of 30.4 cm^2.

More than 240,000 detector channels and a scintillator area of about 360 m^2 will cover the scintillator section of the HGCAL. The scintillator section will be limited to areas where the expected 1 MeV equivalent neutron fluence at an integrated luminosity of 3000 fb^{-1} (expected end-of-life conditions) is less than $5 \times 10^{13}\, n_{eq}/cm^2$. The areas where this fluence is achievable were obtained using FLUKA simulations conducted by the CMS collaboration as shown in fig. 3.4 [10]. The selection criteria for this fluence value was entirely based on the achievable signal-to-noise ratio (SNR) at the end of life for MIPs (see section 3.7).

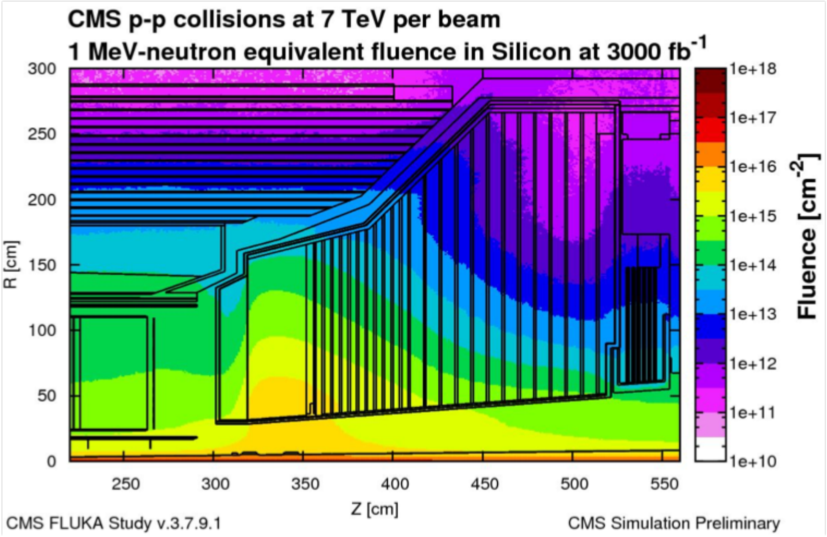

Figure 3.4: CMS FLUKA study showing the area of the HGCAL showing the 1 MeV equivalent neutron fluence in silicon at the end of life. The scintillator section is limited to the area where the expected fluence is below $5 \times 10^{13}\, n_{eq}/cm^2$. Taken from [10]

The scintillator detector module, also known as the Tilemodule, similar to the scintillator tiles themselves, increases in size radially from the beam pipe. Shown in fig. 3.5 is a Tilemodule partially equipped with SiPMs and scintillators.

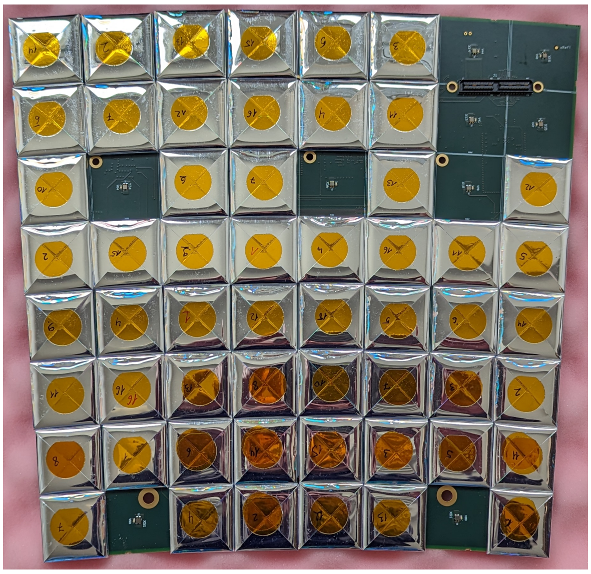

Figure 3.5: A D8 Tilemodule partially equipped with scintillators.

In total, 240,000 detector channels and a scintillator area of about 370 m^2 will cover the scintillator section of the HGCAL. Due to their relative costs compared to silicon sensors, these detectors are cost-effective while maintaining a good performance.

Eight major geometries of Tilemodules cover all positions in the $10\,^\circ$ detector units (SiPM-on-tile units) and the different layers. The Tilemodule sizes range from about $21 \times 15\,\text{cm}^2$ to $45 \times 42\,\text{cm}^2$. Depending on the size of the Tilemodule and its positioning on the HGCAL detector, the geometries are labelled as Tilemodule types A, B, C, D, E, G, J and K. Apart from the alphabet letter, the Tilemodules also come with a number. This number symbolises the number of rings the Tilemodule covers. Each ring on a Tilemodule will consist of 8 channels. For example, a B12 Tilemodule will be placed at a distance of 1082.99 mm from the beamline and will cover 12 rings and have eight columns of tiles. Figure 3.6(a) shows the Tilemodules used in a 10° sector.

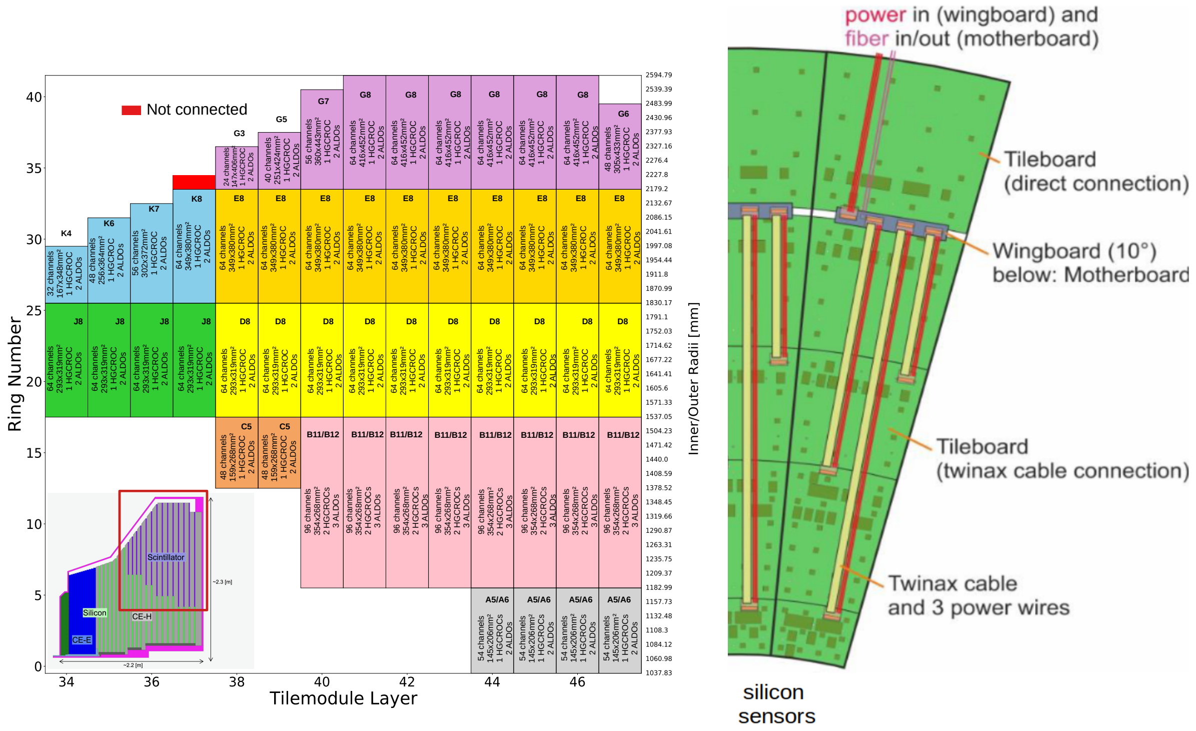
Not connected
Ring Number
Tilemodule Layer
Inner/Outer Radii [mm]
0
5
10
15
20
25
30
35
40
34
36
38
40
42
44
46
K4
K6
K7
K8
J8
G3
G5
G7
G8
G6
E8
D8
C5
B11/B12
A5/A6
32 channels
167x348mm²
1 HGCROC
2 ALDOs
64 channels
293x319mm²
1 HGCROC
2 ALDOs
96 channels
354x268mm²
2 HGCROCs
3 ALDOs
54 channels
145x206mm²
1 HGCROCs
2 ALDOs
Scintillator
Silicon
CE-H
CE-E
2594.79
2539.39
2483.99
2430.96
2377.93
2327.16
2276.4
2227.8
2179.2
2132.67
2086.15
2041.61
1997.08
1954.44
1911.8
1870.99
1830.17
1791.1
1752.03
1714.62
1677.22
1641.41
1605.6
1571.33
1537.05
1504.23
1471.42
1440.0
1408.59
1378.52
1348.45
1319.66
1290.87
1263.31
1235.75
1209.37
1182.99
1157.73
1132.48
1108.3
1084.12
1060.98
1037.83
power in (wingboard) and
fiber in/out (motherboard)
Tileboard
(direct connection)
Wingboard (10°)
below: Motherboard
Tileboard
(twinax cable connection)
Twinax cable
and 3 power wires
silicon
sensors

(a) (b)

Figure 3.6: (a) shows the base layout of Tilemodule geometry to be used in the HGCAL. The alphabet letter symbolises the different types of Tilemodules, generally categorised by the distance to the beamline, while the number symbolises the number of rings the Tilemodule covers. The Tilemodules shown here cover a $10\,^\circ$ sector. Thirty-six similar sectors (with minor variations) cover the scintillator section of a single end-cap. Two such end-caps exist in either direction of the beamline. (b) shows the top view of a $15\,^\circ$ sector showing only the scintillator Tilemodules, taken and modified from [75]. The Tilemodules in (a) corresponds to the Tilemodules in (b) at the same radial position.

Up to five Tilemodules placed one after the other radially from the beamline direction form a basic $10\,^\circ$ detector unit. One and a half such sectors are shown in fig. 3.6(b). Scintillator and silicon detector modules are assembled into common cassettes. A full cassette will cover $60\,^\circ$ and is the default cassette needed for the final assembly of the detector. These are also the default cassettes used in the CE-E. A half cassette will cover $30\,^\circ$ and is the default size used in the CE-H. Three $10\,^\circ$ detector units are combined to form a half cassette, and two half cassettes are combined to form a full cassette during assembly. Six such full cassettes close the ring around the beampipe. They will operate at a temperature of $-30\,°\mathrm{C}$ and under hypoxic conditions (about 3 % O_2) with CO_2 used for cooling.

The current layout of the Tilemodules has been optimised to get the best SNR during the detector operation period with information obtained from studies done in the past. However, many studies conducted, including those performed in the scope of this thesis, will impact the final layout of the HGCAL scintillator detector area. One of the main motivations of this thesis is to optimise the detector layout to ensure its performance based on SNR requirements until the detector's end of life (see section 3.7).

3.3.3 Front-End Electronics

Each Tilemodule comprises one or two readout chips known as High Granularity Calorimeter Read-Out Chip (HGCROC). Each HGCROC has 72 data channels and can read data from up to 72 SiPM-on-tiles. The exact number of detector channels could vary between 40 and 96 for the different board sizes, though the vast majority have 64 detector channels or less. Therefore, the majority of the Tilemodules use a single HGCROC. In Tilemodules that have more channels, two HGCROCs will be used. Currently, only B-type tileboards will consist of more than a single HGCROC.

Within a basic 10 ° detector element, all signals to and from the Tilemodules, as well as the power, are exclusively provided through a single connector as shown in fig. 3.6(b). Twin-axial cables for the fast differential signals and individual wires for the supply voltages connect the Tilemodules in a 10 ° sector to the motherboard via an intermediary board known as a wingboard.

The motherboard consists of two types of concentrator chips, ECON-D and ECON-T, as shown in section 3.3.3. Information from each HGCROC is sent via two data e-links (at 1.28 Gbps each) and four trigger e-links (at 1.28 Gbps each) to the ECON-D (data) and two ECON-Ts (trigger) on the motherboard respectively. The ECON-D performs a zero suppression and concentration of the data from the HGCROCs before transmitting the data at rates up to 1.28 Gbps. The ECON-Ts, which obtain trigger information from the HGCROCs, select and compress interesting HGCROC trigger data according to preprogrammed trigger algorithms in real-time and transmit this data at rates up to 1.28 Gbps. Data from the ECON-D is collected at one Low Power GigaBit Transceiver (LpGBT) ASIC, while the data from the two ECON-Ts are collected at the second Low Power GigaBit Transceiver (LpGBT) ASIC. The information is sent to the back-end via the VTRX+ chip, which optically transmits the data via optical fibres to the back-end DAQ FPGA located in the service cavern. The back-end generates the L1-trigger, which, alongside the 320 MHz clock, slow and fast commands are sent via the VTRX+ to one of the LpGBT. This LpGBT distributes the clock, slow and fast commands, and the L1-trigger information to the rest of the front-end electronics as shown in section 3.3.3.

The Tilemodules also host the Giga-Bit Transceiver - Slow Control Adapter (GBT-SCA) chip, responsible for all slow control tasks. This includes monitoring the bias voltages provided to the SiPMs, the LED system (used for light yield calibrations) and the other onboard electronics, and monitoring the temperature of the Tilemodule and its components (via eight PT-1000 platinum temperature sensors onboard). The GBT-SCA is also responsible for configuring the HGCROCs onboard the Tilemodule.

Another essential regulator on the Tilemodule is the ALDO version 2 (ALDOv2) ASIC

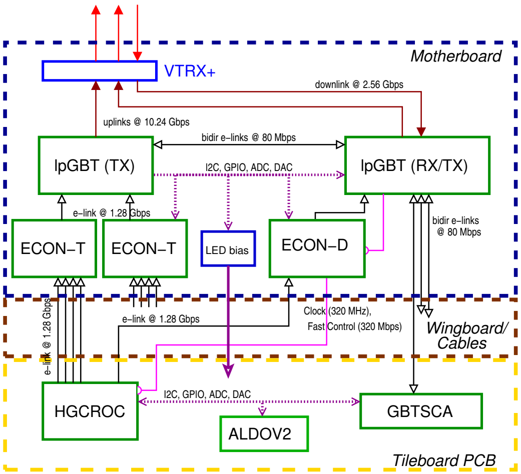
Motherboard
VTRX+
downlink @ 2.56 Gbps
uplinks @ 10.24 Gbps
bidir e–links @ 80 Mbps
lpGBT (TX)
I2C, GPIO, ADC, DAC
lpGBT (RX/TX)
e–link @ 1.28 Gbps
bidir e–links @ 80 Mbps
ECON–T
ECON–T
LED bias
ECON–D
e–link @ 1.28 Gbps
e–link @ 1.28 Gbps
Clock (320 MHz),
Fast Control (320 Mbps)
Wingboard/ Cables
HGCROC
I2C, GPIO, ADC, DAC
GBTSCA
ALDOV2
Tileboard PCB

Figure 3.7: The front-end electronics system of the scintillator section includes the relevant modules on which they lie (Tilemodules, Wingboard and Motherboard). Taken from [76].

regulator. The ALDOv2 ASIC [77] has become a central component of the Tilemodule's powering concept [75]. The ALDOv2 is an adjustable low dropout linear regulator capable of providing power via two low-voltage and two high-voltage outputs. The first low voltage output provides up to 3.3 V voltage with a maximum of 500 mA current. The second low voltage output provides up to 3.3 V voltage with a maximum of 20 mA current. The first out of these outputs will supply power to the components on the Tilemodule, except the SiPMs. The SiPM bias voltage is provided via the high voltage outputs of the ALDOv2. Each of the high voltage outputs can provide up to 70 V voltage and a maximum of 25 mA current. On a typical Tilemodule such as a D8 Tilemodule, the two high voltage ALDOv2 channels will power the SiPMs on the two halves of the Tilemodule. Though in the latest Tilemodule prototypes, the GBT-SCA steer the ALDOv2, in future Tilemodules, the HGCROC will steer the ALDOv2 chip.

At least two ALDOv2 regulators are foreseen to be used in each Tilemodule, with only the low voltage outputs used in the second ALDOv2 (hence referred to as ALDOv2 LV in this thesis). However, a third ALDOv2 may also be used in a few Tilemdoules to cope with the high leakage currents expected from the irradiated SiPMs towards the detector's end of life. The number of ALDO regulators on the current layout of the HGCAL scintillator Tilemodules are given in fig. 3.6(a).

3.4 HGCROC: Front-End Read Out Chip for the HGCAL

The HGCROC [13, 14] is the front-end electronic ASIC designed for the HGCAL upgrade. It is a mixed analogue and digital ASIC designed and implemented for the readout of signals from silicon sensors and SiPMs.

The HGCROC provides charge measurements via an analog-to-digital converter (ADC) for smaller amplitudes and time-over-threshold (TOT) measurement for larger amplitudes. The HGCROC also provides hit time information with a time-of-arrival (TOA) measurement. The HGCROC can read the charge and timing information from up to 72 readout sensors using two 1.28 Gbps electronic links. Four 1.28 Gbps trigger links also send summed and compressed data on the deposited charge used for the Level-1 trigger generation.

The HGCROC also comes in two versions, one to read out data from the hexagonal silicon sensors and another to read out data from the SiPM-on-Tiles. The HGCROC made for the SiPM can send short pulses to the LED system to emit a few photons to calibrate the SiPMs. Apart from this and the presence of the current conveyor mentioned later, the HGCROC versions made for the different sensors are identical.

The earliest generation of readout chip used in silicon was the SKIROC_CMS, inspired by the SKIROC chip developed by the CALICE collaboration for the SiW prototype calorimeter. Similarly, the earliest generation Tilemodules featured the AHCAL prototype calorimeter developed by the CALICE collaboration, which contained a SPIROC as the readout chip [78]. Omega Microelectronics developed the SKIROC and SPIROC chips within the CALICE collaboration [11, 79], targetting future electron-positron colliders. The SKIROC and SPIROC chips were first adapted into the SKIROC_CMS to contain a 40 MHz LHC-like readout and then to the two iterations of HGCROC by Omega Microelectronics. These iterations were called HGCROCv2 [13] and HGCROCv3 [14] and were used to read SiPM-on-tiles on the Tilemodules discussed in this thesis.

The HGCROCv2 and HGCROCv3 have an analogue front-end, a mixed signal block and digital blocks. Figure 3.8 illustrates these blocks for HGCROCv3 . HGCROCv2 has a similar block structure, with minor differences explained in the coming sections.

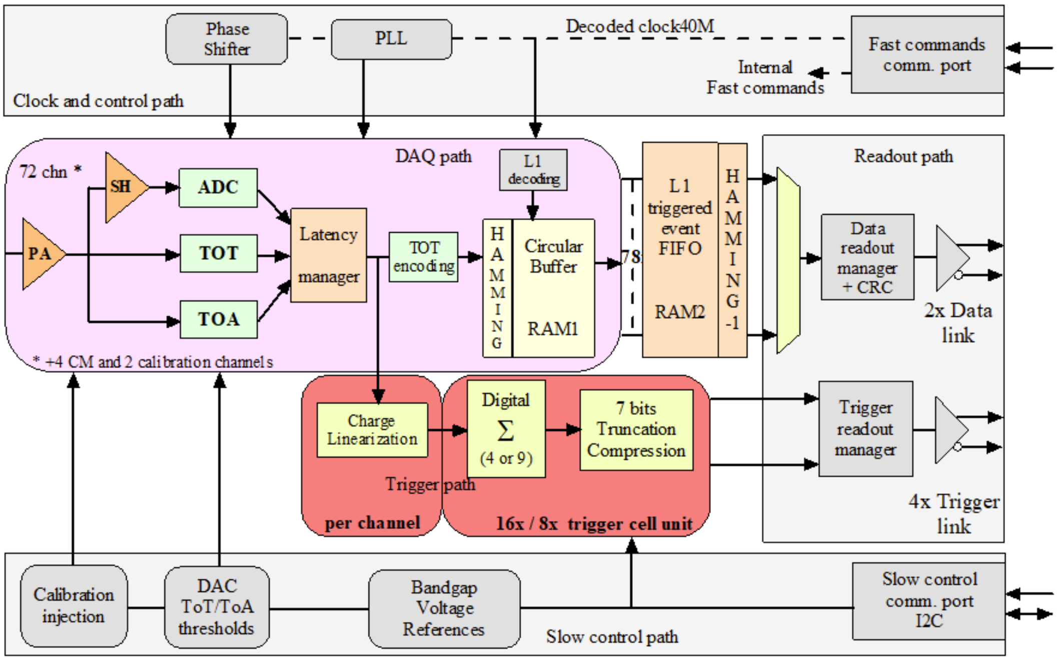
Phase Shifter
PLL
Decoded clock40M
Fast commands comm. port
Internal Fast commands
Clock and control path
72 chn *
SH
ADC
PA
TOT
TOA
DAQ path
L1 decoding
Latency manager
TOT encoding
HAMMING
Circular Buffer
RAM1
78
L1 triggered event FIFO
RAM2
HAMMING-1
Readout path
Data readout manager + CRC
2x Data link
* +4 CM and 2 calibration channels
Charge Linearization
Digital Σ (4 or 9)
7 bits Truncation Compression
Trigger path
per channel
16x / 8x trigger cell unit
Trigger readout manager
4x Trigger link
Calibration injection
DAC ToT/ToA thresholds
Bandgap Voltage References
Slow control path
Slow control comm. port I2C

Figure 3.8: Block diagram of the HGCROCv3. Taken from [14]

3.4.1 The Analogue Front-End

The analogue front-end of the HGCROC comprises three distinct sub-parts: a low-noise preamplifier, a shaper and two discriminators [13, 14].

- **The low-noise preamplifier (PA):** The preamplifier converts the input charge from the SiPM signal to a voltage output with the best SNR and a sufficiently adjusted gain tuned to the MIP signal. The signal must be sufficiently short to mitigate the Out-of-Time pileup effect at the shaper output. This stage comprises two blocks.

The first block contains a **current conveyor** with variable gain. The signals from SiPMs are much larger than those obtained from silicon sensors. Since the rest of the HGCROC used for the SiPM-on-tile and silicon sections are identical, the SiPM signals must be scaled down to be compatible with their counterparts. This dampening of the analogue signal is performed via a current conveyor. The current conveyor is controlled by a 4-bit HGCROC digital-to-analogue (DAC) parameter called conveyor gain (or ConvGain for short). The damping factor ranges from 0.025 (for ConvGain=1) to 0.375 (for ConvGain=15) of the initial signal. The availability of the current conveyor is one of the very few differences between the two different HGCROCs designed for the two different HGCAL sensors.

The second block is a charge variable preamplifier. Feedback capacitors (Cf and Cf_comp) and resistors (Rf) provide the gain and shape of the SiPM signal. The resulting signal is sent to the shaper if the amplitude is below the TOT discriminator threshold. If the signal amplitude exceeds this threshold, the feedback discriminator triggers and provides the charge measurement as a TOT. Another discriminator allows the timing information to be measured as a TOA.

- **The shaper (SH):** The shaper has three stages: A Sallen-Key filter, an RC^2 filter and a unity amplifier to drive the ADC. The signals from the SiPMs have a very short rise time, a longer fall time and a very narrow peak, making them prone to jitter and timing misalignments. The shaper aims to obtain a more Gaussian shape from the signal, i.e. broaden the peak such that it is insensitive to these effects, fix the rise time of the signal to about 15 ns and reduce the signal to less than 20 % of the peak value after a single clock cycle of 25 ns to limit the out-of-time pileup.

  The shaper also provides the ability for the user to set the pedestal level of the HGCROC via a channel-wise 6-bit parameter trim_inv (in HGCROCv3) and ref_inv_dac (in HGCROCv2). This parameter is useful when adjusting the pedestals of all channels of the HGCROC to a common value.

- **Two discriminators:** The two discriminators provide the thresholds for the TOT and TOA pulses mentioned in the preamplifier section. The TOT measures the time between when the TOA discriminator is triggered, and the time the TOT discriminator is triggered. Therefore, for a TOT measurement, both discriminators must be triggered. See section 3.4.4 for more information.

The output of the shaper is connected to an ADC, where the analogue voltage signal is converted to a 10-bit ADC value. When the TOT threshold has been triggered, the signal is sent directly from the preamplifier to a time-to-digital converter (TDC), where the TOT value is extracted from the pulse. A second TDC dedicated to extracting the timing information is also used to extract the TOA value. The sampled pulse maxima in ADC and the corresponding values of TOT and TOA taken with an HGCROCv2 are illustrated in fig. 3.9. This image shows the linear rise of the TOT after ADC saturation.

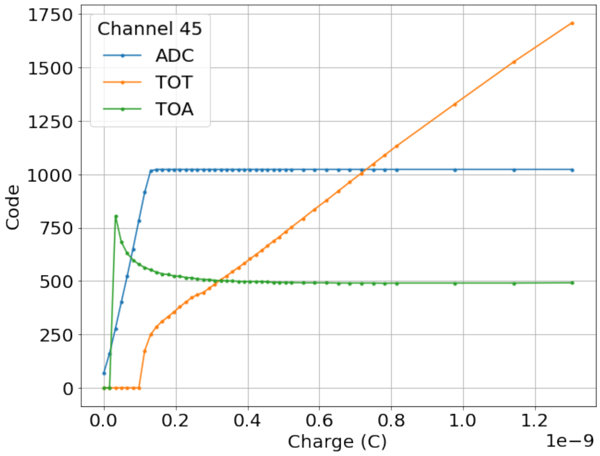

Figure 3.9: ADC, TOT and TOA variations with external charge injection via a pulse generator. The charge pulse was injected to a SiPM (channel 45) on a Tilemodule readout using an HGCROCv2.

3.4.2 The Mixed-Signal Block (Latency Manager)

The mixed-signal block (shown in fig. 3.8 as Latency Manager) consists of a 10-bit delay buffer to align the ADC data with the TOT and TOA. Signals which contain TOT and TOA data have latencies due to the duration of the TOT. Therefore, the delay buffer aligns the ADC with the TOT and TOA data by setting a latency to the ADC [13, 14].

3.4.3 The Digital Block

Following the mixed-signal block, ADC, TOT and TOA are fed into the same data readout path in the digital blocks. The main difference between the HGCROCv2 and HGCROCv3 is in these blocks. In HGCROCv2, the 10-bit ADC, 12-bit TOT and 10-bit TOA are saved as a single word using a circular buffer. In HGCROCv3, the 12-bit TOT is first compressed into 10-bits. The 10 MSBs are saved if TOT[11:9]>0, and the 10 LSBs are saved if TOT[11:9]=0.

Furthermore, HGCROCv3 also saves the ADC from the previous clock cycle (ADC-1) as a 10-bit word. This information is used mainly to determine if a charge from a previous event was present and, therefore, be able to correct it. Furthermore, if no charge is present, this information can be used for pedestal subtraction. ADC and TOT information is multiplexed depending on the TOT to keep the word length the same. If the signal has not reached the TOT threshold, the ADC is saved as a 10-bit word, and TOT is discarded. If the TOT threshold has been reached, the TOT is saved as a 10-bit word, and the ADC information is discarded. The HGCROC also has a mode where the complete 12-bit TOT word is saved instead of the ADC-1, which is advantageous for calibrating TOT to the ADC scale.

The 512-bit circular memory continuously stores the ADC-1, ADC or TOT and TOA information as a FIFO register. A Level 1 Accept (L1A) signal is required to send the data to the back-end. This signal is generated in the back-end when a potentially interesting event triggers the L1 trigger and is sent to the HGCROC via the LpGBT. When an L1A signal is received, the corresponding data in the buffer is read and sent via the two data links to the back-end DAQ system.

3.4.4 L1 Trigger and Signal Sampling

The HGCROC sums up the ADC and TOT information of every four or nine channels (depending on the HGCROC trigger mode) together and sent via four 1.28 Gbps trigger links to the ECON-T and back-end after every bunch crossing. An L1A signal is generated at the back-end only if the data meets the L1-trigger requirements. A fixed delay exists between the L1A signal obtained by the HGCROC and the data in the buffer corresponding to the L1 trigger. A delay is set between the L1A and the buffer to read the correct buffer data. This delay is adjusted in terms of two HGCROC parameters: the bunch crossing offset (or L1A Offset) and phase. The bunch crossing offset is the delay in the number of bunch crossings passed. The phase is for finer delay adjustments to sample the SiPM signal at its maximum. There are 16 phases between consecutive bunch crossing offsets. Once installed in the final experiment, the delays will be set for each of the SiPM-on-tiles to sample the signal at the expected signal maximum. Since the bunch crossing frequency is 40 MHz (or 25 ns), the phase frequency is 40×16 MHz (or $25/16$ ns). Therefore, the delay is given as follows:

$$\text{Delay [ns])} = \text{Bunch Crossing Offset} \times 25\,\text{ns} + \text{Phase} \times \frac{25}{16}\text{ns}. \tag{3.1}$$

The digital block works synchronously with the LHC block provided via the LpGBT. The phase delay between the L1A signal and data shifts the clock of the mixed signal block with respect to the clock of the digital block. The mixed signal block works in phase with this clock defined by the delay. Therefore, the ADC, TOT and TOA are measured with respect to this phase-shifted clock. The delay is set to sample the peak of the SiPM signal as an ADC value. The TOT and TOA are defined with respect to the discriminator thresholds. TOA is the time taken from the start of the previous bunch crossing till the signal crosses the TOA threshold in TDC units. The TOT is the difference in time between the point at which the signal crosses the TOA threshold until the signal falls below the TOT threshold. The TOA threshold must be set to a value less than the TOT threshold for this to work. These definitions are illustrated in fig. 3.10.

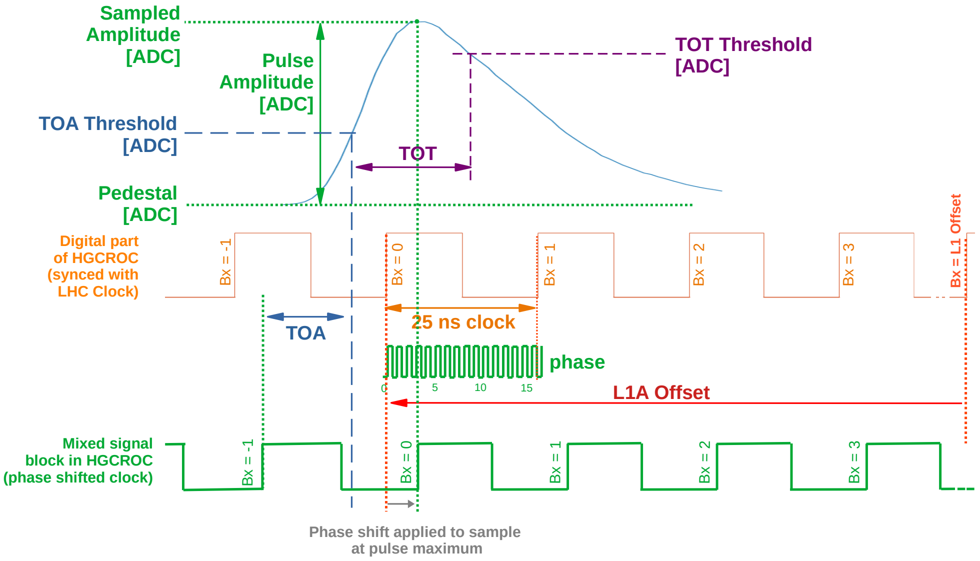
Sampled Amplitude [ADC]
Pulse Amplitude [ADC]
TOT Threshold [ADC]
TOA Threshold [ADC]
TOT
Pedestal [ADC]
Digital part of HGCROC (synced with LHC Clock)
Bx = -1
Bx = 0
Bx = 1
Bx = 2
Bx = 3
Bx = L1 Offset
TOA
25 ns clock
phase
0
5
10
15
L1A Offset
Mixed signal block in HGCROC (phase shifted clock)
Bx = -1
Bx = 0
Bx = 1
Bx = 2
Bx = 3
Phase shift applied to sample at pulse maximum

Figure 3.10: Definitions of ADC, TOT and TOA for a typical SiPM pulse.

This thesis only uses low amplitude signals in the ADC range. Therefore, the TOT and TOA are used sparingly in this thesis. However, the TOA is used to verify certain expectations, which are discussed in detail in the results sections.

3.5 Data Acquisition Systems used for Testing

To generate an L1A signal via the L1-trigger, the entire chain from the HGCROC to the front-end and back-end needs to be implemented. Using such an extensive setup for testing purposes is impractical for several reasons. Some of these electronic systems, such as the ECON-D, still need to be fully developed as of writing this thesis. Therefore, for testing purposes, the functionality of the back-end is given to a DAQ system. The DAQ system must be able to generate the L1A signal needed to acquire data from the SiPMs on Tilemodules (via the HGCROC) without using the trigger path and communicate with other onboard electronics like the GBT-SCA and the remote computer.

3.5.1 The KCU105 DAQ System

For the duration of this research, two such DAQ systems were used. The first system that accomplished the essential DAQ tasks was the FPGA-based commercially-produced KCU105 controller board produced by Xilinx Inc [80] as shown in fig. 3.11.

The connection between the Tilemodule prototype board (tileboard) and KCU105 DAQ is provided via a Twinax adapter connected via the Samtec QSH-DP connector on the front side of the tileboard. This connection provided the fast clock and commands and supplied a trigger signal to take data successfully. The DAQ was also able to configure the HGCROC to the parameters required. The block diagram of this interconnection is shown in fig. 3.12. The initial adapter was produced at Uni Minnesota, while later, similar adapters were produced in-house at DESY. The LED bias voltage and the bias voltage supplied to the SiPMs are also supplied via this adapter.

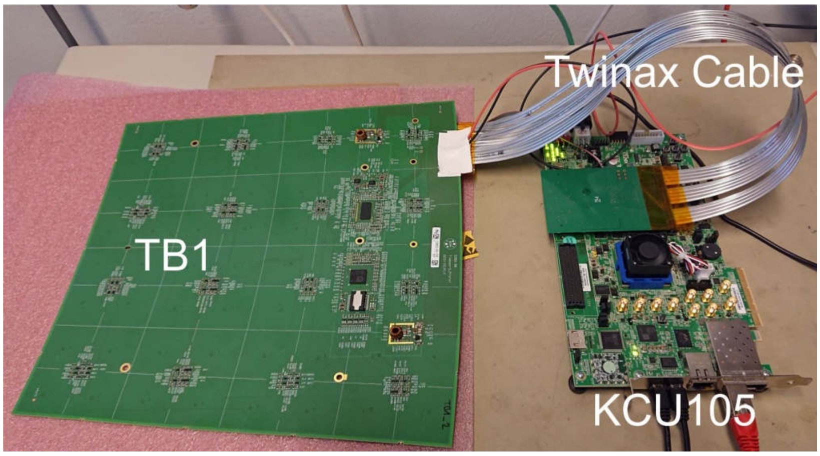

Figure 3.11: A Tilemodule in the typical setup with interconnection via Twinax cable to a DAQ FPGA module (KCU105). Taken from [81]

The firmware used on the KCU105 for the successful data acquisition from the tileboards was developed by the partner institutes OMEGA and LLR using the Xilinx Vivado software. The data-taking scripts were modified in-house at DESY to suit the experiment's needs.

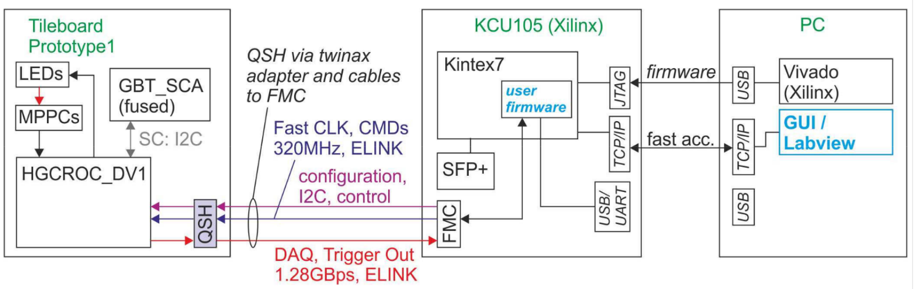
Tileboard Prototype1
LEDs
MPPCs
GBT_SCA (fused)
SC: I2C
HGCROC_DV1
QSH
QSH via twinax adapter and cables to FMC
Fast CLK, CMDs 320MHz, ELINK
configuration, I2C, control
DAQ, Trigger Out 1.28GBps, ELINK
KCU105 (Xilinx)
Kintex7
user firmware
SFP+
FMC
JTAG
TCP/IP
USB/ UART
firmware
fast acc.
PC
USB
TCP/IP
USB
Vivado (Xilinx)
GUI / Labview

Figure 3.12: Block-diagram of the typical interconnection of a Tilemodule to the KCU105 FPGA module (DAQ). Taken from [81]

As mentioned above, all slow control tasks like the configuration of the HGCROCs and the controlling and monitoring of supply voltages, temperatures and SiPM bias voltages are designed to be performed by the GBT-SCA on the Tilemodule. However, this was impossible to implement due to a lack of certain functionalities in the KCU105. Therefore, the HGCROCv2 was directly connected via the I^2C bus connection to the KCU105. Slow-control tasks such as temperature and voltage monitoring and SiPM bias voltage setting could not be done via the GBT-SCA.

As the KCU105 DAQ system cannot communicate with the GBT-SCA, the SiPM over-voltage is provided via an external power supply. In order to ensure a stable over-voltage, the external power is provided via a voltage adapter, which provides a pre-defined SiPM-over-voltage. Four such adapters were available for the over-voltages of 2 V, 3 V, 4 V and 6 V. They provide a bias voltage of 41.6 V, 42.6 V, 43.6 V and 45.6 V respectively. Therefore, whenever the bias voltage needs to be changed, a physical change in the system is required whenever the KCU DAQ system is in use.

The lack of functionalities mentioned above was one of the significant disadvantages of using the KCU105 DAQ system, which was solved only with the TB-tester DAQ system.

3.5.2 The TB-Tester DAQ System

The KCU105 DAQ system was later succeeded by an FPGA-based (Xilinx Zynq) controller board called the TB-Tester DAQ system. It was developed by University of Minnesota (UMN) based on the Hexacontroller DAQ system developed to test the HGCAL silicon sensors on silicon modules (analogous to Tilemodules for the silicon section).

The TB-tester provided the fast clock, fast commands and trigger, similar to the KCU105 DAQ, but with the additional functionality of communicating with the GBT-SCA. This made it possible to set the SiPM supply voltage via the ALDOv2 ASIC, monitor the temperatures from the eight PT-1000 platinum temperature sensors and monitor all voltages on board, including the voltages applied to the SiPMs and the LEDs on the Tilemodule. The ability to set the bias voltage without requiring a hardware change, in particular, made acquiring data for multiple bias voltages much more manageable and less time-consuming.

The TB-tester also saved the timestamp of the trigger in addition to triggering the data acquisition, which was not possible with the KCU105 DAQ system. This was a significant improvement compared to the KCU105 DAQ system, as it allowed less complex algorithms to sample the pulse amplitude from SiPMs via the HGCROC (see section 4.2).

A typical setup showing the interconnection of a Tilemodule and TB-tester is shown in fig. 3.13. A Twinax adapter produced in-house at DESY interconnects the Tilemodule and TB-tester DAQ. The LED bias voltage and the bias voltage supplied to the SiPMs are also supplied via this adapter.

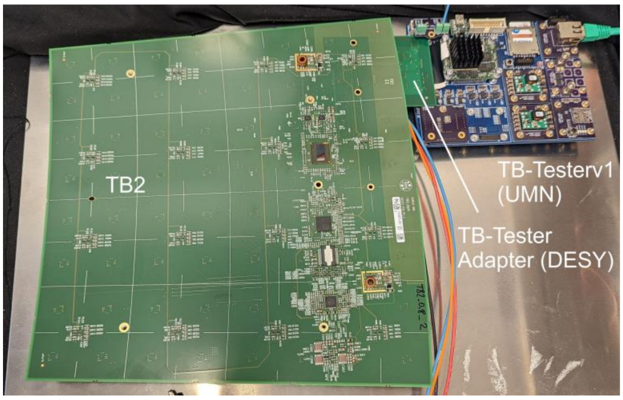
TB2
TB-Testerv1
(UMN)
TB-Tester
Adapter (DESY)

Figure 3.13: Tilemodule in the typical setup with interconnection via adapter board to a DAQ FPGA module (TB-Tester). The light cover to protect from the LED UV light is not shown. Taken from [81]

CERN, Baylor, and University of Minnesota (UMN) developed the software and firmware of the TB-tester. The block diagram of the interconnection of the TB-tester with a Tilemodule is shown in fig. 3.14.

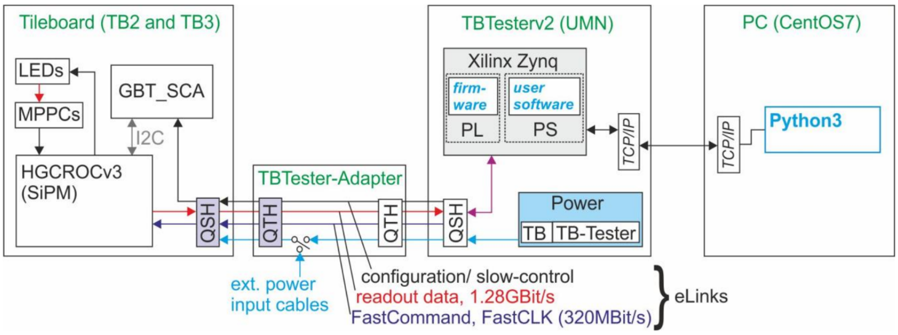
Tileboard (TB2 and TB3)
LEDs
MPPCs
GBT_SCA
I2C
HGCROCv3
(SiPM)
QSH
TBTester-Adapter
QTH
QTH
TBTesterv2 (UMN)
Xilinx Zynq
firm-
ware
PL
user
software
PS
TCP/IP
QSH
Power
TB
TB-Tester
PC (CentOS7)
TCP/IP
Python3
ext. power
input cables
configuration/ slow-control
readout data, 1.28GBit/s
FastCommand, FastCLK (320MBit/s)
eLinks

Figure 3.14: Block-diagram of the typical interconnection of Tilemodule, in this case to the TB-tester DAQ system. Taken from [82]

A summary of the differences between the two data acquisition systems is also found in table 3.1.

3.6 HGCAL Tilemodule Prototypes (Tileboards)

As mentioned in Section 3.3, Tilemodules consist of the SiPM-on-tiles, the readout electronics such as the HGCROC and all other electronics required for the successful data acquisition from

Table 3.1: Differences between the two DAQ systems used with the tileboards

DAQ System	**KCU105**	**TB-Tester**
Hardware Description	FPGA-based evaluation board produced by Xilinx Inc. [80]	Custom-made module developed by UMN
Processing Unit	AMD Kintex Processor	AMD/Xilinx Zynq Processor on a Trenz mezzanine
Firmware Developed	By OMEGA and LLR using Xilinx Vivado	By UMN, CERN and Baylor using Xilinx Vivado
Communication with GBT-SCA	Not possible	Possible
SiPM Bias Voltage	Cannot be set	Set via GBT-SCA and ALDOv2
Voltage Read Out	Not possible	Possible via GBT-SCA
Temperature Read Out	Not possible	Possible via GBT-SCA
Timestamp of trigger events	Unsaved	Saved

the sensors. The research and development, including the designing and testing of Tilemodule prototypes, is done at DESY within the scope of the DESY-FTX-DTA, DESY-FEB and the DESY-ZE groups, drawing inspiration from past experiences from the CALICE AHCAL SiPM-on-tile based prototype [11].

Tilemodule prototypes not fully equipped with SiPMs and scintillators used for testing are often called tileboards. Therefore, the term ’tileboards’ will be used when discussing the prototypes produced at DESY, on which all preliminary tests were conducted.

Three major generations of tileboards have been produced and tested at DESY. Each generation improved the tileboards with newer SiPMs and electronics. The first generation of tileboards was labelled TBv1. Later, newer tileboards, namely TBv2 and TBv3, were developed and tested. Most of these tileboards were D8-type tileboards. The primary motivation for first developing the D8 tileboard was its dimensional similarity to the CALICE AHCAL SiPM-on-tile PCB layer known as the HCAL base unit (HBU) [11]. Like all D8 Tilemodules, these tileboards have 8 × 8 (or 64) SiPM-on-tile channels and have a single HGCROC readout electronic ASIC. All other tileboards were designed after the successful testing of the D8 tileboard. As a result, most of the research done for this thesis was done using D8 tileboards. An overview of all tileboards used in this thesis is given below.

3.6.1 Tileboard Version 1 : TBv1

Tileboard version 1 (TBv1) were the first generation of tileboards developed in late 2019 [81]. TBv1 consists of an HGCROCv2 reading out the SiPMs. Two step-down DC/DC converters (FEAST2.1 [83]) are used to supply voltages of 1.5 V and 3.3 V from a 10 V input voltage while limiting the current. Two linear regulators (LDO) supplying 2.5 V and 1.2 V are used for all noise-sensitive supply voltages for the HGCROC. A labelled image of a TBv1 tileboard is shown in fig. 3.15. The KCU105 DAQ system was primarily used to acquire data and configure the HGCROCv2 onboard the TBv1 tileboards.

The first TBv1 board to be produced was the TB1 tileboard. Subsequently, two versions of the tileboard TB1 were produced to test different SiPMs. These tileboards were labelled TB1.2

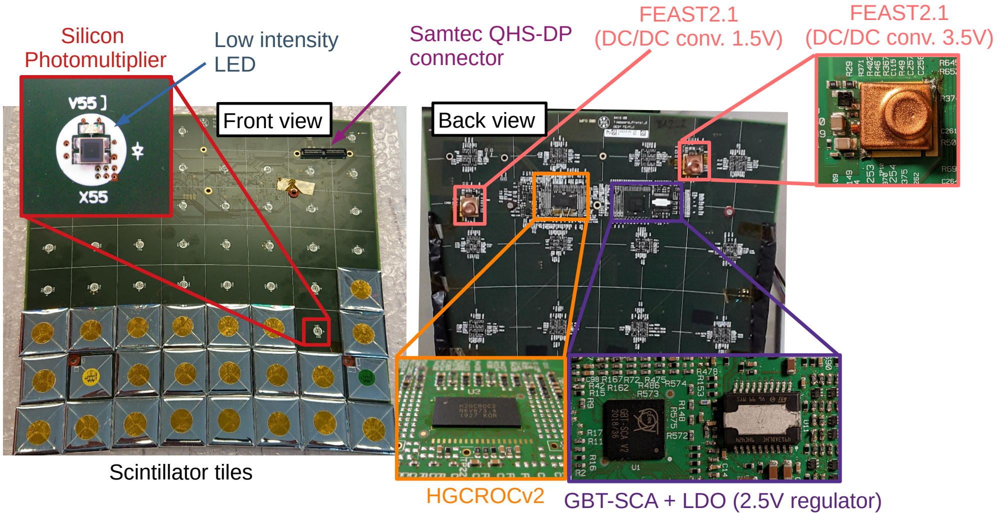

Figure 3.15: Front view and back view of a version 1, D8 Tilemodule prototype with the main sensors (SiPM, scintillator tiles, LED) and electronics (HGCROC readout chip, GBT-SCA)

and TB1.3. The electronics on them remain identical to TB1, except for SiPMs and an updated LED system in TB1.3.

TB1 tileboard used commercially available HPK HDR-2 SiPMs (HPK S14160-XXXX series [55]) with a pitch size of 15 µm and active areas of $1.4 \times 1.4\,\mathrm{mm}^2$ and $2 \times 2\,\mathrm{mm}^2$. As they are commercial products, these SiPMs are not radiation-hard. This tileboard was also not used for this thesis but was the predecessor for all other following tileboards.

The TB1.2 and TB1.3 contain the commercially available HPK HDR-2 SiPMs but with the first generation of radiation-hard packaging custom-made for the HGCAL upgrade (HPK S14160-976X series [72]). Similar to TB1, TB1.2 contains 15 µm and active areas of $1.4 \times 1.4\,\mathrm{mm}^2$ and $2 \times 2\,\mathrm{mm}^2$. In addition, there are five channel slots where SiPMs on specially designed holder PCBs can be mounted onto the tileboard. These slots are handy for testing irradiated SiPMs. The floor plan of TB1.2 is shown in fig. 3.16.

TB1.3 contains 15 µm pitch with active areas of $1.4 \times 1.4\,\mathrm{mm}^2$ and $2 \times 2\,\mathrm{mm}^2$ similar to TB1 and TB1.2, as well as 10 µm pitch with active areas of $2 \times 2\,\mathrm{mm}^2$ and $3 \times 3\,\mathrm{mm}^2$. The main motivation for the TB1.3 tileboard is to test SiPMs of different pitch sizes to see if they can be used in the HGCAL upgrade. The floor plan of TB1.3 is shown in fig. 3.17

3.6.2 Tileboard Version 2 : TBv2

Tileboard version 2 (TBv2) was developed in 2021. Once again, the D8 tileboard became the first tileboard to be built of this version. The majority of the electronics remain the same. This includes the HGCROCv2, FEAST2.1 DC/DC converters, GBT-SCA and LDO regulators. The two linear regulators and the LED system are based on commercial, bipolar components similar to TB1 and are not radiation-hard. The used FEAST2.1 is not radiation hard enough for CMS requirements.

However, there are a few crucial distinctions in TBv2 tileboards that TBv1 did not have.

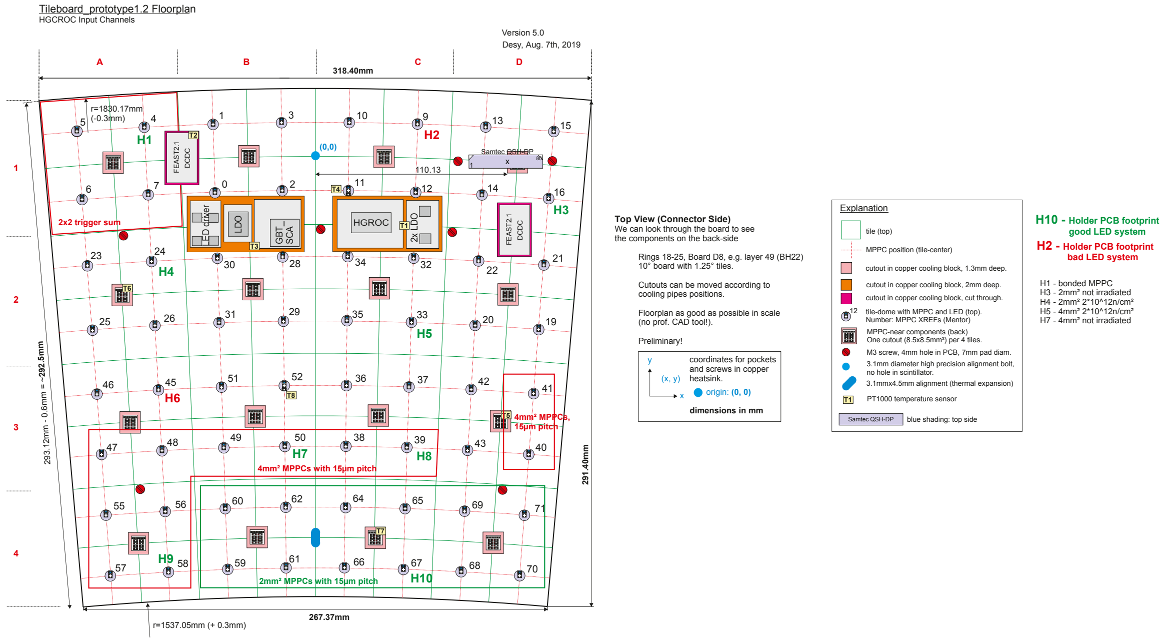
Tileboard_prototype1.2 Floorplan
HGCROC Input Channels
Version 5.0
Desy, Aug. 7th, 2019
318.40mm
267.37mm
291.40mm
HGCROC
LDO
GBT_SCA
LED driver
FEAST2.1 DCDC
2x trigger sum
4mm² MPPCs with 15μm pitch
2mm² MPPCs with 15μm pitch
Explanation
H10 - Holder PCB footprint good LED system
H2 - Holder PCB footprint bad LED system

Figure 3.16: Floor plan of the tileboard TB1.2 including the positions of the on-board electronics and SiPMs [84].

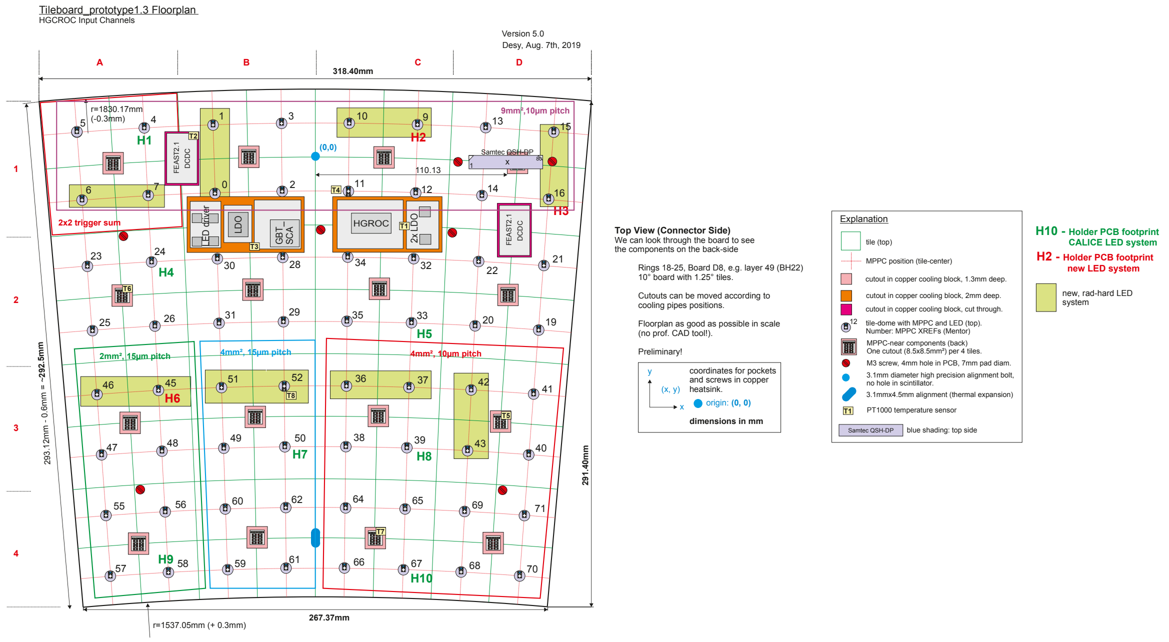
Tileboard_prototype1.3 Floorplan
HGCROC Input Channels
Version 5.0
Desy, Aug. 7th, 2019
318.40mm
267.37mm
291.40mm
HGCROC
LDO
GBT_SCA
LED driver
FEAST2.1 DCDC
9mm², 10μm pitch
2mm², 15μm pitch
4mm², 15μm pitch
4mm², 10μm pitch
Explanation
H10 - Holder PCB footprint CALICE LED system
H2 - Holder PCB footprint new LED system
new, rad-hard LED system

Figure 3.17: Floor plan of the tileboard TB1.3 including the positions of the on-board electronics and SiPMs [84].

The TBv2 tileboard was designed to be compatible with the final DAQ used in the experiment. Therefore, these tileboards primarily was used with the TB-tester DAQ system.

This tileboard also consisted of the new ALDOv2 ASIC regulator for the first time. Steered via the GBT-SCA, the ALDO ASIC can regulate the SiPM bias voltage. Since the TB-tester can communicate with the GBT-SCA, this power regulation could now be done without requiring a hardware change. An external voltage above the needed bias voltage is supplied to the ALDO ASIC, which limits the voltage to the required value. A labelled image of a TBv2 tileboard is shown in fig. 3.18.

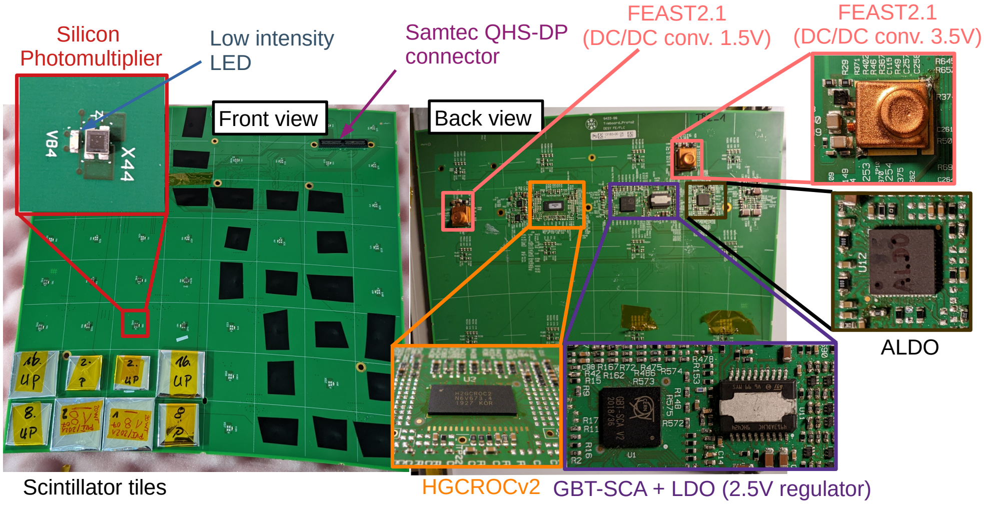

Figure 3.18: Front view and back view of a typical 64-channel tileboard version 2 with the main sensors (SiPM, scintillator tiles, LED) and electronics (HGCROC readout chip, GBT-SCA, ALDO)

TBv2 tileboards use commercially available HPK HDR-2 SiPMs with custom radiation hard packaging similar to the TB1.2 and TB1.3. The SiPMs on TBv2 also have a pitch size of $15\,\mu\mathrm{m}$ and active areas of $1.4 \times 1.4\,\mathrm{mm}^2$ and $2 \times 2\,\mathrm{mm}^2$. The floor plan of TB2 is given in fig. 3.19. TBv2 tileboards come in two variants: TB2 and TB2.1. The only difference between the two boards was using an HGCROCv2 with a larger package in TB2.1, which is expected to be the final package for the HGCROC SiPM version. In terms of functionality, both tileboards are identical.

3.6.3 Tileboard Version 3 : TBv3

Tileboard version 3 (TBv3), developed in 2022, is the latest version. Several changes were made in TBv3 compared to TBv2 tileboards. The FEAST2.1 DC/DC converter on TBv2 was replaced with bPOL12V on TBv3 with a different main coil. The 2.5 V LDO voltage regulator on TBv2 was also removed, and its functionalities were given to an ALDOv2 ASIC on TBv3. As only the low voltage channels of this ALDOv2 are used, this ALDO is typically referred to as ALDOv2 LV to separate it from the other ALDOv2, which provides the bias voltage to the SiPMs (referred to as ALDOv2 BV). The two commercial 1.2 V LDO voltage regulators were also replaced with new LDOs especially designed for the HGCROC operation. A labelled image of a TBv3 tileboard is shown in fig. 3.20.

TBv3 also comes with new HDR-2 SiPMs from HPK with pitch size $15\,\mu\mathrm{m}$ and $2 \times 2\,\mathrm{mm}^2$ active area with an improved radiation hard packaging custom-made for the HGCAL (HPK S16713 prototype series [73]). All components on TBv3 are radiation-hard, making TBv3 the

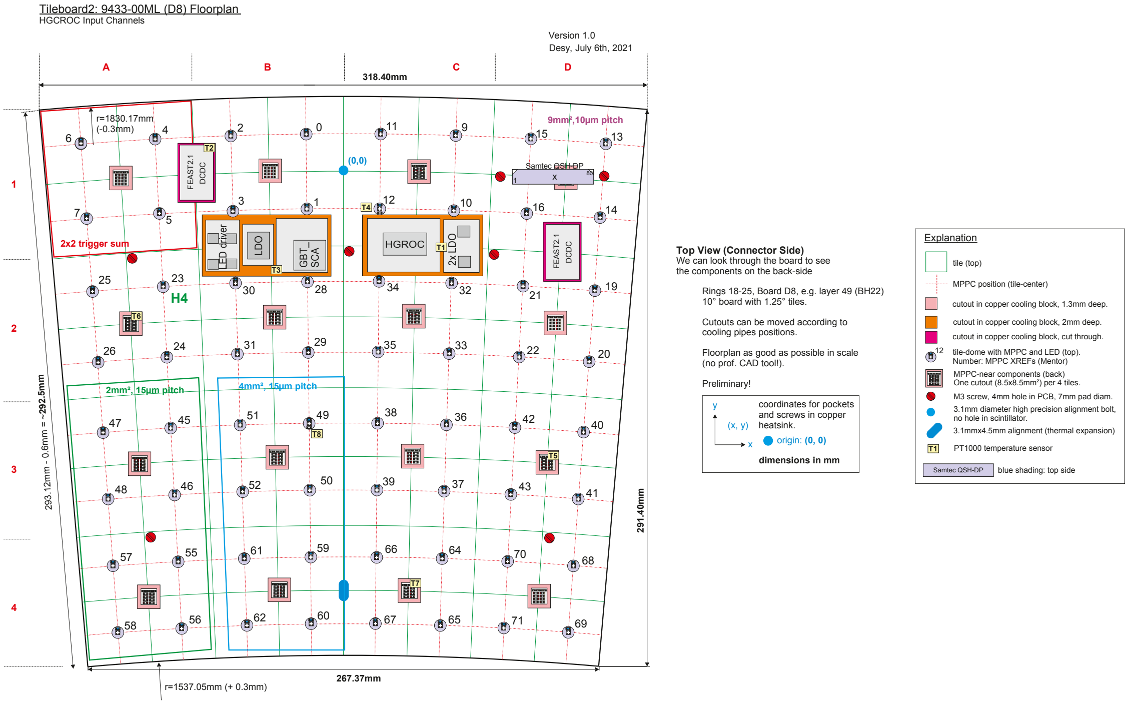
Tileboard2: 9433-00ML (D8) Floorplan
HGCROC Input Channels
Version 1.0
Desy, July 6th, 2021
A
B
C
D
318.40mm
1
2
3
4
r=1830.17mm
(-0.3mm)
9mm², 10µm pitch
Samtec QSH-DP
FEAST2.1 DCDC
LED driver
LDO
GBT-SCA
HGROC
2x LDO
(0,0)
2x2 trigger sum
H4
2mm², 15µm pitch
4mm², 15µm pitch
293.12mm - 0.6mm = ~292.5mm
291.40mm
267.37mm
r=1537.05mm (+ 0.3mm)
T1
T2
T3
T4
T5
T6
T7
T8
Top View (Connector Side)
We can look through the board to see the components on the back-side
Rings 18-25, Board D8, e.g. layer 49 (BH22)
10° board with 1.25° tiles.
Cutouts can be moved according to cooling pipes positions.
Floorplan as good as possible in scale (no prof. CAD tool!).
Preliminary!
y
x
(x, y)
coordinates for pockets and screws in copper heatsink.
origin: (0, 0)
dimensions in mm
Explanation
tile (top)
MPPC position (tile-center)
cutout in copper cooling block, 1.3mm deep.
cutout in copper cooling block, 2mm deep.
cutout in copper cooling block, cut through.
12
tile-dome with MPPC and LED (top). Number: MPPC XREFs (Mentor)
MPPC-near components (back) One cutout (8.5x8.5mm²) per 4 tiles.
M3 screw, 4mm hole in PCB, 7mm pad diam.
3.1mm diameter high precision alignment bolt, no hole in scintillator.
3.1mmx4.5mm alignment (thermal expansion)
PT1000 temperature sensor
Samtec QSH-DP
blue shading: top side

Figure 3.19: Floor plan of the tileboard TB2 including the positions of the on-board electronics and SiPMs [84].

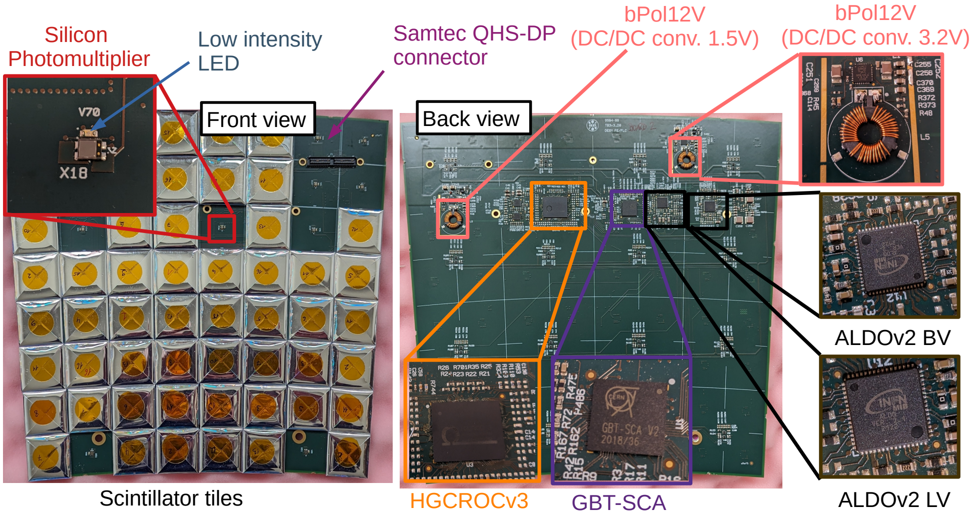
Silicon Photomultiplier
Low intensity LED
Samtec QHS-DP connector
bPol12V (DC/DC conv. 1.5V)
bPol12V (DC/DC conv. 3.2V)
Front view
Back view
V70
X18
ALDOv2 BV
ALDOv2 LV
Scintillator tiles
HGCROCv3
GBT-SCA

Figure 3.20: Front view and back view of a typical 64-channel tileboard version 3 with the main sensors (SiPM, scintillator tiles, LED) and electronics (HGCROC readout chip, GBT-SCA, ALDO)

first fully radiation-hard tileboard. TBv3 uses software and firmware interconnections similar to TBv2, with the TB-tester as the DAQ system. Shown in fig. 3.21 is the floor plan of the TB3 tileboard.

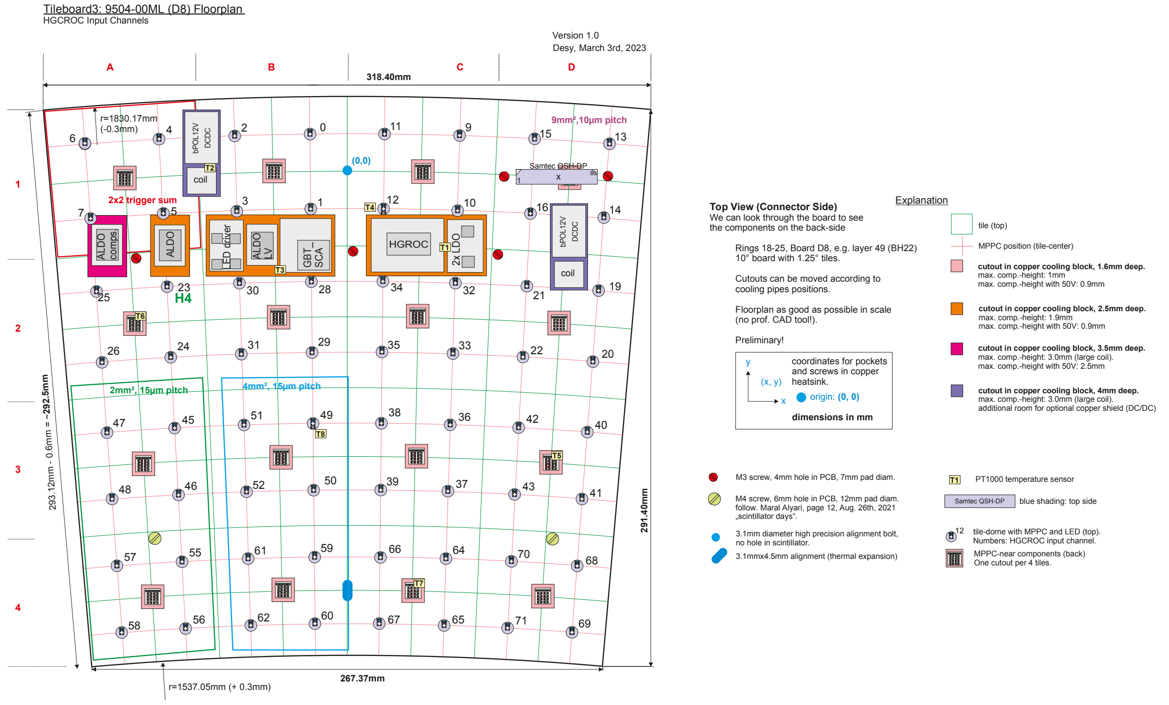
Tileboard3: 9504-00ML (D8) Floorplan
HGCROC Input Channels
Version 1.0
Desy, March 3rd, 2023
A
B
C
D
318.40mm
r=1830.17mm
(-0.3mm)
9mm²,10µm pitch
(0,0)
bPOL12V DCDC
coil
T2
Samtec QSH-DP
2x2 trigger sum
ALDO comps.
ALDO
LED driver
ALDO LV
GBT SCA
HGROC
2xLDO
T1
T3
T4
T5
T6
T7
T8
H4
1
2
3
4
2mm², 15µm pitch
4mm², 15µm pitch
293.12mm - 0.6mm = ~292.5mm
291.40mm
267.37mm
r=1537.05mm (+ 0.3mm)
Top View (Connector Side)
We can look through the board to see the components on the back-side
Rings 18-25, Board D8, e.g. layer 49 (BH22)
10° board with 1.25° tiles.
Cutouts can be moved according to cooling pipes positions.
Floorplan as good as possible in scale (no prof. CAD tool!).
Preliminary!
coordinates for pockets and screws in copper heatsink.
(x, y)
origin: (0, 0)
dimensions in mm
Explanation
tile (top)
MPPC position (tile-center)
cutout in copper cooling block, 1.6mm deep.
max. comp.-height: 1mm
max. comp.-height with 50V: 0.9mm
cutout in copper cooling block, 2.5mm deep.
max. comp.-height: 1.9mm
max. comp.-height with 50V: 0.9mm
cutout in copper cooling block, 3.5mm deep.
max. comp.-height: 3.0mm (large coil).
max. comp.-height with 50V: 2.5mm
cutout in copper cooling block, 4mm deep.
max. comp.-height: 3.0mm (large coil).
additional room for optional copper shield (DC/DC)
M3 screw, 4mm hole in PCB, 7mm pad diam.
M4 screw, 6mm hole in PCB, 12mm pad diam.
follow. Maral Alyari, page 12, Aug. 26th, 2021 „scintillator days“.
3.1mm diameter high precision alignment bolt, no hole in scintillator.
3.1mmx4.5mm alignment (thermal expansion)
PT1000 temperature sensor
blue shading: top side
tile-dome with MPPC and LED (top).
Numbers: HGCROC input channel.
MPPC-near components (back)
One cutout per 4 tiles.

Figure 3.21: Floor plan of the tileboard TB3 including the positions of the on-board electronics and SiPMs [84].

3.6.4 Mini-Tileboard : MiniTB

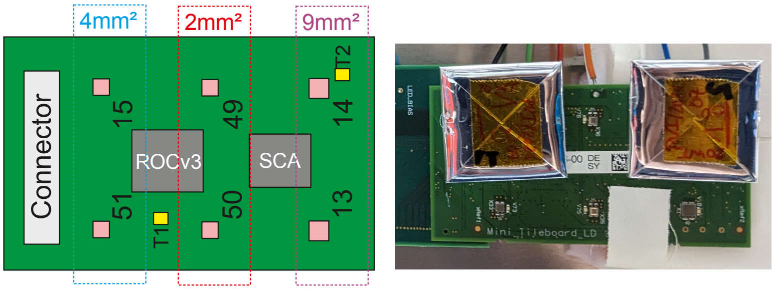
4mm²
2mm²
9mm²
Connector
15
51
ROCv3
T1
49
50
SCA
T2
14
13

(a) (b)

Figure 3.22: (a) shows the floorplan of the mini-tileboard (MiniTB), which includes the HGCROCv3, GBT-SCA and the two temperature sensors (T1 and T2) [84]. (b) shows the mini-tileboard with the SiPM side up and two R18 tiles mounted.

The mini tileboard (MiniTB) developed in 2022 is a complete tileboard consisting of a single HGCROC reading out of six SiPM-on-tile channels. The mini-tileboard has only the essential electronics on board. This includes the LED system, temperature sensors for temperature monitoring, and the GBT-SCA used for slow control. All power, including the SiPM bias voltage, LED bias voltage, tileboard operation voltage and all voltages supplied by the LDOs, DC-DC converters and ALDO chips, are supplied externally. The MiniTB was designed to be irradiated as a whole, providing valuable information on how Tilemodules will function after irradiation.

The MiniTB board used for the studies mentioned in this thesis and shown in fig. 3.22 has an HGCROCv3 chip and HPK HDR-2 SiPMs with improved custom radiation-hard packaging with 15 µm pitch size similar to those used in TBv3 (HPK S16713 prototype series [73]). Out of the six active channels, two contained SiPMs of active area $1.4 \times 1.4\,\text{mm}^2$, two contained SiPMs of active area $2 \times 2\,\text{mm}^2$ and the two remaining SiPMs had an active area of $3 \times 3\,\text{mm}^2$. Like TBv2 and TBv3, the DAQ tasks were done using the TB-tester.

In summary, many tileboards have been developed over the years. The changes between the tileboards are summarised in table 3.2.

Table 3.2: A summary of the different board generations developed over the years

Tileboard	**TBv1**	**TBv2**	**TBv3**	**MiniTB**
Hardware				
HGCROC	version 2	version 2	version 3	version 3
GBT-SCA	Non-functional	Functional	Functional	Functional
ALDO	None	Functional	Functional	Functional
DC/DC converters	FEAST 2.1 and LDOs	FEAST 2.1 and LDOs	bPol12 and ALDOv2 LV	None
SiPMs on-board				
Series	HPK HDR-2 (S14160-976X)	HPK HDR-2 (S14160-976X)	HPK HDR-2 (S16713-XX)	HPK HDR-2 (S16713-XX)
Packaging	Radiation-hard	Radiation-hard	Radiation-hard and improved thermal contact	Radiation-hard and improved thermal contact
Bias voltages for SiPM	Supplied externally	Controlled using ALDOv2 BV via GBT-SCA	Controlled using ALDOv2 BV via GBT-SCA	Supplied externally
Areas	$1.4 \times 1.4\,\text{mm}^2$ $2 \times 2\,\text{mm}^2$	$1.4 \times 1.4\,\text{mm}^2$ $2 \times 2\,\text{mm}^2$	$1.4 \times 1.4\,\text{mm}^2$ $2 \times 2\,\text{mm}^2$ $3 \times 3\,\text{mm}^2$	$1.4 \times 1.4\,\text{mm}^2$ $2 \times 2\,\text{mm}^2$ $3 \times 3\,\text{mm}^2$
Pitch sizes	15 µm 10 µm	15 µm	15 µm	15 µm
DAQ system used with tileboard	KCU105	TB-Tester	TB-Tester	TB-Tester

3.7 Signal-to-Noise Based Requirements for HGCAL Scintillator Section at End-of-Life

With an expected integrated luminosity ($\mathcal{L}$) of $3000\,\text{fb}^{-1}$ by end-of-life, HGCAL uses SiPM-on-Tile technology in demanding radiation conditions for the first time. However, SiPM-on-tiles are less radiation-hard than silicon sensors used in HGCAL. MIPs will be used to calibrate the detector throughout the detector's lifetime, and therefore, the ability to measure MIPs till the end of the detector's lifetime is a vital requirement.

The measure of the strength of the desired signal relative to noise is known as the signal-to-noise ratio (SNR). In the case of SiPM-on-tiles, The signal is measured in terms of light yield, a quantity measuring the size of a MIP signal in p.e. (see section 2.5.1). The signal's noise is measured by measuring the pedestal fluctuation of the SiPM in terms of the standard deviation (see section 2.4.2.4). Therefore, SNR can be written for SiPM-on-tiles as:

$$\text{Signal-to-Noise Ratio (SNR)} = \frac{\text{Light Yield of SiPM-on-Tile}}{\text{Noise of SiPM on Tilemodule}}. \tag{3.2}$$

A large SNR indicates that the signal is distinguishable from noise, and therefore, it is highly desirable to maintain a high SNR throughout the detector's lifespan.

Three main factors affect the SNRs in SiPM-on-Tiles.

- The SiPM-on-Tile performance at starting conditions (i.e. before irradiation),
- The increase in electronic noise of the SiPM with neutron fluence,
- The degradation of scintillator performance with absorption dose.

Due to the radiation-hard package of the SiPM, damage due to IEL is negligibly small, and the majority of the damage is due to NIEL (i.e. neutrons) (see section 2.4.2.7). Therefore, the increase in SiPM noise scales with neutron fluence.

As for the scintillator, damage due to IEL dominates, leading to performance degradation (see section 2.4.1.2). Therefore, the performance of scintillators is modelled using absorption dose.

The HGCAL detector, similar to most detectors, is calibrated using MIPs such as muons. The first study of the SNR requirement for the HGCAL upgrade comes from the TDR [10], where an SNR requirement of five was motivated to identify MIPs successfully. The TDR showed that it was possible to identify the MIP particle in a layer with an efficiency of above 98 % if SNR>5 is maintained in the last 12 layers.

A more recent study within the CMS HGCAL collaboration [85] tracks muons produced in $W \rightarrow \mu\nu_\mu$ events through the tracker, calorimeters and muon system at the expected end-of-life neutron fluences and absorption doses (at $\mathcal{L} = 3000\,\text{fb}^{-1}$). Using dedicated algorithms for track reconstruction, the SiPM-on-tiles at these radiation levels can be calibrated with a 95 % efficiency using 175 such muon events. Under HL-LHC conditions, these events can be obtained within 12.5 hours of acquiring muons, assuming a trigger efficiency of 70 %.

Furthermore, the same study shows that SNR=3 does not impact the physics runs and only impacts the calibration. The SNR will be orders of magnitude higher at the start of life, and therefore, the relative calibrations at the start of life will be quick, which aids in the creation of the first maps of relative calibration.

Nonetheless, to maintain the ability to calibrate the detector in a reasonable time window without harming the physics data runs, it was proposed to limit the area where the SiPM-on-tiles lie to where an SNR>3 can be maintained for MIPs throughout the detector lifetime. This thesis aims to investigate if this is possible within the constraints of the SiPM-on-tile performance after irradiation and comment on improvements that can be made to reach this goal.

During installation, the HGCAL end-caps will be assembled before they are lowered to the CMS cavern and twisted into their final place. Therefore, replacing end-cap detector components will not be possible once the detector has been installed in the CMS cavern. This means that the best way to optimise the performance of the SiPM-on-tiles at the end of life is to improve their performance at the start of life. If one optimises the light yield at starting conditions, one could achieve an SNR>3 at the end of life, even at the highest radiation levels.

Chapter 4

Quantifying the Start of Life Performance of SiPM-on-Tiles on HGCAL Tilemodule Prototypes

Non-irradiated SiPMs and scintillator tiles mounted on HGCAL Tilemodule prototypes (or tileboards) provide a good measurement of the performance of the SiPM-on-tiles with in-situ electronics at the start of the detector lifetime. The detector components will not be replaced during the lifetime of the HL-LHC. Therefore, optimising the starting conditions of the detector remains the only possible way to achieve and maintain the SNR>3 threshold throughout the detector's lifetime.

The primary method of quantifying the performance of such SiPM-on-tiles on tileboards is to test them with particle beams. These tests are performed at dedicated test beam facilities, which provide particle beams of known energy. The signal produced from particle beams is used to measure the MIP maxima from SiPM-on-tiles as mentioned in section 2.5.1, and the onboard LED system is used to observe SPS and measure the SiPM gain as mentioned in section 2.4.2.2. Light yield for the SiPM-on-tile is then calculated by taking the ratio of the MIP maxima and the SiPM gain (see section 2.5.1). Light yield is a purely optical property used to compare different combinations of SiPMs and tiles. This chapter describes the complete procedure developed to measure the light yield accurately and discusses the results obtained from the beam tests over the years.

4.1 Overview of Devices under Test

Over the years, SiPMs fulfilling the HGCAL criteria better and better were developed. Manufacturers of scintillators also developed and optimised their methods to produce tiles, optimising the light output and sensor to sensor uniformity and production speed.

A table listing all SiPMs tested is shown in table 4.1. All SiPMs used are HPK HDR-2 type SiPMs with three different packaging as discussed in section 3.6 and summarised in table 3.2 and table 4.1.

Note that all breakdown voltages mentioned in this section are the turn-off voltages (V_{br}(TO)) of the SiPMs measured by HPK. Therefore, all over-voltages discussed in this section are derived

Table 4.1: Overview of all SiPMs used. All SiPMs were HDR-2 type SiPMs with custom-made radiation hard packaging. Two models were better used: HPK S14160-976x series used in TBv1 and TBv2 tileboards, and HPK S16713-xx used in TBv3 tileboards. Parameters quoted from [72, 73]

SiPM series model	**active area**	**pitch size**	**number of cells**	**breakdown voltage (V_{br})**
HPK S14160-9766	$1.4 \times 1.4\,\mathrm{mm}^2$	15 µm	$8,480$	38.0 ± 0.3 V
HPK S14160-9768	$2 \times 2\,\mathrm{mm}^2$	15 µm	$17,520$	38.0 ± 0.3 V
HPK S16713-01	$1.4 \times 1.4\,\mathrm{mm}^2$	15 µm	$8,649$	38.0 ± 0.1 V
HPK S16713-02	$2 \times 2\,\mathrm{mm}^2$	15 µm	$17,459$	38.0 ± 0.1 V
HPK S16713-03	$3 \times 3\,\mathrm{mm}^2$	15 µm	$39,770$	38.0 ± 0.2 V

with respect to the turn-off voltages (V_{br}(TO)) of the SiPMs measured by HPK. For more details about the turn-off voltage, refer section 2.4.2.8.

Table 4.2 gives an overview of the different scintillators tested on tileboards over the years. Unlike the SiPMs that must be soldered onto the tileboards, the scintillators are glued onto the tileboards. On prototype boards, this is done using double-sided tape to make it easier to replace during beam tests to test many tiles from different manufacturers produced using different technologies. This includes tiles produced by Institute for High Energy Physics (IHEP) in Protvino, Russia, Institute for Scintillation Materials (ISMA) in Kharkiv, Ukraine, Fermi National Accelerator Laboratory (FNAL) in the USA and North Illinois University (NIU) in the USA.

These tiles were either cast tiles or injection-moulded tiles. The main difference between cast and injection-moulded is the method used to manufacture the tiles, which is found in section 2.4.1. For simplicity, the tile codes listed in table 4.2 will be used to describe the specific scintillators discussed throughout this thesis.

Multiple versions of the same tiles were produced and tested over the years. These include injection-moulded tiles produced by IHEP and FNAL. The IHEP injection moulded tiles (IHEP inj-mould) were labelled as v1, v2, v3 and v3(dot) in the order in which they arrived at DESY over the years. The sole difference between the versions is the scintillator material composition.

In 2022, FNAL also began the production of injection moulded tiles using a polystyrene-based material (FNAL inj-mould). Two batches with minor composition differences were eventually sent to DESY and labelled in batches 1 and 2. They were produced in late 2022, and both tile performances were measured in March 2023. The differences in tile batches were due to varying conditions under which the tiles were produced.

4.2 Beam Tests with SiPM-on-Tiles

As of writing this thesis, twelve beam tests have taken place between 2020 and 2023 with different combinations of SiPMs and scintillators using different tileboard generations and DAQ systems. Almost all of these tests were conducted at the DESY-II test beam facility in Hamburg (a member of the Helmholtz Association (HGF)) [15], except for one at the CERN SPS facility.

The electron beam used at the DESY-II test beam facility is produced using two targets as sketched in fig. 4.1 [15]. The DESY-II synchrotron is primarily used as a booster ring for

Table 4.2: Overview of all scintillator tiles used. * Performance of FNAL cast tiles was quantified only using ^{90}Sr source-based setup explained later in this chapter.

Tile Code	**Scintillator material**	**Material Producer**	**Production Technology**	**Tile Producer**
IHEP cast	BC-408 [46]	Saint-Gobain S.A., France	cast	IHEP, Protvino, Russia
EJ cast	EJ-208 [47]	Eljen Technologies, USA	cast	NIU, USA
ISMA cast	BC-408	Saint-Gobain S.A., France	cast	ISMA, Kharkiv, Ukraine
IHEP inj-mould	polystyrene-based material	IHEP, Protvino, Russia	injection-moulded	IHEP, Protvino, Russia
FNAL inj-mould	polystyrene-based material	FNAL Chicago, USA	injection-moulded	FNAL Chicago, USA
FNAL cast *	BC-412 [46]	Saint-Gobain S.A., France	cast	FNAL Chicago, USA

the PETRA-III synchrotron. A fibre target produces photons from electrons travelling in the DESY-II ring. This target is placed so electrons travelling further away from the beam centre pass through the fibre target. This ensures that the activities at PETRA are unharmed during beam tests. Electrons passing through the fibre target produce photons via bremsstrahlung. These photons then pass through a second target, producing electrons and positrons via pair production. A dipole magnet and a collimator select particles of the desired energy. Electrons of energies between 1 GeV to 5 GeV can be selected with an energy spread of 5 %. The beam rate of electrons ranges from a few Hz to 100 kHz.

Each DESY-II test beam area has a beam shutter and two collimators. The primary collimator is the collimator located behind the dipole magnet and uses a combination of a horizontal and a vertical collimator unit. The main part of each unit is a pair of motorised 100 mm thick jaws made out of tungsten whose position can be remotely controlled from the hut. A holder for a second collimator is also present in each area in addition to the other systems in place. Various lead collimators of varying opening sizes are available for any required beam size. A typical collimator used for the experiment in this thesis has an opening of 1 × 1 cm². All collimators are about 40 cm long. Detailed collimator descriptions can be found in [15].

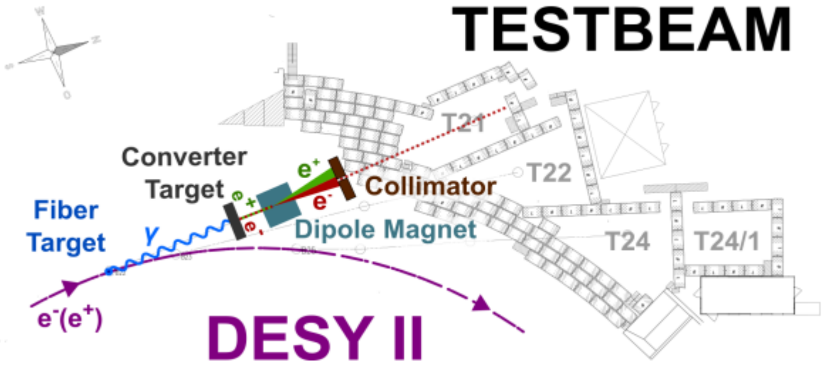

Figure 4.1: DESY-II test beam facility layout. Taken from [15]

4.2.1 Test Setup

The setups used at all beam tests since 2020 are very similar, as they were optimised for the characterisation of SiPM-on-tiles on tileboards. Furthermore, the same test setup was used at the CERN SPS test beam in October 2021. The basic block diagram of this setup is sketched in fig. 4.2. The tileboard and DAQ system were mounted on an aluminium holder plate and placed vertically on a steel and aluminium frame. This frame is then placed on a movable stage before the beam. The stage is moved via two remote controls from the beam hut with a precision of up to 0.1 mm. Photos from a beam test are shown in fig. 4.3. In order to avoid external light contamination, the setup was covered with a thick black cloth.

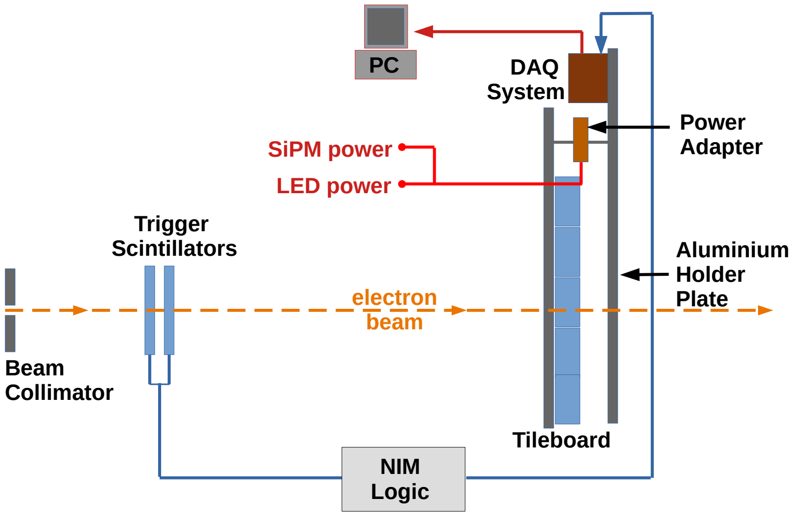

Figure 4.2: The basic setup of the Tilemodule and DAQ system used at beam tests conducted at DESY-II and CERN SPS test beam facilities

The beam tests over the years saw the use of all tileboards discussed in section 3.6. TBv1 tileboards used the KCU105 DAQ system, while the TBv2, TBv3, and MiniTB tileboards used the TB-tester for data acquisition. The differences between the different DAQ systems are also explained in section 3.5 and summarised in table 3.1.

A typical data run for characterising SiPM-on-tiles used electrons of 3 GeV energy. The primary assumption used here is that electrons passing through 3 mm thick plastic scintillators at this energy behave like MIPs. As explained in section 2.3.2, the most probable electron energy losses in 3 mm thick plastic at these energies remain relatively unchanged. One of the tests conducted at the SPS test beam facility at CERN was to validate this scenario using 120 GeV muons as discussed in section 4.6.

Two PMTs attached to trigger scintillators are triggered in coincidence to read out the data from the SiPM-on-tiles on the tileboard when a particle passes. Two discriminators first filter most dark counts from the PMTs out before taking the coincidence of the signal. To trigger data acquisition from the SiPM-on-tiles the KCU105 DAQ requires a 1.3 V, 500 ns square pulse while the TB-tester DAQ require a 1.3 V, 500 ns square pulse. This is generated by a gate generator in the presence of a coincidence trigger from the pair of trigger PMTs and fed to the DAQ.

During a triggered event, the signal peak is sampled and digitised by the HGCROC. Depend-

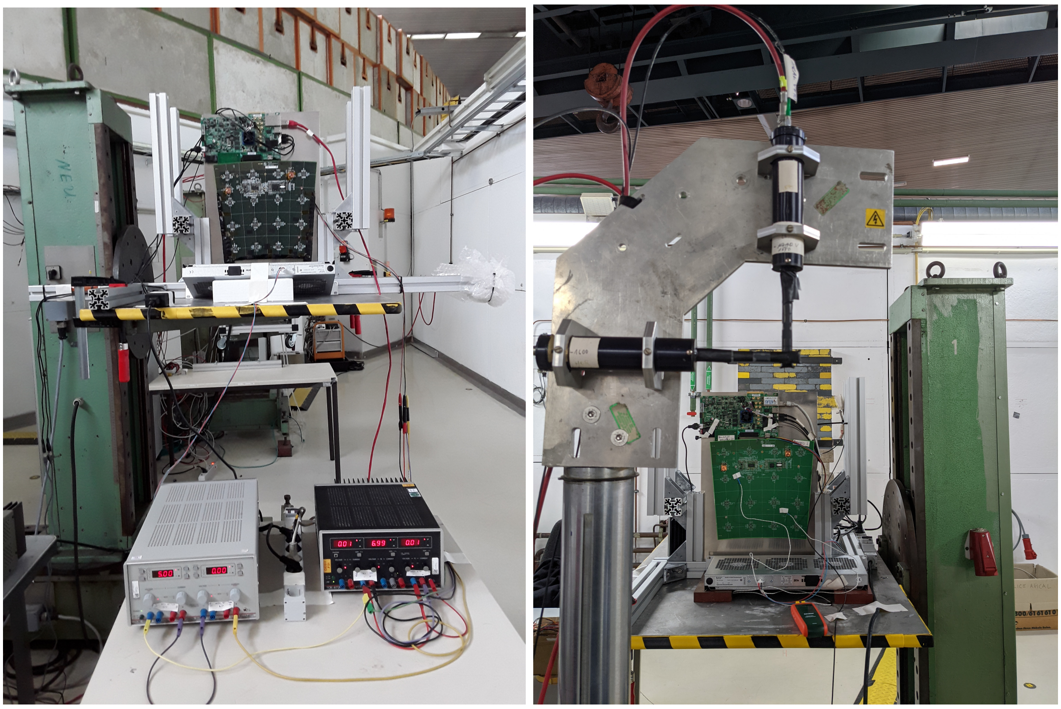

(a) (b)

Figure 4.3: Photos of a beam test setup on the movable stage at DESY-II: (a) tileboard alongside the power supplies used for powering; (b) trigger scintillators used in addition to the tileboard.

ing on the signal size, this sampled value could be in either ADC or TOT scales. In the presence of a false trigger, the sampled value will be at the pedestal level with a slight fluctuation due to noise.

In order to test the trigger precision, one of the tests conducted was to scan a SiPM-on-tile by aiming the beam at different parts of the tile and measuring the occupancy of MIP events triggered. The beam collimator has an opening of $1 \times 1\,\text{mm}^2$. The scan aimed the beam at 7×7 points on and around the tile. For non-irradiated SiPMs, due to the high signal-to-noise ratios (SNR>20), the pedestal and electron signals are distinct and separated. A simple ADC threshold of 20 ADC is used to separate the pedestal from the MIP events.

The results of this test, as seen in fig. 4.4, show that if the beam is located close to the centre of the tile, less than 1 % of the events triggered contains no signal. These could be false positive triggers due to noise in the PMTs, tile inefficiencies or the electrons stopping or deflecting before reaching the tile. As the beam is moved to the edges of the tile, the fraction of triggered events having no signal in this particular tile increases. This is explained by the triggered electrons not hitting the tile under test.

4.2.1.1 Over-Voltage Supply

The over-voltage depends on the breakdown voltage of the SiPM and the bias voltage supplied as given by eq. (2.18). However, the breakdown voltage is temperature-dependent and will change with irradiation. In order to control the over-voltage, the bias voltage is supplied via the ALDO voltage regulator ASIC for TBv2 and TBv3. The ALDO regulator is absent on TBv1, so the

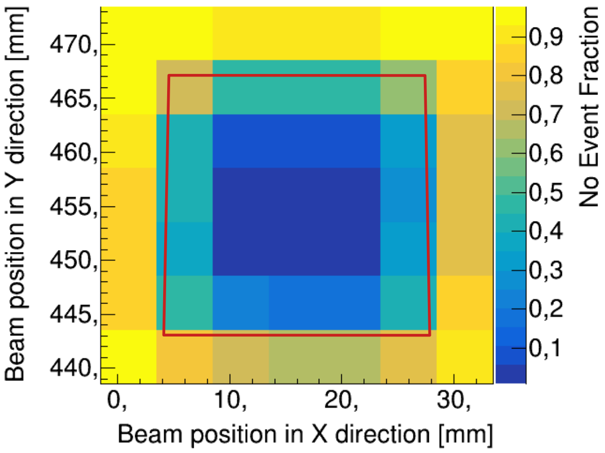

Figure 4.4: The fraction of triggered events with no signal observed as a function of the beam position with respect to the stage holding the Tilemodule in place. The rough dimensions of the bare R2 tile used for the measurement are shown in red.

voltage is supplied directly to the SiPMs. The supplied voltage can be further tuned channel-wise through the 'InputDAC' parameter of the HGCROC. This parameter typically decreases the supply voltage by acting as a voltage divider. A sketch visualising this is shown in fig. 4.5.

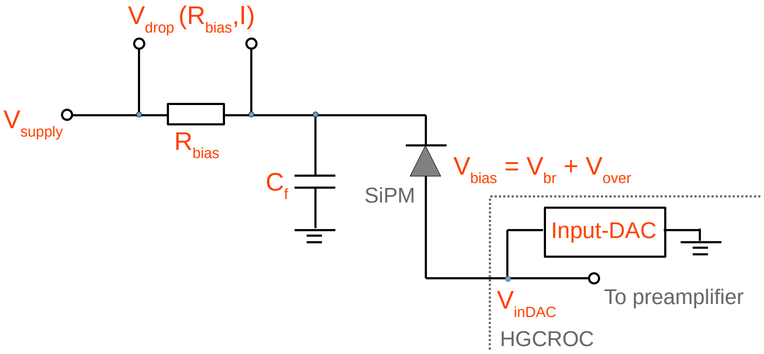

Figure 4.5: Sketch showing the interplay between the bias voltage, breakdown voltage and input DAC voltage.

Therefore, the bias voltage of the SiPM is the difference between the supply voltage provided by the ALDO and the voltage drop from the InputDAC. Furthermore, there exists a voltage drop across the safety resistor. Therefore, eq. (2.18) can be reformulated as:

$$V_{over} = V_{supply} - V_{br} - V_{inDAC} - V_{drop}. \tag{4.1}$$

However, for a non-irradiated SiPM, the leakage current passing through the SiPM is negligibly small. As a result, the voltage drop across the safety resistor is negligibly small. Therefore, for non-irradiated SiPMs,

$$V_{over} = V_{supply} - V_{br} - V_{inDAC}. \tag{4.2}$$

The effect of temperature is also an essential factor to consider. As the breakdown voltage is temperature sensitive, the correct breakdown voltage for the associated temperature must be supplied to supply the over-voltage needed. However, as the temperature is often unstable in a test beam setting, the temperature is monitored, and the over-voltage is recalculated based on the correct breakdown voltage offline. The light yield is then adjusted to the needed over-voltage using the temperature-breakdown voltage relationship discussed later in section 4.4.1.

4.2.2 Data Analysis Method using a Template Fit for KCU105 DAQ

The HGCROC was designed to function at the HL-LHC's collision frequency of 25 ns. However, the beam used at DESY-II is asynchronous to the HGCROC clock. Therefore, the SiPM signal could arrive at any time within a single clock cycle of the HGCROC.

The earlier setups at test beams used the KCU105 DAQ system alongside TBv1 tileboards. As mentioned in section 3.5, the KCU105 DAQ lacks many functionalities compared to the TB-tester, including its inability to save the timestamps of the trigger events. Since no timing information from the trigger is saved, it is impossible to guarantee that the pulse is sampled at its peak.

The method used to extract a signal at its peak is to sample multiple points for the same event along the signal and reconstruct the signal offline using a template fit to extract the peak. This is possible because the shaped SiPM pulse is longer than 25 ns. Six consecutive bunch crossings (bx) are sampled when the KCU105 DAQ receives a trigger. Denoting bx=0 as the first sampled bunch and bx=5 as the last, the bunch for which the trigger was generated is set at around bx=2. The pulse is then reconstructed using a skewed Gaussian function given by:

$$s(x, a, h) = 2 \cdot a \cdot f(x) \cdot c(x) + h, \tag{4.3}$$

where a is the amplitude of the signal, h is the pedestal, $f(x)$ and $c(x)$ are the probability density function and cumulative density function of Gaussian distributions given by:

$$f(x) = \frac{1}{\sqrt{2\pi}\sigma} \exp\left(-\frac{(x-\mu)^2}{2\sigma^2}\right), \tag{4.4}$$

$$c(x) = \frac{1}{2}\left(1 + \text{erf}\left(\alpha \cdot \frac{(x-\mu)}{\sqrt{2}\sigma}\right)\right), \tag{4.5}$$

where μ and σ are the mean and standard deviation respectively, α is the skewness and erf(z) is the error function given by:

$$\text{erf}(z) = \frac{2}{\pi} \int_0^z \exp(-t^2) dt. \tag{4.6}$$

An example of a few electron events sampled and fitted with the template fit described above is given by fig. 4.6.

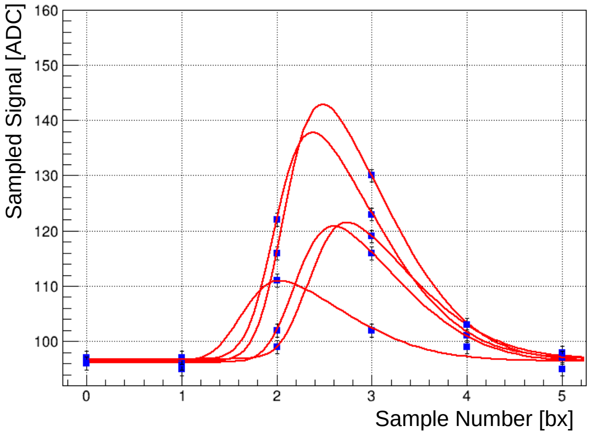

Figure 4.6: Five events acquired with a 3 GeV electron beam using TB1.3 tileboard using the KCU105 DAQ. The six consecutive points sampled were used to reconstruct the SiPM pulse to extract the peak.

Parameters a and μ are left as free parameters in eqs. (4.3) to (4.6). The first sample point bx$= 0$ is sampled before the signal arrives, and therefore, this point can be used as the pedestal h. The signal maxima lie typically between bx$= 2$ and bx$= 3$.

The values for α and σ were fixed to 4.26 and 0.81 for $1.4 \times 1.4\,\mathrm{mm}^2$ SiPMs on the tile boards and to 3.91 and 0.95 for $2 \times 2\,\mathrm{mm}^2$ SiPMs. These values were obtained by fitting LED data from different channels for the different SiPM sizes using the same template fit function. The $3 \times 3\,\mathrm{mm}^2$ SiPMs were never measured on TBv1 tileboards; therefore, these parameters were never calculated.

Once the pulse amplitudes have been extracted from all signals, they are plotted in a histogram as given in fig. 4.7. Given that the signals are due to energy loss in thin layers, the distribution should follow a convoluted Landau-Gaussian function described in section 2.3.2. This function's maximum (referred to as MIP maximum in this thesis. See section 2.3.2) fitted on the data gives the most probable charge deposit in a SiPM-on-tile. Since the particles behave like MIPs, this information calculates the light yield associated with the SiPM-on-tile.

This method, which was developed in the context of this thesis, was used to extract the MIP peak from all test beam data taken between August 2020 and October 2021 with TBv1 and in a few test beams in 2022, while the use of TBv1 tileboards was gradually being phased out. This method was used to observe the first physics signal from SiPM-on-tiles readout via HGCROCs from Tilemodules designed for the HGCAL experiment.

4.2.2.1 Verification using Time-of-Arrival

The TOA measures the time the signal takes to cross the TOA threshold from the start of the previous HGCROC clock cycle as sketched in fig. 3.10. Therefore, the TOA can extract timing information from the pulse. However, TOA information obtained from the HGCROC had yet to be investigated enough to use it for signal peak extraction. On the other hand, the template fit method measures the position of the signal amplitude in terms of the number of samples (bx).

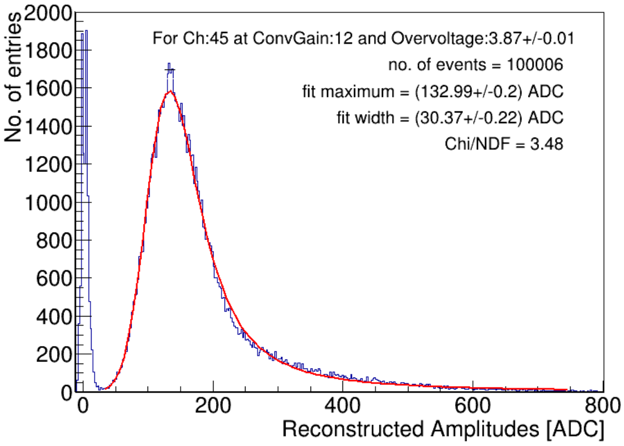

Figure 4.7: Distribution of SiPM pulse amplitudes from MIP-like events. A convoluted Landau-Gaussian function extracts the fit maximum.

This value should correlate to the TOA information saved by the HGCROC. Therefore, TOA verifies whether the template fit reconstruction gives meaningful results. One correlation plot between TOA and the sample point at which the amplitude was measured from the template fit is shown in fig. 4.8.

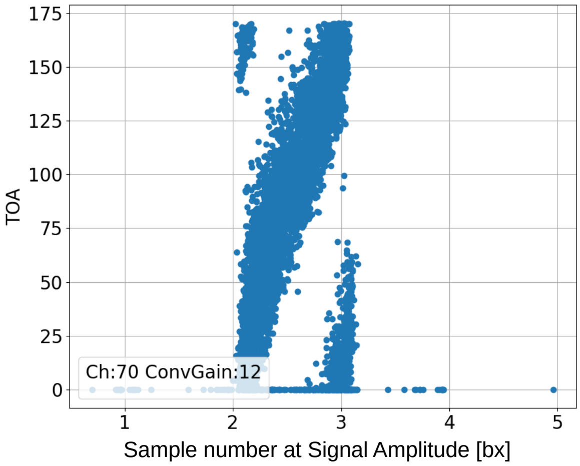

Figure 4.8: Correlation between TOA acquired by the TDC in the HGCROC and the timing of the pulse maxima obtained using the template fit

There are three visible bands in fig. 4.8. They correspond to three different scenarios. As mentioned previously, the beam is asynchronous to the system. This means the pulse may peak earlier or later than it is sampled. If the pulse maximum and the time the pulse crosses the TOA threshold are in the same bunch crossing, the TOA and delay will increase proportionally. Pulses 2 and 3 in fig. 4.9 show this scenario. It is also possible that the signal passes the TOA threshold in the previous bunch crossing while the pulse maximum is in the current bunch crossing. This is shown by pulse 1 in fig. 4.9. The result would be a point with a large TOA and a small delay.

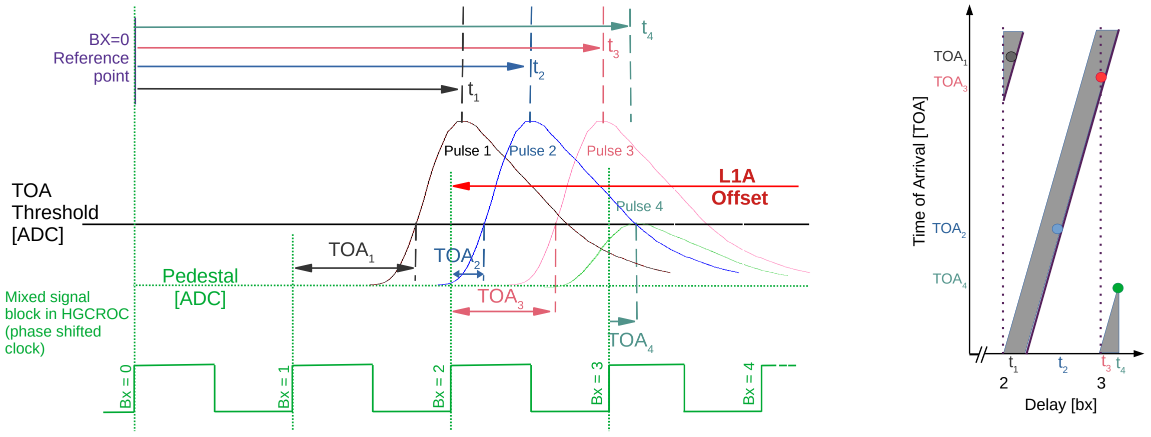

(a) (b)

Figure 4.9: Sketch visualises the interplay between TOA and the delay measured by the template fit method. The template fit calculates the delay at which the signal peak is sampled t while TOA is the time at which the signal crosses the TOA threshold.

The TOA still needs to be corrected for time-walk. The TOA exponentially drop with increasing pulse amplitude. This means that the TOA for pulses with smaller amplitudes is much larger than for pulses with larger amplitudes. The comparison of TOA and ADC is shown in fig. 3.9 where the time-walk effect can be seen. The black line in fig. 4.9 gives the theoretical TOA after time-walk correction, while the grey band gives the associated increase in width due to time-walk.

This time-walk is also the reason for the third scenario in fig. 4.8 (or pulse 4 in fig. 4.9). The signal may have been triggered within the same bunch-crossing interval as the rest of the triggered events. However, if the pulse amplitude is small, the TOA may be sampled with respect to the next clock cycle, resulting in a small TOA value and a large sample number.

4.2.3 Data Analysis Method using Trigger Timestamps of TB-Tester DAQ

The TB-tester DAQ system succeeded the KCU105 DAQ system for the newer generations of Tilemodules: TBv2, TBv3 and MiniTB. The TB-tester has been used almost exclusively with the tileboards since late 2021. Among many of the changes brought forward with the TB-tester, the most important for the analysis was the ability of the TB-tester to measure and save the timestamp of all triggered events (as 'TrigTime') with a resolution of 0.8 ns.

The TrigTime gives the timestamp at which the TB-tester DAQ detects the coincidence trigger signal from the PMTs. However, the HGCROC only starts counting the trigger offset from the following digital block clock cycle. This means an electron detected earlier in the cycle will have a smaller TrigTime value and arrive too early at the tileboard to measure the peak. Therefore, the signal will be sampled at the tail. This is shown by pulses 1 to 3 in fig. 4.10. If the signal arrives too late, the TrigTime will take a larger value, and the signal will be sampled at the rising edge. This is shown by pulse 5 in fig. 4.10. Only signals arriving in phase with the phase-shifted clock will be sampled at the peak. Pulse 4 in fig. 4.10 illustrates this situation.

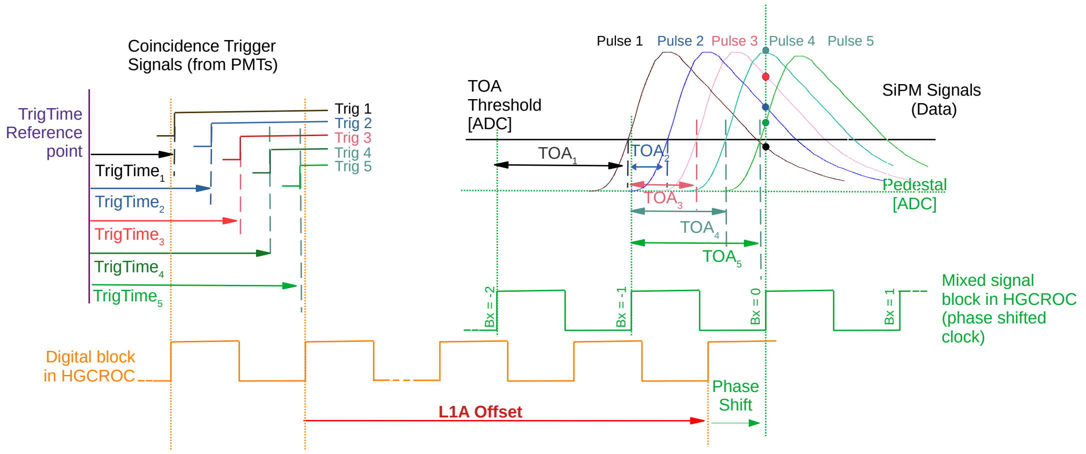
Coincidence Trigger
Signals (from PMTs)
TrigTime
Reference
point
TrigTime$_1$
TrigTime$_2$
TrigTime$_3$
TrigTime$_4$
TrigTime$_5$
Trig 1
Trig 2
Trig 3
Trig 4
Trig 5
Digital block
in HGCROC
L1A Offset
TOA
Threshold
[ADC]
TOA$_1$
TOA$_2$
TOA$_3$
TOA$_4$
TOA$_5$
Pulse 1
Pulse 2
Pulse 3
Pulse 4
Pulse 5
SiPM Signals
(Data)
Pedestal
[ADC]
Bx = -2
Bx = -1
Bx = 0
Bx = 1
Mixed signal
block in HGCROC
(phase shifted
clock)
Phase
Shift

Figure 4.10: Sketch showing the relationship between TrigTime, TOA and ADC based on the trigger and data signals. The sampling point of the ADC is depicted as dots.

If the bunch crossing offset (see section 3.4.4) is reduced by one, the signal will always be sampled too early, and as a result, only the rising edge will be visible. Similarly, if the bunch crossing offset is increased by one, the signal will always be sampled at its tail. Therefore, the ADC vs. TrigTime plot traces the SiPM signals due to the electrons as a function of time. Shown in fig. 4.11 are three sets of 200,000 electron events sampled at consecutive bunch crossings 25 ns apart placed next to each other in descending order of bunch crossing offsets.

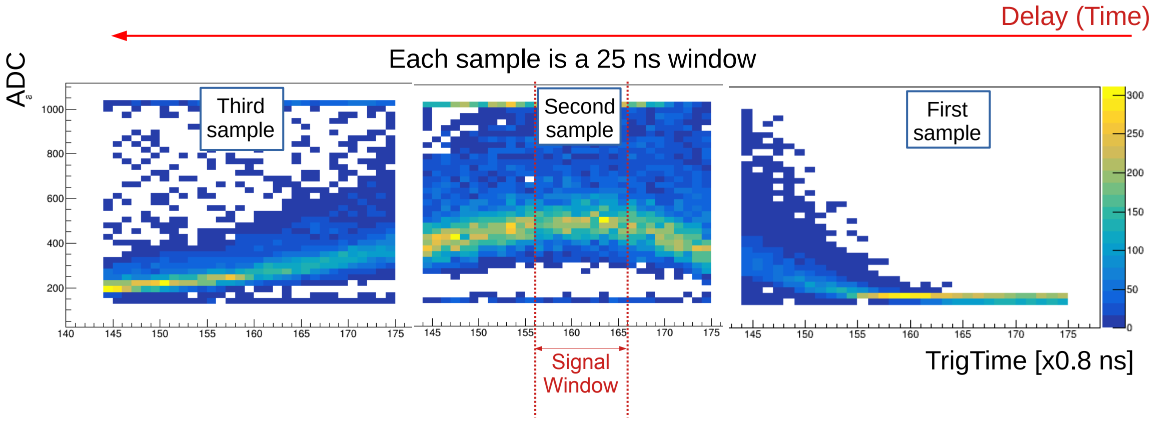

Figure 4.11: Sampled ADC value vs. TrigTime of events measured by the TB-tester DAQ. The yellow band follows the peak of each bin on the x-axis. The pedestal is the continuous blue line at roughly 140 ADC across all three sampled data.

The pulse amplitude is the most important parameter that needs to be extracted. A simple method to extract the pulse amplitude is to take the data from the time bin with the highest mean amplitude and fit a Landau-Gaussian function. Though this method offers the best dataset to extract the pulse maxima, it uses only 4 % of the events. Therefore, more events are needed to be statistically significant. Instead, a 10-bin (or 8 ns) TrigTime window around the pulse maxima was used to measure the pulse amplitude. This corresponds to about $1/3$ of the events. A resulting histogram for a channel is shown in fig. 4.12. From this, a convoluted Landau-Gaussian function is used to obtain the fit maximum.

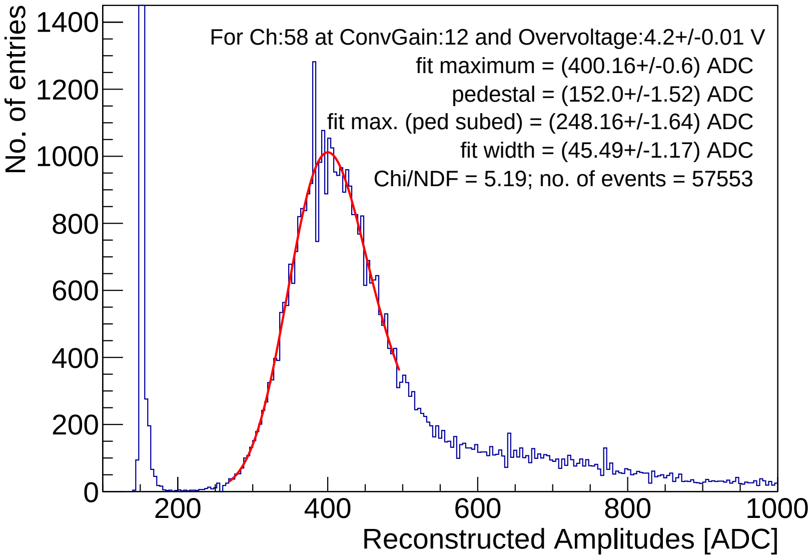

Figure 4.12: The histogram obtained using a 10-bin time interval at which the pulse from the SiPM-on-tile is at its peak. A Landau-Gaussian convoluted function is used to obtain the pulse amplitude. The corrected pulse amplitude is obtained after subtracting the pedestal value, also given in the plot.

The pedestal peak is also visible below the electron peak in fig. 4.11. This peak is generated by events where data taking was triggered, but the particle did not pass through the channel of interest. Therefore, the charge sampled is the pedestal ADC value. This is the continuous blue line visible at roughly 140 ADC in fig. 4.11. A threshold is defined so that the pedestal and signal peaks are separated. For the example shown in fig. 4.11, the threshold was set at 200 ADC. The median of the pedestal peak in ADC is used as the pedestal value for the said channel.

Once the pedestal and fit maximum have been found in a channel, the most probable deposition by MIPs (or the MIP maximum) is calculated by taking the difference between the two quantities. The parameter fit. max (ped subed) in fig. 4.12 gives this pedestal-subtracted MIP maximum for this channel.

The relatively large χ^2/ndf value is due to a differential non-linearity (DNL) present in the HGCROC. More about the DNL effect of the HGCROC is discussed later in section 4.3.2.1. This effect has a negligible impact on the position of the MIP due to the large ADC range across which the signal lies.

4.2.3.1 Verification of TrigTime using Time-of-Arrival (TOA)

The TrigTime is the arrival time of the trigger signal at the TB-tester. This means that the TOA must correlate with the TrigTime. The TOA vs. TrigTime measurement for a channel is shown in fig. 4.13.

Two bands are seen in fig. 4.13. If the TOA threshold is reached in the previous bunch, the TOA value will also take a large value. This is the case of pulse 1. If the TOA threshold is within the next bunch crossing, they will take a smaller value. As the electron delay increases, the TrigTime and TOA will also increase, as seen in the case of pulses 2 to 5.

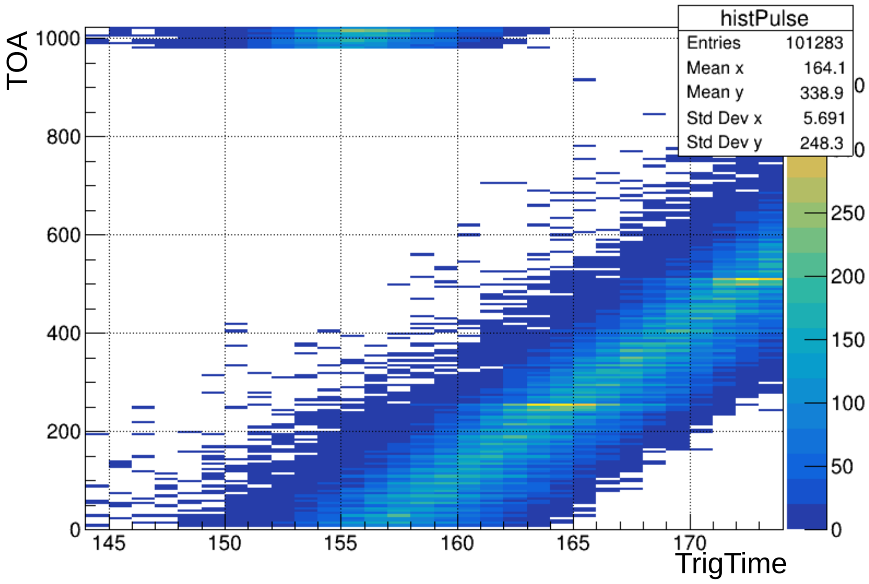

Figure 4.13: Correlation between TOA acquired by the TDC in the HGCROC and the trigger timestamp of the TB-tester DAQ

4.2.4 Reproducibility of MIP Maxima using the Two Analysis Methods

The April 2022 beam test at DESY compared the two analysis methods used to extract the signal's amplitude. Since ADC values from six consecutive bunch crossings are required to extract the signal amplitudes, 10,000 electron events were taken from six consecutive bunch crossings from four channels. However, under this mode of operation, the TrigTime cannot be extracted for the events due to firmware issues in the TB-tester.

Therefore,100,000 events were taken separately from one bunch crossing for the same four channels, including the TrigTime information. The data was then analysed using the two methods described above and are shown in fig. 4.14. The MIP maxima plotted here show the most probable charge deposition by the MIPs in the SiPM-on-tile measured by the HGCROC in ADC units and extracted using a convoluted Landau-Gaussian function as described previously. As shown here, the four channels obtained similar results with a deviation less than 8 %.

4.3 SiPM Gain Determination

The gain measurement at test beams is essential to convert the signal from the ADC scale to the number of SiPM pixels fired in a SiPM. Therefore, the determination of SiPM gain is repeated at every test beam for every SiPM channel under test, recorded in the same conditions as the beam data.

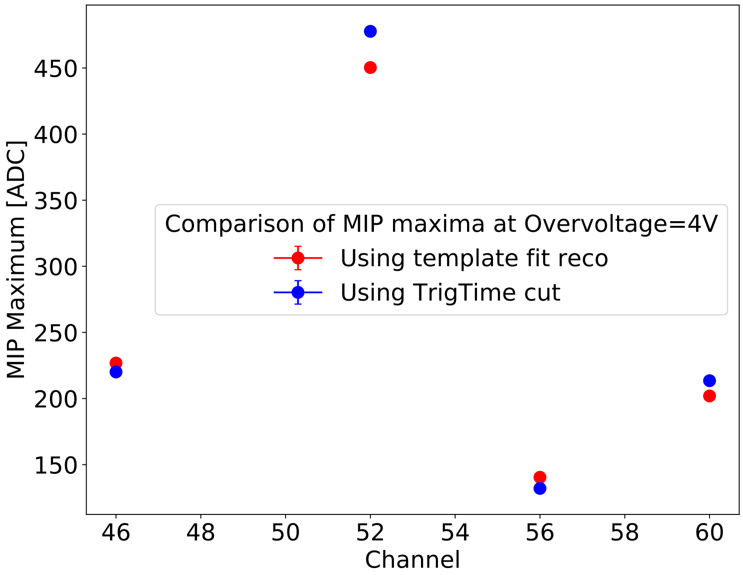

Figure 4.14: MIP maxima obtained using template fit method and TrigTime method using the same TB2 Tilemodule and TB-tester DAQ system at the DESY beam test held in April 2022. The statistical errors of the measurement are negligibly small, and therefore, error bars are not visible.

4.3.1 Methodology

The gain measurement uses dedicated LED runs by injecting low-amplitude light pulses into each scintillator tile. The low-intensity LEDs are mounted next to every SiPM as shown in fig. 3.15, fig. 3.18 and fig. 3.20. The DAQ system sends a trigger to the LED driver and the HGCROC. The LED driver then sends a pulse to the LEDs on the tileboard. When the LEDs receive a pulse, they produce photons in the SiPM-sensitive UV frequency range. Thanks to the scintillator tiles, these photons are reflected back to the SiPMs. This, in turn, produces avalanches in a few pixels of the SiPM, producing a pulse.

The trigger that the HGCROC receives prompts it to send the data to the DAQ system. The delay between the trigger and the sampling point of the signal is adjustable using the bunch crossing offset and phase parameter mentioned in section 3.4.4. The signal pulse sampled at its maximum using the LED system plotted on a histogram produces an SPS (see section 2.4.2.2).

The gain extraction from an SPS is done in two steps within the ROOT Framework. As a first step, the positions and amplitudes of all peaks are found using ROOT TSpectrum. The distance between the first two peaks is used as the initial estimate of the gain. As a second step, a multi-Gaussian function ($M(x)$) is defined as follows:

$$M(x) = \sum_{i=1}^{N_p} m_i(x) = \sum_{i=1}^{N_p} a_i \cdot \exp\left\{-\frac{1}{2}\left(\frac{x-b_i}{c_i}\right)^2\right\}, \tag{4.7}$$

where N_p is the total number of peaks fitted in the SPS, $m_i(x)$ is the ith Gaussian peak whose properties are given by a_i, b_i, and c_i. Here, a_i, b_i, and c_i are the peak heights, positions in ADC and standard deviations of the peaks fitted, respectively. The initial gain and peak positions obtained from the TSpectrum are used to constraint the position of b_i as:

$$b_i = b_1 + g \cdot i, \tag{4.8}$$

where g is the initial gain estimate, and b_1 is the position of the first peak. The gain is left as a free parameter such that the distance between all peaks will stay constant. This is the same method used for the gain calibration of the SiPMs on the CALICE Analogue Hadronic Calorimeter (AHCAL) prototype produced in 2018 [86].

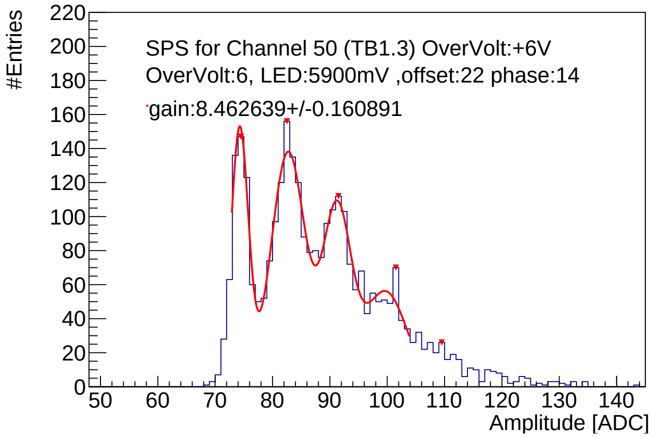

Figure 4.15: A typical single photo-electron spectra obtained from a TB1.3 Tilemodule using a SiPM over voltage of 6 V and LED bias voltage of 5.9 V

The gain measurements must be performed under the same conditions as the MIP measurements such that the light yields are measured under the same conditions. This includes parameters such as over-voltage, temperature and other HGCROC settings such as the current conveyor gain explained in section 3.4.1. The conveyor gain is set at 12 for most measurements discussed in this chapter.

4.3.2 Gain Measurement Strategy

The gain measurement requires optimised settings for each channel. The optimal delay settings in terms of bunch crossing offset and phase under which the SiPM signal maximum is sampled change from channel to channel by a few nanoseconds. Furthermore, a few hundred millivolts may change the optimal LED voltage that needs to be supplied. In addition, the HGCROC has a known differential non-linearity, leading to unstable gain fits.

A step-wise strategy was developed to extract the correct gain, described below. The strategy of SiPM gain extraction described here was developed in the scope of this thesis.

4.3.2.1 Differential Non-Linearity Correction

The ADC in the HGCROC converts the SiPM signal into a digital ADC value. Ideally, an analogue unit's step size corresponding to a single digital bit stays constant. However, this step size may vary for electronic reasons, causing certain bits to have a smaller step size while others have a larger one. This effect is known as differential non-linearity (DNL).

A test performed at DESY in 2021 [87] illustrated in fig. 4.16 shows the DNL effect in the HGCROC. This test was conducted by first injecting charge via the HGCROC to a single channel and observing the DNL. Then, the test was repeated for the same channel, but now with all channels injected with charge simultaneously. The charge injected was varied, such that the amplitude had a nearly constant probability between 100 ADC and 300 ADC. The amplitude distribution in ADC would be relatively flat if no DNL effect were present.

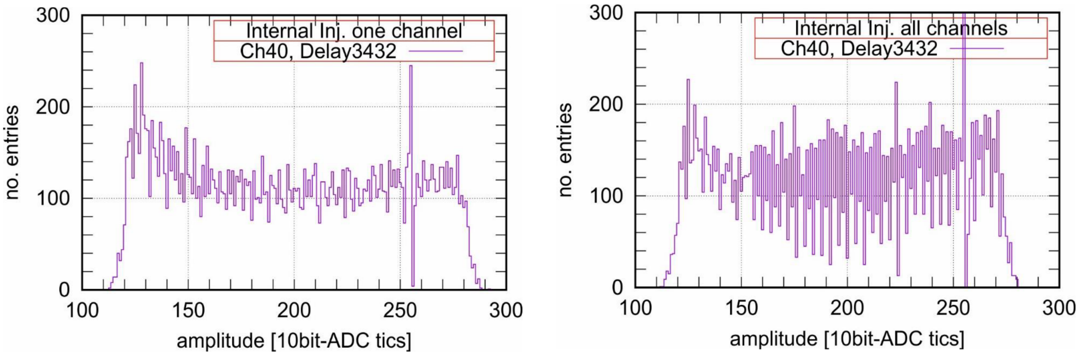

(a) (b)

Figure 4.16: The DNL effect in the conversion of charge to ADC scale by the HGCROC as observed at DESY [87]. (a) shows the DNL when just one channel is injected with a charge. (b) shows the DNL in the same channel when all channels are injected with charge.

As seen in fig. 4.16, every second bin of the HGCROC ADC scale is smaller than the remaining bins, resulting in more data accumulated in every second bin. The DNL is also much worse in bins of powers of 2, such as 256. Furthermore, fig. 4.16(b) shows that the DNL increases in severity if the load on HGCROC is large. Since the load varies with the constraints under which the measurement occurs, it is impossible to measure the DNL with such a flat distribution and correct this.

As the DNL only affects neighbouring bins, its effects cancel out over extended bin ranges. As typical MIP spectra range across hundreds of ADCs at beam tests, this DNL effect minimally impacts MIP maxima measurements (see fig. 4.12). However, DNL significantly affects the SiPM gain measurement taken using SPS as it spans only a few ADC bins, as shown in fig. 4.17(a).

The solution to this problem was to take multiple LED runs at different pedestal values. The pedestal value of each channel is determined by a parameter called 'ref_inv_dac' in HGCROCv2 and 'trim_inv' in HGCROCv3. An increment in this parameter increases the pedestal value by about 3 ADCs in HGCROCv2 and 1 ADC in HGCROCv3, rounded to the closest whole number. These values were determined by varying ref_inv_dac or trim_inv (depending on the HGCROC generation) and measuring the pedestal gradient. Since the pedestal shifts by about 3 ADC or 1 ADC, the SPS entire spectra are also shifted by about 3 ADC or 1 ADC per unit increase in 'ref_inv_dac' or 'trim_inv'. Three datasets were taken from the channels, one at the nominal ref_inv_dac or trim_inv value, one after incrementing the parameter value by one for all channels and another after incrementing the parameter value by two for all channels. Then, the data from the two latter datasets are manipulated as follows:

$$\mathrm{ADC_{new}} = \mathrm{ADC_{raw}} - 3\,\mathrm{ADC} \times (\mathrm{ref\_inv\_dac_{final}} - \mathrm{ref\_inv\_dac_{nominal}}) \tag{4.9}$$

or

$$\mathrm{ADC_{new}} = \mathrm{ADC_{raw}} - 1\,\mathrm{ADC} \times (\mathrm{trim\_inv_{final}} - \mathrm{trim\_inv_{nominal}}). \tag{4.10}$$

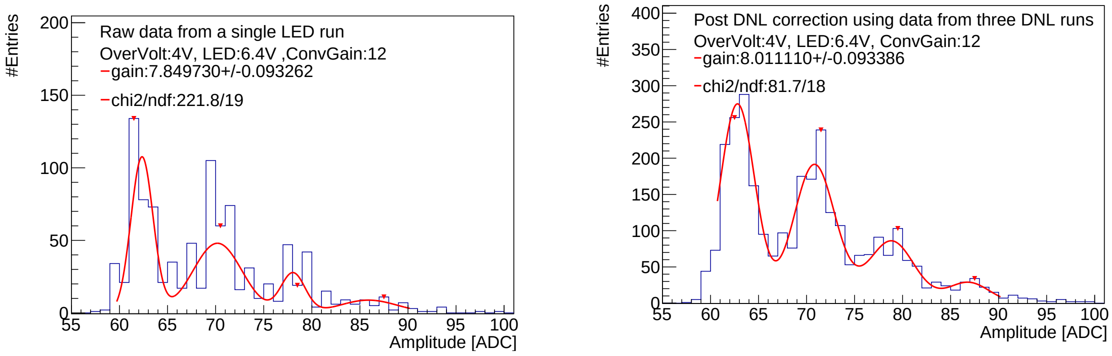

(a) (b)

Figure 4.17: (a) shows the raw SPS obtained from LED pulses are heavily affected by the differential non-linearity of the ADC of the HGCROC while (b) shows the SPS for the same channel after DNL reduction using multiple datasets with different pedestals

The ADC bin summed the three datasets, which averages the DNL effect. The post-processed SPS obtained for the same dataset is shown in fig. 4.17(b). The gain can then be measured using eq. (4.7). If the fit has a $\chi^2/NDF < 10$, the gain for this channel, LED bias voltage and delay settings are saved.

The decision to take three datasets stems from trial runs, which showed slightly better results when three datasets were combined instead of two. However, recent tests have been revisited using only two datasets for SPS processing. However, these studies are outside the scope of this thesis.

4.3.2.2 Optimal LED Intensity for Different SiPMs

Once the DNL correction has been made, one can compare the gains obtained from multiple runs at different LED intensities. The intensity of the LED is controlled by the bias voltage supplied to the LED. If a SiPM sees too little or no light, only a single pedestal peak will be visible on the ADC spectra. If the SiPM sees too much light, the SPS peaks begin to merge to form a broad single peak. An example of the variation of SPS across five different LED bias voltages for the same channel can be found in fig. 4.18.

Empirically, the LED bias voltage giving the optimal SPS varies by up to 500 mV. Therefore, up to five different datasets are taken in steps of 100 mV to sample all the optimal LED bias voltages for all channels for each channel and delay setting (bunch crossing offset and phase). The gains obtained for different LED bias voltages are then averaged. This gives a single SiPM gain value for each channel and delay setting.

4.3.2.3 Sampling the Peak of the Pulse

The next thing to consider is the difference in peak positions with respect to the delay. The exact peak of the pulse can be $1-5$ ns earlier or later for different channels on the same tileboard. The dependence of the gain on the delay follows a curved trajectory as seen in fig. 4.19 for SiPMs of two different sizes. The gain at the peak of these curves is taken as the gain of the

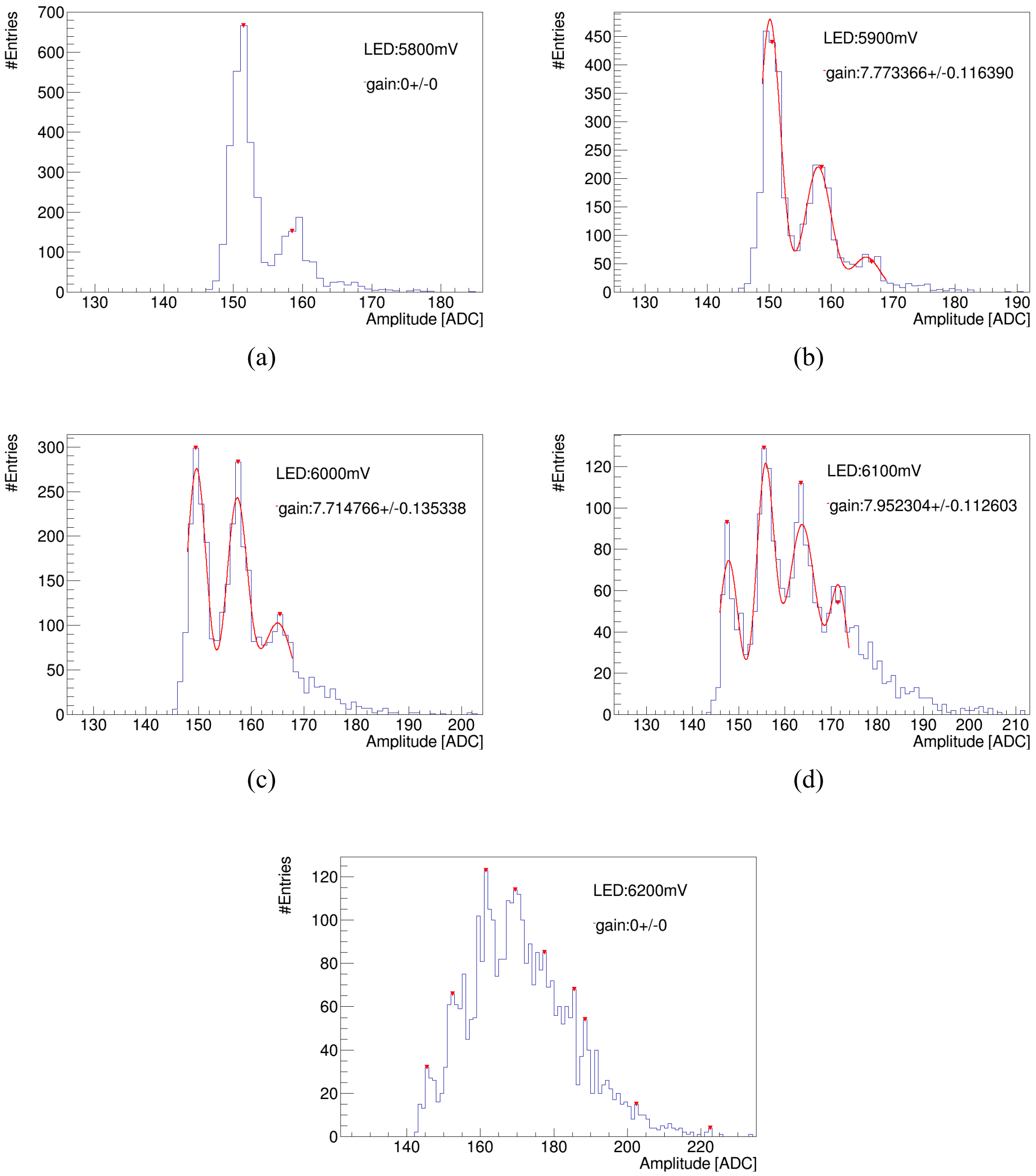

(a) (b) (c) (d) (e)

Figure 4.18: Single photo-electron spectra obtained across five different LED bias voltages for the same SiPM, keeping all other conditions constant.

SiPM for that channel.

This method is repeated for every SiPM channel. The final gains are saved once the SiPM gains are obtained for all channels. This is used to calculate the light yield. The temperature during data taking is monitored during the LED run. All the LED runs for the different configurations take place within a few hours, and therefore, the temperature variations are minor (typically less than 1 °C). Therefore, the average temperature of the LED run is taken as the final temperature of the run.

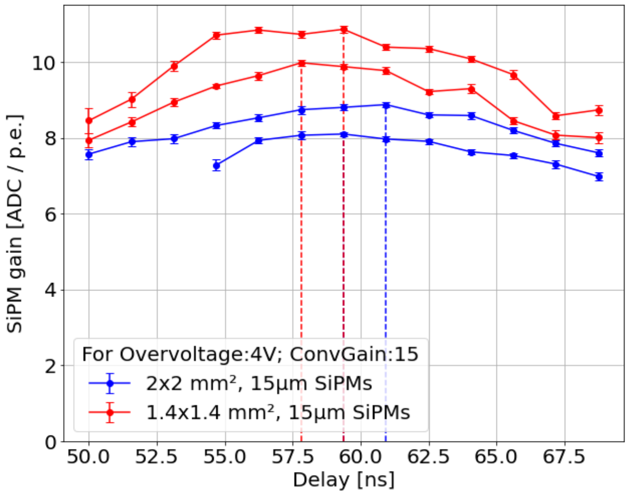

Figure 4.19: SiPM gain vs. signal delay used for data acquisition for three selected channels on a TB1.2 tileboard of two different SiPM sizes. The vertical dotted lines show the delay at which the maximum SiPM gain is obtained for that respective channel. The error bars give the statistical errors of the gain measurement as described in section 4.3.2.4.

4.3.2.4 SiPM Gain Uncertainties

The SiPM gain uncertainties obtained from the multi-Gaussian fits for each channel and configuration. If multiple fits exist for a given channel and delay, the gain uncertainty $\delta\mu$ is estimated to be:

$$\delta\mu = \sqrt{\frac{\Sigma_{i=1}^{N}\sigma_i^2}{N}} \tag{4.11}$$

where σ is the standard deviation of the distribution of SiPM gains measured for different LED runs with N good fits. As the peak gain for each channel is defined as the gain of that SiPM, the gain uncertainty at the same point is taken as the gain uncertainty of the channel.

4.3.2.5 Linearity of the Gain at Lower SiPM Over-Voltages

As mentioned in section 2.4.2.2, the SiPM gain varies linearly with SiPM over-voltage. An over-voltage of around 2 V with respect to $V_{br}((\text{TO}))$ is foreseen to be the operating voltage of the SiPMs at the HGCAL. However, seeing SPS and measuring the gains at these low over-voltages with an HGCROC is impossible. As a result, the linearity of the SiPM gain as a function of over-voltage is used to estimate the SiPM gain for low over-voltages.

Many tests have been conducted on the linearity of the SiPM gain with respect to over-voltage using different readout systems by testing individual SiPM-on-tiles with laser systems. However, doing such tests with tileboards is much more difficult due to the inability to measure gains at lower over-voltages. The DNL also plays a part in this, as the DNL averaging method described above may also increase the width of the individual Gaussian peaks in the SPS. Nevertheless, tests quantifying the linearity using HGCAL Tilemodules were conducted for the first time in the context of this thesis.

In order to do this test, LED data is collected at up to four different over-voltages ranging from 3 V to 6 V. As a common bias voltage is supplied to the entire tileboard, the over-voltage may vary by up to ±0.3 V. The real over-voltages of all channels are calculated using the breakdown voltages provided for each SiPM by HPK.

An additional correction to the over-voltage is done to account for the difference in temperature between the beam test measurements and the 25 °C at which HPK measures the breakdown voltage. More on this correction is given later in section 4.4.1. The plot shown in fig. 4.20 accounts for all these corrections.

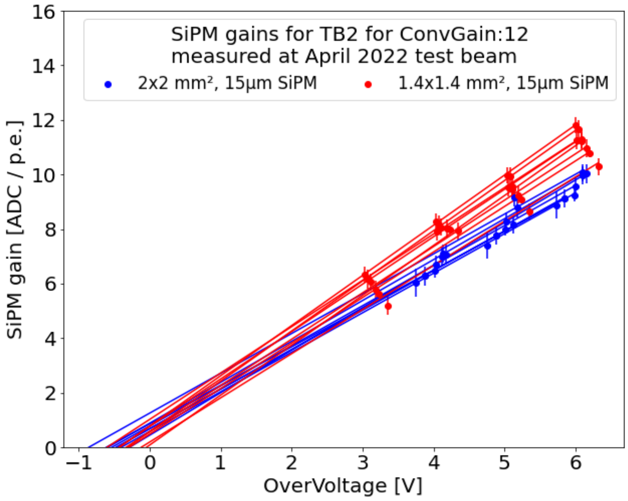

Figure 4.20: Variation of SiPM gain with over-voltage measured using channels on TB2 tileboard

As seen in fig. 4.20, the gains of the different channels do not converge at 0 ADC at an over-voltage of 0 V. This is due to the limited resolution in the ADC scale and the DNL of the HGCROC, which predominantly affects the smaller over-voltages, as explained previously. Therefore, the gains tend to be over-estimated at lower over-voltages, resulting in the gain having a negative offset at $V_{over} = 0$ V. Reducing the number of low over-voltage measurements does not improve the fit either, as it increases the range in which the fit is extrapolated. As a result, the gain at over-voltage 2 V has a higher uncertainty. This shows why the linearity of gain studies using Tilemodules is sub-optimal.

A typical beam test would measure light yields at over-voltages of 2 V and 4 V. Since SPS is visible at 4 V, this requires only the gain measurement at 4 V. However, since the gain at 2 V is only measurable using gains measured at multiple other over-voltages, it takes a larger time (up to four times) to acquire SPS data.

In subsequent beam tests, light yields were predominantly measured at an over-voltage of 4 V with the SIPM's PDE curve used to scale the light yields down to 2 V. More on this is discussed later in section 4.5.1.

4.3.3 Gain Dependence on SiPM Size

One significant finding from SiPM gain results is that the gains of $2 \times 2\,\text{mm}^2$ SiPMs are lower than $1.4 \times 1.4\,\text{mm}^2$ SiPMs. This is seen in fig. 4.19 and in fig. 4.21. This difference in gain is due to a difference in pulse shapes between different SiPM sizes. On TBv1 and TBv2 tileboards where the same HGCROC generation (HGCROCv2) is used, the mean gain at an over-voltage of 4 V and conveyor gain of 12 for $1.4 \times 1.4\,\text{mm}^2$ SiPMs and $2 \times 2\,\text{mm}^2$ SiPMs were measured to be 7.90 ± 0.12 ADC/p.e. and 6.61 ± 0.08 ADC/p.e. respectively.

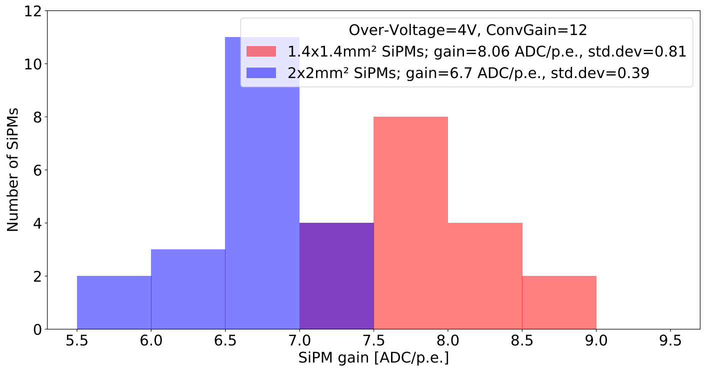

Figure 4.21: Comparison of SiPM gains of two different SiPM sizes for Over-Voltage=4 V and conveyor gain=12. The 39 SiPMs shown here are on three tileboards (TB1.2, TB1.3 and TB2) read out using HGCROCv2.

Since all SiPMs are from the same series, the discharge from a SPAD cell of the different SiPMs ideally produces the same amount of charge. That means the gains should be the same for all SiPMs. However the $2 \times 2\,\text{mm}^2$ SiPMs have twice the active area of the $1.4 \times 1.4\,\text{mm}^2$ SiPMs. This means that the $2 \times 2\,\text{mm}^2$ SiPMs have a higher effective capacitance than the $1.4 \times 1.4\,\text{mm}^2$ SiPMs resulting in longer pulses and smaller amplitudes obtained from $2 \times 2\,\text{mm}^2$ SiPMs than the $1.4 \times 1.4\,\text{mm}^2$ SiPMs. The HGCROC reads this analogue signal, shapes it and then samples the pulse at the relevant delay to measure the gain. Therefore, this measurement is sensitive to the change in pulse shape, resulting in smaller gains for larger SiPM sizes.

Figures 4.19 and 4.20 show that with the default HGCROC shaper capacitance, the difference in gain between the $2 \times 2\,\text{mm}^2$ and $1.4 \times 1.4\,\text{mm}^2$ SiPMs is about 20 % to 25 %. SiPMs with larger numbers of SPADs also have a higher noise due to the increased probability of random cell excitations due to thermal noise. Therefore, under the same conditions, the $3 \times 3\,\text{mm}^2$ SiPMs will have a gain 20 % to 25 % less than the $2 \times 2\,\text{mm}^2$ with a larger noise. The ADC scale's limited resolution means measuring the gain from $3 \times 3\,\text{mm}^2$ under the same HGCROC settings would be challenging. Therefore, special HGCROC settings are needed to obtain SiPM gains from $3 \times 3\,\text{mm}^2$ SiPMs.

4.3.3.1 Gain Measurement from $3 \times 3\,\text{mm}^2$ SiPMs

With the default HGCROC shaper capacitance (Cf=10 and Cf_comp=10), the combination of higher noise and lower gain makes it impossible to measure the gains from $3 \times 3\,\text{mm}^2$ SiPMs for all over-voltages. The solution to this issue was to use different HGCROC shaper parameters (Cf=6 and Cf_comp=6) such that the pulse is shorter and measure the gain only at high over-voltages and conveyor gain settings such as 6 V and 15 respectively.

As explained in section 3.4.1, the main objective of the shaper is to shape the signal to be more Gaussian, thereby reducing the jitter and timing misalignments. If the shaper capacitances are reduced, the rise time is shorter, and the pulse width is smaller. This will increase the charge concentration at the peak, effectively increasing the SiPM gain measured. In addition, the higher over-voltage and conveyor gain also increase the SiPM gain. The SiPM gain vs. delay plot for two different SiPMs measured under the special shaper parameters at an over-voltage of 6 V and conveyor gain of 15 is shown in fig. 4.22. The reason for using an over-voltage of 6 V is that this is the highest HPK recommended over-voltage for these SiPMs. Similarly, a conveyor gain 15 is the maximum current conveyor gain setting possible with the HGCROC.

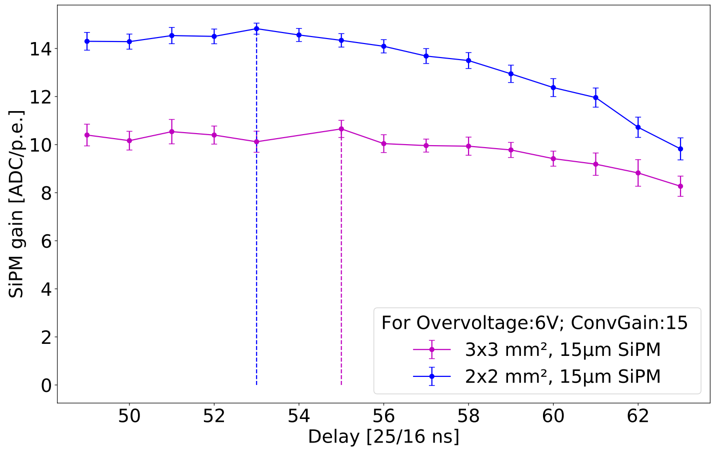

Figure 4.22: SiPM gain vs. delay of pulse acquisition for two channels containing two different SiPM sizes on the MiniTB tileboard. The vertical dotted lines show the delay at which the pulse amplitude can be obtained for that respective channel. The error bars give the statistical errors of the gain measurement from the multi-Gaussian fit and average the gain obtained using different LED bias voltages.

The gain of the $3 \times 3\,\text{mm}^2$ SiPM was measured to be 10.95 ± 0.03 ADC/p.e. at an over-voltage of 6 V and conveyor gain of 15. The gain of the $2 \times 2\,\text{mm}^2$ SiPM was measured to be 15.26 ± 0.03 ADC/p.e. under the same conditions. This means that the gain of the $3 \times 3\,\text{mm}^2$ SiPM is about 30 % smaller than the $2 \times 2\,\text{mm}^2$. Based on the linearity of gain with conveyor gain and over-voltage, at an over-voltage of 4 V, conveyor gain of 12 and under the special shaper settings, a gain of approximately 5.8 ADC/p.e. and 8.1 ADC/p.e. can be expected from the $3 \times 3\,\text{mm}^2$ and $2 \times 2\,\text{mm}^2$ respectively. Given that a gain of 6.61 ± 0.08 ADC/p.e. was measured from the $2 \times 2\,\text{mm}^2$ SiPMs, for the same over-voltage and conveyor gain, but under the default shaper parameters, this indicates that the gain from the $3 \times 3\,\text{mm}^2$ SiPM under the default shaper parameters would be approximately 4.73 ADC/p.e.. The limited ADC resolution and the DNL prevents the measurement of any gain value below about 5 ADC/p.e. for $2 \times 2\,\text{mm}^2$ SiPMs. Larger SiPM sizes also have a larger pedestal width. This means that the threshold of measuring the gain for $3 \times 3\,\text{mm}^2$ SiPMs is at a threshold even higher than this estimated 5 ADC/p.e. limit. Therefore, it is clear from this experiment that it would be impossible to measure the gains of the $3 \times 3\,\text{mm}^2$ SiPMs even under these special parameters at an over-voltage of 4 V and conveyor gain of 12. Therefore, the recommendation would be to measure the gain at an over-voltage of

6 V and for conveyor gain of 15 using the special setting even at the final experiment.

As the Rf, Cf and Cf_comp parameters are set to all SiPMs readout using an HGCROC half globally, and each HGCROC typically reads out SiPMs of half the Tilemodule, this means that the $3 \times 3\,\mathrm{mm}^2$ SiPMs cannot share the same Tilemodule half as $2 \times 2\,\mathrm{mm}^2$ SiPMs if they are readout by the same HGCROC half.

4.4 Determination of Light Yields

Section 4.2 discussed the methods used to measure the MIP maxima in ADC units while section 4.3 discussed the method used to determine the gain of the SiPM in terms of ADC per photo-electron (p.e.). Therefore, light yield is directly calculated by taking the ratio of these two measurements (see eq. (2.35)) as:

$$\text{Light Yield [p.e.]} = \frac{\text{MIP Maximum [ADC]}}{\text{SiPM Gain [ADC/p.e.]}}. \tag{4.12}$$

4.4.1 Light Yield Correction for Over-Voltage and Temperature

Light yield can only be calculated if the SiPM over-voltage and all HGCROC parameters, including conveyor gain, remain constant between the MIP and gain measurements. As all HGCROC parameters are set via a configuration script, using the same configuration script to take beam and LED data ensures that the HGCROC parameters stay constant between the two measurements.

However, ensuring a constant over-voltage is much more tricky. As the breakdown voltage of the SiPMs is temperature dependent, a change in temperature during measurements changes the over-voltage. As the beam test area has no temperature control, the temperatures at which the gain and MIP maximum measurements were acquired often differed by a few degrees. Furthermore, the temperatures at which these measurements were acquired will also change from beam to beam test. The breakdown voltage also varies from SiPM to SiPM, meaning the over-voltage under which the SiPMs operate varies from channel to channel. All these reasons mean adjusting the light yield to a fixed over-voltage is vital to comparing light yields between SiPMs, tileboards and beam tests.

The light yield adjustment to a fixed set of conditions is done via two steps and is summarised in fig. 4.23. First, the SiPM gains are adjusted to the initial conditions under which the MIP measurements were made. With this, the light yield can be calculated for the conditions under which the MIP measurement occurred. As a second step, the light yields are then adjusted to the final conditions required. Typically light yields are computed for an over-voltage of 2 V and 4 V.

Eight PT1000 temperature sensors are included in the tileboards to measure the temperatures at which the SiPMs operate precisely. The TB-tester DAQ system can read these out via the GBT-SCA to determine the temperature of the SiPMs. The KCU105 DAQ, however, cannot read out these temperature sensor data due to its inability to communicate with the GBT-SCA. Therefore, when using the KCU105 DAQ, two thermistors were taped onto the tileboard to read the temperatures externally.

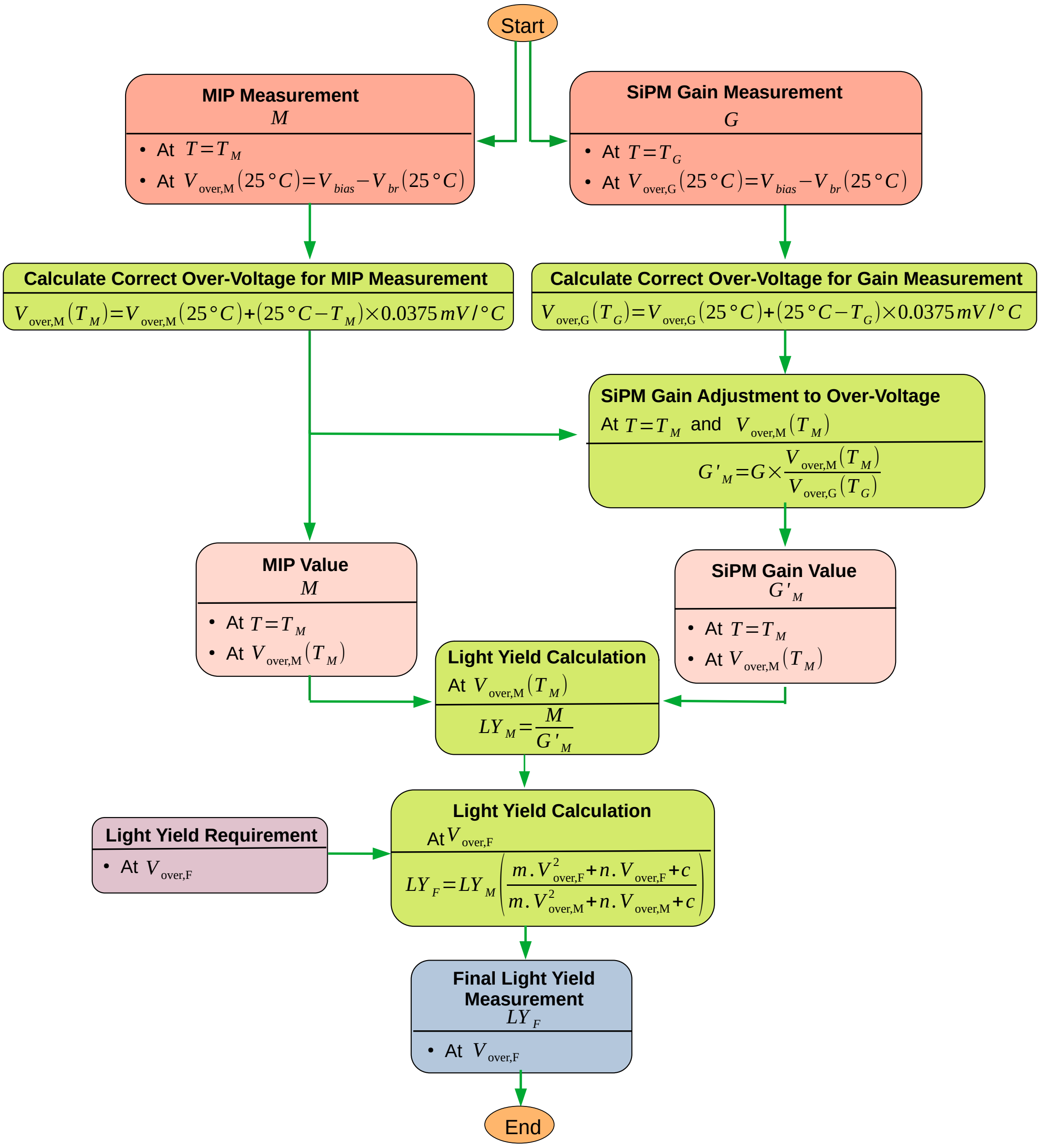
Start
MIP Measurement
M
At T=T_M
At V_over,M(25°C)=V_bias−V_br(25°C)
SiPM Gain Measurement
G
At T=T_G
At V_over,G(25°C)=V_bias−V_br(25°C)
Calculate Correct Over-Voltage for MIP Measurement
V_over,M(T_M)=V_over,M(25°C)+(25°C−T_M)×0.0375mV/°C
Calculate Correct Over-Voltage for Gain Measurement
V_over,G(T_G)=V_over,G(25°C)+(25°C−T_G)×0.0375mV/°C
SiPM Gain Adjustment to Over-Voltage
At T=T_M and V_over,M(T_M)
G'_M=G×V_over,M(T_M)/V_over,G(T_G)
MIP Value
M
At T=T_M
At V_over,M(T_M)
SiPM Gain Value
G'_M
At T=T_M
At V_over,M(T_M)
Light Yield Calculation
At V_over,M(T_M)
LY_M=M/G'_M
Light Yield Requirement
At V_over,F
Light Yield Calculation
At V_over,F
LY_F=LY_M((m.V²_over,F+n.V_over,F+c)/(m.V²_over,M+n.V_over,M+c))
Final Light Yield Measurement
LY_F
At V_over,F
End

Figure 4.23: Flow chart showing the steps taken to obtain the final light yields adjusted to the needed over-voltage (V_{over}) and 25 °C temperature.

The breakdown voltage measured by HPK is measured at a temperature of 25 °C. To correctly determine the over-voltage, the breakdown voltage is calculated for the temperature at which the MIP and gain measurements were taken. The breakdown voltage increases linearly with temperature. HPK measures the breakdown voltage - temperature gradient as 34 mV/K. However, measurements done within the HGCAL collaboration measured this quantity to be 37.5 mV/K [74], and therefore, this was the value used for this thesis for the voltage adjustment. Once this value is known, the over-voltage is calculated using the following equation:

$$V_{over}(T) = V_{bias} - V_{br}(25\,^{\circ}\mathrm{C}) + (25\,^{\circ}\mathrm{C} - T) \cdot 0.0375\,\mathrm{V/K}, \tag{4.13}$$

where $V_{over}(T)$ is the temperature-adjusted over-voltage at temperature T. This equation is used twice to calculate the over-voltages under which the SiPM gain and MIP measurements were acquired. Once the correct over-voltages have been calculated, one of the measured values must be adjusted so that both the SiPM gain and MIP maxima are determined for the same over-voltage. The easier option of the two is to adjust the SiPM gain to the same over-voltage under which the MIP maximum was obtained as the SiPM gain changes linearity with over-voltage. That is:

$$G_M = G \times \frac{V_{over,M}}{V_{over,G}}, \tag{4.14}$$

where G is the gain measured at over-voltage $V_{over,G}$, $V_{over,M}$ is the over-voltage at which the MIP maxima was measured, and G_M is the gain calculated for the over-voltage $V_{over,M}$. Now that both the MIP maximum and SiPM gain are at the same over-voltage, the light yield can be measured using eq. (4.12) for the same over-voltage.

In order to compare light yields across multiple beam tests, one needs to standardise the light yields to fixed conditions, meaning a fixed over-voltage. As shown by eq. (2.36), the light yield is proportional to the PDE of the SiPM. The PDE curve was found on the datasheet [72] as a function of over-voltage. A second-order polynomial, given by :

$$\text{PDE} = m_1 \cdot V_{over}^2 + m_2 \cdot V_{over} + c \tag{4.15}$$

is used to model this curve, and m_1, m_2 and c were determined as $-0.72\,\mathrm{V}^{-2}$, $10.0\,\mathrm{V}^{-1}$ and $4.41\,\mathrm{V}^{-1}$ respectively. This is shown in fig. 4.24.

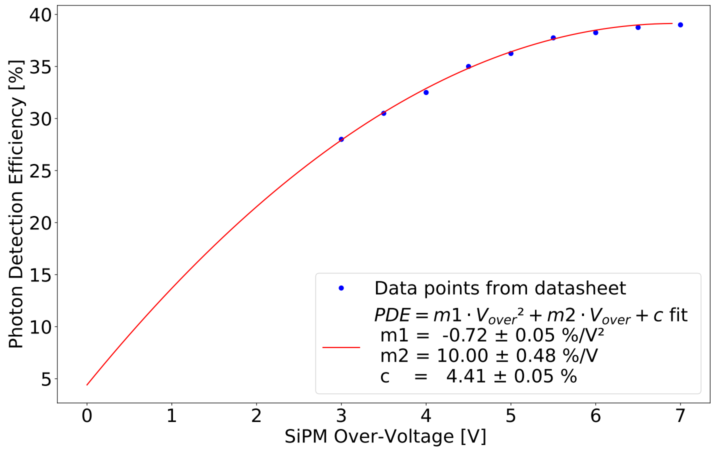

Figure 4.24: Photon detection efficiency vs. SiPM over-voltage plot. The data were obtained from the SiPM datasheet [72]. The PDE is fitted using a second-order polynomial.

Since PDE is proportional to the light yield, we have:

$$\text{Light Yield} \propto m_1 \cdot V_{over}^2 + m_2 \cdot V_{over} + c \tag{4.16}$$

Since m_1, m_2 and c are known, the light yield at a specific over-voltage (V_{over}) can be obtained using the following equation:

$$\text{Light Yield}' = \text{Light Yield} \cdot \left(\frac{m_1 \cdot (V'_{over})^2 + m_2 \cdot (V'_{over}) + c}{m_1 \cdot (V_{over})^2 + m_2 \cdot (V_{over}) + c} \right), \tag{4.17}$$

where Light Yield$'$ is the final light yield calculated at V'_{over} from the light yield measured at V_{over}. These equations are typically used to correct the minor differences in over-voltages provided to the SiPM. Hence, the changes in light yields are typically small. However, a test was proposed and conducted to test the algorithm's robustness.

Three light yield data sets are measured at over-voltages of 2 V, 3 V and 4 V. While the MIP maxima and the gains for over-voltages of 3 V and 4 V, and the MIP maxima for an over-voltage of 2 V were directly measured at the beam test, the gain extrapolation described previously was used to measure the gain at an over-voltage of 2 V for this exercise. Using the above equations, light yields measured at 2 V and 4 V are used to derive the light yield at 3 V. The differences on average between the derived data and measured data at 3 V over-voltage are observed to be less than 10 %. This was done for nine different SiPM-on-tile channels, and the results are shown in fig. 4.25. These observed differences are expected to be dominated by the uncertainties in the SiPM gain measurements.

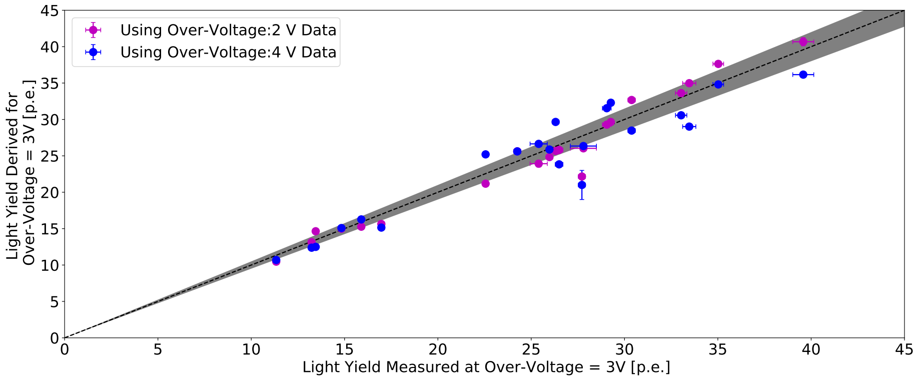

Figure 4.25: Light yield derived to an over-voltage of 3 V using 2 V and 4 V data sets and eq. (4.17). The black dotted line plots the points at which the two different light yields are identical, while the grey area shades the area within a 5 % deviation of this black line. Error bars show the statistical uncertainties of the measurement.

4.4.2 Uncertainty of Light Yield Measurements

The uncertainties of the light yield measurements can be categorised as statistical and systematic.

As the name suggests, the statistical uncertainties are due to the statistical fluctuations. These uncertainties have been calculated by taking the fit uncertainties from the Landau-Gaussian and multi-Gaussian functions used to obtain the MIP maximum and SiPM gain, respectively. Error propagation is then used to estimate the statistical uncertainty.

For most channels, the statistical uncertainties for most MIP maximum measurements are in the range of a few ADCs and mostly constant with the MIP maximum measured. Therefore, the statistical uncertainties measured for larger MIP maxima are less than 1 %. However, the statistical uncertainty of the gain averages at about 8 % of the measurement. As a result, larger light yields have a statistical uncertainty dominated by the gain uncertainty of about 8 %.

The primary source of uncertainties dealt with in the system is systematic uncertainties. This includes light yield variations due to variations in SiPM or scintillator quality, defects in the tile wrapping, uncertainties in supplied bias voltages, etc. These sources of systematic uncertainties are more significant than statistical uncertainties.

One way to estimate with the systematic uncertainties is to repeat the exact light yield measurements over multiple beam tests for multiple SiPM-on-tiles under multiple conditions such as different over-voltages as shown in fig. 4.26. For a given over-voltage, the light yield should be the same. Therefore, the uncertainty of the mean ($\delta\mu$) can be measured by taking the standard deviation of the sample.

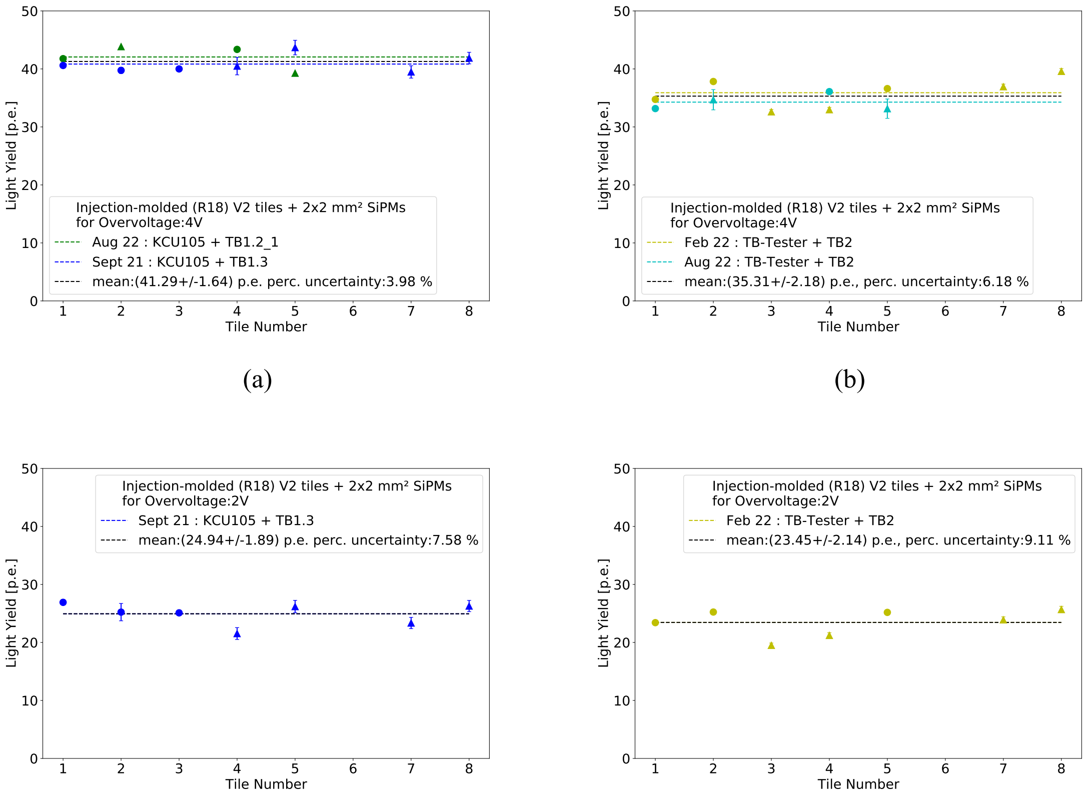

(a) (b)

(c) (d)

Figure 4.26: Multiple light yields were measured for the same seven IHEP injection-moulded tiles over different beam tests and SiPMs and Tilemodules. (a) and (c) used TBv1 tileboards for over-voltages of 4 V and 2 V respectively, while (b) and (d) used TBv2 tileboards for over-voltages of 4 V and 2 V. The final uncertainties are given as a fraction of the mean light yields. Light yields from $1.4 \times 1.4\,\mathrm{mm}^2$ SiPMs (shown by triangles) have been increased by a factor of 2.04 in order to be combined with $2 \times 2\,\mathrm{mm}^2$ SiPM data (shown by circles).

The light yields from $1.4 \times 1.4\,\mathrm{mm}^2$ SiPMs have been multiplied by a factor of 2.04 in fig. 4.26 as light yield scales with the SiPM size. This scaling is discussed in detail later in section 4.5.1.

Different SiPMs are coupled with the same tiles to obtain the light yields shown in fig. 4.26. A trend can be seen in light yield from tile to tile. For example, tile number 3 generally exhibits a low light yield, while tile number 8 exhibits a higher light yield. This trend is because scintillator-to-scintillator variations in quality and wrapping non-uniformities dominate the systematic uncertainty.

The light yield has been adjusted for over-voltage variations from channel-to-channel and tileboard-to-tileboard. For TBv1 tileboards holding IHEP injection-moulded scintillators produced for the ring 18 (R18) of the detector with SiPMs operating at an over-voltage of 4 V (see fig. 4.26(a)), the observed percentage uncertainty is 3.99 % of the measurement. However, for TBv2 tileboards holding the same tiles, the observed percentage uncertainty is 6.13 % of the measurement (see fig. 4.26(b)). The breakdown voltages of the individual SiPMs on TBv2 tileboards are unknown due to a technical fault during the tileboard assembly. This resulted in a more significant uncertainty of the over-voltages of SiPMs on the TBv2 tileboards, resulting in a more significant percentage uncertainty in TBv2 light yield results than TBv1.

Furthermore, larger uncertainties are observed for light yield measurements at an over-voltage of 2 V in comparison to the measurements at an over-voltage of 4 V due to the gain extrapolation method mentioned before used to extract the SiPM gain at an over-voltage of 2 V. For an example, the measured percentage uncertainty for the injection-moulded tiles on TBv1 tileboard and SiPMs operating at 4 V and 2 V is 3.99 % and 7.58 % of the light yield respectively (see fig. 4.26(a) and fig. 4.26(c)). As a result, light yields measured at 4 V are primarily used to draw conclusions from in this thesis.

4.4.3 Reproducibility of Light Yield for Different Conveyor Gains

As previously mentioned, light yield is purely optical based solely on the SiPM and scintillator properties. This means that the light yield is independent of the conveyor gain. One test of this is to change the conveyor gain and measure the light yields at multiple conveyor gains. Results shown in fig. 4.27 show the linear rise of the MIP maxima as a function of the conveyor gain used.

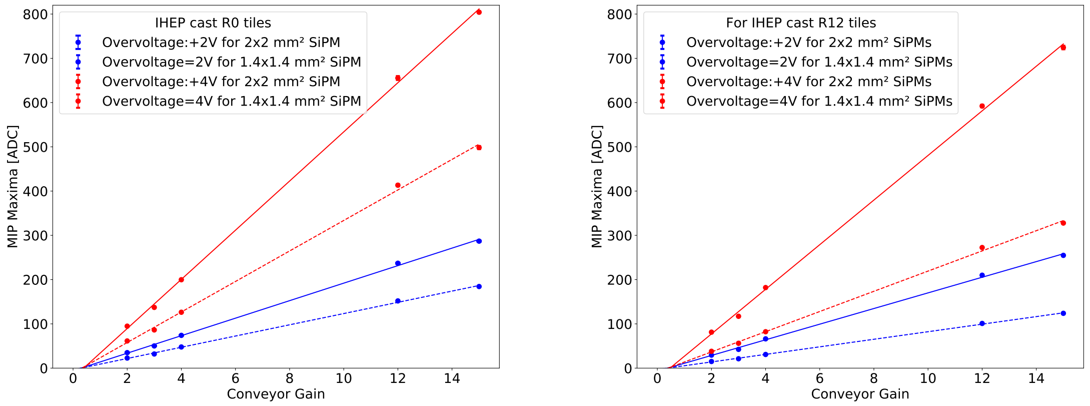

(a) (b)

Figure 4.27: MIP maxima obtained from different IHEP cast tiles of two different tile sizes. (a) is for the smallest tiles (to be used in ring R0 of the detector) of 22.50 mm tile edge length, and (b) is for tiles of 29.48 mm tile edge length (to be used in ring R12 of the detector).

The basic functionality of the current conveyor is described in section 3.4. Since the current multiplication factor increases linearly with conveyor gain, the increase of MIP maxima from tiles with conveyor gain is expected, as seen in fig. 4.27.

The exact relationship is expected for the SiPM gain. This was confirmed with SPS data taken with conveyor gains ranging between 10 and 15. However, the SiPM gain is not measurable for lower conveyor gains than this. Since the conveyor gain multiplies the SiPM gain and MIP maximum by the same factor, the light yield must be independent of the conveyor gain. Therefore, the best way to investigate the SiPM gain relationship with conveyor gain is to observe the relationship of light yield as a function of conveyor gain in the range where the SiPM gain was measurable. Figure 4.28 shows the observed light yield for different conveyor gains compared to the light yield observed at conveyor gain 12. The figure shows that the light yields measured for different conveyor gains agree with those measured with a conveyor gain 12 with a maximum deviation of 15 %.

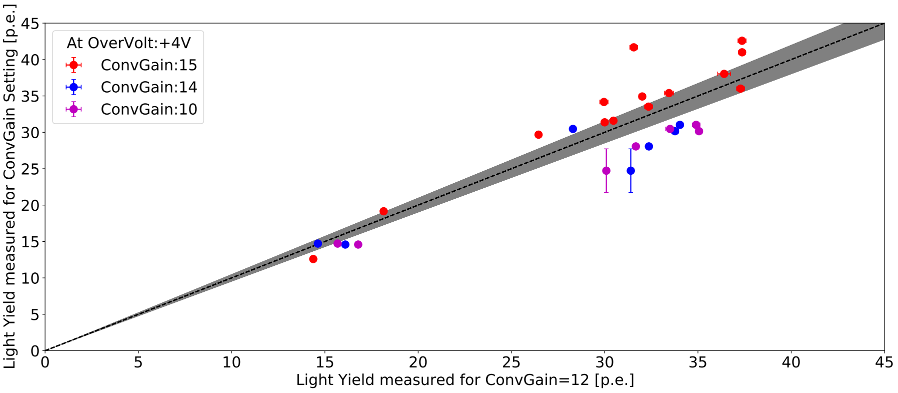

Figure 4.28: Light yields measured for different conveyor gains for an over-voltage of 4 V compared with the light yield measured for a conveyor gain of 12. The black dotted line plots the points at which the two different light yields measured are identical, while the grey area shows the area within a 5 % deviation of this black line

4.4.4 Reproducibility of Light Yields for Different Tile Board Generations

One important test is to validate that light yields over different tile board generations still produce the same light yields. Figure 4.26 shows the light yields from the same seven IHEP injection-moulded tiles measured with two different tileboards. Based on this data, light yields from the first-generation tile boards perform 10 % better than their second-generation counterpart.

A possible explanation for the difference in light yield is better optical performance on TBv1 tileboards due to white paint around the SiPM as shown in fig. 4.29. These white paint dots are painted around the SiPM such that photons are reflected back to the scintillator, which would otherwise escape the tileboard. They were present in TBv1 but absent in both TBv2 and TBv3. The CALICE collaboration with the AHCAL prototype [88] has also observed such effects.

In order to prove this hypothesis, the area around the SiPMs on a TBv2 tileboard was covered in white tape. This tileboard was then put into the beam, and the light yields were measured. A photo of this modified tileboard can be found in fig. 4.29(c). As seen in the results shown in fig. 4.30, the light yields indeed did improve once the white stickers were added to similar levels seen with the TBv1 tileboards, supporting the hypothesis.

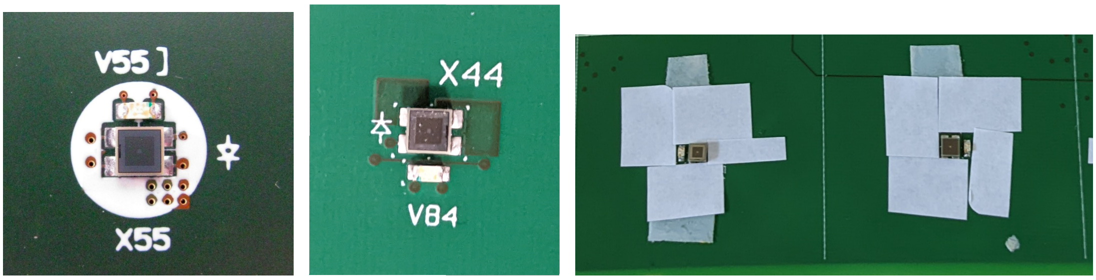

(a) (b) (c)

Figure 4.29: The SiPM area on two generations of tileboards. (a) is from a TBv1 tileboard, while (b) is from a TBv2 tileboard. (c) shows the modified TBv2 tileboard with white stickers surrounding the SiPMs to recreate the white paint around SiPMs in TBv1 tileboards.

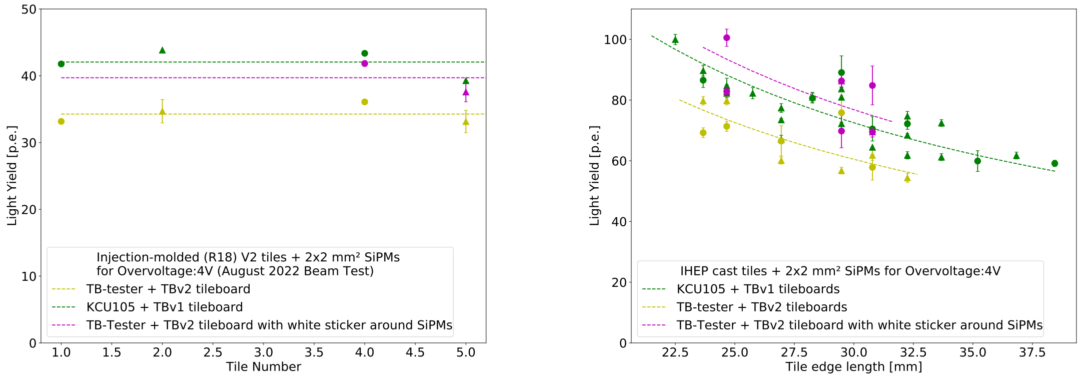

(a) (b)

Figure 4.30: Change in light yields due to the effect of the white paint dot. (a) compares the light yield from identical IHEP-produced injection-moulded tiles placed on the same SiPM on a TB2 Tileboard before (yellow) and after (purple), adding the white paint dot. The same tiles are also placed on SiPMs on TBv1, which contains the white paint dot (green). (b) compares the light yields from cast tiles on TBv2 tileboards (yellow) and after (purple) adding the white paint dot. The green curve gives the light yield from TBv1 tileboards, which contains the white paint dot.

The primary outcome of these tests is that all light yields are reproducible; however, due to the lack of highly reflective white paint around SiPMs on TBv2, TB3 or miniTB tileboards, the light yields are about 10 % lower. As a result, all light yields obtained from TBv2, TB3 or miniTB tileboards are scaled up by 10 % to account for this effect in the remainder of this thesis.

4.5 Comparison of Light Yields for Different SiPM-on-Tile Configurations

The light yield of SiPM-on-tiles is known to be influenced by factors such as tile size and SiPM's area. The exact relations of these two factors are given by eq. (2.39). Figure 4.31 shows light yields from IHEP cast, and EJ cast tiles exhibit these properties. Multiple experiments observed that for a fixed over-voltage, the light yield is also inversely proportional to the square root of the scintillator area [62, 63]. Therefore, light yield can be fitted using the function given as:

$$\text{light yield} = \frac{k}{\sqrt{\text{scintillator area}}} \tag{4.18}$$

where k is a constant which depends on scintillator and SiPM properties. The fit agrees well with the data for all over-voltages as observed in fig. 4.31. Similar results were seen for all other tile materials used.

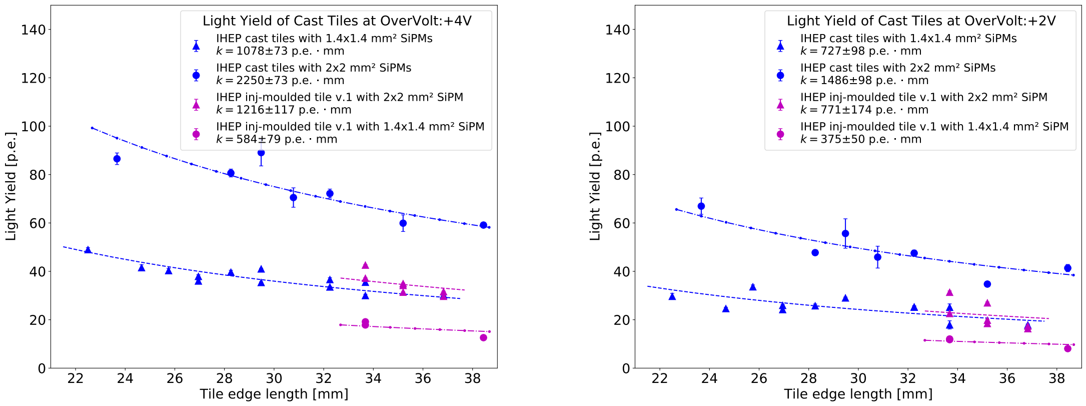

(a) (b)

Figure 4.31: Light yields from IHEP cast tiles and IHEP version 1 injection-moulded tiles as observed for 4 V and 2 V over-voltages. The fit uses the relation light yield $= \frac{k}{\sqrt{\text{scintillator area}}}$.

4.5.1 Effect of SiPM Size on Light Yield

The light yield increases as a function of the active area of the SiPM. The area increases by a factor of 2.04 between $1.4 \times 1.4\,\text{mm}^2$ and $2 \times 2\,\text{mm}^2$. Therefore, the light yield must also increase by the same factor. As seen in fig. 4.31, the ratios of parameter k between $2 \times 2\,\text{mm}^2$ and $1.4 \times 1.4\,\text{mm}^2$ is measured to be 2.09 ± 0.15 for the IHEP cast tiles and 2.08 ± 0.34 IHEP inection-moulded v1 tiles at an over-voltage of 4 V. This value agrees with the increased SiPM size within the uncertainties of the experiment.

This is also true for $3 \times 3\,\text{mm}^2$ SiPMs whose area and, therefore, light yield increases by a factor of 2.25 in comparison to $2 \times 2\,\text{mm}^2$ SiPMs. One such example is given in fig. 4.32 where the light yields have been measured from a $3 \times 3\,\text{mm}^2$ SiPM and a $2 \times 2\,\text{mm}^2$ SiPM both coupled with the same scintillator tile. The $3 \times 3\,\text{mm}^2$ SiPM has a 2.29 ± 0.04 higher light yield than the $2 \times 2\,\text{mm}^2$ SiPM as expected.

Since this relationship was established for all SiPMs used, all light yields are scaled to the $2 \times 2\,\text{mm}^2$ SiPMs by multiplying the light yields obtained from other SiPMs by the ratio of SiPM active areas. That is:

$$\text{light yield} = \frac{k(\text{for } 4\,\text{mm}^2\text{ SiPM})}{\sqrt{\text{scintillator area}}} \cdot \frac{\text{SiPM active area}}{4\,\text{mm}^2}. \tag{4.19}$$

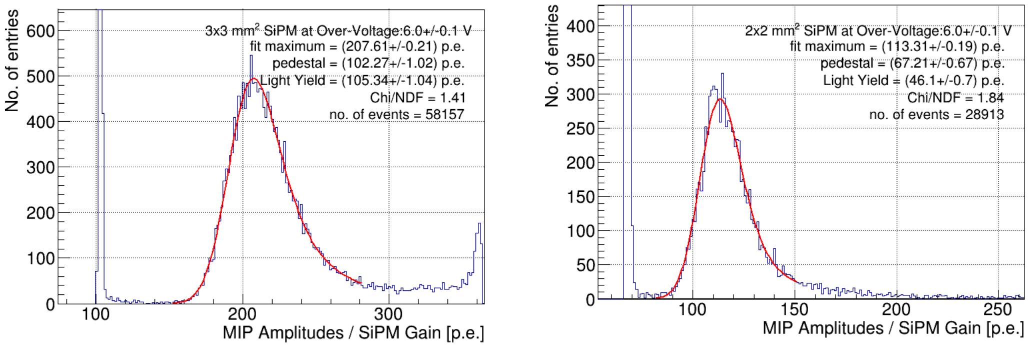

(a) (b)

Figure 4.32: MIP spectra rescaled to p.e. units using SiPM gains for two channels with the same scintillator placed on top. (a) is a channel with a $2 \times 2\,\mathrm{mm}^2$, and (b) is a channel with a $3 \times 3\,\mathrm{mm}^2$ SiPM. Both channels have the same IHEP v2 scintillator tile. Light yield of the $3 \times 3\,\mathrm{mm}^2$ SiPM is 105.34 ± 1.04 p.e. and the light yield $2 \times 2\,\mathrm{mm}^2$ SiPM is 46.1 ± 0.7 p.e..

4.5.2 Effect of Over-Voltage on Light Yield

As discussed in section 4.4.1, light yield is also proportional to the PDE of the SiPM. This was used to derive eq. (4.17) and apply light yield adjustments for deviations in over-voltage. Therefore, eq. (4.19) can be transformed using eq. (4.17) as:

$$\text{light yield}(V_{over}) = \frac{k(\text{for } 4\,\mathrm{mm}^2 \text{ SiPM})}{\sqrt{\text{scintillator area}}} \cdot \frac{\mathrm{PDE}(V_{over})}{\mathrm{PDE}(V'_{over})} \cdot \frac{\text{SiPM active area}}{4\,\mathrm{mm}^2} \tag{4.20}$$

where $\mathrm{PDE}(V'_{over})$ is the PDE at the measured over-voltage and $\mathrm{PDE}(V_{over})$ is the PDE at which the light yields are needed derived using. Equation (4.20) is given in terms of the $2 \times 2\,\mathrm{mm}^2$ SiPM. This equation is only valid if all SiPMs have the same pitch size, which is true for the SiPMs used here. In addition, this equation can be used to estimate the light yield of different SiPM and tile sizes. This equation was later used to calculate SNR expected at the detector end-of-life discussed in chapter 7.

4.5.3 Effect of Scintillator Material on Light Yield

Once the reproducibility of light yields between Tilemodules and beam tests is ensured, comparing light yields of different scintillator materials is finally possible.

Over the years, light yields of all four versions of the IHEP injection-moulded tiles were measured at beam tests. The first two versions were tested with TBv1 Tilemodules, while the latter (version 3 and version 3 (dot)) used TBv2 Tilemodules. Similarly, the injection-moulded tiles produced at FNAL were wrapped, and their performances were measured at beam tests on TBv3 tileboards. Figure 4.33(a) shows the light yields of these SiPMs as a function of the scintillator's edge length.

Based on the fits from fig. 4.33(a), the best-performing tiles were the IHEPv3 injection-moulded tiles. With each generation of IHEP injection-moulded tiles, light yields have improved.

The light yields from the FNAL batch 1 tile are about 4 % lower than the IHEP version

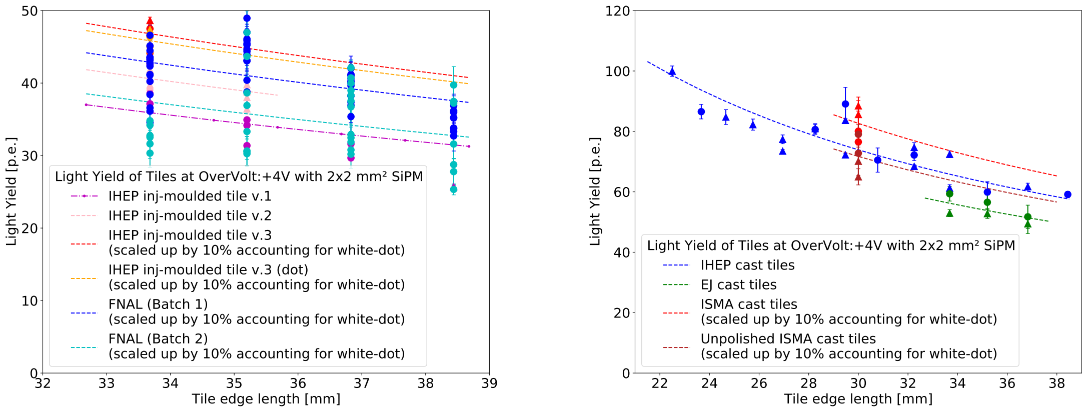

(a) (b)

Figure 4.33: Light yields from all tiles measured at beam tests at a SiPM over-voltage of 4 V. (a) shows the light yields of all injection-moulded tiles. (b) shows the light yields of all cast tiles. The fit used the relation light yield $= \frac{k}{\sqrt{\text{scintillator area}}}$. Error bars give the statistical uncertainties of each light yield measurement.

3 tiles, while the batch 2 tiles performed 14 % poorer than the batch 1 tiles on average. The performance of these tiles is summarised in table 4.3.

Table 4.3: Overview of light yields measured for all IHEP injection moulded tiles. All values were measured or scaled for $2 \times 2\,\text{mm}^2$ operating at $V_{over} = 4\,\text{V}$.

Injection-Moulded Tiles	k [p.e. · mm]	Improvement [%]
IHEP inj-moulded version 1	1226 ± 123	baseline
IHEP inj-moulded version 2	1354 ± 52	10.4
IHEP inj-moulded version 3	1497 ± 64	22.1
IHEP inj-moulded version 3 (dot)	1467 ± 44	19.6
FNAL inj-moulded batch 1	1441 ± 119	17.5
FNAL inj-moulded batch 2	1259 ± 186	2.7

The cast tiles also exhibit different light yields as illustrated in fig. 4.33(b). These were all commercially produced BC-408 and EJ-208 tiles but machined at different institutes. The results show that the unpolished BC-408 naturally exhibits a higher light yield than unpolished EJ-208 by roughly 12 %. The exact improvements are given in table 4.4. Furthermore, when the ISMA tiles were polished, light yields improved by 11.8 %, indicating that light yields can be improved by polishing the tiles. However, it is worth noting that ISMA tiles were only available in $30 \times 30\,\text{mm}^2$ square size.

Note that the light yields from the NIU BC-412 cast tiles were not measured on tileboards at beam tests when writing this thesis. These measurements come from the ^{90}Sr source-based setup discussed in section 4.7. However, plans have already been made to measure the light yields of these tiles on tileboards in an upcoming beam test at DESY-II.

Table 4.4: Overview of light yields measured for all cast tiles. values were measured or scaled for $2 \times 2\,\text{mm}^2$ SiPMs operating at $V_{over} = 4\,\text{V}$

Cast Tiles	k **[p.e. $\cdot$ mm]**	Improvement [%]
IHEP cast	2220 ± 165	baseline
EJ cast	1950 ± 91	12.2
ISMA cast (unpolished)	2153 ± 176	-3.0
ISMA cast (polished)	2482 ± 161	11.8
using ^{90}Sr source-based setup (see section 4.7)		
NIU BC-412 cast	3222 ± 95	45.1

4.6 Reproducibility of Light Yields with Muon Beam at SPS Facility, CERN

A particular beam test was conducted at the test beam facility at CERN's Super Proton Synchrotron facility (SPS facility) in October 2021 to reproduce light yields in a different environment and with 120 GeV muons. Muons at this energy passing through scintillator tiles can be considered as MIPs. Therefore, this offers the perfect scenario to compare light yields measured with 3 GeV electrons at DESY beam tests with light yields measured at SPS with MIP particles.

4.6.1 Test Setup

The same setup used at the DESY-II beam test facility (see section 4.2) was used at the SPS. Images from this beam test are shown in fig. 4.34. The final setup also included a light-tight cover over the setup to prevent light contamination. Tileboard TB1.3 was used at this test beam with the KCU105 DAQ system. The beamline was shared with colleagues working on the silicon sensors needed for the HGCAL upgrade, with their setup placed in front of the tileboard and with the tileboard using the beam parasitically. A common trigger scintillator pair was used for both setups. Gains of the SiPMs were also measured at both beam tests and used to calculate the light yield.

Eleven IHEP injection moulded version 2 tiles were equipped on the TB1.3 tileboard. This included five tiles placed on $1.4 \times 1.4\,\text{mm}^2$ SiPMs (channels 47, 48, 55,56 and 57) and six on $2 \times 2\,\text{mm}^2$ SiPMs (channels 49, 50, 59, 60, 61 and 62). These tiles were first measured at a beam test held at DESY a week before the SPS facility beam test, and the same tileboard was then taken to SPS without changing the tile configuration on the board.

Since the KCU105 DAQ system was used, the template fit method described in section 4.2.2 was used to extract the MIP maxima. The analysis of the data, including the light yield adjustment to over-voltage and temperature, followed the same procedure described in section 4.4.1.

4.6.2 Results and Discussion

The results of this beam test are shown on fig. 4.35. The averages of the two light yield results agree within 5 % of each other.

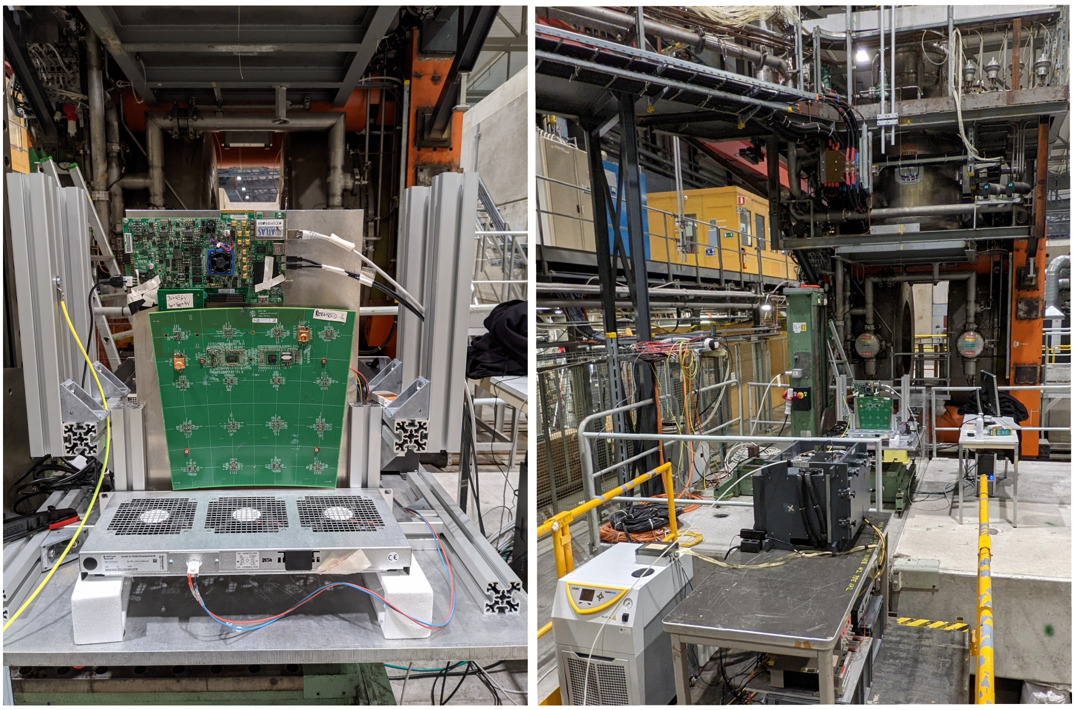
(a) (b)

Figure 4.34: Beam test setup used at SPS, CERN test beam facility. The setup is identical to that used at DESY. TB1.3 was used here with the KCU105 DAQ system. The beamline was shared with colleagues working on the silicon sensors needed for the HGCAL upgrade, with their setup placed in front of the Tilemodule, with the Tilemodule using the beam parasitically. The common trigger scintillator pair was used for both setups. (a) shows the tileboard and KCU DAQ system on the aluminium frame placed. (b) shows the position of the setup with respect to the stage and the silicon sensor setup.

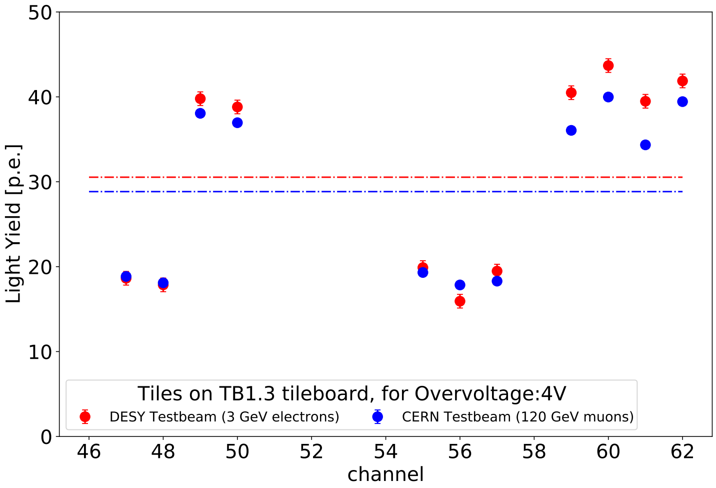

Figure 4.35: Light yields measured at the DESY test beam facility with 3 GeV electrons in comparison with light yields measured at the CERN, SPS test beam facility with 120 GeV muons.

The fact that the mean light yields agree within 5 % of each other indicates that the assumption made about the 3 GeV electrons resembling MIPs is valid. Theoretically, electrons of 3 GeV energy passing through very low-density materials such as plastics lie in the region with the relativistic rise on the Bethe-Bloch equation described in eq. (2.10). However, the most probable energy loss for electrons in plastic scintillators at 3 GeV energy remains relatively at the same value, with only the tail of the Landau function extending.

4.7 Reproducibility of Light Yields with Strontium-90 Source

Beam tests with Tilemodules and SiPMs are essential to validate the performance of the Tilemodules in the final detector. However, repeating such measurements for every scintillator developed by vendors and institutes is not only time-consuming but also logistically inefficient. The organisation of beam tests at DESY-II or other test beam facilities requires preparations well in advance, and a typical test beam runs for a week, so the amount of data that can be taken is limited. Furthermore, with the dates for the start of tiles and Tilemodules production approaching, it is essential to have a setup independent of beam tests for the quick measurement of light yields to ensure the quality of the tiles during final production.

The setup developed at DESY for this purpose uses a ^{90}Sr source, producing low energy electrons up to about 2.2 MeV. ^{90}Sr has a half-life of 28.79 years and beta decay into ^{90}Y. The electrons produced have a maximum energy of about 550 keV. ^{90}Y is also unstable and beta decay into ^{90}Zr with a half-life of 64.1 hours. These electrons have a maximum energy of about 2.2 MeV.

The ^{90}Sr source-based setup was developed at DESY for the quality control and quality assurance of the produced and wrapped tiles. A brief description of the ^{90}Sr setup can be found in [89]. The setup taken from [89] is also shown in fig. 4.36.

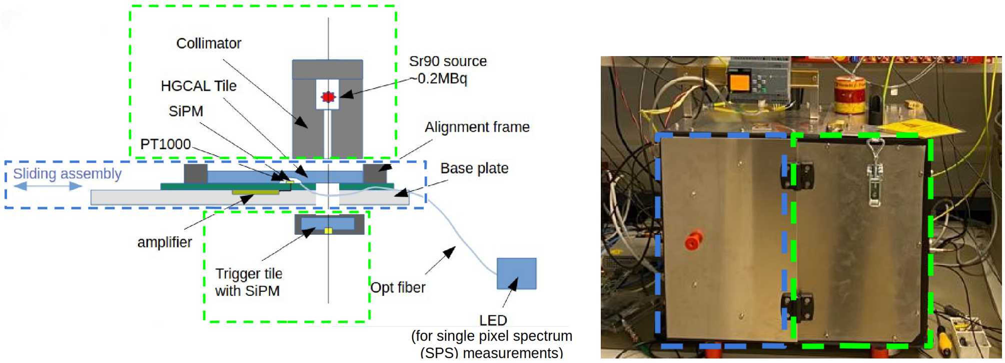

(a) (b)

Figure 4.36: ^{90}Sr source-based light yield setup developed for quality control and assurance. (a) shows a sketch of the setup, and (b) shows the setup with the corresponding areas marked. Electrons from the source pass through the HGCAL tile (tile under test) and pass through the trigger tile, which triggers data taken from the SiPM under the HGCAL tile. Taken from [89].

The setup consists of two areas marked in green and blue in fig. 4.36. The ^{90}Sr source sits on one area (marked in green) completely insulated using steel. The second area (marked in blue) is the loading area, where the tile under test is placed on an alignment frame atop a slider such that the tile's dome covers the SiPM on the slider. Once the slider is slid into the area containing the ^{90}Sr source, the tile sits perfectly between the ^{90}Sr source and a much smaller trigger tile with its SiPM. This trigger tile and SiPM are perfectly underneath the ^{90}Sr source such that electrons produced at the source pass through the tile under test and then through the trigger tile to produce a signal at the trigger SiPM. This, in turn, triggers the data taken from the SiPM underneath the tile under test. The electrons from the ^{90}Sr source pass through the tile and trigger the data taken from the SiPM on the slider.

Electrons in the keV range are typically absorbed via ionisation. As the energy increases, the probability of electrons stopping in the scintillator reduces due to decreased stopping power. Therefore, only the higher energy electrons in the MeV range pass through the tile. Though these electrons are not MIPs, they produce a signal in thin scintillators similar to MIPs, with the maxima increasing by a few per cent compared to a MIP maximum. Therefore, a ^{90}Sr source-based setup can reproduce light yields observed at test beams. As the SiPM on the slider is part of the setup and remains unchanged for all tile measurements, this setup has an inherently lower systematic uncertainty on the light yield for tile that arises due to SiPM-to-SiPM variations on the tileboards.

4.7.1 Results and Discussion

A few tiles were measured at beam tests with tileboards and with the ^{90}Sr setup introduced here to verify if they perform similarly. This test's results are shown in fig. 4.37.

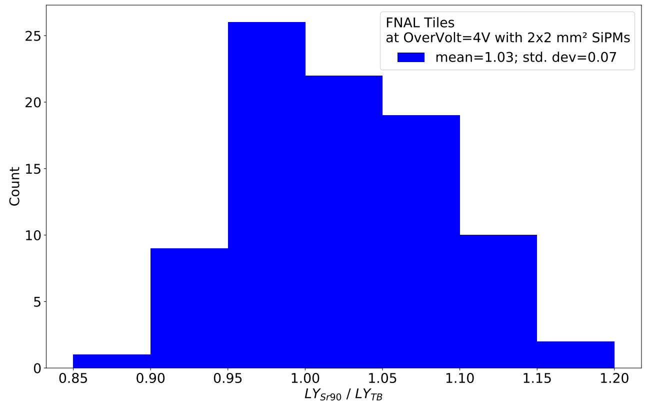

Figure 4.37: ratio of light yields measured by the ^{90}Sr setup (LY_{Sr90}) and light yield measured with tileboards at beam tests (LY_{TB}) for the same 89 FNAL tiles.

As shown in fig. 4.37, the ratio between light yields was 1.03 ± 0.07. The 3 % deviation in results on average could be attributed to the marginally more significant ionisation losses by low energy electrons in the scintillator when using the ^{90}Sr source. However, these losses are negligibly small compared to the systematic uncertainties in the light yield measurement.

Given that the same scintillators are used in both setups, the main contribution to the systematic uncertainties in this measurement comes from the variations in SiPM properties between channels. These measurements were done using the TBv3 tileboards. HPK did not provide the individual breakdown voltages of the SiPMs on the TBv3 tileboards. Instead, only a mean breakdown voltage was provided for the entire reel. As a result, the breakdown voltage may vary from channel to channel by a maximum of 100 mV. Furthermore, the March 2023 beam test at which these measurements were done was the first beam test with tileboards read out with HGCROCv3 chips. Due to configuration issues, it was not possible to observe SPS from all channels on the tileboards at the time, and therefore, a mean value of the SiPM gain was assigned for the channels where the gain was not observed. These two factors primarily resulted in the larger systematic uncertainty in light yield obtained from the beam tests. Since then, the configuration scripts have been modified to prevent this issue from repeating. Therefore, the standard deviation could be reduced if this measurement is redone at a future beam test.

4.8 Latest Tile Studies using ^{90}Sr Setup

In early 2023, a wide variety of tiles were produced by FNAL in collaboration with NIU, which included a new BC-412 cast tile type referred to as ”NIU cast”. Though these cast tiles were not tested at beam tests on tileboards, their performances were quantified at DESY using the ^{90}Sr source-based setup [90]. The SiPM on the source-based setup also does not have the white paint dot mentioned in section 4.4.4 and, therefore, has the same drop in light yield. Therefore, the light yields measured from the NIU cast tiles were scaled up by 10 % to account for the white paint dot on TBv1 tileboards.

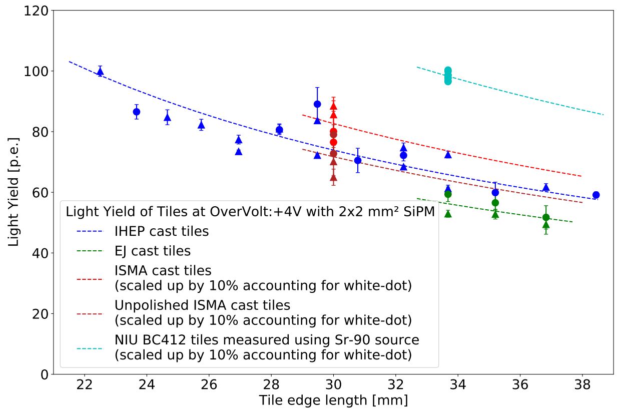

Figure 4.38: comparison of light yields of all cast tiles measured, including the NIU cast tile measured using the ^{90}Sr source-based setup. All light yields were scaled for the $2 \times 2\,\text{mm}^2$ SiPMs. The fit parameter for NIU cast tile $k = 3222 \pm 95\,\text{p.e.} \cdot \text{mm}$.

The fit parameter k was measured to be $3222 \pm 95\,\text{p.e.} \cdot \text{mm}$ making the NIU cast tile the best-cast tile produced and tested for the HGCAL experiment.

Chapter 5

Investigation of the Performance of Irradiated SiPMs on Tilemodule Prototypes

Irradiation of SiPMs changes many of the SiPM properties. This includes the increase in noise due to the leakage current and the change in breakdown voltage due to the change in dopant concentration on the silicon substrate. This was discussed in detail in section 2.4.2.7. Due to all these changes to the SiPM properties, it is essential to understand how SiPMs on Tilemodules behave after irradiation and validate if meaningful information can be obtained from these devices after accumulating high radiation levels at end-of-life. This chapter contains the methodology developed to measure the performance of irradiated SiPMs on Tilemodules.

SiPMs will be used in areas of the HGCAL detector in areas where the expected 1 MeV equivalent neutron fluence at the end-of-life is below $5 \times 10^{13}\,\mathrm{n_{eq}/cm^2}$. However, due to the large leakage currents in the order of several milliamperes passing through these SiPMs, operating them at room temperature would heat them and possibly damage them. Using climate chambers would allow their operation at low temperatures. However, due to the thick walls of the climate chambers acting as absorbers, their performances cannot be quantified at beam tests with 3 GeV electrons.

Therefore, beam tests were conducted at DESY-II [15] with SiPMs irradiated to a 1 MeV equivalent neutron fluence of $2 \times 10^{12}\,\mathrm{n_{eq}/cm^2}$ mounted onto the Tilemodule prototypes at room temperature. Previous studies conducted by the collaboration [91] found that the leakage current flowing through $2 \times 10^{12}\,\mathrm{n_{eq}/cm^2}$ fluence SiPMs at room temperature is roughly the same value as that flowing through $5 \times 10^{13}\,\mathrm{n_{eq}/cm^2}$ fluence SiPMs operated at $-30\,^{\circ}\mathrm{C}$, given that they are both operated at an over-voltage of 2 V. Therefore, SiPMs irradiated to $2 \times 10^{12}\,\mathrm{n_{eq}/cm^2}$ neutron fluence are ideal candidates to validate the SiPM's performance at the detector end-of-life with beam tests conducted at room temperature.

The non-irradiated SiPMs on the tileboards were also used to understand the behaviour of noisy SiPMs like the SiPMs after irradiation. When the noise increases in the SiPM, the signal and the pedestal peaks increase in width. These two curves can be separated for non-irradiated SiPMs containing large SNRs. However, as the irradiation level increases, the SNR reduces to a point where the pedestal peak overlaps with the signal peak. The indistinguishability of the signal from the pedestal results in a loss of accuracy of energy measurements. Therefore, this chapter has also investigated the interplay between the efficiency at which MIPs can be measured (MIP efficiency) and the percentage of pedestal contamination in the MIP measurements (noise occupancy) as a function of SNR. All studies discussed in detail in this chapter were conducted in the context of this thesis.

Irradiated SiPMs used for these tests were irradiated with neutrons at the JSI neutron facility in Ljubljana [92]. This included $1.4 \times 1.4\,\mathrm{mm}^2$ SiPMs as well as $2 \times 2\,\mathrm{mm}^2$ SiPMs of 15 µm pitch size [93]. They were all HPK HDR-2 SiPMs with custom radiation-hard packaging (HPK S14160-976X, see table 4.1).

5.1 Determination of the Breakdown Voltages of Irradiated HGCAL SiPMs

Section 2.4.2.8 explains the difference between the two breakdown voltage definitions used in this thesis. As a summary, the point at which SiPM gain becomes zero is known as the turn-off voltage ($V_{br}(\mathrm{TO})$) and is the breakdown voltage definition used by Hamamatsu Photonics K.K. (HPK). The second definition of breakdown voltage is obtained from the current vs. bias voltage relationship, where the breakdown voltage is defined as the voltage at which the increment of current is at its maximum. That is (from eq. (2.34)):

$$V_{br}(\mathrm{IV}) = \left(\frac{1}{I} \cdot \frac{dI}{dV_{bias}}\right)_{peak}.$$

All performance measurements done so far with SiPMs were conducted at an over-voltage defined with respect to the HPK-defined breakdown voltage. However, precisely measuring the turn-off voltage proved challenging with tileboards due to the limited gain resolution described in section 4.3.2.5.

Measuring the breakdown voltage using the relative-derivative method is also impossible via tileboards in their original state. This requires measuring the current passing through the SiPM, which cannot be done for individual SiPMs with the tileboards. Furthermore, the current passing through non-irradiated SiPMs is minimal. However, the tileboard can be modified to measure currents and the current vs. voltage relationship.

5.1.1 Difference between Breakdown Voltage Definitions

As previously mentioned, the turn-off voltage and the voltage obtained via the relative-derivative method are commonly used definitions of breakdown voltages. The breakdown voltage difference between the two definitions is similar for a given SiPM type and will remain similar even after irradiation. Let us call this difference V_{offset} which is defined as:

$$V_{\mathrm{offset}} = (V_{br}(\mathrm{IV}))_{\text{non-irrad}} - (V_{br}(\mathrm{TO}))_{\text{non-irrad}} = (V_{br}(\mathrm{IV}))_{\mathrm{irrad}} - (V_{br}(\mathrm{TO}))_{\mathrm{irrad}}. \tag{5.1}$$

HPK quotes the breakdown voltage using the turn-off definition before irradiation. Therefore:

$$(V_{br}(\mathrm{TO}))_{\text{non-irrad}} = V_{br}(\mathrm{HPK}), \tag{5.2}$$

Let us define the voltage degradation due to irradiation as V_{deg}. That is the difference between the breakdown voltage measured before and after irradiation using the relative derivative method. This is given as:

$$V_{\text{deg}} = (V_{br}(\text{IV}))_{\text{irrad}} - (V_{br}(\text{IV}))_{\text{non-irrad}}. \tag{5.3}$$

Using eqs. (5.1) to (5.3), one can define $(V_{br}(\text{IV}))_{\text{irrad}} - V_{br}(\text{HPK})$ as:

$$(V_{br}(\text{IV}))_{\text{irrad}} - V_{br}(\text{HPK}) = V_{\text{deg}} + V_{\text{offset}}. \tag{5.4}$$

Neutron irradiation increases the SiPM noise and the pedestal width to a point where SPS is no longer visible. As a result, gain is not directly measurable from irradiated SiPMs. Therefore, it is impossible to measure $V_{br}(\text{TO})_{\text{irrad}}$ for these devices.

However, it is possible to measure the breakdown voltages of SiPMs on tileboards before and after irradiation using the relative derivative with a few adjustments to the tileboard. If the same method can then be used to determine the breakdown voltages of non-irradiated SiPMs, this would allow the comparison of light yields at the same over-voltage using the exact breakdown voltage definition. Furthermore, this will also measure the change in breakdown voltage due to the neutron irradiation (V_{deg}) and the difference between breakdown voltage definitions (V_{offset}).

5.1.2 Methodology and Test Setup

This experiment was conducted with three tileboards, including six irradiated SiPMs and four non-irradiated SiPMs. The leakage current passing through non-irradiated SiPMs remains negligible, while for irradiated SiPMs, this value is non-negligible. As sketched in fig. 4.5, the SiPMs on the tileboard are in series with a safety resistor. For irradiated SiPMs in a dark environment, the leakage current passing through the SiPM is proportional to the voltage drop across the safety resistor. Therefore, a Keithley 2000 series multimeter [94] was connected in parallel to the safety resistor. Since the resistance is known, the leakage current passing through the SiPMs can be deduced.

Unlike irradiated SiPMs, which see leakage currents in the order of a few hundred microamperes, non-irradiated SiPMs see leakage currents well below a microampere, even at higher over-voltages in a dark environment. Therefore, measuring the change in leakage current passing through non-irradiated devices in dark conditions is impossible. However, one can increase the photocurrent passing through the SiPM using a light source mounted externally providing a constant intensity of light such as a laser or light emitting diode (LED). A blue-light emitting LED was used for this purpose, as shown in fig. 5.1. The LED is placed directly aligned with the non-irradiated SiPMs under test.

The experiment was conducted by changing the bias voltage supplied to the SiPM and measuring the voltage drop across the resistor. As shown in eq. (4.1), the actual bias voltage supplied via the electronics on the tileboard to the SiPM (V_{bias}) is derived to be:

$$V_{bias} = V_{supply} - V_{inDAC} - V_{drop} \tag{5.5}$$

5.1.3 Results

The increased current passing through the non-irradiated SiPMs, thanks to the external LED, makes it possible to measure the current passing through the SiPM as a function of the bias

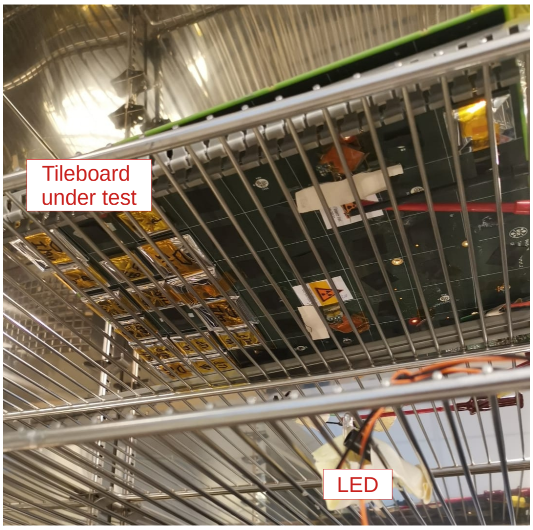

Figure 5.1: LED placed under the tileboard containing the SiPMs under test

voltage as shown in fig. 5.2(a). The relative derivative method was then used to derive the breakdown voltage $(V_{br}(\mathrm{IV}))_{\text{non-irrad}}$. A Gaussian fit was used to extract the maximum of the peak as shown in fig. 5.2(b). The $(V_{br}(\mathrm{IV}))_{\text{non-irrad}}$ measured, $(V_{br}(\mathrm{HPK}))$ supplied by HPK and the difference between the two measurements is given in table 5.1.

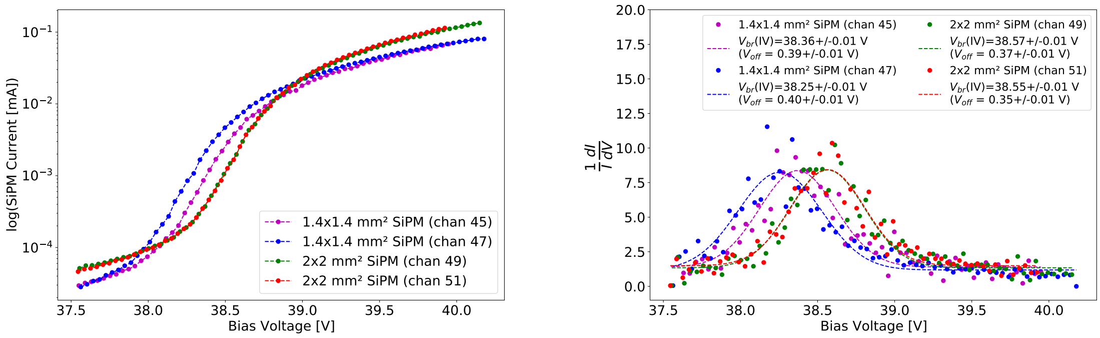

(a) (b)

Figure 5.2: Determination of $(V_{br}(\mathrm{IV}))_{\text{non-irrad}}$ using the relative derivative method for the six non-irradiated SiPMs mounted on tileboard TB1.3. (a) shows the current passing through the SiPM in log scale vs voltage curves for four non-irradiated SiPMs while (b) shows the $\frac{1}{I}\cdot\frac{dI}{dV}$ vs voltage curves for the same SiPMs. The fit on (b) uses a Gaussian function with its mean used to determine $(V_{br}(\mathrm{IV}))_{\text{non-irrad}}$.

In comparison with the breakdown voltage measured by HPK, the mean voltage deviation V_{offset} from the four non-irradiated SiPMs shown in fig. 5.2(b) was measured to be:

$$V_{\text{offset}} = 0.37 \pm 0.02\,\mathrm{V}. \tag{5.6}$$

The uncertainty is the standard deviation of the four voltage offset measurements.

Table 5.1: Overview of $V_{br}(\mathrm{IV})_{\text{non-irrad}}$ measured using LED based system and $V_{br}(\mathrm{HPK})$ supplied by HPK for non-irradiated SiPMs on TB1.3 tileboard.

SiPM channel	**SiPM size**	$V_{br}(\mathrm{IV})$ **measured**	$V_{br}(\mathrm{HPK})$ **supplied**	**Difference**
Chan 45	$1.4 \times 1.4\,\mathrm{mm}^2$	38.36 ± 0.01 V	37.97 V	0.39 ± 0.01 V
Chan 47	$1.4 \times 1.4\,\mathrm{mm}^2$	38.25 ± 0.01 V	37.85 V	0.40 ± 0.01 V
Chan 45	$2 \times 2\,\mathrm{mm}^2$	38.57 ± 0.01 V	38.20 V	0.37 ± 0.01 V
Chan 45	$2 \times 2\,\mathrm{mm}^2$	38.55 ± 0.01 V	38.20 V	0.35 ± 0.01 V

The irradiated SiPMs required no additional light due to their inherent noise. $V_{br}(\mathrm{IV})_{\text{irrad}}$ were measured for six irradiated SiPMs as described above and are shown in fig. 5.3. The $(V_{br}(\mathrm{IV}))_{\text{non-irrad}}$ measured, $(V_{br}(\mathrm{HPK}))$ supplied by HPK and the difference between the two measurements is given in table 5.2.

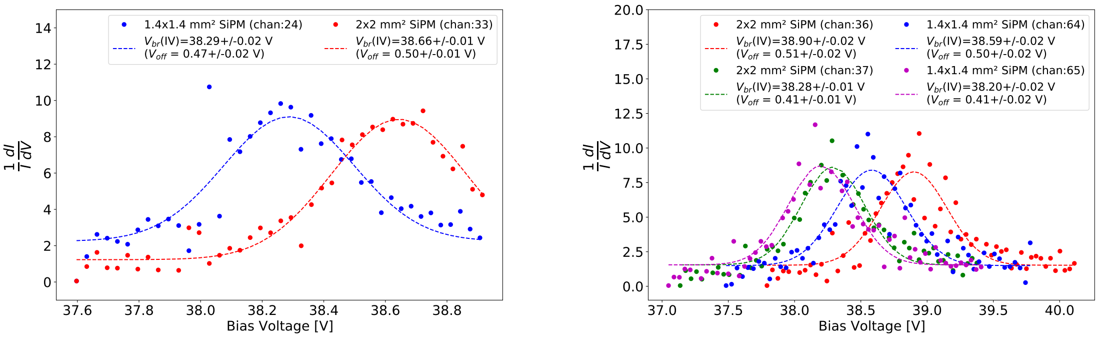

(a) (b)

Figure 5.3: Determination of $(V_{br}(\mathrm{IV}))_{\text{irrad}}$ using the relative derivative method for the six irradiated SiPMs mounted on two tileboards. (a) are for the two SiPMs mounted on TB1.2. (b) are for the four SiPMs mounted on TB2.1. The fit on (b) uses a Gaussian function with its mean used to determine $(V_{br}(\mathrm{IV}))_{\text{irrad}}$.

Table 5.2: Overview of $V_{br}(\mathrm{IV})_{\text{irrad}}$ measured using LED based system and $V_{br}(\mathrm{HPK})$ supplied by HPK for non-irradiated SiPMs on TB1.2 and TB2.1 tileboard.

SiPM channel	**SiPM size**	$V_{br}(\mathrm{IV})$ **measured**	$V_{br}(\mathrm{HPK})$ **supplied**	**Difference**
TB1.2				
Chan 24	$1.4 \times 1.4\,\mathrm{mm}^2$	38.29 ± 0.01 V	37.82 V	0.47 ± 0.01 V
Chan 33	$2 \times 2\,\mathrm{mm}^2$	38.66 ± 0.01 V	37.16 V	0.50 ± 0.01 V
TB2.1				
Chan 64	$1.4 \times 1.4\,\mathrm{mm}^2$	38.59 ± 0.02 V	38.09 V	0.50 ± 0.02 V
Chan 65	$1.4 \times 1.4\,\mathrm{mm}^2$	38.20 ± 0.02 V	37.82 V	0.47 ± 0.02 V
Chan 45	$2 \times 2\,\mathrm{mm}^2$	38.90 ± 0.02 V	38.39 V	0.51 ± 0.02 V
Chan 45	$2 \times 2\,\mathrm{mm}^2$	38.28 ± 0.01 V	37.87 V	0.41 ± 0.01 V

The mean measured deviation between $V_{br}(\mathrm{IV})_{\text{irrad}}$ and $V_{br}(\mathrm{HPK})$ for the six irradiated SiPMs shown in fig. 5.3 and table 5.2 was 0.47 ± 0.04 V. The uncertainty given here is the standard deviation. Using eq. (5.4) we therefore have:

$$V_{\text{deg}} + V_{\text{offset}} = 0.47 \pm 0.04\,\mathrm{V}. \tag{5.7}$$

Since $V_{\text{offset}} = 0.37 \pm 0.02\,\text{V}$,

$$V_{\text{deg}} = 0.10 \pm 0.05\,\text{V}. \tag{5.8}$$

5.1.4 Discussion

The change in breakdown voltage due to irradiation and the difference between the breakdown voltage definitions have been previously measured by other institutes within the HGCAL collaboration [91, 95]. Figure 5.4 shows the differences between the HPK-defined operation voltage (V_{OP}(HPK)) and the breakdown voltage measured using the relative derivative method (VB(CERN)) for 384 non-irradiated HGCAL-type SiPMs as discussed in [91]. Each batch of 48 SiPMs comes from a single reel produced by HPK. The operational voltage is defined as the bias voltage that needs to be supplied to maintain an over-voltage of 2 V with respect to V_{br}(HPK). That is:

$$V_{OP}(\text{HPK}) = V_{br}(\text{HPK}) + 2\,\text{V}, \tag{5.9}$$

and

$$\text{VB(CERN)} = V_{br}(\text{IV})_{\text{non-irrad}}. \tag{5.10}$$

Since V_{br}(HPK) - $V_{br}(\text{IV})_{\text{non-irrad}} = V_{\text{offset}}$,

$$V_{\text{offset}} = 2\,\text{V} - (V_{OP}(\text{HPK}) - \text{VB(CERN)}). \tag{5.11}$$

Based on fig. 5.4, $V_{OP}(\text{HPK}) - \text{VB(CERN)} =\sim 1.7\,\text{V}$. Therefore, with a maximum fluctuation of 10 mV for the first four and last reel of SiPMs V_{offset} is about 0.3 V. The other three reels have a $V_{\text{offset}} = 0.36\,\text{V}$ with similar SiPM-to-SiPM fluctuations. This shows that the exact V_{offset} fluctuates from reel to reel, however the overall V_{offset} value remains in the range between 0.25 V to 0.40 V. Given that the measured V_{offset} from tileboards were $V_{\text{offset}} = 0.37 \pm 0.02\,\text{V}$, this result agrees with the results from the HGCAL collaboration, which used dedicated setups.

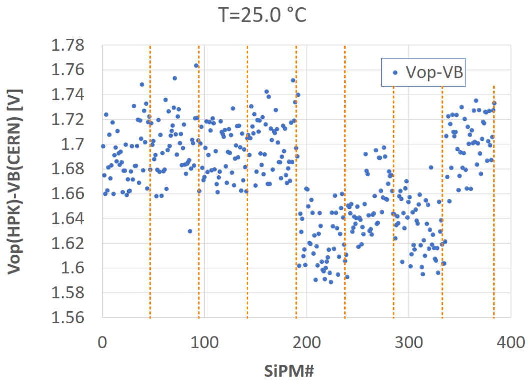

Figure 5.4: LED placed under the tileboard containing the SiPMs under test. The vertical orange lines roughly separate the SiPMs of different reels. Here, $V_{OP}(\text{HPK}) = V_{br}(\text{HPK}) + 2\,\text{V}$ and $\text{VB(CERN)} = V_{br}(\text{IV})_{\text{non-irrad}}$. Taken from [74].

The change in breakdown voltage with irradiation was also investigated within the collaboration. For an irradiation of $2 \times 10^{12}\,\text{n}_{\text{eq}}/\text{cm}^2$ a deviation of about 0.025 V is expected

[95]. However, the tileboard measurements showed an increase in breakdown voltage (V_{deg}) to 0.10 ± 0.05 mV. That is a factor four increase in breakdown voltage compared to what was reported by the collaboration.

However, the tileboards are not optimised for such measurements. Out of the six irradiated SiPMs, four have a V_{offset} about 0.5 V while the other two about 0.4 V. A V_{offset} of 0.4 V suggests no increase in breakdown voltage at all. The most likely explanation for the difference of 100 mV is systematic uncertainties in the applied bias voltage. The bias voltage measurement is set using the ALDOv2 chip (ALDOv2 BV) for TBv2 tileboards. However, as reported in [96] and shown in fig. 5.5, the bias voltages generated by the ALDOv2 BV have a very low-frequency noise caused by the GBT-SCA. The maximum shift in voltage was reported as 50 mV as shown in fig. 5.5. The period between 3000 s and 4000 s in fig. 5.5(a) also suggests that a voltage shift of up to a few tens of millivolts can take place for extended periods which will potentially shift the breakdown voltage measured by the same amount of voltage. Therefore, the V_{deg} measured with the tileboard may have a larger uncertainty than reported.

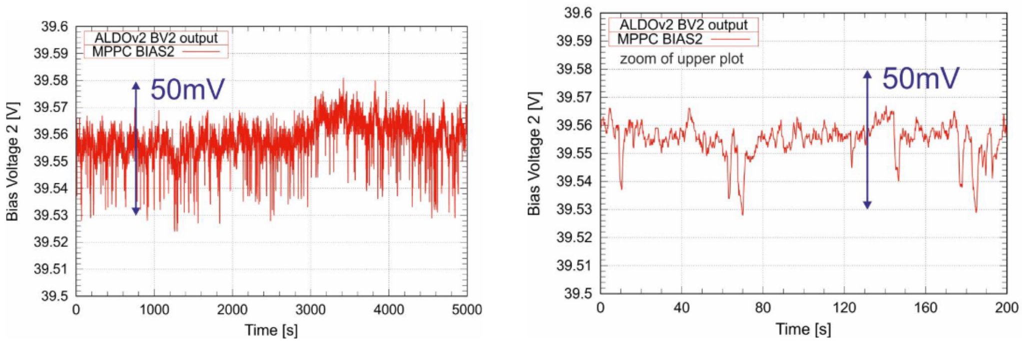

(a) (b)

Figure 5.5: Bias voltages generated via the ALDOv2 BV chip steered via the GBT-SCA on a TBv2 tileboard as reported in [96]. (a) shows the variations for 5000 s (or 1 hr and 23 min), while (b) shows the short-period variations (∼ min).

The fix for this deviation in bias voltage supplied by the ALDOv2 BV has been implemented. However, it will only be available for the final version of the HGCROC (labelled HGCROC3b), the version foreseen to be used in the final experiment. The ALDOv2 BV will be steered via the HGCROCv3b in the final experiment instead of the GBT-SCA.

In an attempt to measure the breakdown voltage in real-time from SiPM-on-tiles on tileboards, the relationship between pedestal mean and leakage current was investigated. More on this can be found in appendix A.

The HPK measured individual breakdown voltages of non-irradiated SiPMs on tileboard TB2.1 are unknown. However, the same method discussed in section 5.1.2 is used to measure and calculate the relative derivative-based breakdown voltage for these SiPMs. The fig. 5.6 shows and table 5.3 tabulates the results of this measurement.

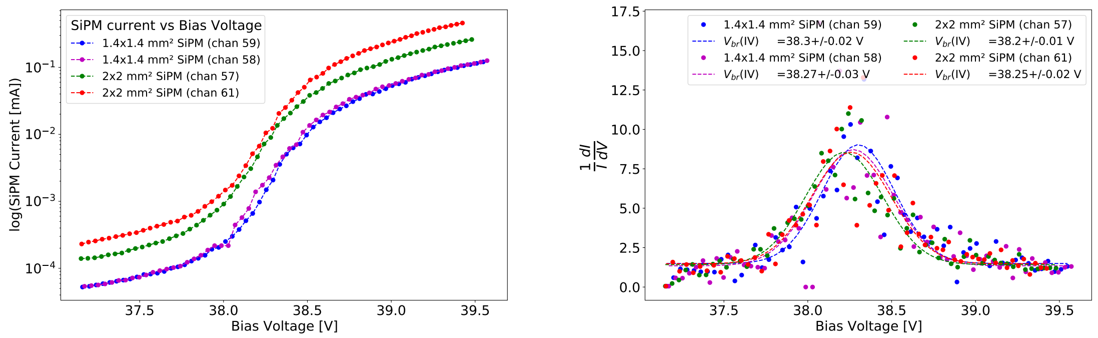

(a) (b)

Figure 5.6: The determined relative-derivative breakdown voltage for the non-irradiated SiPMs on TB2.1. (a) shows the ln(I) vs. voltage curves for the SiPMs while (b) shows the $\frac{1}{I} \cdot \frac{dI}{dV}$ vs. voltage curves for them. The fit on (b) uses a Gaussian function with its mean used to determine $(V_{br}(\text{IV}))_{\text{non-irrad}}$.

Table 5.3: Overview of $V_{br}(\text{IV})_{\text{non-irrad}}$ measured using LED based systemfor non-irradiated SiPMs on TB2.1.

SiPM channel	**SiPM size**	$V_{br}(\text{IV})$ **measured**
Chan 58	$1.4 \times 1.4\,\text{mm}^2$	38.27 ± 0.03 V
Chan 59	$1.4 \times 1.4\,\text{mm}^2$	38.30 ± 0.02 V
Chan 57	$2 \times 2\,\text{mm}^2$	38.20 ± 0.01 V
Chan 61	$2 \times 2\,\text{mm}^2$	38.25 ± 0.02 V

5.2 MIP Response of Irradiated SiPMs

The SiPM noise measured on the tileboards is defined as the standard deviation of the pedestal peak (see section 2.4.2.4). Leakage current passing through the SiPM is correlated to the noise. Due to the negligible leakage current flowing through non-irradiated SiPMs, they exhibit mostly electronic noise, which is small at around 1 ADC. As irradiation levels increase, the noise increases, increasing the pedestal fluctuations. Signals are also convoluted with these pedestal fluctuations, which also results in the broadening of signal peaks.

Studies conducted within the collaboration [74] with HDR-2 SiPMs with custom radiation-hard packaging have shown that the gain measured for SiPMs irradiated up to $5 \times 10^{13}\ \text{n}_{\text{eq}}/\text{cm}^2$ is about 10 % lower than the gain measured with non-irradiated SiPMs at the same over-voltage. Similarly, the number of photons measured with these irradiated devices is also about 10 % lower than with non-irradiated SiPMs. These measurements were done with dedicated setups sampling the signals and noise at a temperature of $-30\,°\text{C}$. The study discussed in this section experiments how the MIP response from irradiated SiPMs on tileboards measured with 3 GeV electron beams vary compared to non-irradiated SiPMs.

5.2.1 Methodology and Test Setup

The measurement procedure follows the same as described in section 4.2. All measurements were made at the DESY-II test beam facility at DESY, Hamburg [15] over one week in April 2022. All irradiated and non-irradiated SiPMs discussed here were HDR-2-typed SiPMs (S14160-976X) with custom radiation-hard packaging.

The SiPMs under test were mounted on the TB2.1 tileboard as shown in fig. 5.7(a). Two of them are $1.4 \times 1.4\,\text{mm}^2$ while the other two are $2 \times 2\,\text{mm}^2$ devices. As a first run, four identical cast tiles produced by ISMA, Ukraine, were placed on four non-irradiated SiPMs, and the MIP maxima were obtained.

Afterwards, the same TB2.1 was equipped with four of the $2 \times 10^{12}\,\text{n}_{\text{eq}}/\text{cm}^2$ fluence SiPMs discussed earlier as shown in fig. 5.7(b). Similar to the non-irradiated counterparts, two of them were $1.4 \times 1.4\,\text{mm}^2$ while the other two were $2 \times 2\,\text{mm}^2$. As a second run, the four identical cast tiles on the non-irradiated SiPMs were placed on the irradiated SiPMs, and the MIP peaks were obtained.

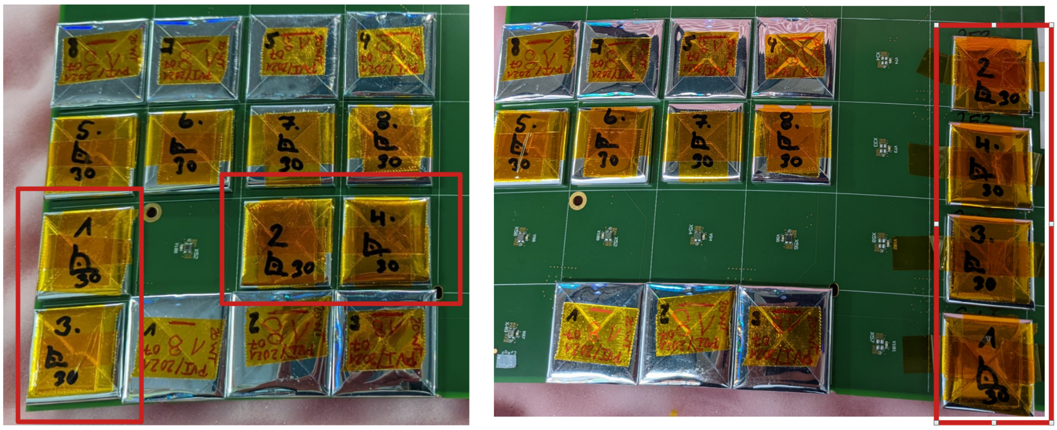
(a) (b)

Figure 5.7: Tileboard TB2.1 with irradiated SiPMs and non-irradiated SiPMs. The first data run configuration is shown in (a), where cast tiles from ISMA, Ukraine, were placed on the non-irradiated SiPMs (marked in red). As shown in (b), the same tiles were placed on the four irradiated SiPMs (marked in red) for the second data run.

As mentioned earlier, noise increases the width of the pedestal and signal peaks. In highly irradiated SiPMs like those discussed in this chapter, the widths of the pedestal and signal have increased to a point where the two peaks merge, making them indistinguishable. Two such cases have been shown in figs. 5.13 and 5.14 and are discussed later in this chapter in detail. Under such conditions, it is impossible to measure the MIP maxima correctly.

Two sets of data are needed to measure the MIP maximum of each SiPM-on-tile channel: a dataset where all events contain a particle in the tile studied and a dataset of pedestal data without a particle. The latter is relatively easy to obtain. A random trigger is used to acquire data from the SiPM, and a Gaussian function is used to fit the data. The pedestal mean, and standard deviation are taken from the fit as shown in fig. 5.8. While the pedestal mean is used for pedestal subtraction, the standard deviation measures the SiPM noise in ADC units.

Obtaining a dataset that only contains events with particles is much more complex and

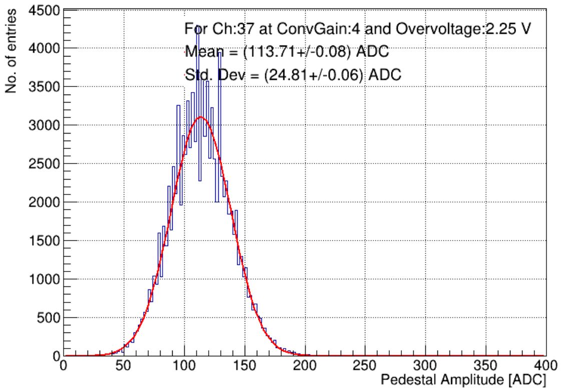

Figure 5.8: histogram showing the pedestal events for the same SiPM shown in fig. 5.9 measured at approximately the same over-voltage

requires fine-tuning the electronics system. The first step in this process is to reduce the ”false trigger” rate as much as possible. False triggers are events that successfully trigger data, but the data obtained has no visible signal. They can take place for multiple reasons, one of which is the noise from the PMTs. However, two PMTs operated in coincidence should reduce this rate to less than a few false triggers per million. The trigger scintillators are $1 \times 1\,\text{cm}^2$ in area. Therefore, only the electrons within this area will pass through the trigger and the tileboard. The beam collimator opening is aligned perfectly with the trigger scintillators and reduced to an area of $1 \times 1\,\text{mm}^2$ as potentially an additional level to reduce the false trigger rate.

The largest fraction of false triggers come due to the misalignment of the electron beam with the SiPM-on-tile of interest. A triggered electron may miss the scintillator tile and therefore, a signal is not produced. So, it is vital to align the tile with the beam and trigger scintillators. Due to the large noise, this task is impossible to complete using irradiated SiPMs. Therefore, a tile containing a non-irradiated SiPM is scanned using the electron beam with a similar method described and shown in fig. 4.4. Once the central point of the tile is found, the central point of the irradiated SiPMs is calculated using the geometry of the tileboard and the stage is moved such that the beam is aligned with the irradiated SiPM. Once this procedure has been completed, beam data is collected using 3 GeV electrons. The MIP maximum of the beam data is measured using the same procedure described in section 4.2.3. The result of one such MIP maximum measurement is shown in fig. 5.9.

MIP spectra and pedestal data were collected for over-voltages ranging from 1.4 V to 2.2 V in 0.2 V incremental steps for the four irradiated SiPMs on the tileboard and for an over-voltage of 2 V for the four non-irradiated SiPMs. These over-voltages are calculated using the nominal breakdown voltages measured by HPK (V_{br}(HPK)) measured at 25 °C temperature. This also does not include the shift in breakdown voltage with irradiation and the voltage drop across the safety resistor in series with the SiPM (as shown in fig. 4.5) for irradiated SiPMs. Therefore, the actual over-voltages needed to be recalculated offline.

Since the breakdown voltage based on the relative derivative definition was measured, the light yields from non-irradiated SiPMs and irradiated SiPMs can be compared for a given over-voltage with respect to the relative derivative breakdown voltage, taking into account all factors, such as the voltage drop across the safety resistor and change in breakdown voltage due to irradiation (V_{deg}). As V_{offset} is also known, one can also convert between the two definitions of breakdown voltages.

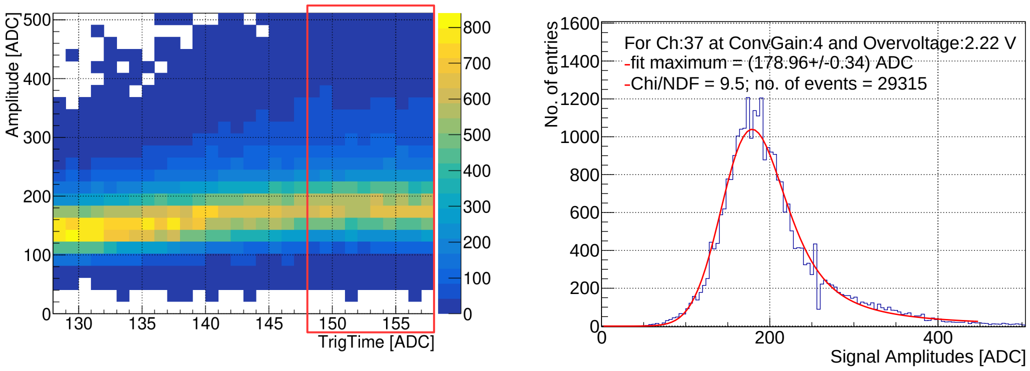

(a)

(b)

Figure 5.9: (a) shows the ADC vs. TrigTime spectra for one of the SiPMs irradiated to $2 \times 10^{12}\ \mathrm{n_{eq}/cm^2}$ fluence. An 8 ns TrigTime window around the peak (shown in red) is used to sample the signal peak. The resulting histogram is shown in (b), where a Landau-Gaussian function extracts the MIP maximum.

Due to the large amounts of leakage currents flowing through the SiPMs (in the order of 1 mA), higher conveyor gains cannot be used for data acquisition as it would saturate the ADC range of the HGCROC. Therefore, data is acquired at a conveyor gain of 4 from these SiPMs.

Similarly, 3 GeV electron events from non-irradiated SiPMs were also collected at an overvoltage of 2 V using a conveyor gain of 12. This allowed the measurement of the SiPM gains for the non-irradiated SiPMs, allowing for converting MIP data to light yields.

Studies by the University of Hamburg for the same SiPM generation [97, 98] shows that no reduction in gain is expected for SiPMs irradiated to $2 \times 10^{12}\ \mathrm{n_{eq}/cm^2}$. Therefore, the mean gain for non-irradiated SiPMs of the different SiPM sizes (see fig. 4.21) rescaled using the conveyor gain were used to estimate the light yields from the irradiated SiPMs.

The beam test at which these measurements were taken was the first time the TrigTime analysis method was used. However, since the non-irradiated SiPM data was taken in the early stage of the test beam, it still uses the template fit method. The reproducibility study of MIP response between the TrigTime and template fit methods described in section 4.2.4 also confirms that both methods yield similar results with deviations less than 8 %.

5.2.2 MIP Adjustment due to noise

Due to noise, the Landau function describing the MIP spectra from SiPMs is smeared by a Gaussian function as described in section 2.3.2. This was why a convoluted Landau-Gaussian function was used to describe the MIP spectra from SiPM-on-tiles in chapter 4. Since the Landau function is skewed, the Gaussian smearing shifts the position of the MIP maximum to higher values. Due to their large noise, irradiated SiPMs have a shifted MIP maxima compared to non-irradiated SiPMs. To compare the light yields between irradiated and non-irradiated SiPMs, this noise contribution must be subtracted from the irradiated SiPMs or added to the non-irradiated SiPMs.

Adding noise to a dataset is much easier than removing noise from a dataset. Therefore, noise was added to the non-irradiated SiPMs in the following way. First, the standard deviations of the four irradiated SiPMs were calculated from pedestal data for different over-voltages as shown in fig. 5.10. A linear fit was then used for each of the channels, and from this linear fit, an estimated standard deviation was obtained for each of the non-irradiated SiPMs, which had the same scintillator tile mounted on top. These four estimates are shown as triangles in fig. 5.10.

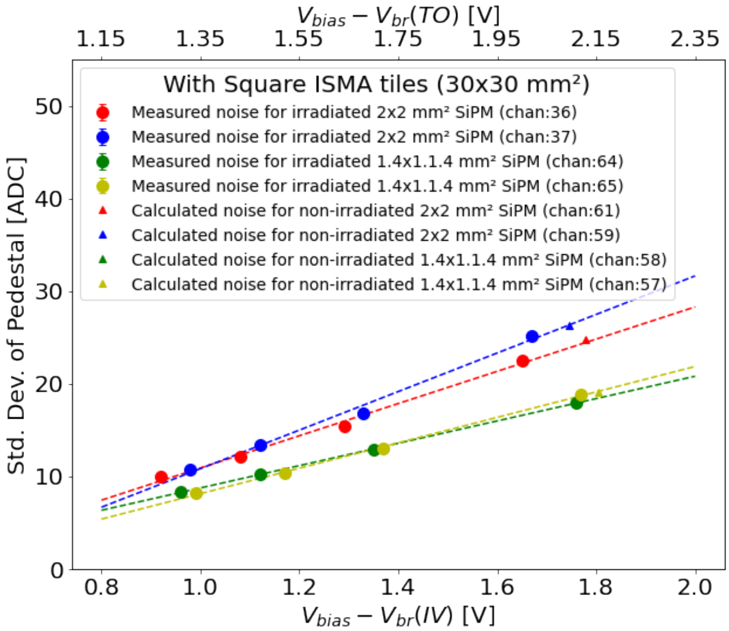

Figure 5.10: The standard deviations of the pedestal data obtained from irradiated SiPMs for different over-voltages are shown as circles. A linear fit estimates the standard deviation required to smear the MIP spectra obtained from non-irradiated SiPMs (shown as triangles). The over-voltage in terms of $V_{br}(TO)$ and $V_{br}(IV)$ are given in the two x axes.

These estimated standard deviations were then used to smear the MIP data from the respective non-irradiated SiPMs by introducing a random Gaussian generator function. Each data point was smeared using the standard deviation from the corresponding irradiated SiPM containing the same tile. For this exercise, the noise of non-irradiated SiPMs is considered negligible. Once the MIP spectra have been artificially smeared, the MIP maxima are extracted using a Landau-Gaussian fit.

5.2.3 Results and Discussion

Figure 5.11 compares the final light yields between irradiated and non-irradiated SiPMs after all the corrections and adjustments. The error bars include the contribution from the uncertainty in the breakdown voltage calculations and statistical uncertainties arising from the SiPM gain measurement. At lower over-voltages, the increase in light yield is roughly linear. Therefore, a linear function is used to show the trend of the light yield with over-voltage.

The light yields measured for irradiated SiPMs and non-irradiated SiPMs under the same conditions show that they are within the uncertainties of the experiment. This means that no reduction in light yield is expected for SiPMs at an irradiation level of $2 \times 10^{12}\,\mathrm{n_{eq}/cm^2}$ of 1 MeV equivalent neutron fluence in silicon.

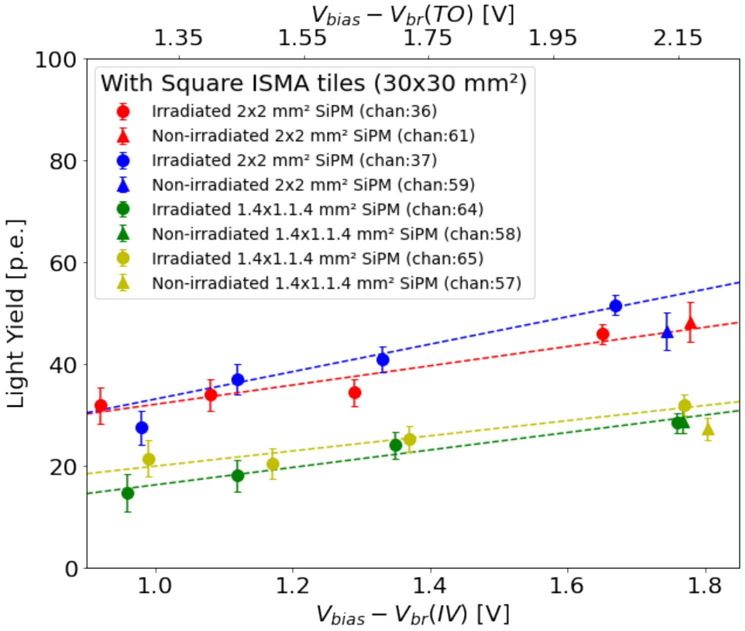

Figure 5.11: comparison of light yields after smearing the spectra for non-irradiated SiPMs and the corresponding irradiated SiPMs with the same tile. A linear function shows the trend of the light yield increase with over-voltage. The over-voltage in terms of $V_{br}(TO)$ and $V_{br}(IV)$ are given in the two x axes.

Most importantly, this experiment shows that meaningful MIP information can still be extracted from irradiated SiPMs. This was the first successful attempt to extract MIP information from irradiated SiPMs mounted on Tilemodule prototypes and use the HGCROC for readout.

The SNR is calculated by dividing the signal obtained from fig. 5.11 with the noise obtained from fig. 5.10. The SNR as a function of over-voltage obtained from the irradiated SiPMs is shown in fig. 5.12.

The fig. 5.12 shows no clear evidence of how SNR varies with over-voltage due to the higher uncertainties at lower over-voltages. Three of the four SiPMs show a slight dip in SNR below an over-voltage of 1.35 V with respect to V_{br}(TO). This is similar to what was measured within the collaboration [74] despite the large uncertainties. More about this SNR is discussed in chapter 7.

Another observation is that the SNR of all four of these SiPMs is below three for this particular combination of SiPM-on-tiles. An SNR>3 is required to calibrate the detector at the most optimal speed throughout its lifetime. However, it is worth remembering that this combination of SiPM and tile for this noise level is not expected in the HGCAL experiment. In the areas where the fluence is highest, i.e. where the noise reaches these numbers at the end-of-life, the intended tiles are smaller in size, and the SiPMs are possibly larger. As discussed in section 4.4, larger SiPMs in combination with smaller tiles yield higher light yields. As light yield scales with the number of pixels undergoing avalanches N_{pix} and noise scales as a function of $\sqrt{N_{pix}}$, using smaller tiles and larger SiPMs would increase the SNR. The combination used for this exercise was intended solely to show that light yield and PDE do not change at this irradiation level and that measuring MIPs at low SNR environments is possible if the conditions are very clean. The study on the detector layout optimisation using SNR is found in chapter 7.

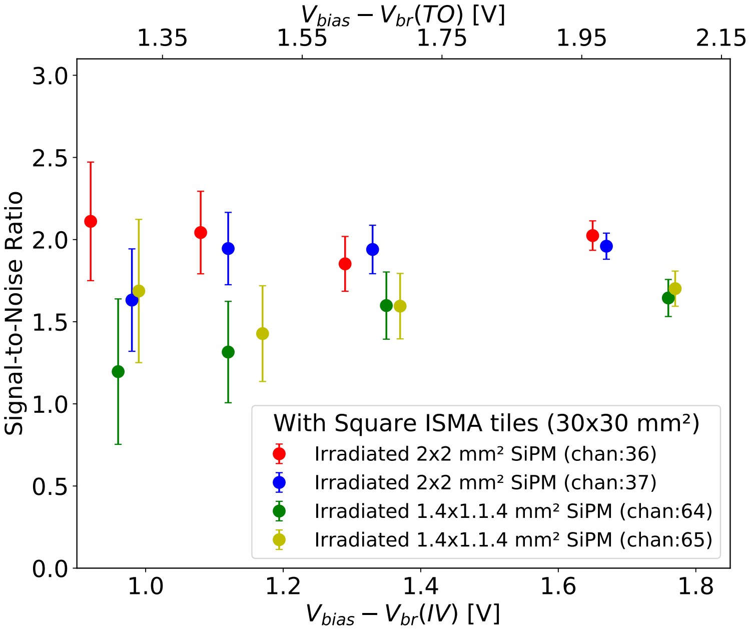

Figure 5.12: SNR as a function of over-voltage for the four irradiated SiPMs. The over-voltage in terms of $V_{br}(TO)$ and $V_{br}(IV)$ are given in the two x axes.

5.3 Impact of Pedestal Noise on Irradiated SiPMs

For two irradiated SiPMs, beam data was taken with a higher false trigger rate to investigate the impact of noise at over-voltages ranging from 1.4 V to 2.2 V taken at a conveyor gain of 4. These data sets were then compared with a pure noise run in the same conditions and a data run with an estimated false trigger rate of less than 2 %.

Figures 5.13 and 5.14 show the impact of the pedestal noise on the MIP for the two 2×2 mm² SiPMs. The contaminated beam data run shown in fig. 5.13 has a roughly 40 % contamination rate while the contaminated beam run shown in fig. 5.14 has a roughly 50 % contamination rate.

The results from channel 37 (see fig. 5.13) and 36 (see fig. 5.14) show two degrees of pedestal noise contamination and how it affects the signal indistinguishability. Even a 40 % contamination is hard to separate at lower voltages. As the contamination increases to 50 %, the signal becomes more indistinguishable even at higher over-voltages, with only a shoulder indicating the existence of a MIP peak. This reiterates the importance of reducing noise contamination in order to be able to separate the signal from the noise. However, this study also shows that one can determine the position of the MIP peak with a pedestal contamination of 40 % or lower. This means one can separate the signal from the noise even if the SNR is below three with a single hit on a triggering layer without additional information. Therefore, sophisticated reconstruction algorithms like those discussed in [85] can reduce the noise contamination further below to obtain the MIP spectra and infer the light yield. One could also study the effect of pedestal contamination on the MIP measurement using SiPMs on Tilemodules, as done in the next section.

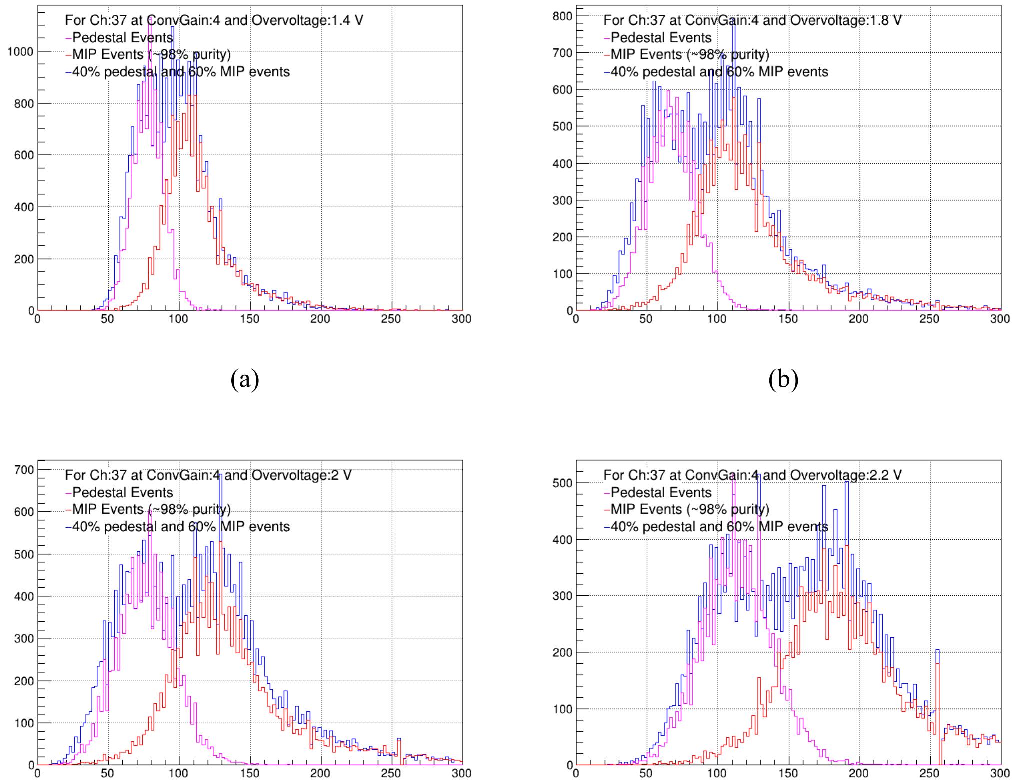

(a) (b)

(c) (d)

Figure 5.13: Separation of the pedestal and MIP peaks for channel 37, which contains a $2\times 2\,\mathrm{mm}^2$ SiPM irradiated to 2×10^{12} $\mathrm{n}_{\mathrm{eq/cm^2}}$ fluence for over-voltages of roughly (a) 1.4 V, (b) 1.8 V, (c) 2.0 V and (d) 2.2 V. The blue curves are pedestal-contaminated MIP data estimated to have a contamination of about 40 %. The pink and red curves show a pure noise run and a data run with less than 2 % pedestal noise contamination.

5.4 MIP Efficiency vs. Noise Occupancy Measurement

The purity of the MIP response signal and the contamination of the pedestal with the signal is an important measurement to understand the real impact of noise on the signal. A small experiment was conducted using only non-irradiated SiPMs to estimate the impact of noise in the signal.

5.4.1 Methodology and Test Setup

Similar to what was described in section 5.2.2, each data point of the MIP spectra from non-irradiated SiPMs are smeared using a random Gaussian function with a standard deviation given by:

$$\text{Gaussian smear factor} = \frac{\text{MIP maxima of SiPM-on-tile}}{\text{SNR needed}} \tag{5.12}$$

The SNRs used for this exercise include 1, 2, 3, 4, 5 and 1000 of the MIP maxima values. The SNR of 1000 was used purely for testing the algorithm, as this should give the same MIP

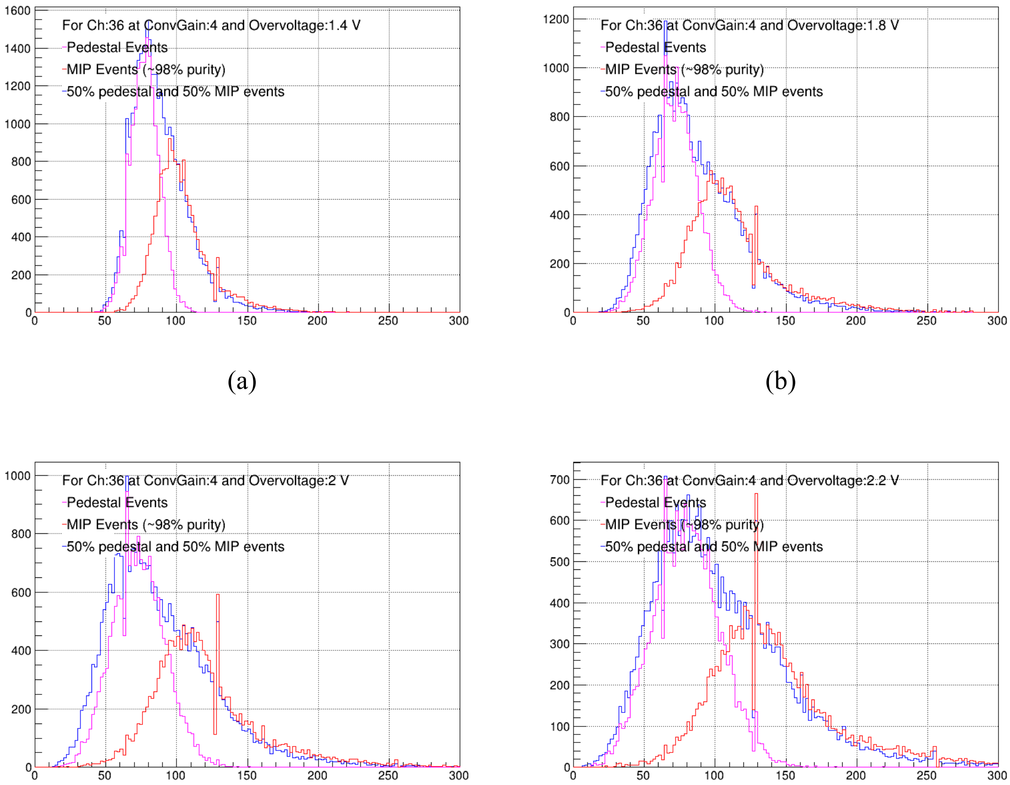

(a) (b)

(c) (d)

Figure 5.14: Separation of the pedestal and MIP peaks for channel 36, which contains a 2 × 2 mm² SiPM irradiated to 2×10^{12} $\mathrm{n_{eq/cm^2}}$ fluence for over-voltages of roughly (a) 1.4 V, (b) 1.8 V, (c) 2.0 V and (d) 2.2 V. The blue curves are pedestal-contaminated MIP data estimated to have a contamination of about 50 %. The pink and red curves show a pure noise run and a data run with less than 2 % pedestal noise contamination.

maxima as the case with no Gaussian smearing. Shown in fig. 5.15 are four MIP peaks from a single channel with varying levels of Gaussian noise convoluted. Note that the pedestal peak is centred around 0 ADC and has been removed for this exercise. Therefore, the peak represents the pedestal subtracted MIP maxima.

The noise convolution with the signal results in widening the MIP peak. This has consequences on several aspects of the signal. As evident from fig. 5.15, the increase in noise increases the MIP maximum. For the case where the SNR=2 (see fig. 5.15(d)), the MIP position has increased by approximately 6 %.

The same Gaussian smearing factor is also used to smear the pedestal peak. Given that the initial standard deviation of the pedestal peak from the non-irradiated SiPMs is close to 1 ADC, the standard deviation of the resulting pedestal peaks takes approximately the value as the smearing factor.

It is anticipated that a data cut of half the MIP's expected maximum value will be used to filter noise events. We thus define the **MIP efficiency** as the fraction of MIP events with a MIP maximum value larger than this threshold. Similarly, we define **noise occupancy** as the fraction of pedestal noise events with a value above this threshold.

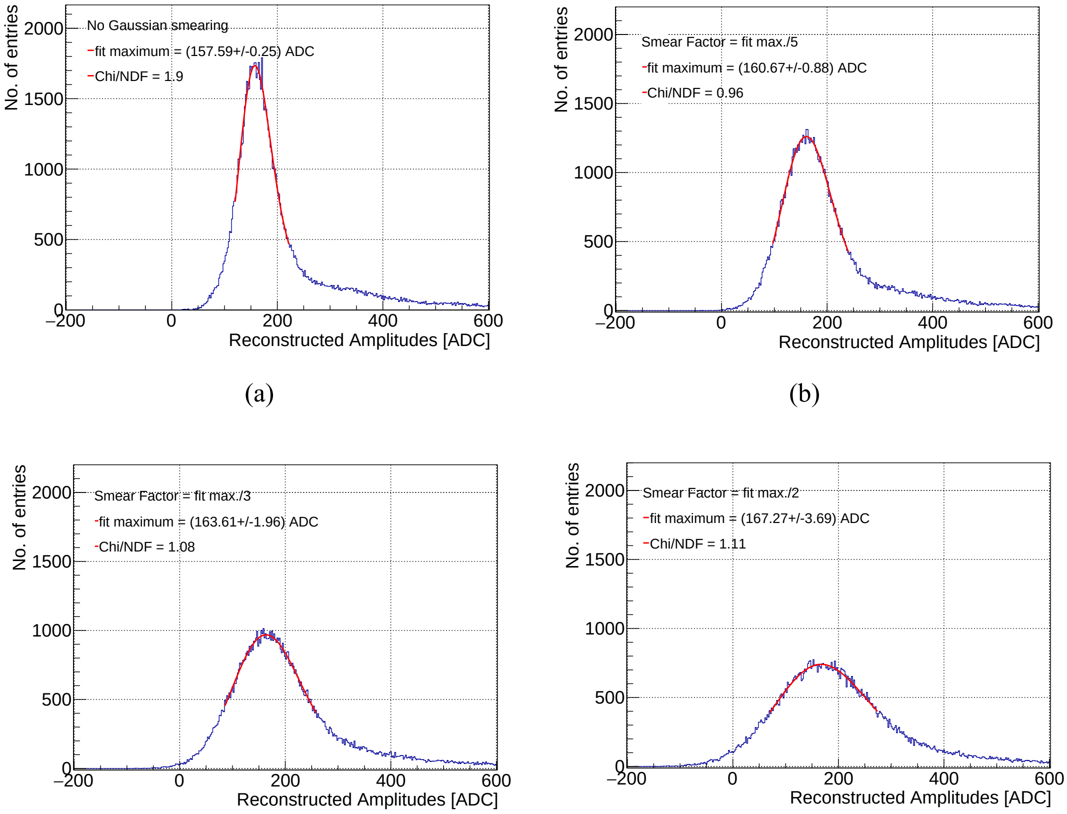

(a) (b)

(c) (d)

Figure 5.15: MIP peaks obtained from a non-irradiated SiPM (channel 59 on TB2.1) measured by varying noise generated via a Gaussian smearing factor ((a) no smearing, (b) SNR=5, (c) SNR=3 and (d) SNR=2). The data were taken at an over-voltage of around 2 V with respect to the turn-off voltage for conveyor gain 12. A Landau-Gaussian fit is used to fit the MIP peak from which the MIP maximum is extracted for each case.

Note that the threshold was selected with respect to the MIP maximum obtained from the noise-convoluted MIP spectra.

5.4.2 Results and Discussion

Shown in fig. 5.16 are the MIP efficiencies and noise occupancies for the four different non-irradiated channels and how they vary with different smearing factors. Similarly, one can plot the MIP efficiency as a function of the noise occupancy as shown in fig. 5.17.

The MIP efficiencies shown on fig. 5.16 for the four channels show the efficiency at which MIP events can be identified using a $0.5\times$ MIP maxima cut gets worse as the SNR reduces. Based on fig. 5.16, identifying above 90 % of the MIP events for all four channels is possible if the signal has an SNR>3.

The noise occupancy shows the contamination level of the MIP data in the case of a $0.5\times$ MIP maxima cut. The noise, which has been assumed to be Gaussian, increases from about 7 % for SNR>3 to above 16 % for SNR<2. This implies that more than one in every six events

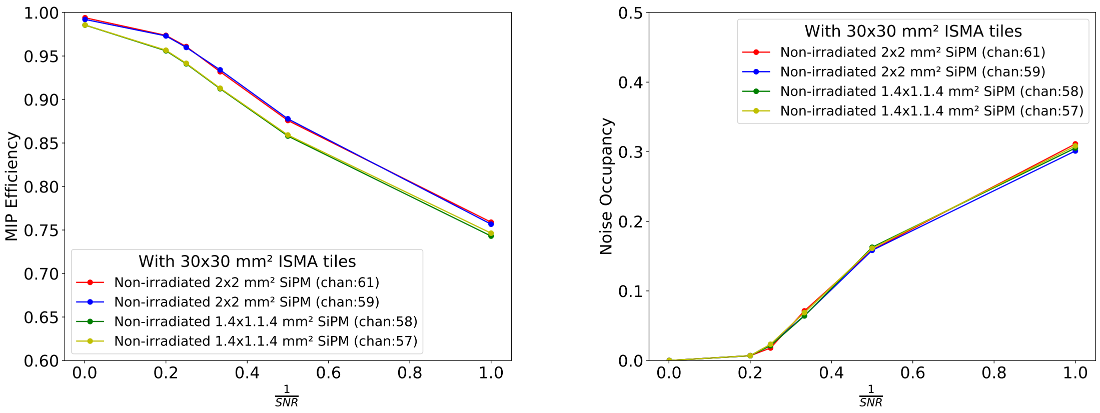

(a) (b)

Figure 5.16: MIP efficiencies and noise occupancies were measured for four different non-irradiated channels as a function of the Gaussian smear factor (or SNR). A threshold at half the MIP maximum value calculates the MIP efficiencies and noise occupancies.

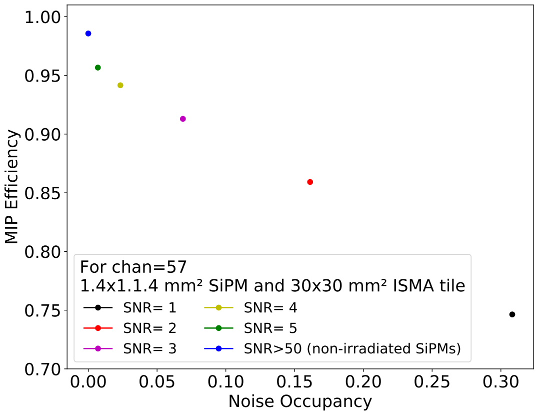

Figure 5.17: MIP efficiency as a function of noise occupancy plotted for channel 57 for different smear factors (or SNR). A threshold at half the MIP maximum value calculates the MIP efficiencies and noise occupancies.

identified as a MIP will be a noise hit if SNR<2. This is further emphasised in fig. 5.17 where the noise occupancies and MIP efficiencies have been directly compared.

The constraint to limit the use of SiPM-on-tiles to where SNR>3 is achievable also can be motivated using fig. 5.17. This figure shows that one can obtain a precision of over 90 % with less than 7 % contamination with just the information from the trigger layer confirming the existence of a MIP event in this channel. Given that the expected fluence is lower in the outer sections of the SiPM-on-tile section, resulting in lower noise (see fig. 3.4), one can safely assume that with accurate tracking information, the precision at which MIPs can be identified will be better. More studies have been conducted on the variation of SiPM noise with fluence and can be found in chapter 6.

Chapter 6

Study of Current and Noise from SiPMs on Tilemodule Prototypes

The HGCAL scintillator section will be limited to areas where the expected 1 MeV equivalent neutron fluence at an integrated luminosity of $3000\,\mathrm{fb}^{-1}$ (expected end-of-life conditions) is less than $5 \times 10^{13}\,\mathrm{n_{eq}/cm^2}$. Partner institutes have measured the leakage current from HGCAL SiPMs irradiated to $5 \times 10^{13}\,\mathrm{n_{eq}/cm^2}$, operated at $-30\,^{\circ}\mathrm{C}$ [74]. Since an increased leakage current increases the SiPM noise as explained in section 2.4.2.4, a noise measurement in terms of pedestal width obtained with in-situ electronics and a simultaneous measurement of leakage current will allow to make predictions about the SiPM noise at detector end-of-life.

The irradiated SiPMs used for these tests are the same as discussed in chapter 5. These SiPMs were irradiated with neutrons at the JSI neutron facility in Ljubljana [92] to a 1 MeV neutron equivalent fluence of $2 \times 10^{12}\,\mathrm{n_{eq}/cm^2}$ [93]. This included $1.4 \times 1.4\,\mathrm{mm^2}$ SiPMs and $2 \times 2\,\mathrm{mm^2}$ SiPMs. Further noise vs. current studies were conducted with non-irradiated SiPMs in addition to the irradiated SiPMs to understand if they behave differently. This chapter consists of studies conducted to evaluate the noise vs. current relationship between irradiated SiPMs and non-irradiated SiPMs of different SiPM sizes, on different Tilemodule prototypes (tileboards) and readout using different generations of HGCROCs.

6.1 Noise vs. Leakage Current Relationship between Irradiated SiPMs

Two setups were used to measure the electronic noise and leakage current relationship for irradiated SiPMs. The first setup exploited the dependence of leakage current and SiPM noise with temperature. The second setup keeps the temperature and voltage constant but changes the current and noise by using a constantly illuminating external LED.

6.1.1 Measurement by Variation of Temperature

The current passing through a SiPM is temperature dependent. A decrease in temperature reduces the number of random thermal excitations of electrons in the silicon substrate. Therefore, this leads to a decrease in leakage current passing through the SiPM for a fixed over-voltage. This results in the reduction of the SiPM noise as discussed in section 2.4.2.4. Therefore, controlling the temperature can control both the leakage current and SiPM noise.

6.1.1.1 Methodology and Test Setup

The tileboards with irradiated SiPMs are placed in a climate control chamber as shown in fig. 6.1. The SiPMs are connected in series on the tileboard with a safety resistor as shown in fig. 4.5. A Keithley 2000 series multimeter [94] is connected in parallel to the safety resistor, which allowed the measure of V_{drop}. Since the resistance is known, the leakage current flowing through the SiPM (I_{leak}) could be measured.

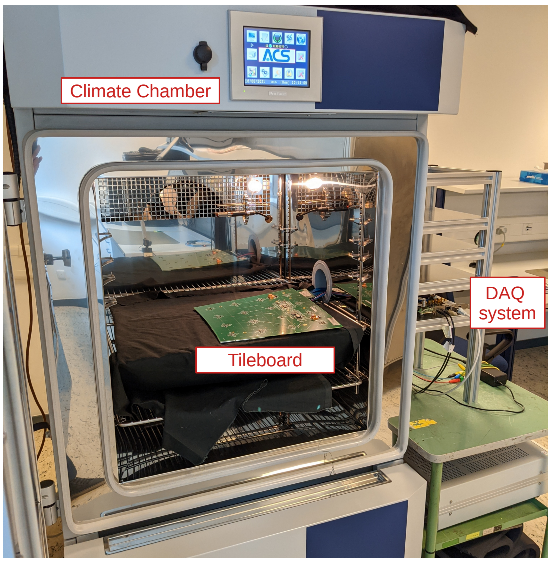

Figure 6.1: Tileboard in climate chamber setup used for measuring the noise vs. leakage current relationship of irradiated SiPMs.

The noise of the SiPMs on the tileboards are calculated by taking the standard deviation of 1000 pedestal events taken in dark conditions using a random trigger. The tileboard is covered with a light-tight blanket to prevent light contamination for these measurements. Additionally, another blanket covered the climate chamber from the outside as a second level of light shielding.

The over-voltage V_{over} is given by eq. (4.1). The SiPM bias voltage V_{bias} is controlled by changing the V_{inDAC} values via the HGCROC for measurements taken from TB1.2. On TBv2, TBv3 and MiniTB, V_{bias} is varied using the ALDOv2 BV regulator.

The PT-1000 temperature sensors on-board the TBv2, TBv3 and MiniTB are used to monitor the temperatures of the SiPMs on the tileboards. This was made possible as these tileboards were operated via the TB-Tester DAQ system. However as TBv1 tileboards were operated with the KCU-105 DAQ, two externally monitored PT-1000 sensors were mounted right next to the irradiated SiPMs touching the thermal contact. The climate chamber also has its own temperature measuring thermistor which was useful in comparing the temperature difference between what was supplied and the temperature of the SiPMs on the tileboard.

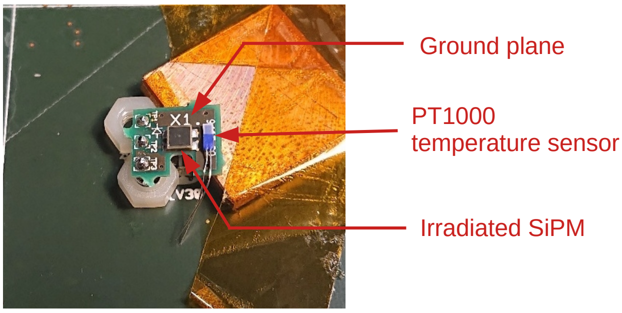

Figure 6.2: PT-1000 temperature sensors mounted close to an irradiated SiPM on TB1.2

HPK HDR-2 SiPMs have a voltage-temperature coefficient of 37.5 mV/K [74]. This information was used to calculate the voltages needed to be supplied to the SiPM to maintain an over-voltage of 2 V while changing the temperature. The temperatures were changed between −30 °C and 40 °C in steps of about 10 °C.

Similar to chapter 4, all over-voltages are measured relative to $V_{br}(\text{TO})$. For non-irradiated SiPMs, this is equal to the breakdown voltage measured by HPK $V_{br}(\text{HPK})$ (see section 2.4.2.8). However, with irradiation, the breakdown voltage increases. This increase was measured to be 0.10 ± 0.05 V for SiPMs irradiated to 2×10^{12} $\text{n}_{\text{eq}}/\text{cm}^2$ neutron fluence (see section 5.1). Therefore, a breakdown voltage of $V_{br}(\text{HPK}) + 0.1$ V is assumed to be the breakdown voltage of these irradiated SiPMs.

Since the over-voltage is sensitive to temperature, input DAC of the HGCROC (V_{inDAC}), as well as voltage drop across the safety resistor (V_{drop}), eq. (4.1) and eq. (4.13) are used to calculate the over-voltage accurately. However, increasing the supply voltage also increases the leakage current flowing across the irradiated SiPMs, increasing V_{drop}. Therefore, the increase in over-voltage is lower than expected, making it difficult to calculate the exact voltage necessary to be supplied to get the desired over-voltage.

Therefore, in order to obtain values for an over-voltage of 2 V, leakage current and noise is measured for multiple supply voltages in the range where a 2 V over-voltage can be expected. A linear fit interpolates the current and noise at the desired over-voltage of 2 V as shown in fig. 6.3. The points along the 2 V line are then used to compare the increase in noise as a function of leakage current.

The leakage current does not vary linearly with the over-voltage. However, the deviations from the linear behaviour are only apparent over large variations in voltage. Therefore, it is justified to use a linear fit for the current vs. over-voltage relationship in small over-voltage increments where the current variation are sufficiently linear.

Since noise is given by eq. (2.29), a fit can be used as follows:

$$\text{Noise [ADC]} = A' \cdot \sqrt{I_{leak}\ [\text{mA}]} + B' \tag{6.1}$$

where A' is the proportionality constant and B' is the offset.

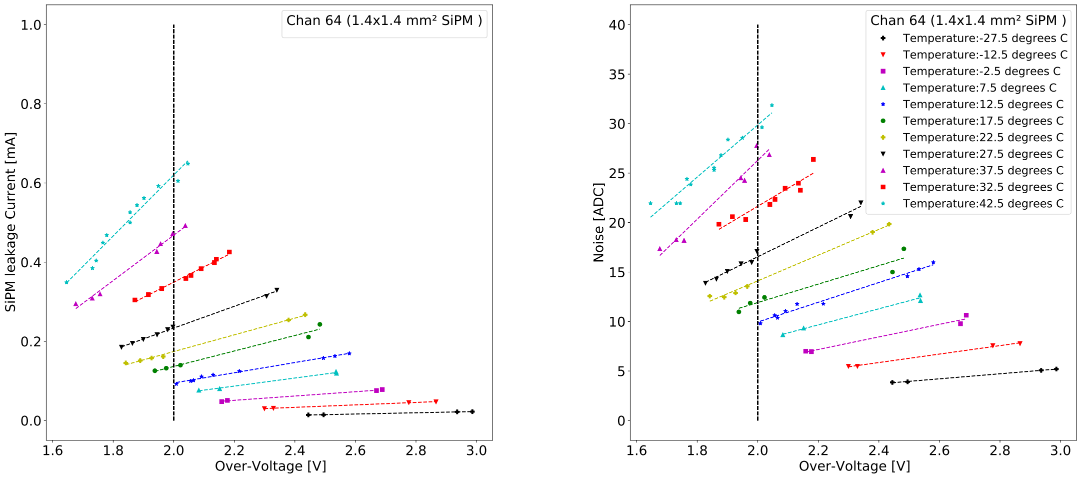

(a) (b)

Figure 6.3: Variation of leakage current passing through the SiPM (a) and the noise of the SiPM and readout electronics (b) as a function of over-voltage for different temperatures and for an irradiated $1.4 \times 1.4\,\text{mm}^2$ SiPM. Both plots share the same legend given in (b).

6.1.1.2 Re-scaling of the SiPM Noise to the Photo-Electron Scale

Equation (2.28) shows that noise and current can only be compared for SiPMs with identical gains. Therefore in order to eliminate the effect of SiPM gain, the noise was scaled using the SiPM gain as:

$$\text{Noise [p.e.]} = \frac{\text{Noise [ADC]}}{\text{SiPM gain [ADC/p.e.]}} = A \cdot \sqrt{I_{leak}\,\text{[mA]}} + B \tag{6.2}$$

where A and B are A' and B' expressed in p.e.$/\sqrt{\text{mA}}$ and p.e. respectively. The newly obtained noise is given in the photo-electron (p.e.) scale, similar to light yield.

The SiPM gain is typically measured at an over-voltage of 4 V and at a conveyor gain setting of 12 as SPS are not visible at lower over-voltages (see section 4.3). The noise measurements are conducted at an over-voltage of 2 V and at lower conveyor gains typically below 4. Therefore, the gain must first be calculated for the same settings for which the noise measurements were taken. Since the SiPM gain changes linearly with over-voltage and conveyor gain, one can re-scale the SiPM gain as:

$$\frac{G_{\text{rescaled}}}{G_{\text{measured}}} = \frac{2\,\text{V}}{4\,\text{V}} \cdot \frac{Cgain}{12}. \tag{6.3}$$

where G_{measured} is the measured gain, G_{rescaled} is the gain rescaled to the needed conveyor gain $Cgain$ (i.e. the conveyor gain at which the noise was measured).

Measuring the gain of irradiated SiPMs is impossible with the assembled tileboards due to the increased noise levels. However, a study conducted with irradiated HGCAL SiPMs shows that the SiPM gain does not change in comparison to non-irradiated SiPMs at $2 \times 10^{12}\ \text{n}_{\text{eq}}/\text{cm}^2$ neutron fluence [97]. Therefore, the mean SiPM gain for each SiPM size is obtained from non-irradiated SiPMs readout using the same or similar tileboard generation. This SiPM gain, re-scaled to the conditions in which the noise was obtained, is used to re-scale the noise to p.e. scale according to eq. (6.2). As the channel-to-channel gain differs by about 5 %, this introduces a 5 % uncertainty to the re-scaled noise.

6.1.1.3 Results and Discussion

The noise vs. leakage current results from six irradiated SiPMs are shown in fig. 6.4 for an over-voltage of 2 V. Using a single fit, A and B were measured to be $32.95 \pm 0.36\,\text{p.e.}/\sqrt{\text{mA}}$ and $-1.51 \pm 0.20\,\text{p.e.}$ respectively. Based on the fit values from the six SiPMs, the percentage uncertainty of A for SiPMs on TBv1 and TBv2 tileboards which contain HGCROCv2 chips is less than 2 %.

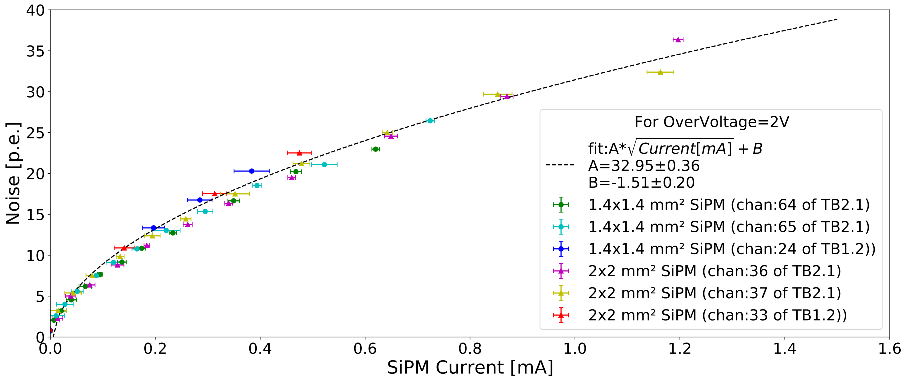

Figure 6.4: Noise vs. leakage current plot measured for the six irradiated SiPMs of two different SiPM sizes for an over-voltage of 2 V. Each noise and leakage current point for a given SiPM was measured at different temperatures ranging between -30 °C and 45 °C. A single fit is used for all channels. Uncertainties were derived from the linear fits used to extract noise and current.

Figure 6.4 shows that despite using two different tileboards and having different SiPM sizes, the dependence of noise on current is similar for all six SiPMs. This was the very first measurement of noise from irradiated SiPMs on tileboards readout via the HGCROC, and it shows that the noise scales as expected with leakage current for irradiated SiPMs.

This method depends on a temperature scan to change the noise and current passing through a SiPM. The SiPMs are electronic devices that heat up during operation. As the SiPM breakdown voltage is temperature dependent, this increase in temperature effectively decreases the over-voltage at which the SiPM operates. This effect is known as self-heating. It is possible that self-heating itself is temperature dependent.

Investigating the potential effect of self-heating was one of the prime motivations for the mounting of PT-1000 temperature sensors in contact with the ground plane for thermal contact to the irradiated SiPMs on TB1.2 as shown in fig. 6.2. The difference in temperature between the SiPM and the climate chamber measures how much the SiPM heats up. This difference is measured to be between 1.0 °C and 3.5 °C for temperatures ranging between -30 °C and 30 °C respectively as shown in fig. 6.5.

Evident from fig. 6.5, the temperature difference increases with temperature until about 0 °C and then stays constant. This suggests that self-heating might play a role at higher temperatures.

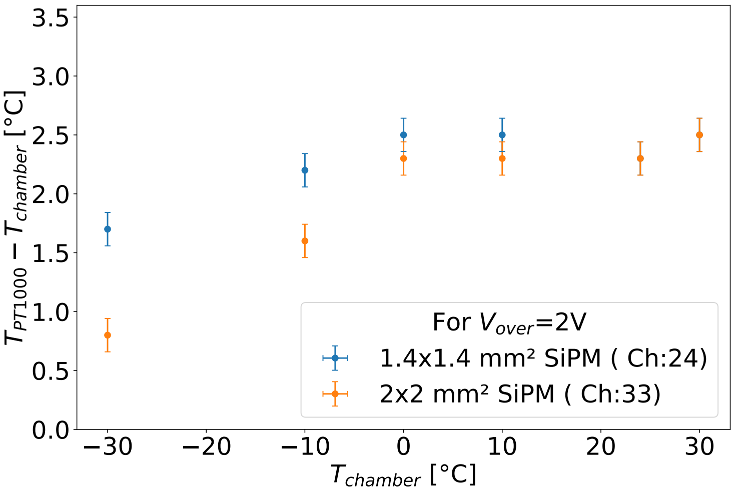

Figure 6.5: The variation of the temperature difference measured via the climate chamber thermostat and the PT1000 on the ground plane as a function of the climate chamber temperature.

However, given that the temperature from the PT-1000 is used for the calculation of the over-voltage, the effects of self-heating is already included in the voltage measurement.

However, self-heating may be underestimated if the thermal contact between the temperature sensor and SiPM is bad. The motivation for this comes from studies conducted at the University of Hamburg [99]. This study measured the temperature via two PT-1000 sensors, one placed directly next to the SiPM on a common thermal contact, and the other sensor placed outside the thermal contact. The difference between the two sensors was about 2 °C for a SiPM operated at 2 V at −30 °C. This results in an underestimation of the temperature and hence the SiPM is operating at a lower over-voltage.

However, a difference in self-heating of 2 °C corresponds to a decrease of the bias voltage by 75 mV. The fits similar to those shown in fig. 6.3 established that a change in over-voltage by less than 100 mV changes the noise by less than 5 % with respect to the current. Therefore, this effect is within the uncertainties of the experimental approach.

Nevertheless, a new setup was proposed to verify if this effect is large, in which the temperature remains constant throughout the experiment. By keeping the temperature constant and remeasuring the current-noise relationship, one can keep the temperature-dependent self-heating to a constant level. This setup and the results are discussed in section 6.1.2.

6.1.2 Measurement by Variation of LED Intensity

An increase in current passing through the SiPM could be due to noise or due to external photon passing through the SiPM cells creating avalanches. While the procedure above measures how the noise varies with leakage current, one can also use photo-current to establish how noise varies with current.

To do this, one must increase the photo-current levels passing through the SiPM while retaining the Poisson distribution of light detection. One way of performing this is to place an

LED, which emit photons randomly at a constant intensity near the SiPM, and use a random trigger to measure the current flowing through the SiPM and the fluctuation of the pedestal. The current produced with the LED mimics a leakage current and effects of noise without varying the temperature.

6.1.2.1 Methodology and Test Setup

A blue LED is placed underneath the exposed tileboard as shown in fig. 5.1 and the climate chamber is made light-light from the outside using a thick black rubber sheet to cover the window which is the only part exposed to the outside. This cover ensured the LED is the only source of photons the SiPMs would see. The intensity of the light is varied by changing the voltage supplied to the LED. The higher the intensity, the more photons are detected; therefore, more current passes through the SiPMs.

For this experiment, the TB1.2 tileboard is used, which contained one $1.4 \times 1.4\,\mathrm{mm}^2$ and one $2 \times 2\,\mathrm{mm}^2$ SiPM irradiated to $2 \times 10^{12}\,\mathrm{n_{eq/cm^2}}$. These are two of the same SiPMs used in section 6.1.1. Therefore, the results are directly comparable. The method of obtaining the current and noise is identical to the previous experiment. One of the differences between the setups is that the climate chamber was fixed to a temperature of 25 °C and the measurements were conducted at a fixed bias-voltage. This allowed to maintain the expected self heating at a constant level. The temperature sensors onboard also monitor any fluctuations in temperature while the experiment is carried out.

The same bias voltage is supplied to the SiPMs and is calculated assuming that both SiPMs have exactly the same breakdown voltage. However, the breakdown voltages of the two SiPMs are not identical. Therefore, the true over-voltage was calculated offline (2.00 V and 1.78 V for the two SiPMs). In order to compare the curves, the noise and current values along over-voltages of 2.00 V and 1.78 V for the two SiPMs are extracted from the linear fits as shown in fig. 6.3.

6.1.2.2 Results and Discussion

Figure 6.6 shows the noise vs. current curves obtained from the two different setups operated at the same over-voltage. As the SiPMs have different breakdown voltages and were powered using a common voltage supply, the over-voltages they operated at were slightly different. To compare the results from the two setups, the linear fit as shown in fig. 6.3 was extended to 2.00 V and 1.78 V such that the noise vs. current curves can be compared at the same over-voltage.

As apparent from the results, the relationship between noise and current is very similar between the two different setups. This shows that if the self-heating exists, it is a small effect and therefore does not affect the overall conclusions drastically. It also shows that the current produced by the LED light is sufficiently incoherent and therefore this technique can be used to estimate the relationship between current and noise.

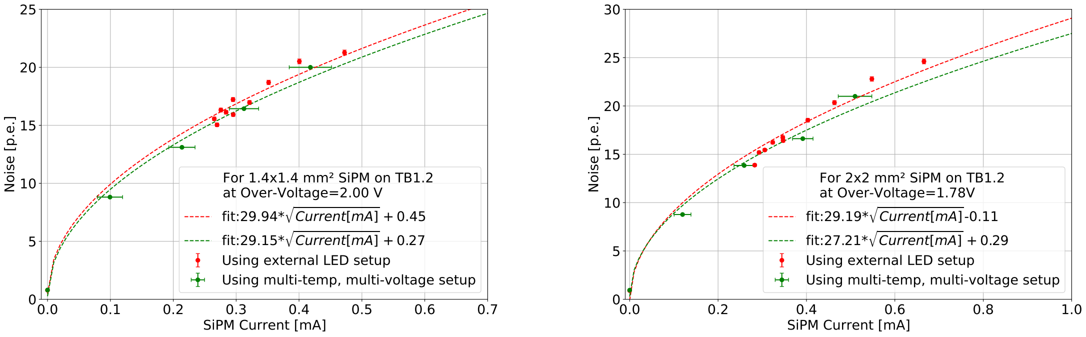

(a) (b)

Figure 6.6: Comparison between the two measurement methods extracting the noise vs. leakage current relationship at the same over-voltage. (a) shows the comparison between the two measurements for the $1.4 \times 1.4\,\mathrm{mm}^2$ SiPM while (b) shows the comparison for the $2 \times 2\,\mathrm{mm}^2$ SiPM. The uncertainties for the data from the multi-temperature setup were derived from the linear fits used to extract noise and current. The uncertainties for the LED setup are due to uncertainties in over-voltage measurement.

6.2 Noise vs. Current Relationship for Different HGCROC Generations

Until this point, all measurements of noise-current relationships were established using irradiated SiPMs on TBv1 and TBv2. Both these tileboards use HGCROCv2 for data readout. With the advent of TBv3 and MiniTB containing an HGCROCv3, it was important to validate that the noise and leakage current levels remain the same.

In order to investigate the difference between the different HGCROC versions, two irradiated SiPMs on TBv2 were removed and soldered onto the MiniTB tileboard. The noise and currents were measured using the temperature variation method described in section 6.1.1.

As the MiniTB has no power regulator onboard, all bias and supply voltages were supplied externally using power supplies. The noise and currents were measured for multiple temperatures for irradiated SiPMs such that linear fits can be used to extract the noise and current at an over-voltage of 2 V as conducted in section 6.1.1.

6.2.1 Results and Discussion

The comparison of noise vs. current relationships for the two irradiated SiPMs on board TBv2 and MiniTB are shown in fig. 6.7.

Figure 6.7 shows that for the same current there is a 10 % to 20 % difference between the noise measured on the MiniTB compared to the TBv2s. Since HDR-2 SiPMs are used on both tileboards, no difference should exist between the noise measured at the same leakage current. The existence of any difference indicates that something has changed between the two different tileboard electronics.

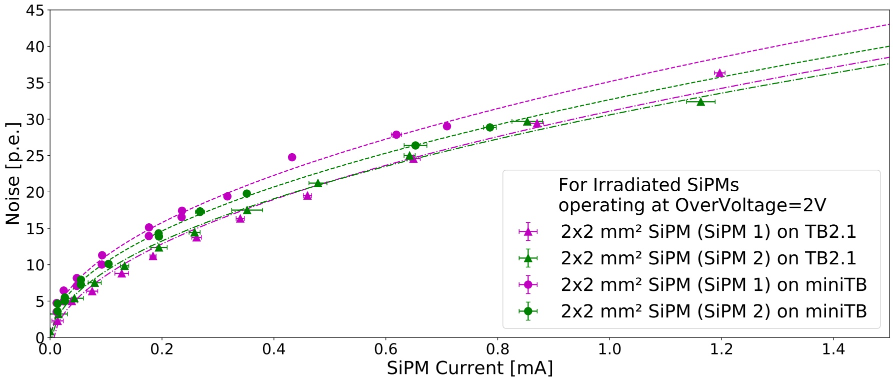

Figure 6.7: The noise vs. leakage current variation for the same two irradiated SiPMs on TBv2 containing a HGCROCv2 and MiniTB containing a HGCROCv3 at an over-voltage of 2 V. Uncertainties were derived from the linear fits used to extract noise and current.

As mentioned in section 2.4.2.4, the overall noise measured is a result of the individual noise from the SiPM and the electronics on the tileboard including the HGCROC. Since the MiniTB does not have any power regulators onboard, it is possible that there is additional noise from the power lines which was picked up by the SiPM. The over-voltage is also reliant on the temperature measurement obtained from the on-board PT-1000 read via the GBT-SCA. The GBT-SCA requires a fixed, stable power supply in order to convert the temperature values accurately. However, since the power is unregulated,the temperature measurement may have been inaccurate, leading to an inaccurate over-voltage measurement.

However, noise vs. leakage current were measured from non-irradiated SiPMs on the TB3 tileboard which has all the proper power regulators onboard. These SiPMs exhibited the same increased noise levels as observed from non-irradiated SiPMs on the MiniTB as seen in fig. 6.8 proving that the lack of regulators on the MiniTB had little impact on the noise. This leaves the HGCROC version to be the sole difference between the two tileboards that can cause such a difference in noise.

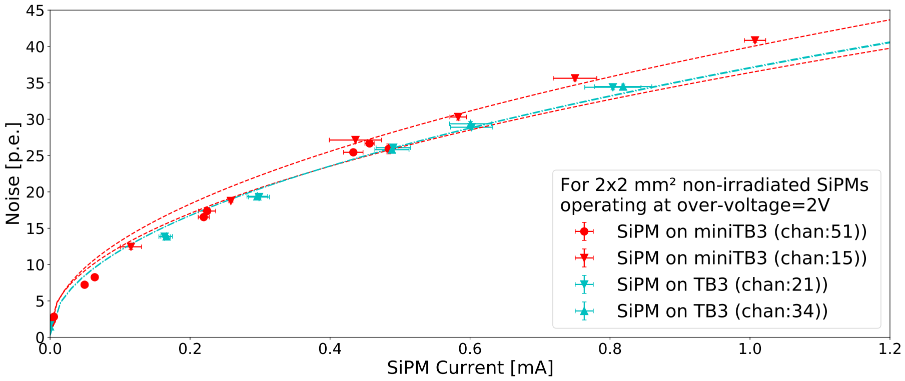

Figure 6.8: The noise vs. leakage current variation for non-irradiated SiPMs on TB3 and MiniTB at an over-voltage of 2 V. Both tileboards contain HGCROCv3 chips. Uncertainties were derived from the linear fits used to extract noise and current.

HGCROCv3 is relatively new at the time of this thesis and has yet to be tested to the full extent at DESY. One hypothesis is that the preamplifier of the HGCROCv3 has not been optimised for proper data taking yet: This includes parameters such as Cf, Cf_comp and Rf which are responsible for the pulse shape characteristics which impacts the gain of the SiPM and may result in elevated noise levels.

However, since the noise is re-scaled using the SiPM gain and the SiPM gain is also sensitive to most of the same scenarios to which the noise is sensitive to, most effects due to poor optimisations of the chip should be mostly suppressed. Therefore, elevated noise might indicate an increase in the inherent noise of the new HGCROCv3 chip.

One other change between the two HGCROC version is the package in which the HGCROC came in. The HGCROCv3 was packaged using the packages from two vendors. While the HGCROCv3 with the first package could not be operated at DESY, the second package featured increased base noise levels due to grounding issues. The measurements presented here are from the HGCROCv3 version with the noisy package mounted on the MiniTB and TBv3. The same increase in noise was observed with HGCROCs produced for the silicon sensors. These issues are planned to be solved only with HGCROCv3b, which is foreseen to be the chip version to be installed in the final detector. If the increased noise is purely a package issue, the noise levels will return to the same values as seen with HGCROCv2 during the detector operation.

The noise is an important parameter determining the SNR at the detector’s end of life. Therefore reducing the noise as much as possible is vital for good physics capabilities at HL-LHC. For this reason, further investigations why the HGCROCv3 features higher noise levels and how to reduce it further is a study still in progress within the CMS collaboration and at DESY.

6.3 Noise vs. Current Relationship for Different Non-Irradiated SiPMs

All measurements of noise-current relationships until this point were performed using irradiated SiPMs. However, similar tests can be performed for non-irradiated SiPMs, if the current levels passing through the SiPMs can be raised. The only way to increase the current flow through non-irradiated SiPMs is to use an external LED, as discussed in section 6.1.2. The main motivations behind these tests were to compare the noise vs. current relationship between irradiated and non-irradiated SiPMs and between different SiPM sizes. In this context, the $3 \times 3\,\mathrm{mm}^2$ SiPM measurements were conducted for the very first time.

The MiniTB tileboard was mainly used for this experiment. It contains six SiPMs out of which the noise-current relationship was measured for four SiPMs using a green LED operating in DC mode as described in section 6.1.2. These SiPMs include one $1.4 \times 1.4\,\mathrm{mm}^2$, two $2 \times 2\,\mathrm{mm}^2$ and one $3 \times 3\,\mathrm{mm}^2$ SiPMs.

6.3.1 Results and Discussion

The noise vs. current curves from these four non-irradiated SiPMs are compared to the previously mentioned irradiated SiPMs on the MiniTB are shown in fig. 6.9.

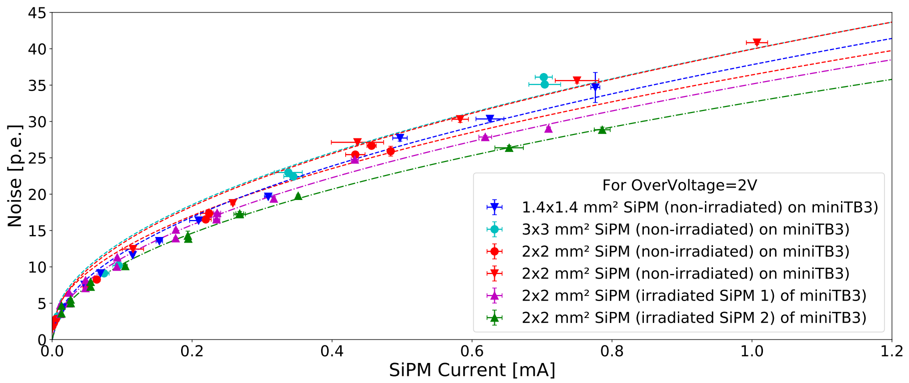

Figure 6.9: Comparison of noise vs. current relationships between four non-irradiated SiPMs and two irradiated SiPMs on MiniTB Tileboard operating at an over-voltage of 2 V.

The first observation is that the SiPMs on the MiniTB exhibit a higher variation in noise than what was observed with SiPMs on TBv1 and TBv2 combined. While the percentage uncertainty of A was less than 2 % for TBv1 and TBv2 SiPMs (see fig. 6.4), the percentage uncertainty of A was calculated to be 15 % for SiPMs on TBv3 and MiniTB. Reasons for this higher noise variation between channels could potentially be for same reasons discussed in section 6.2.

Apart from that, one additional uncertainty is that the exact breakdown voltage is unknown for SiPMs on TBv3 and MiniTB. The reel sent by the manufacturer HPK for these SiPMs only contained an average breakdown voltage. As a result, these SiPMs may have a difference in over-voltage varying by up to 100 mV. In addition to the change in noise and leakage current, the gain of the SiPM can vary by up to 5 % due to variations in breakdown voltages. Since the noise is re-scaled using gain, the noise may also vary by up to 5 %.

The $3 \times 3\,\text{mm}^2$ SiPM shows similar noise levels to the other SiPMs, but in comparison to the average value, has a marginally higher noise. Since only one $3 \times 3\,\text{mm}^2$ SiPM was measured, it is hard to generalise this observation. However, the fact that the noise from this SiPM is within the range of the other SiPM sizes is very promising. This means that for SNR extrapolations, it is possible to use a single fit to extrapolate how the noise will increase with irradiation (see section 6.4).

However, it must be noted that the leakage current level is also a function of SiPM size. Since the $3 \times 3\,\text{mm}^2$ SiPM is 2.25 times the size of the $2 \times 2\,\text{mm}^2$ SiPM, the current passing through the SiPM is also 2.25 times higher at any given fluence in comparison to the $2 \times 2\,\text{mm}^2$ SiPM. Based on this, the two SiPMs of different sizes will follow the same noise vs. leakage current curve, but the $3 \times 3\,\text{mm}^2$ SiPM will have a 2.25 times higher leakage current or about 1.5 times higher noise than the $2 \times 2\,\text{mm}^2$ SiPMs at any given neutron fluence and over-voltage. The dependence on over-voltage is especially critical because the HGCROC has a current limit of 1.2 mA. The $3 \times 3\,\text{mm}^2$ SiPMs operating at an over-voltage of 2 V may be limited by this current and therefore, using such devices may require the eventual decrease in over-voltage. More information on this study can be found in chapter 7.

Another observation is that the irradiated SiPMs exhibit the lowest noise at investigated leakage currents. The noise levels observed from the irradiated SiPMs are about 10 % lower than the non-irradiated SiPMs.

The noise vs. leakage current for irradiated SiPMs were measured using the multi-temperature setup while the non-irradiated SiPMs were measured using the external LED setup. The comparison of the two setups showed no major difference between the results from the two setups, and therefore any difference coming from the setups should be small.

The difference could be due to statistical fluctuations due to the uncertainty in breakdown voltages for the non-irradiated SiPMs mentioned above. With the non-irradiated SiPMs, the exact breakdown voltage is unknown. But for the irradiated SiPMs, the exact breakdown voltages were known. Therefore, the over-voltage uncertainty in the irradiated SiPMs were much lower that for the non-irradiated SiPMs. However, the difference observed is much larger than the 5 % effect estimated from the gain uncertainty.

The difference could also be due to irradiation itself. Irradiation changes the structure of the silicon substrate, including damage to the optical trenches which increases the probabilities for crosstalk and after-pulsing. Since non-irradiated SiPMs do not have such damage, the noise may differ from the irradiated SiPMs. However, the measurements suggest that the noise measured at higher irradiation is better than the extrapolated values from the curves before irradiation which is opposite to the expectation. Furthermore, no damage to the trenches has been observed so far at irradiation up to $5 \times 10^{13}\ \mathrm{n_{eq}/cm^2}$.

Another possibility is that the SiPM gain of the irradiated SiPMs has reduced compared to non-irradiated SiPMs due to irradiation. Therefore, the noise is underestimated in these calculations resulting in a smaller noise. However, multiple studies conducted by the University of Hamburg using SiPMs of the same series (S14160 series single cell studies [97]) and using the SiPMs with the radiation-hard package custom-made for the HGCAL upgrade (S14160-976X series [98]) showed that the SiPM gain does not change for SiPMs irradiated to $2 \times 10^{12}\ \mathrm{n_{eq}/cm^2}$ fluence.

The difference also could be from a more fundamental difference in the SiPMs. The irradiated SiPMs on TBv1, TBv2 and later on MiniTB were produced in 2020 and belong to the HPK S14160 generation of SiPMs which are HDR-2 type SiPMs with the radiation-hard packaging (see table 4.1). The non-irradiated SiPMs on TB3 however were from the HPK S16713 series which are similar SiPMs with a custom package. In principle, these two SiPMs should perform very similarly. But the difference could indicate that something internally has changed. This is a rather unlikely scenario as the only difference between the SiPMs is the package. The cells are reportedly identical between the two types of SiPMs.

In conclusion, the difference between noise observed between irradiated and non-irradiated SiPMs for the same levels of current is not well understood and further investigations maybe necessary.

To extrapolate the performance from these SiPMs, a two fits are used extract the scaling factor from all irradiated SiPMs and non-irradiated SiPMs as shown in fig. 6.10 and the summary of the fit parameters are given in table 6.1. Since the curves from the irradiated SiPMs are the much more likely scenario, the fit parameters for the irradiated SiPMs are used as the default scenario for the extrapolation with the fir parameters from the non-irradiated SiPMs used as a worst-case scenario.

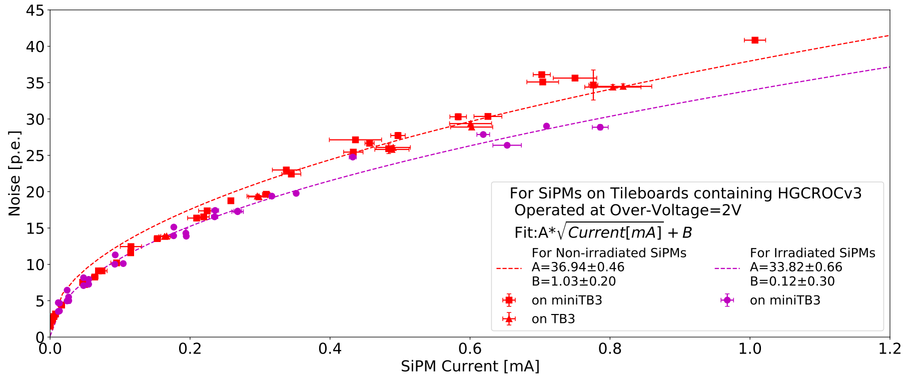

Figure 6.10: Comparison of noise vs. current relationships between six non-irradiated SiPMs (four on MiniTB and two on TB3) and two irradiated SiPMs on MiniTB (both containing HGCROCv3 chips) operating at 2 V. Two fits are used for the non-irradiated and irradiated SiPMs separately.

6.4 SiPM Noise Extrapolation to HL-LHC End-of-Life Conditions

The current vs. voltage curves from the three HDR-2 SiPM sizes irradiated to $5 \times 10^{13}\ \mathrm{n_{eq}/cm^2}$ were measured at a temperature of $-30\,°\mathrm{C}$ by the CMS HGCAL collaboration [74] and are shown in fig. 6.11. Numerically it was found that dark current scales linearly with SiPM active area for the three different SiPM sizes. As the collaboration measured the over-voltages with respect to $(V_{br}(\mathrm{IV}))_{\mathrm{irrad}}$ [74], one can use V_{offset} (see section 5.1) to convert the over-voltage defined for the two different breakdown voltage definitions.

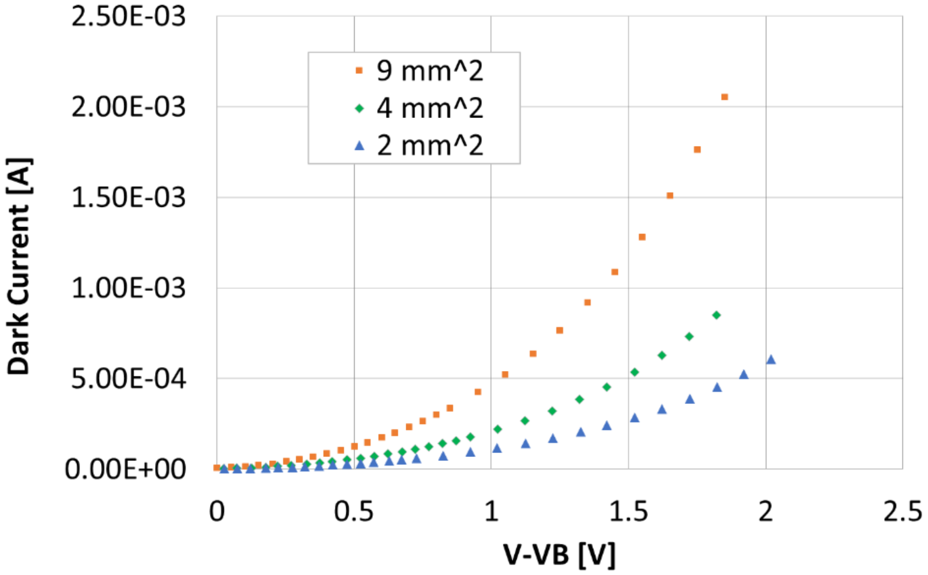

Figure 6.11: The I-V curves from three SiPMs irradiated to $5 \times 10^{13}\ \mathrm{n_{eq}/cm^2}$ at $-30\,°\mathrm{C}$. Taken from [74]. VB here is the breakdown voltage of the SiPMs measured w.r.t. the IV-definition $(V_{br}(\mathrm{IV}))$. The dark current measured here is the same as leakage current.

We want to measure the leakage current values from the three different SiPM sizes irradiated to $5 \times 10^{13}\,\mathrm{n_{eq}/cm^2}$ at $V_{over} = 2\,\mathrm{V}$ for $(V_{br}(\mathrm{TO}))_{\mathrm{irrad}}$ definition. Since $V_{\mathrm{offset}} = 0.37 \pm 0.02\,\mathrm{V}$ (see section 5.1), we extract the leakage current values at $V_{over} = 1.65\,\mathrm{V}$ for the three different SiPMs. For the $2 \times 2\,\mathrm{mm^2}$ SiPMs and $3 \times 3\,\mathrm{mm^2}$ SiPMs, the leakage current was measured to be $660\,\mu\mathrm{A}$ and $1.5\,\mathrm{mA}$ respectively. This is an increase in current by a factor of 2.25 as expected.

Since the leakage current is known, the A and B parameters can be obtained from the fits calculated separately for tileboards containing HGCROCv2 and HGCROCv3 using eq. (6.2). Table 6.1 presents the noise at the end of life ($\mathcal{L} = 3000\,\mathrm{fb^{-1}}$) calculated for the different HGCROCs operating at $V_{over} = 2\,\mathrm{V}$ with respect to $(V_{br}(\mathrm{TO}))_{\mathrm{irrad}}$. The parameters were obtained using a single fit for all SiPMs read out from the same HGCROC version.

In general, these fit parameters scale with fluence, integrated luminosity and SiPM active area. Therefore, one can define an equation to calculate the noise level of a given SiPM of a certain area at a given time (in terms of integrated luminosity) at a given location in the detector (given by fluence) with respect to the noise of a $2 \times 2\,\mathrm{mm^2}$ SiPM after a neutron fluence of $5 \times 10^{13}\,\mathrm{n_{eq}/cm^2}$ (N_{EOL}) as:

$$\left(\frac{\text{Noise [p.e.]}}{N_{EOL}\ \text{[p.e.]}}\right) = \sqrt{\left(\frac{\text{fluence}}{5 \times 10^{13}\,\mathrm{n_{eq}/cm^2}}\right) \times \left(\frac{\text{int. lumi}}{3000\,\mathrm{fb^{-1}}}\right) \times \left(\frac{\text{SiPM area}}{2 \times 2\,\mathrm{mm^2}}\right)}. \tag{6.4}$$

It is this equation that is used to extrapolate the noise of the SiPM and electronics during the lifetime of the detector. The required fluence values are taken from a fluence map produced using FLUKA simulations of the CMS layout [100]. Based on the HGCROC used, the noise N_{EOL} used in this equation should be taken from table 6.1.

Table 6.1: Overview of expected noise for different HGCROC generations for SiPM-on-tiles operating after a fluence of $5 \times 10^{13}\,\mathrm{n_{eq}/cm^2}$ working at $V_{over} = 2\,\mathrm{V}$ w.r.t. $(V_{br}(\mathrm{TO}))_{\mathrm{irrad}}$. The noise and current were calculated for $2 \times 2\,\mathrm{mm^2}$ SiPMs using eq. (6.2). For other sizes, multiply the leakage current by the scaling factor of SiPM area and use eq. (6.4) to calculate the noise.

HGCROC Version	**Noise vs Current Fit Parameters**		**Highest at End-of-Life Conditions**	
	A [p.e./$\sqrt{\mathrm{mA}}$]	B [p.e.]	**Leakage Current [mA]**	**Noise [p.e.] (N_{EOL})**
HGCROCv2 Irradiated SiPMs	32.95	-1.51	0.660	**24.04**
HGCROCv3				
Irradiated SiPMs	33.82	0.12	0.660	**27.60**
Non-irradiated SiPMs	36.94	1.03	0.660	**31.04**

Chapter 7

Signal-to-Noise Ratio Extrapolations of the HGCAL Scintillator Section

The latest luminosity estimates from CERN [8] suggest that an integrated luminosity ($\mathcal{L}_{int}$) of 3000 fb^{-1} can be collected in the total duration of the LHC operation by the CMS experiment (see fig. 3.1). Given that the estimated $\mathcal{L}_{int}$ to be collected at the end of phase 1 is about 450 fb^{-1}, this is an additional $\mathcal{L}_{int} =\sim 2600\,\mathrm{fb}^{-1}$ collected during the LH-LHC duration of 10 years.

The scintillator section of the HGCAL was limited to the area where a SNR of at least three can be maintained up to $\mathcal{L}_{int} = 3000\,\mathrm{fb}^{-1}$ collected exclusively during the HL-LHC operation. However, since these estimates were made, many parameters must be updated in the model.

SNR is mathematically defined as the ratio between light yield and the pedestal width (which we define here as SiPM noise) acquired from the SiPM-on-tile signals on Tilemodules as given in eq. (3.2). As the radiation levels increase, the SNR decreases due to the loss of scintillator light yield and increased noise in the SiPM. The SNR>3 requirement is motivated by a study conducted by the CMS HGCAL collaboration [85], which shows that by using dedicated reconstruction algorithms, the pedestal contamination in MIP data could be reduced to less than 5 % with 12.5 hours of data taking targetting muons produced in $W \rightarrow \mu\nu_\mu$ events. MIP efficiency vs. noise occupancy studies conducted in section 5.4 also showed that an efficiency of over 90 % with less than 7 % contamination can be obtained with just the information from the trigger layer confirming the existence of a MIP event in this channel.

With the new studies conducted on scintillators, SiPMs and Tilemodules, it is essential to accurately model the SNR and ensure that the SiPM-on-tiles performance is maintained at SNR>3 until the detector end-of-life. As a result, it is essential to update existing SNR models and make necessary changes to the layout to ensure its performance. This chapter describes the mathematical model used to model the SNR, its evolution with $\mathcal{L}_{int}$, the performance at the expected hardware conditions and suggested layout changes to improve the SNR.

7.1 Mathematical Model

The mathematical model was first developed within the HGCAL collaboration to estimate the end-of-life performance (after $\mathcal{L}_{int} = 3000\,\mathrm{fb}^{-1}$) of the SiPM-on-tiles for the TDR of the CMS HGCAL upgrade [10]. However, this model needs to be updated with the latest information based on experimental data. This includes new light yield measurements of non-irradiated SiPM-on-tiles (start-of-life conditions), new noise measurements from SiPMs on Tilemodule prototypes and new models for scintillator degradation with irradiation.

The default scenario of the model assumes a collection of up to $\mathcal{L}_{int} = 3000\,\text{fb}^{-1}$ in the 10-year operation time of the HL-LHC by the CMS experiment. However, in order to account for the uncertainties of the light yield and noise measurements as well as fluence and dose rates calculated from FLUKA extrapolations, a second scenario with $\mathcal{L}_{int} = 3600\,\text{fb}^{-1}$ in the same 10-year period was added to the model to introduce a safety margin. This was performed by increasing the expected absorbed dose and neutron fluence rates by 20 %. The different components and considerations of the model are discussed in more detail below.

7.1.1 SiPM-on-tile Positions

The current version of the HGCAL has 47 layers, out of which 14 contain Tilemodules as discussed in section 3.3. This is the same layout which is implemented in the mathematical model. The model implements a 10 ° sector of the scintillator section as shown in fig. 3.6(a) because the detector comprises 36 similar 10 ° sectors with minor differences. The expected neutron fluence, absorbed dose, and the expected performances of the SiPM-on-tiles follow a rotational symmetry around the beam axis. Since the two end-caps are also identical, it is possible to estimate the performance of the entire detector by modelling a single 10 ° sector of one of the end-caps.

The tile geometry is first derived from a regular grid as shown in fig. 7.1. Each tile is trapezoidal with the width of a tile at the tile centre in the nth ring given by w_n. Let d_n be the distance from the centre of the detector to the centre of the tile. Let t be the number of tiles in a 10 ° sector. Therefore, the angle covered by a tile $\delta\phi$ is:

$$\delta\phi = \frac{10}{t} \cdot \frac{\pi}{180}. \tag{7.1}$$

Let:

$$\delta\phi_{segment} = \frac{\delta\phi}{2}. \tag{7.2}$$

Then,

$$\tan(\delta\phi_{segment}) = \frac{w_n}{2 \cdot d_n}. \tag{7.3}$$

Since all tiles in a ring are equal in size, the central positions of the tiles in that ring are calculated using eq. (7.3).

In order to find the central tile position of the tiles in the $n+1$th ring, the tile height (h_n) is chosen to be the same as its width. That is:

$$h_n = w_n, \tag{7.4}$$

and therefore, the distance to the tile centre of a tile in the $n+1$th row is given by:

$$d_1 = d_0 + \frac{1}{2} \cdot h_0 + \frac{1}{2} \cdot h_1. \tag{7.5}$$

Therefore,

$$d_{n+1} = d_n + \frac{1}{2} \cdot h_n + \frac{1}{2} \cdot h_{n+1}. \tag{7.6}$$

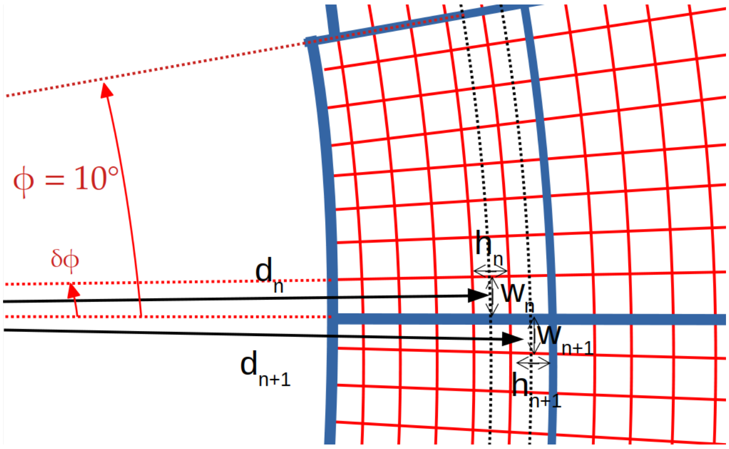

Figure 7.1: The tile positions in the scintillator section. The width of the tile w_n is measured along the tile centre, and the height of the tile h_n is measured along the radial direction. The distance from the centre of the detector to the centre of the tile is given by d_n. $\delta\phi$ gives the angle covered by a single tile.

Using eq. (7.6) iteratively, tile centres of all the detector rings are generated.

In the original geometry, two rings of tiles are chosen to share the exact tile dimensions to reduce the number of tile sizes that need to be produced. Therefore, the tile centres are recalculated by taking the average height of the tiles in the two adjacent rings and correcting the tile centres in the rings accordingly. That is, if h_n and h_{n+1} are the tile heights of rings n and $n+1$, the final height of the tiles in these rings would be h' where:

$$h' = \frac{h_n + h_{n+1}}{2}. \tag{7.7}$$

Let $l_{\text{inner},n}$ be the distance from the detector centre to the inner edge of the nth ring:

$$l_{\text{inner},n} = d_n - 0.5 \cdot h_n, \tag{7.8}$$

then, the adjusted centre positions given by d'_n and d'_{n+1} are:

$$d'_n = 0.5 \cdot h' + l_{\text{inner},n}, \tag{7.9}$$

and

$$d'_{n+1} = 1.5 \cdot h' + l_{\text{inner},n}. \tag{7.10}$$

The width of the two rings will be given by w'_n where,

$$w'_n = w'_{n+1} = 2 \cdot d'_n \cdot \tan(\delta\phi_{segment}). \tag{7.11}$$

A similar approach can be used if three rings have the same tile dimensions. Under such a system, the average heights of rings n, $n+1$ and $n+2$ will be:

$$h'' = \frac{h_n + h_{n+1} + h_{n+2}}{3}. \tag{7.12}$$

If $l_{\text{inner},n}$ is the distance from the detector centre to the inner edge of the nth ring, the adjusted centre positions are given by d''_n, d''_{n+1} and d''_{n+2} where:

$$d''_n = \frac{1}{2} \cdot h'' + l_{\text{inner},n}, \tag{7.13}$$

$$d''_{n+1} = \frac{3}{2} \cdot h'' + l_{\text{inner},n}, \tag{7.14}$$

and

$$d''_{n+2} = \frac{5}{2} \cdot h'' + l_{\text{inner},n}. \tag{7.15}$$

The width of the three rings will be given by w''_n where,

$$w''_n = w''_{n+1} = w''_{n+2} = 2 \cdot d''_n \cdot \tan(\delta\phi_{segment}) \tag{7.16}$$

Despite the many equations used to generate the geometry, the entire geometry has only two free parameters: $\delta\phi$ and d_n. Therefore, the exact positions of tile centres of all tiles in the scintillator section are generated using $\delta\phi$ and the knowledge of the position of one fixed tile centre d_0.

The original model only allowed for averaging two rings to have the exact tile dimensions. The possibility of averaging three rings, as described above, was added to the model in the scope of this thesis for reasons discussed later in this chapter.

This model was also used to decide the Tilemodule layout shown in fig. 3.6(a). A 10 ° sector in the default scenario contains eight SiPM-on-tiles per ring. The Tilemodule types were decided based on the distance from the beamline, expected neutron fluence, and absorbed dose rates at the detector end-of-life. Under the default geometry, 42 rings containing 21 different scintillator sizes make the 10 °. The sector contains eight main Tilemodule types.

The model was simplified for ease of computation by merging the tiles on each ring in a 10 ° to contain one cell. This is because SiPMs and scintillator tiles used on each ring and layer will be identical; therefore, the light yield, noise and SNR are expected to be the same. The dose and fluence at the cell centre are used as the global fluence and dose of the cell. As they lay relatively equidistant from the interaction point, the difference in fluence and dose rates within the cell are considered negligibly small.

7.1.2 Neutron Fluence and Absorbed Dose

The information on neutron fluence (f) and absorbed dose (D) are generated using two fourth order polynomials:

$$f = 10^{p_f}, \tag{7.17}$$

and

$$D = 10^{p_D}, \tag{7.18}$$

where

$$p_f(R, L) = c_{f0}(L) + c_{f1}(L) \cdot R + c_{f2}(L) \cdot R^2 + c_{f3}(L) \cdot R^3 + c_{f4}(L) \cdot R^4, \tag{7.19}$$

and

$$p_D(R, L) = c_{D0}(L) + c_{D1}(L) \cdot R + c_{D2}(L) \cdot R^2 + c_{D3}(L) \cdot R^3 + c_{D4}(L) \cdot R^4, \qquad (7.20)$$

respectively. Here, c_{fi} and c_{Di} (where $i = 0, 1, 2, 3, 4$) are fluence and dose constants generated for each ring R and layer L of the HGCAL using FLUKA simulations by the CMS collaboration [100]. The fluence obtained is in 1 MeV neutron equivalent units per square centimetre ($\mathrm{n_{eq}/cm^2}$) and absorbed dose is given in units of (krad/hr) after $\mathcal{L}_{int} = 3000\,\mathrm{fb}^{-1}$ ($\mathcal{L}_{int} = 3\,\mathrm{ab}^{-1}$), as expected to be achieved in the 10-year runtime. The dose and fluence at the tile locations are shown in fig. 7.2. A constant instantaneous luminosity is assumed throughout the HL-LHC runtime for this model, resulting in a constant fluence and dose rate. It is also assumed that the HL-LHC program begins with $\mathcal{L}_{int} = 0$. Therefore, fluence and dose increase linearly with increasing $\mathcal{L}_{int}$ as shown in fig. 7.3. Under these assumptions, this model can be used to extrapolate the performance of the detector even at higher doses and fluences beyond the runtime of the detector.

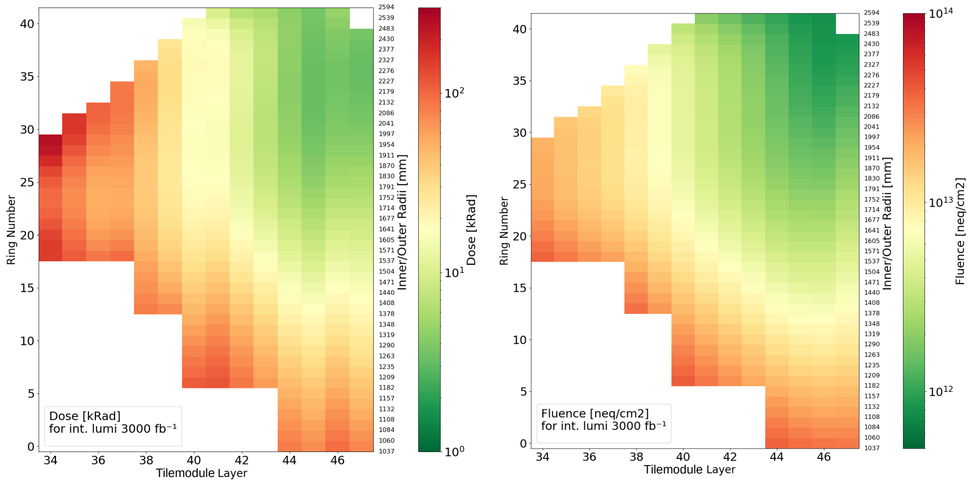

(a) (b)

Figure 7.2: (a) shows the absorption dose map and (b) shows the neutron fluence map for each ring and layer of the HGCAL SiPM-on-tile section for an integrated luminosity of $3000\,\mathrm{fb}^{-1}$. Each cell contains eight SiPM-on-tile cells whose dose and fluence are assumed to be constant throughout the cell.

As evident from fig. 7.2, the channels closest to the interaction point and the beampipe have the highest dose and fluence rates. In addition, the channels in the frontmost layers (34 to 37) also receive some of the highest dose and fluence rates. These channels are located close to the barrel and end-cap transition. Between the two detectors lies a gap to facilitate cables. This gap results in more radiation reaching these layers than most other scintillator layers, which results in elevated fluence and dose rates.

7.1.3 Light Yields

The light yields at the start of life were measured using Tilemodule prototypes (tileboards) at beam tests as introduced in chapter 4. These tests also showed that the light yield scales with the SiPM size, tile size and depends on the tile material as given by eq. (4.20). Using this

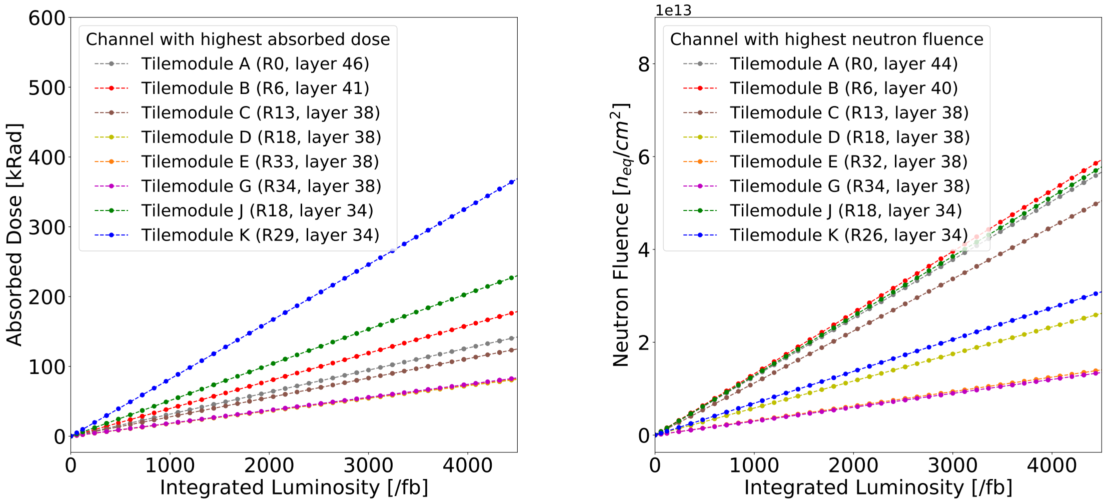

(a) (b)

Figure 7.3: (a) shows the absorbed dose and (b) shows the neutron fluence as a function of integrated luminosity for a few selected channels of different Tilemodule sections.

information, one can generate an initial light yield for a SiPM-on-tile map, similar to the fluence and dose.

Light yield is measured primarily at $V_{over} = 4\,\text{V}$ (under turn off definition, see section 2.4.2.8) as the SiPM gain is not measurable at lower over-voltages. Operation at a higher over-voltage is beneficial as the breakdown voltages are sensitive to changes in temperature. Assuming the SiPMs are supplied with a fixed bias voltage, the change in breakdown voltage due to temperature fluctuations will have a more significant impact at lower over-voltages than higher over-voltages.

However, the detector is foreseen to be operated at $V_{over} = 2\,\text{V}$. This is because even though higher over-voltages such as $V_{over} = 4\,\text{V}$ produce larger light yields, the SiPM noise increases by a larger factor than the light yield at higher over-voltages (see fig. 6.11 [74]). Therefore, the SNR is lower at higher over-voltages while the best SNR is obtained between 1 V and 2 V (see fig. 7.15). As the noise is inherently low in non-irradiated SiPMs, this does not affect the performance at start-of-life. However, as time progresses, it will be impossible to maintain the SNR>3 threshold for the SiPM-on-tiles.

Two such PDE curves exist. The first is the PDE measured by HPK, available on the datasheet. This curve adjusted the light yields based on differences in breakdown voltages discussed in section 4.4.1. The second PDE curve is the curve measured within the collaboration [74]. The advantage of this curve is that it extends down to over-voltages below 3 V, unlike the HPK-measured PDE. Therefore, this PDE curve was used to scale the light yield to 2 V. Figure 7.4(a) shows the PDE curve [74] measured with the third-order polynomial parametrisation used to scale light yield down to an over-voltage of 2 V.

Figure 7.4(b) compares the PDE curve measured by the CMS collaboration with the curve measured by HPK. The PDE measured within the CMS collaboration uses a relative PDE scale. Therefore, the HPK PDE measured at an over-voltage of 4 V has been used to rescale the curve measured by the CMS collaboration to compare the two curves for this plot. The curves agree

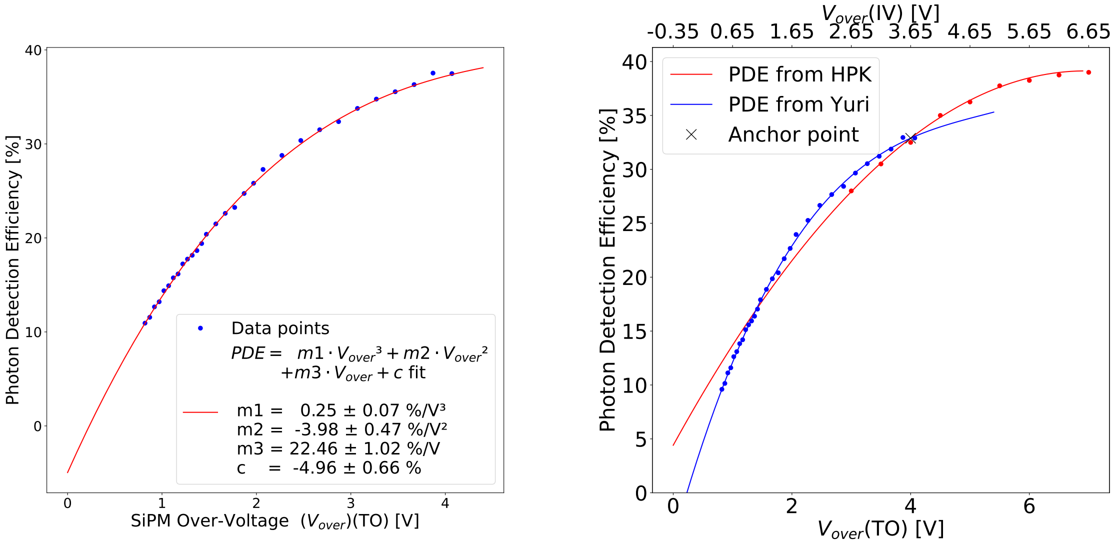

(a) (b)

Figure 7.4: (a) shows the PDE vs. over-voltage measured for HGCAL SiPMs as given in [74]. (b) compares the PDE curve measured by the collaboration with the curve measured by HPK. As the PDE measurement done within the CMS collaboration is a relative PDE curve, in order to compare the two curves, the HPK PDE measurement at an over-voltage of 4 V is used to rescale the curve measured by the CMS collaboration accordingly.

reasonably well between $1.5\,\mathrm{V} < V_{over}(\mathrm{TO}) < 4.0\,\mathrm{V}$. However, deviations begin to get larger outside of this over-voltage range.

Studies with SiPMs irradiated to a neutron fluence of $2 \times 10^{12}\,\mathrm{n_{eq}/cm^2}$ show no drop in light yield compared to non-irradiated SiPMs (see section 5.2). However, light yields measured by the collaboration show a drop of less than 10 % for SiPMs irradiated to $5 \times 10^{13}\,\mathrm{n_{eq}/cm^2}$ neutron fluence relative to non-irradiated SiPMs [74]. This drop in performance has not been accounted for in the SNR extrapolations but is assumed to be covered by the scenario where $\mathcal{L}_{int} = 3600\,\mathrm{fb}^{-1}$ is considered as the end-of-life scenario.

7.1.4 SiPM Noise

The dependence of the noise level on leakage current for different SiPM sizes is studied extensively in chapter 6. The scaling of noise with leakage current is given by eq. (6.1), and the extrapolation of the noise to any fluence or integrated luminosity is given by eq. (6.4). Since all the scaling parameters are known, the noise scaling with leakage current was implemented in the SNR extrapolation model to obtain the noise for every SiPM in the context of this thesis.

The noise scaling used in this section is obtained from irradiated SiPMs read out using HGCROCv3 ASICs on Tilemodule prototypes. The noise observed using the HGCROCv3 ASICs is higher than when the HGCROCv2 was used, as discussed in section 6.2. Though further studies are needed to understand why the noise has increased, the issue causing the noise increase may be resolved before the detector assembly. Therefore, the noise may return to the values observed with the HGCROCv2. The noise of irradiated SiPMs read out using HGCROCv3

ASICs gives a conservative estimate of the SNR expected at the detector's end-of-life.

The leakage current passing through SiPMs irradiated to $5 \times 10^{13}\ \mathrm{n_{eq}/cm^2}$ neutron fluence was measured using dedicated setups in the context of the HGCAL within the collaboration (see section 6.4 [74]). The increase in leakage current with fluence is assumed to be linear in this SNR model.

These SiPMs were irradiated in dedicated irradiation facilities. Once outside the facility, these SiPMs anneal within a few days, making it impossible to measure the true leakage current passing through the SiPMs before annealing. Therefore, the leakage currents used in the model to estimate the noise already includes the annealing effects. Annealing at 0 °C during the three-month long year-end technical stops (YETS) scheduled once per year estimates the leakage currents to recover by about 10 % after every year-end technical stops (YETS) [101]. Since the noise scales as a square root of leakage current, this is only a 3.3 % effect on noise.

Therefore, SNR model will be most accurate just after the three-month long year-end technical stops (YETS) and the noise may deviate by up to 3.3 % during normal operation. This is a rather small uncertainty and its effects are considered to be covered by the scenarios where $\mathcal{L}_{int} = 3600\ \mathrm{fb}^{-1}$ is considered as the end-of-life scenario.

7.1.5 Scintillator Tile Performance Degradation with Irradiation

Section 2.4.1.2 briefly introduced signal degradation with irradiation. Equations (2.15) and (2.16) model the performance effects caused by the permanent damage of the scintillators in high radiation environments while eq. (2.17) models the performance effects caused by the temporary damage.

The current end-cap of the CMS HCAL uses scintillators as the active material and is read out using wavelength-shifting fibres connected to PMTs. Studies have been conducted to disentangle the radiation effects on the scintillator from the fibres and PMTs. Based on data from this detector, the best estimate of the permanent damage dose constant is given by [10]:

$$D_{perm} = 3.6 \times 10^6 \cdot \text{Dose Rate}^{0.5}, \tag{7.21}$$

which is the value used in the SNR extrapolation to estimate the permanent damage.

The temporary damage was first studied in hypoxic and low-temperature environments using in-situ readouts by the University of Maryland in late 2022 in the context of the HGCAL experiment [16]. Two BC-412 cast scintillator tiles and one FNAL-produced injection moulded tile were irradiated at a dose rate of 30 rad/hr in this study at 3 % oxygen and −30 °C temperature. The data were fitted with a double exponential fit. The difference in scintillator performance between the two BC-412 tiles is in the order of 2 %. However, the tile with the worst performance was used in the SNR extrapolation to account for any uncertainties. The fit values for K, D_1 and D_2 (using the double exponential fit given in eq. (2.17)) for the two scintillator materials and are given in table 7.1 [16].

Let us assume that L_0 is the light yield at the start-of-life (before irradiation), L_{perm} is the light yield after permanent damage only, and L_{perm} is the light yield after temporary damage only.

Then fractional light yield after permanent damage is given by eq. (2.15). Similarly, the fractional light yield after temporary damage only is given by eq. (2.17). Therefore, the light

Table 7.1: Values of constants needed to calculate the scintillator temporary damage per year assuming $\mathcal{L}_{int} = 300\,\mathrm{fb}^{-1}$ per year was achieved [16].

Parameter	**For PVT based tiles (cast)**	**For PS based tiles (inj-moulded)**
K	0.08	0.07
D_1	170 krad	140 krad
D_2	4600 krad	7300 krad

yield after both permanent and temporary damage is given by L_{comb} and is calculated using:

$$\left(\frac{L_{comb}(d)}{L_0}\right) = \left(\frac{L_{perm}(d)}{L_0}\right) \cdot \left(\frac{L_{temp}(d)}{L_0}\right). \tag{7.22}$$

Therefore, during the nine-month operation of the HGCAL per year, the light yield for each SiPM-on-tile is modelled using eq. (7.22).

As mentioned in section 2.4.1.2, radicals which produce temporary damage are annealed at higher temperatures than the levels at which the HGCAL operates. Though further studies are ongoing, it is estimated that it would be possible to anneal the temporary damage of the scintillator by raising the temperature to 0 °C during the three-month year-end technical stops (YETS). That is, after the YETS:

$$\left(\frac{L_{temp}(d)}{L_0}\right) = 1. \tag{7.23}$$

Therefore, at the restart after the YETS, the fractional light yield would recover to:

$$\left(\frac{L_{comb}(d)}{L_0}\right) = \left(\frac{L_{perm}(d)}{L_0}\right) \tag{7.24}$$

Due to the complete annealing of temporary damage, the initial light yield of the following cycle will be the light yield after the permanent damage L_{perm}. The light yield will then continue to drop as given by eq. (7.22) and eq. (7.24) during the following operation cycle and YETS periods. This results in a cycle of light yield reduction and yearly annealing as shown in fig. 7.5.

Permanent damage to the scintillator was already implemented in the model. However, the degradation of scintillator performance due to temporary damage was implemented based on the study conducted by the University of Maryland [16] in the scope of this thesis.

7.1.6 Signal-to-Noise Ratio

The SNR is given in its most basic form by eq. (3.2). The light yield is measured at beam tests with SiPM-on-tiles on Tilemodule prototypes. Radiation reduces the light yield due to radiation damage to the scintillator. Similarly, radiation damage of the SiPM on Tilemodules increases the noise of the SiPM.

The light yields from FNAL-produced injection-moulded (batch 1) and NIU machined BC-412 cast tiles coupled to $2 \times 2\,\mathrm{mm}^2$ and $3 \times 3\,\mathrm{mm}^2$ SiPMs are used in the final layout scenarios. The values for the light yields were acquired from the beam tests described in chapter 4 and are scaled with scintillator and SiPM sizes using eq. (4.20).

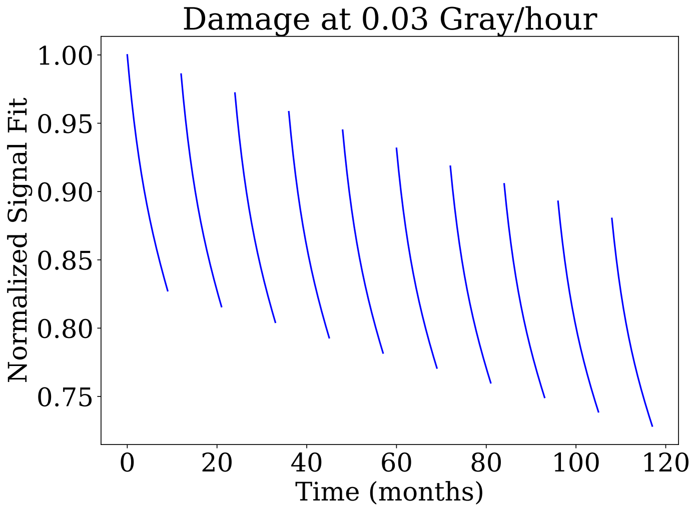

Figure 7.5: Signal degradation normalised to the initial signal over time due to temporary and permanent radiation damage. For tiles with 30 rad/hr dose rates and assuming an integrated luminosity of 300 fb^{-1} is delivered by LHC annually. Taken from [102].

The noise vs. current relationship obtained from irradiated SiPMs coupled to HGCROCv3 (see chapter 6) as given in table 6.1 is used as the default SiPM noise scenario. Similarly, the degradation in scintillator performance and resulting light yield loss due to irradiation (see section 7.1.5) is also modelled using the parameters given in table 7.1.

The final SNR in the mathematical model considers all these factors. Table 7.2 gives an overview of all parameters used for the calculation of SNR at an over-voltage of 2 V.

7.1.7 Layout

The default layout of the HGCAL scintillator section as of writing this thesis consists of the following:

- A, B and C Tilemodules with 2 × 2 mm^2 sizes SiPMs and BC-412 cast tiles,
- J and K Tilemodules with 3 × 3 mm^2 sizes SiPMs and BC-412 cast tiles,
- Front four layers of D, E and G Tilemodules with 2 × 2 mm^2 sizes SiPMs and BC-412 cast tiles, and
- Back six layers of D, E and G Tilemodules with 2 × 2 mm^2 sizes SiPMs and polystyrene-based injection-moulded tiles produced at FNAL.

This layout is illustrated in fig. 7.6.

Table 7.2: Overview of parameters used for the calculation of the SNR at an over-voltage (V_{over}(TO) $= 2\,\mathrm{V}$).

Parameter	**value**
Light yield scaling factor (k) before iradiation (see eq. (4.20))	
NIU BC-412 cast with $2 \times 2\,\mathrm{mm}^2$ SiPM (see table 4.3)	$3222 \pm 15\,\mathrm{p.e.} \cdot \mathrm{mm}$
FNAL inj-moulded batch 1 with $2 \times 2\,\mathrm{mm}^2$ SiPM (see fig. 4.38)	$1441 \pm 17\,\mathrm{p.e.} \cdot \mathrm{mm}$
Photon Detection Efficiency (PDE) (see fig. 7.4(a))	
m_1	$0.25 \pm 0.07\,\%/\mathrm{V}^3$
m_2	$-3.98 \pm 0.47\,\%/\mathrm{V}^2$
m_3	$22.46 \pm 1.02\,\%/\mathrm{V}$
c	$-4.96 \pm 0.66\,\%$
Noise of irradiated SiPMs	
after a fluence of $5 \times 10^{13}\,\mathrm{n_{eq}}/\mathrm{cm}^2$ (see table 6.1)	
On Tilemodule with HGCROCv2	
A	$32.95\,\mathrm{p.e.}/\sqrt{\mathrm{mA}}$
B	$-1.51\,\mathrm{p.e.}$
On Tilemodule with HGCROCv3	
A	$33.82\,\mathrm{p.e.}/\sqrt{\mathrm{mA}}$
B	$0.12\,\mathrm{p.e.}$
Permanent damage (see section 7.1.5)	
Dose constant D	$3.6 \times 10^6 \cdot (\text{Dose Rate [krad/hr]})^{0.5}$
Temporary damage per year (see table 7.1)	
(for int. lumi. of $300\,\mathrm{fb}^{-1}$ **at Dose Rate**$= 0.3\,\mathrm{kRad/hr}$**)**	
For NIU BC-412 cast tiles	
K	0.08
D_1	170 krad
D_2	4600 krad
For FNAL injection-moulded tiles	
K	0.07
D_1	140 krad
D_2	7300 krad

7.2 Signal-to-Noise Ratio For HGCAL Default Configuration

Figure 7.7 shows the SNR of the SiPM on tiles after collecting $\mathcal{L}_{int} = 3000\,\mathrm{fb}^{-1}$ in 10 years (as expected at the detector end-of-life) with updated signal and noise extrapolations as discussed in the previous section. Even at this level, many areas of the detector have SNR<3, which does not meet the requirements. This statement is especially true for J, K, B and C Tilemodules.

Figure 7.8 shows the SNR in the case where the SiPM-on-tiles receive $\mathcal{L}_{int} = 3000\,\mathrm{fb}^{-1}$ in 10 years, at a 20 % higher fluence and dose rate than what was estimated. This scenario is mathematically equivalent to the case where the detector receives $\mathcal{L}_{int} = 3600\,\mathrm{fb}^{-1}$ in 10 years. As mentioned, this scenario accounts for the uncertainties and leaves a safety margin.

This scenario will be used in all SNR extrapolations shown in this thesis from this point onwards, where all predictions are made about the detector performance.

The increase in fluence increases the leakage current by the same factor, thereby increasing the SiPM noise by the square root of this factor. The increase in dose reduces the light yield due

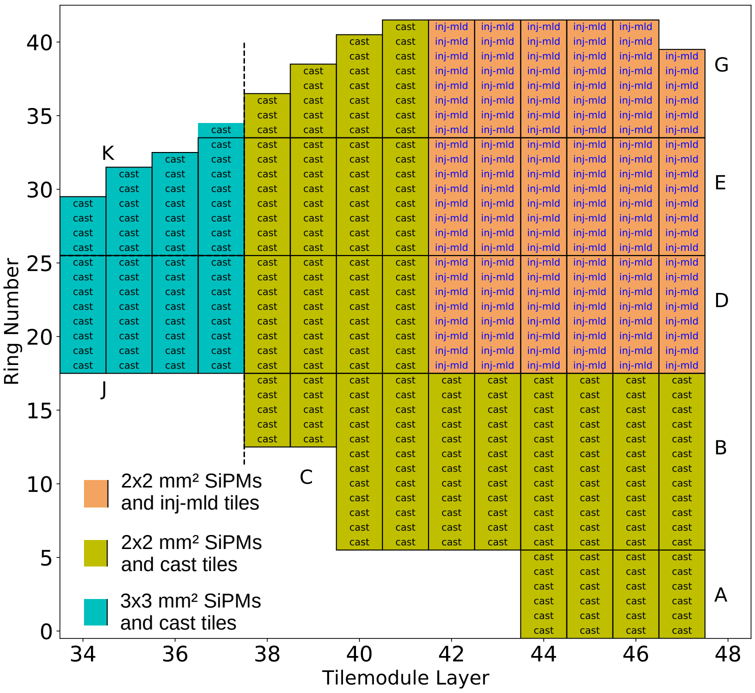

Figure 7.6: Default Tilemodule layout of the HGCAL scintillator section. Each cell consists of eight SiPM-on-tiles on a single layer and ring. Only NIU machined BC-412 cast tiles are assembled on the cells reading ’cast’, and FNAL produced injection-moulded (batch 1) tiles on the cells reading ’inj-mld’.

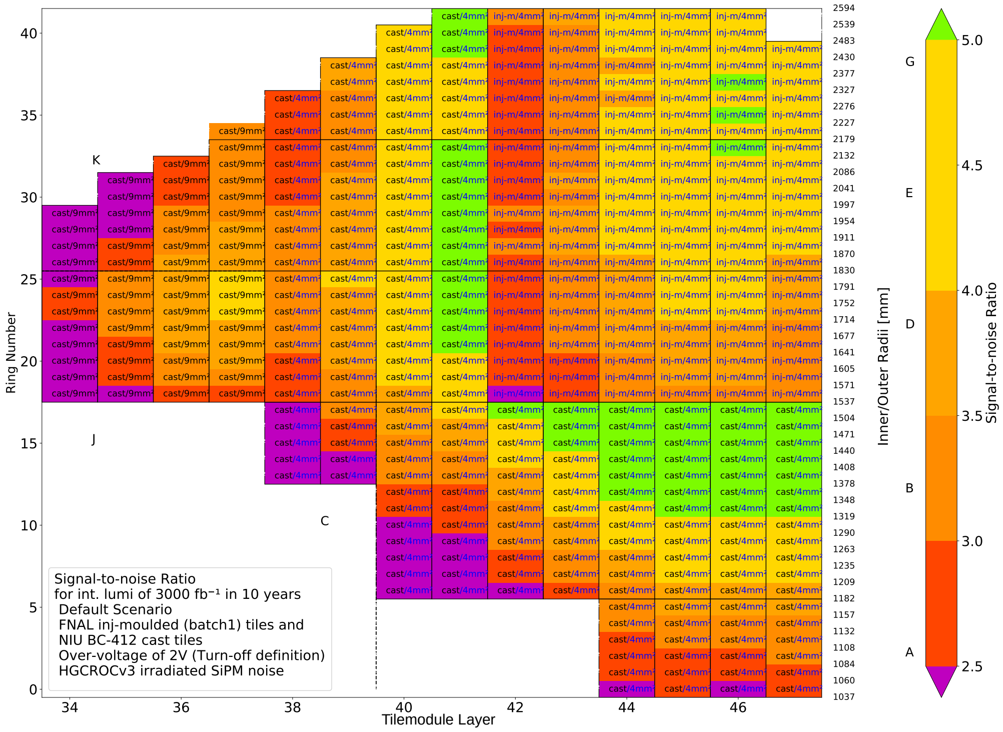

Figure 7.7: SNR after an integrated luminosity of 3000 fb^{-1} received over a 10-year period. The red and purple cells indicate the areas where SNR<3 and SNR<2.5, respectively.

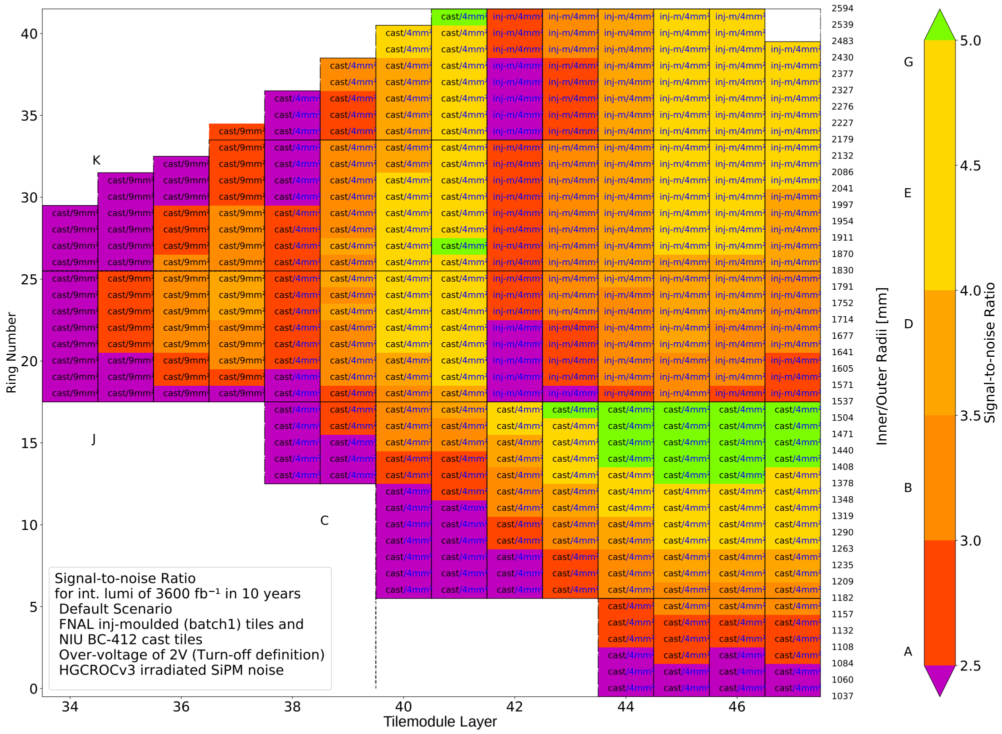

Figure 7.8: SNR with 20 % higher fluence and dose rates after an integrated luminosity of $3000\,\mathrm{fb}^{-1}$ over a 10-year period (equivalent to $\mathcal{L}_{int} = 3600\,\mathrm{fb}^{-1}$ collected over a 10-year period). The red and purple cells indicate the areas where SNR<3 and SNR<2.5, respectively.

to scintillator degradation. Under these conditions, it is evident that the A-boards and two layers of the D, E, and G Tilemodules would perform poorly even before the planned end-of-life.

7.3 Evaluating Strategies to Improve SNR

As detailed in section 4.5, the light yield scales linearly with the SiPM's active area and inversely scales with the square root of the scintillator tile area. Furthermore, cast tiles exhibit almost twice the light yield of injection-moulded tiles.

The SiPM with the largest area will also have the largest SNR at the same radiation level. This is because light yield scales as a function of number of cells fired in the SiPM (N_{pix}) while the noise scales as a function of $\sqrt{N_{pix}}$ as it follows a Poisson distribution (see section 2.4.2.4).

These properties of light yield are advantageous and can be used to improve the SNR at the end of life. This optimisation includes:

- Using larger SiPMs,
- Using scintillator materials which produce the highest light yields,
- Using smaller tiles,

in the most irradiated areas. Therefore, $3 \times 3\,\mathrm{mm}^2$ SiPMs will be used in areas with the highest expected neutron fluence. However, the larger SiPMs are, in general, more expensive than the smaller SiPMs, increasing the costs of the detector. They also draw more power than the smaller tiles, resulting in a more significant power requirement. The $3 \times 3\,\text{mm}^2$ SiPMs also come in a larger packaging with a different footprint than the $2 \times 2\,\text{mm}^2$ SiPMs. Therefore, dedicated Tilemodule PCBs must be produced for areas where $3 \times 3\,\text{mm}^2$ SiPMs are assembled.

Despite the higher light yield exhibited by PVT-based cast tiles, they are costly and time-consuming to produce compared to polystyrene tiles-based injection-moulded tiles. Therefore, cast tiles are limited to areas where the expected fluence and dose rates are the highest, while the rest of the detector is produced using injection-moulded tiles. Since scintillator tiles are glued onto the Tilemdoule, no changes to the Tilemodules are necessary if the scintillator tiles need changing.

The end-cap radial geometry dictates the scintillator tile size used in the Tilemodule. However, the smallest tile sizes lie closest to the beam pipe, where the expected radiation doses and fluences are among the largest. Since the smallest scintillator sizes produce the largest light yield, the detector is naturally optimised for this scenario.

However, this does not apply to areas containing J-type and K-type Tilemodules. J-type and K-type Tilemodules contain tiles larger than those on A-type Tilemodules, resulting in smaller light yields. They also experience some of the highest doses and fluences in the detector (see fig. 7.2). This results in a worse SNR in this region as seen in figs. 7.7 and 7.8.

The most drastic change would be to change the granularity of the tiles, as this will require a major change in the geometry. Using smaller tiles increases the number of tiles and SiPMs required to fill the same area. This increase in SiPM-on-tile count will also increase the power consumption of the detector.

Using these strategies, four detector layouts are proposed to improve the performance of the HGCAL scintillator section and are discussed below.

7.3.1 Layout Scenario 1

One alternative layout scenario would feature the replacement of the $2 \times 2\,\text{mm}^2$ SiPMs with $3 \times 3\,\text{mm}^2$ SiPMs in:

- the A and C Tilemodule areas,
- the front three layers (40 to 42) of B Tilemodule areas,
- the firstmost layer (38) of D, E and G,

and,

- use cast tiles in layers 42 to 44,

to improve the SNR. The SNR of the resulting layout at $\mathcal{L}_{int} = 3600\,\text{fb}^{-1}$ is shown in fig. 7.9.

7.3.2 Layout Scenario 2

A second layout scenario proposes the same layout changes proposed in layout 1. In addition, this scenario proposes to increase the granularity of the front four layers (J and K Tilemodules).

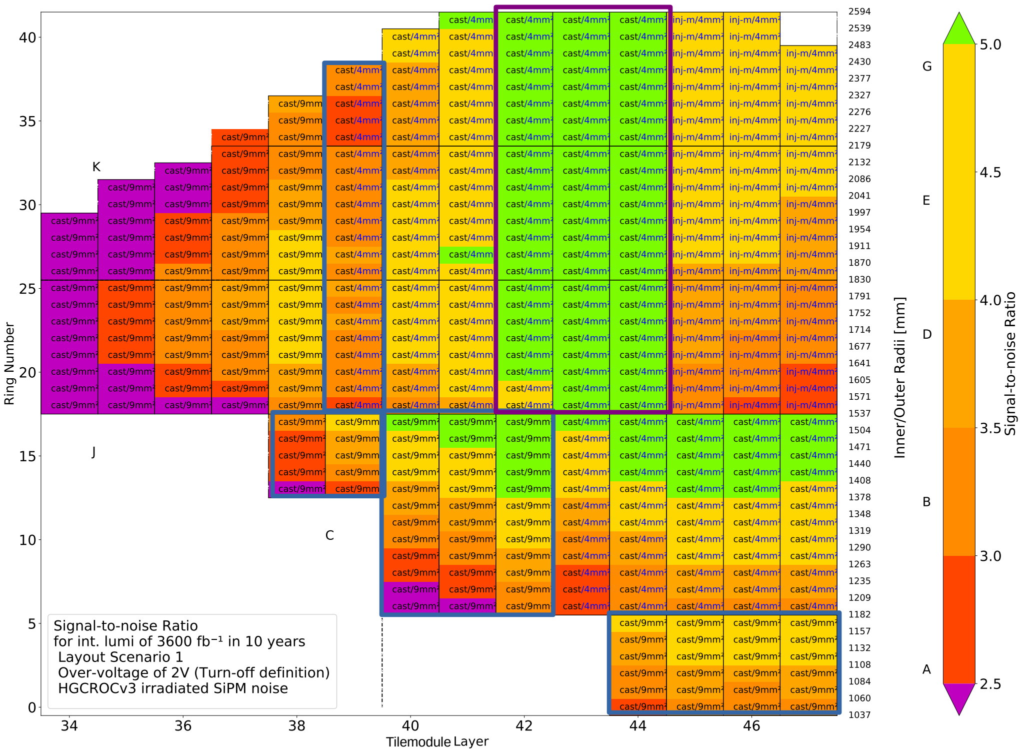

Figure 7.9: SNR from layout scenario 1 after $\mathcal{L}_{int} = 3600\,\text{fb}^{-1}$ over a 10-year period. The blue boxes mark all the areas where $2 \times 2\,\text{mm}^2$ SiPMs were replaced by $3 \times 3\,\text{mm}^2$ SiPMs. The purple box marks where injection moulded tiles were replaced with cast tiles.

That is, the area which previously held 2×2 number of SiPM-on-tiles will now contain 3×3 SiPM-on-tiles. This change would increase the number of SiPM-on-tiles by a factor of 2.25 in the area covered by J and K Tilemodules. The SNR under layout scenario 2 after $\mathcal{L}_{int} = 3600\,\text{fb}^{-1}$ is shown in fig. 7.10.

7.3.3 Discussion of Layout 1 and Layout 2

Layout scenario 1 improves the SNR in all the areas where SiPMs have been replaced. Similar improvements are seen in the areas where cast tiles replace injection-moulded tiles. However, the biggest flaw in this layout is that no changes are made to J and K Tilemodules to improve their performances. These are the Tilemodules which have the lowest reported SNRs at the end-of-life. These are also the areas which already contain the best-performing tile material and the larger SiPM. Therefore, increasing the granularity is the only way to improve the SNR further. This was the motivation for the layout scenario 2.

With layout scenario 2, the SNR improves in J and K layers compared to layout 1. A healthy SNR>3 can also be maintained in most cells. This layout shows that the combination of high granularity, better scintillating material and larger SiPMs will improve the SNR of the overall detector. However, the proposed changes would increase production costs and the time needed for production. Table 7.3 shows the number of SiPMs and scintillator tiles and the area of scintillator material needed to produce the detector under these layouts compared to the default layout.

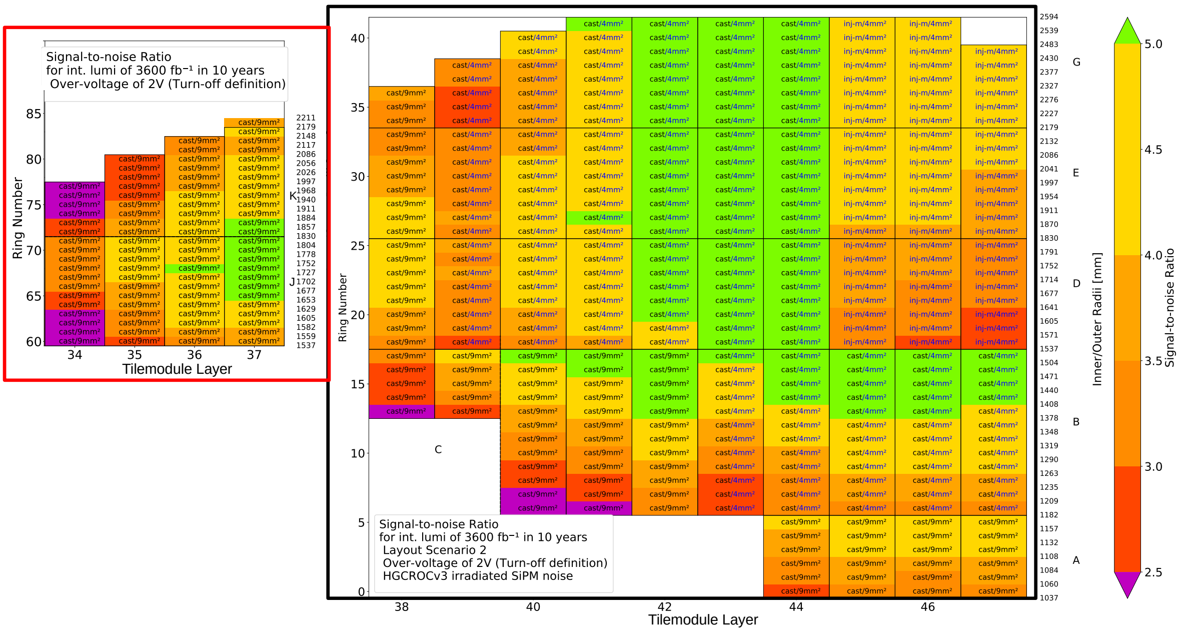

Figure 7.10: SNR for layout scenario 2 after an integrated luminosity of 3600 fb^{-1} over a 10-year period. The red box marks all the areas where each area containing 2 × 2 SiPM-on-tile channels is replaced with 3 × 3 SiPM-on-tile channels. The black box marks the area which remains unchanged from layout 1.

The difference in cost between the different SiPM sizes is less than a factor of two when ordered in bulk. Therefore, the increase in production costs of the detector due to this change is manageable. However, additional detector design and operation changes are expected to occur using more 3 × 3 mm² SiPMs.

Most Tilemodules operate with one ALDOv2 in high voltage mode (ALDOv2 BV), which provides the bias voltages to all SiPMs on the Tilemodule along two channels each providing up to 25 mA current [75]. Each HGCROC channel powers a single SiPM and is functional up to a current of 1.2 mA. The 2.25 times larger current flowing through the 3 × 3 mm² SiPMs in comparison to the 2 × 2 mm² SiPMs would mean that a leakage current of close to 1.5 mV will pass through the SiPMs in the most irradiated areas. Tilemodules consisting of at least eight rings of 3 × 3 mm² SiPMs operating at an over-voltage of 2 V after tolerating large radiation fluences will reach this current limit before reaching the detector end-of-life. One way to prevent impeding this current limit by the 3 × 3 mm² SiPMs is to use an additional ALDO regulator on these Tilemodules. However, this requires a redesigning of the Tilemodule PCB. Furthermore, the current limit per HGCROC channel cannot be changed. This means operating the most irradiated SiPMs at an over-voltage of 2 V would be impossible. This means the over-voltage must be further reduced to accommodate the 3 × 3 mm² SiPMs. More about this option is discussed later in this chapter.

The difference in footprints between the 3 × 3 mm² SiPMs and the 2 × 2 mm² SiPMs means that dedicated Tilemodule PCBs must be produced for areas where 3 × 3 mm² SiPMs replaced the 2 × 2 mm² SiPMs. One of the layout changes suggested in layout scenario 1 was to replace only a fraction of B, D, E and G Tilemodules containing 2 × 2 mm² SiPMs with 3 × 3 mm² SiPMs. This requires the design and production of additional Tilemodule varieties, making the design and production process more complex and time-consuming.

No changes to the PCBs are necessary when selecting between the tiles of different scintillator materials. However, the cost of producing cast tiles is over twice as much as producing injection moulded tiles. Cast scintillator material is typically bought in bulk as large sheets and is cut down using dedicated machines. Injection-moulded tiles, on the other hand, require only the molten plastic injected into the mould to cool down. This entire process takes a much shorter time than machining cast tiles. Therefore, increasing the number of cast tiles also increases the time necessary for production.

As a logical consequence, the change in granularity proposed for J and K Tilemodules will also increase the number of cast tiles and SiPMs required, increasing the detector cost. However, this is the only strategy available to improve the J and K Tilemodules. The change in granularity would feature the replacement of the J8 Tilemodule containing 64 SiPM-on-tiles (8×8 SiPM-on-tiles) with a J12 Tilemodule containing 144 SiPM-on-tiles (12×12 SiPM-on-tiles). Similar transformations need to be applied to the K-type Tilemodules as well. Since the HGCROC can handle 72 SiPM-on-tiles at most, the new J and K Tilemodules will need two HGCROCs and up to three ALDO power regulators on-board with two of them supplying the bias voltages to the SiPMs (ALDOv2 BV). Since each ALDOv2 BV has two high voltage channels each, the four channels can supply up to 100 mV of current in total.

This mode of operation, where a single Tilemodule is powered by three ALDOv2 ASICs and readout by two HGCROCs, is not new in the HGCAL. The B-type Tilemodules have twelve rings (96 SiPM-on-tiles) and are powered and read out in the same way. However, the B-type Tilemodules are much larger than the J and K Tilemodules. Therefore, a complete redesign of these Tilemodules is necessary to contain multiple HGCROCs, ALDO chips, other electronics and the SiPMs in spaces closer together. This inevitably results in more time and labour requirements.

In conclusion, the changes proposed to the detector layout would improve the SNR of the detector at end-of-life, but implementing these changes would increase the overall costs, power, time and labour requirements. Therefore, a third layout scenario was investigated to minimise these increases.

7.3.4 Layout Scenario 3

A layout scenario 3 proposes a more realistic solution to improve performance, considering costs, power, time and labour constraints. The proposal would be to use:

- a higher granularity in J and K Tilemodules as proposed in layout scenario 2,
- $3 \times 3\,\mathrm{mm}^2$ SiPMs on every channel of A and C Tilemodules,
- $3 \times 3\,\mathrm{mm}^2$ SiPMs only on the bottom four rings of all B Tilemodules,
- injection-moulded tiles on layers 43 and above for D, E and G Tilemodules.

The resulting SNR scenario after $\mathcal{L}_{int} = 3600\,\mathrm{fb}^{-1}$ is shown in fig. 7.11. The changes to the number of channels and the material area are given in table 7.3. This scenario is much more cost-effective but has more areas where the SNR is below 3.

Due to the lesser number of $3 \times 3\,\mathrm{mm}^2$ SiPMs and cast tiles used, the changes suggested in layout scenario 3 are cheaper to produce than in layout scenario 2. Since all Tilemodules of a

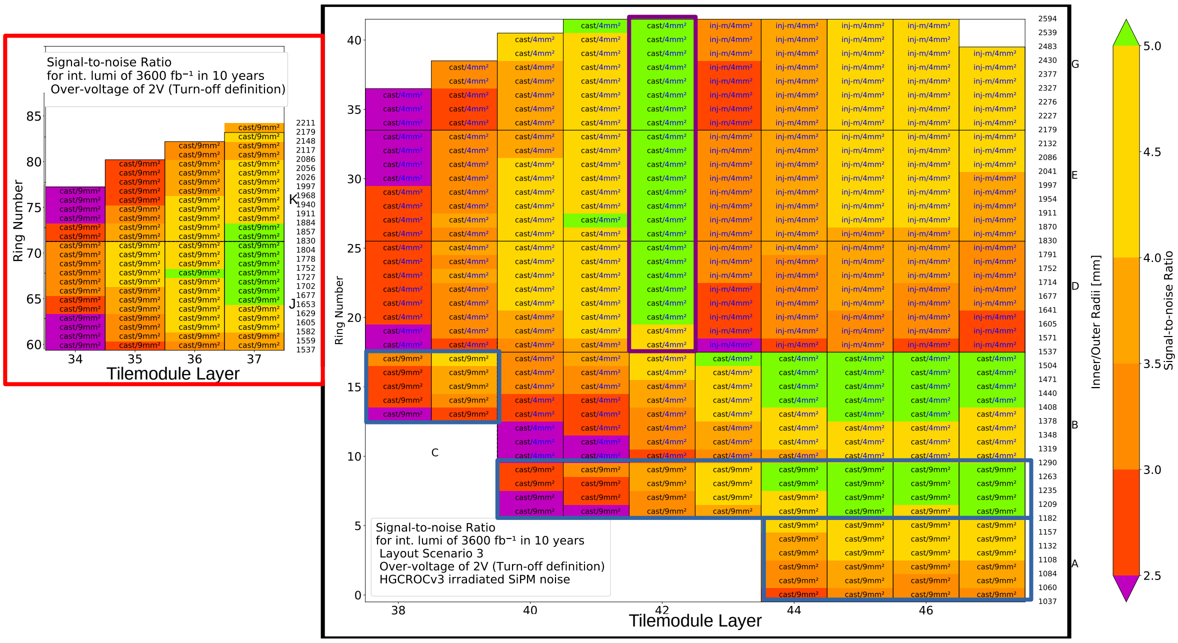

Figure 7.11: SNR from Layout scenario 3 after an integrated luminosity of 3600 fb^{-1} over a 10-year period. The red box marks areas with increased granularity. The black box marks the area where the granularity was not changed. The blue boxes show the areas where 3 × 3 mm² SiPMs replace 2 × 2 mm² SiPMs. The purple box shows the area where cast tiles replace injection moulded tiles. All these changes are with respect to the default scenario shown in fig. 7.8.

Table 7.3: Number of SiPMs, scintillator tiles and total area of scintillator material needed to produce the HGCAL scintillator section for both end-caps under the proposed layout scenarios.

	Default Layout	**Layout 1**	**Layout 2**	**Layout 3**
3 × 3 mm² **SiPMs**	33 408	84 672	126 432	113 184
2 × 2 mm² **SiPMs**	206 784	155 520	155 520	168 768
Total number of SiPMs	**240 192**	**240 192**	**281 952**	**281 952**
Injection-moulded tiles	81 792	40 320	40 320	67 968
Injection-moulded area	1 594 723 cm²	779 876 cm²	779 876 cm²	1 323 107 cm²
Cast tiles	158 400	199 872	241 632	213 984
Cast area	2 075 014 cm²	2 889 861 cm²	2 887 530 cm²	2 344 298 cm²
Total number of tiles	**240 192**	**240 192**	**281 952**	**281 952**

single type have the same layout, this scenario does not produce new Tilemodule types, which would save production time and is less labour-intensive than layout scenario 2.

Instead, layout scenario 3 proposes to use 3 × 3 mm² SiPMs in the bottom four rings in all B Tilemodules. The B-type Tilemodules have up to 12 rings. The bottom four rings are powered by one HGCROC and ALDOv2 BV, and another HGCROC and ALDOv2 BV power the top eight rings. This is because the bottom four rings will receive the highest radiation dose on the Tilemodule; these SiPMs will draw the largest currents. Using 3 × 3 mm² SiPMs in the bottom four rings will result in a much smaller increase in the material cost compared to layout scenario 2. The only redesign needed on the B-type Tilemodules is replacing the pad sizes so that the 3 × 3 mm² can be placed.

Another proposal could be to replace the bottom six rings of the B-type Tilemodules with

3 × 3 mm² SiPMs. However, this would mean that the HGCROC reading out the SiPMs on the top eight rings will need to read out both sizes of SiPMs. As mentioned in section 4.3.3.1, it is very likely that two different sets of shaper parameters will need to be used for the two different SiPM sizes. The shaper parameters are set globally per HGCROC half, which will readout SiPMs from four rings. Given this constraint, either the eight bottom rings need to be replaced with 3 × 3 mm² SiPMs or the 3 × 3 mm² SiPMs must be limited to just the bottom four rings. For convenience, the current B12 Tilemdoule prototype design is shown in fig. 7.12.

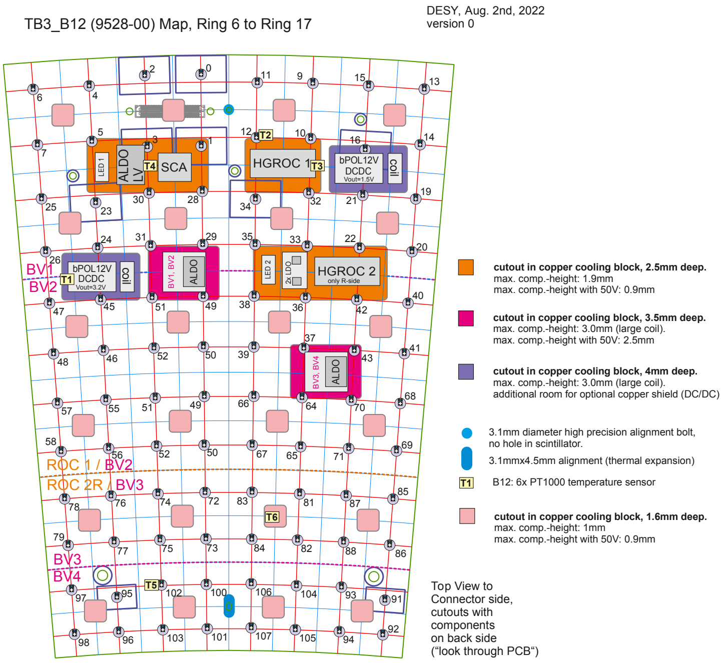
TB3_B12 (9528-00) Map, Ring 6 to Ring 17
DESY, Aug. 2nd, 2022
version 0
ALDO LV
SCA
LED 1
T4
HGROC 1
T2
T3
bPOL12V DCDC Vout=1.5V
coil
BV1
BV2
bPOL12V DCDC Vout=3.2V
T1
BV1, BV2
ALDO
LED 2
2x LDO
HGROC 2 only R-side
BV3, BV4
ALDO
ROC 1 / BV2
ROC 2R / BV3
T6
BV3
BV4
T5
cutout in copper cooling block, 2.5mm deep.
max. comp.-height: 1.9mm
max. comp.-height with 50V: 0.9mm
cutout in copper cooling block, 3.5mm deep.
max. comp.-height: 3.0mm (large coil).
max. comp.-height with 50V: 2.5mm
cutout in copper cooling block, 4mm deep.
max. comp.-height: 3.0mm (large coil).
additional room for optional copper shield (DC/DC)
3.1mm diameter high precision alignment bolt, no hole in scintillator.
3.1mmx4.5mm alignment (thermal expansion)
T1 B12: 6x PT1000 temperature sensor
cutout in copper cooling block, 1.6mm deep.
max. comp.-height: 1mm
max. comp.-height with 50V: 0.9mm
Top View to Connector side, cutouts with components on back side ("look through PCB")

Figure 7.12: The floorplan of the B12 Tilemodule prototype (TBv3 generation tileboard). BV1 and BV2 are the two high-voltage lines of the first high-voltage ALDOv2 ASIC, and BV3 and BV4 are the two high-voltage lines of the second high-voltage ALDOv2 ASIC. The top eight rings are read out by the first HGCROC (ROC1), and the bottom four rings are read out by the second HGCROC (ROC2) [84].

It would also be possible to use one HGCROC to readout SiPMs in the bottom six rows and the second HGCROC to readout the SiPMs in the top six rows. However, this would also require redesigning the B-type Tilemodule, which would be labour-intensive and time-consuming. If 3 × 3 mm² SiPMs are used in the bottom eight rings of the B-type Tilemodules, this would require even a more significant number of 3 × 3 mm² SiPMs than what was proposed with the layout scenario 2.

Therefore, to limit the increase in cost, the best option would be to limit the use of 3 × 3 mm² SiPMs to the bottom four rings of the B-type Tilemodules.

However, under this proposal, areas in the detector will have an SNR<3. This includes layers 38 and rings 10, 11 and 12 of the B-type Tilemodules in layers 40 and 41. However, this is a more conservative scenario to keep a safety margin in case of a higher fluence and dose rate, larger noise or smaller light yields. The SNR also improves after every YETS mostly due to the annealing of the scintillators. The SNR after annealing and after $\mathcal{L}_{int} = 3600\,\text{fb}^{-1}$ is presented in fig. 7.13. To illustrate how SNR changes with $\mathcal{L}_{int}$, the trend for the five worst performing channels are shown in fig. 7.14(a). Two of these channels are on the front four layers with higher granularity, and three are in the latter part of the detector with the default granularity.

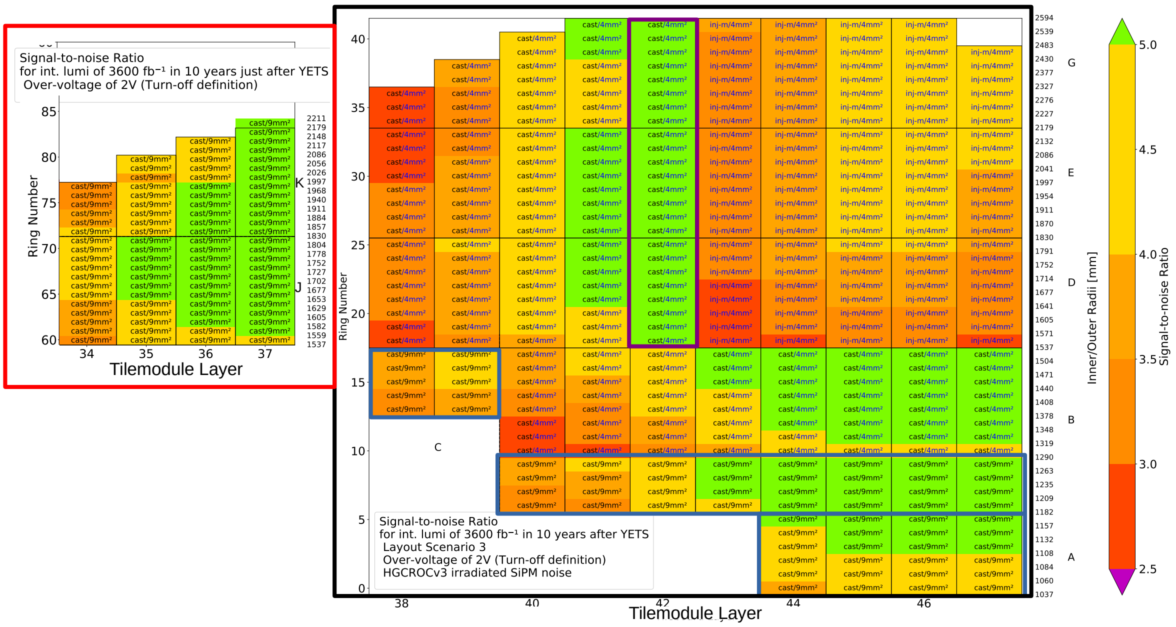

Figure 7.13: SNR from layout scenario 3 just after YETS, after $\mathcal{L}_{int} = 3600\,\text{fb}^{-1}$. The blue boxes show the areas where $3 \times 3\,\text{mm}^2$ SiPMs replace $2 \times 2\,\text{mm}^2$ SiPMs. The purple box shows the area where injection-moulded tiles replace cast tiles. The red box marks the area with increased granularity. The black box marks the area where the granularity was not changed. All these changes are with respect to the default scenario shown in fig. 7.8.

Figure 7.14(a) shows that the scintillators' annealing during YETS is vital to maintain an SNR>3. The SNR will fall below three due to temporary damage of the scintillator in the latter stages, but the SNR will recover after the scheduled YETS to above 3. The projections also show that, excluding a few months, the detector will maintain an SNR>3 until its design luminosity of $\mathcal{L}_{int} = 3000\,\text{fb}^{-1}$.

Figure 7.14(b) also shows the noise of the best performing SiPM-on-tile in each Tilemodule type. A noise of less than 1 p.e. is needed in order to separate the SPS peaks to monitor the SiPM gain. This means that the gain calibration is only possible in the first few months of operation for most of the Tilemodules. After this point, measuring the gain and the light yield will be impossible. However, since studies have shown that the gain does not change until at least a neutron fluence of $2 \times 10^{12}\,\text{n}_{\text{eq}}/\text{cm}^2$, an initial calibration of light yield for MIPs is sufficient to estimate the light yield for MIPs for many years. Once the gain calibration is impossible, the MIP signals will be used to calibrate the SiPM-on-tiles.

7.3.5 Over-Voltage Optimisation

Currently, it is foreseen that the HGCAL scintillator section will operate at an over-voltage of 2 V measured with respect to the turn-off voltage (see section 2.4.2.8). However, measurements from partnering institutions [74] have shown that the best SNR is obtained if the detector is operated at an over-voltage between 1.2 V and 1.8 V (or 0.85 V and 1.45 V with respect to relative derivative

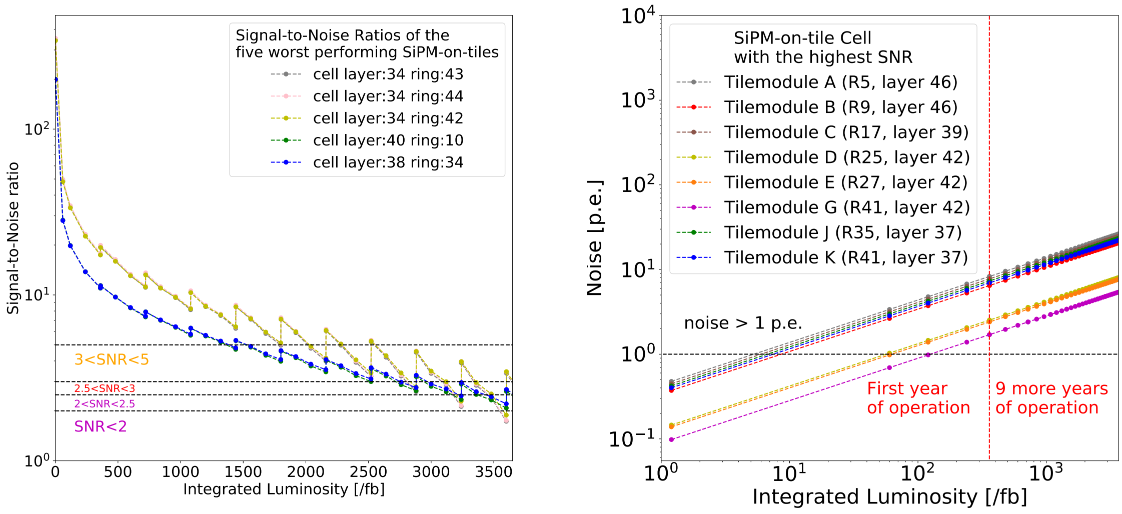

(a) (b)

Figure 7.14: (a) shows the SNR as a function of $\mathcal{L}_{int}$ for the five worst performing SiPM-on-tile cells while (b) shows the noise as a function of $\mathcal{L}_{int}$ for the tile with the best SNR of each Tilemodule type. These numbers were generated for layout scenario 3, assuming the detector collects $\mathcal{L}_{int} = 3600\,\mathrm{fb}^{-1}$ in 10 years.

voltage). This estimate was validated by calculating the SNR for $\mathcal{L}_{int} = 3000\,\mathrm{fb}^{-1}$ for varying over-voltages as shown in fig. 7.15. The SNR calculated for a single SiPM-on-tile channel using the PDE curves measured by HPK and CMS collaboration is shown in fig. 7.15. Since HPK measures their PDE for over-voltages down to 3 V, no data is available to estimate the behaviour of the PDE curve below an over-voltage of 3 V. Therefore, a large extrapolation uncertainty exists when estimating the PDE at lower over-voltages. This is why the large deviations between the SNR are calculated at lower over-voltages. However, the two curves agree within 5 % of each other above 1.2 V.

Based on these curves, the best SNR is obtained at an over-voltage of 1.4 V (with respect to the turn-off voltage and using the curve measured by the CMS collaboration). However, lower over-voltages are more sensitive to temperature changes, and therefore, as a compromise, the best operating over-voltage would be 1.65 V. The PDE at 1.65 V is only 2 % lower than the PDE at 1.4 V. The SNR of the detector after integrating a luminosity of $3600\,\mathrm{fb}^{-1}$ operating at an over-voltage of 1.65 V is shown fig. 7.16. As evident from both fig. 7.16 and fig. 7.15, a 10 % improvement in SNR can be expected if the detector is operated at an over-voltage of 1.65 V instead of at 2 V towards the end-of-life.

This option may also be necessary due to current limitations in using the $3 \times 3\,\mathrm{mm}^2$ SiPMs in the most irradiated areas. Figure 7.17(a) shows the leakage current drawn by each SiPM-on-tile channel operating at an over-voltage of 2 V in the ring and layer after $\mathcal{L}_{int} = 3600\,\mathrm{fb}^{-1}$. This figure shows that the most irradiated $3 \times 3\,\mathrm{mm}^2$ SiPMs operating at an over-voltage of 2 V will draw more than a 1.2 mA leakage current which is the highest current which the HGCROC can provide. This would be fine if the SiPMs were operated at an over-voltage of 1.65 V as shown in fig. 7.17(b). Since the leakage current scales exponentially with over-voltage (see fig. 6.11), a reduction to an over-voltage of 1.65 V will allow the continuous operation of the SiPMs without

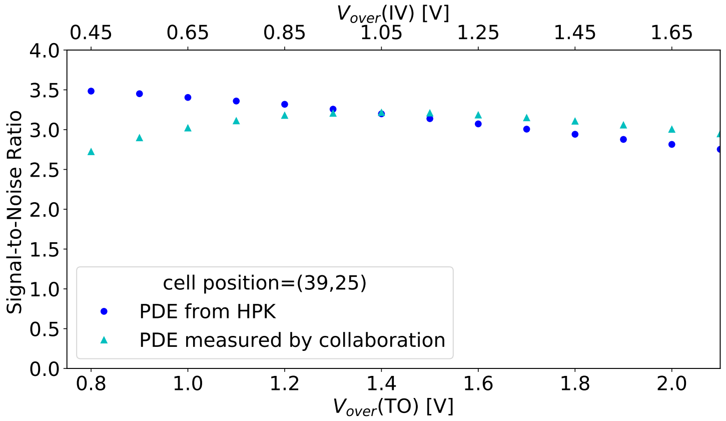

Figure 7.15: SNR calculated for the same SiPM-on-tile cell using the PDE curves obtained from HPK and the CMS collaboration [74] as a function of over-voltage. The over-voltage relative to the turn-off definition is given as OV_TO, and the over-voltage relative to the relative-derivative definition is given as OV_IV. See section 2.4.2.8 for the difference between the two breakdown voltage definitions. The SNR is calculated for $\mathcal{L}_{int} = 3000\,\text{fb}^{-1}$ for layout scenario 1.

reaching saturation or current limits.

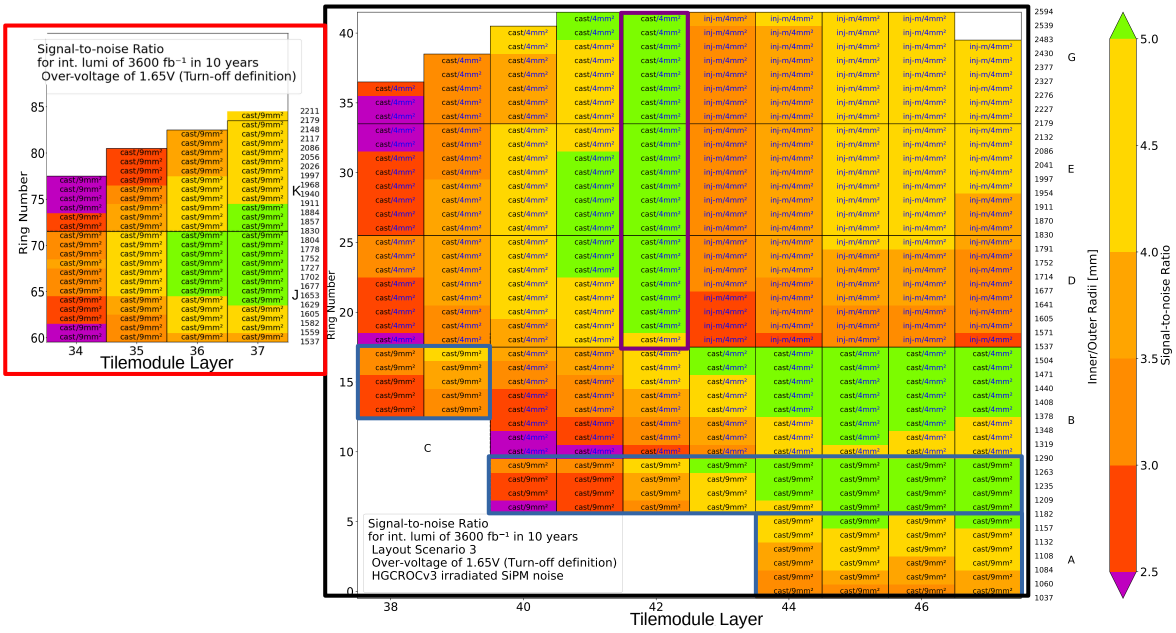

Figure 7.16: SNR operating at an over-voltage of 1.65 V employing layout scenario 3 after $\mathcal{L}_{int} = 3600\,\text{fb}^{-1}$ over a 10-year period. The blue boxes show the areas where 3×3 mm² SiPMs replace 2×2 mm² SiPMs. The purple box shows where injection moulded tiles replace cast tiles. The red box mark the area where the granularity was increased. The black box marks the area where the granularity was not changed. All these changes are with respect to the default scenario shown in fig. 7.8.

However, operating at lower over-voltages has consequences for the detector performance. The breakdown voltage of the SiPMs manufactured by HPK may deviate by a maximum of 100 mV with respect to each other. HPK will only provide an average breakdown voltage of the SiPMs on a reel containing several hundred SiPMs. This means that the breakdown voltage of the vast majority of the SiPMs will be unknown. The bias voltage will be set globally to all the SiPMs on the Tilemodule at the experiment. The SiPM-to-SiPM bias voltage adjustments can only be made if the breakdown voltage is known. This means that the over-voltage could vary by up to 100 mV from SiPM-to-SiPM if the breakdown voltage cannot be determined for all SiPMs. A method proposed to measure the breakdown voltage using Tilemodules and its electronics is discussed in appendix A. However, the proposed method has yet to be investigated thoroughly and remains only a possible solution as of writing this thesis.

Furthermore, though the temperature will generally be maintained at $-30\,^{\circ}\mathrm{C}$, the temperature can deviate by about 2 °C to 3 °C depending on the cooling. Since the breakdown voltage of SiPMs vary with a 37.5 mV/°C coefficient, a 3 °C difference in temperature introduces a further uncertainty of 112.5 mV. Typically, the temperature deviations will be measured using the on-board temperature sensors. However, only two of these sensors monitor the temperature of two SiPMs. Therefore, there is an uncertainty in the temperature between SiPMs. If one assumes that the variation in temperature between different SiPMs is 3 °C in addition to the breakdown voltage uncertainties discussed previously, the real over-voltage supplied to the SiPMs could deviate by up to about 220 mV between SiPMs.

This means that for a globally set target over-voltage of 2 V, the actual over-voltage under which the SiPMs operate could deviate by up to 11 %. Since the SiPM gain has a linear dependence with over-voltage, the gain will change by 11 %. If the globally set target over-voltage is 1.65 V, the actual over-voltage under which the SiPMs operate could deviate by up to 13.3 %. This will change the gain by 13.3 %. Since the gain will not be measurable at this point due to the large noise, this change in gain will be a source of uncertainty. As the numbers show, as the over-voltage reduces, the percentage uncertainty increases.

This variation in gain also shows the importance of regular calibration using MIPs. These uncertainties can be reduced by calibrating the detector performance to the MIP signal. However, it is important to maintain an SNR>3 to calibrate the detector regularly.

7.3.6 Layout Scenario 4

In layout scenario 4, a more power-consuming and expensive scenario is proposed, which guarantees a good performance while limiting labour and time constraints. This scenario proposes the exclusive use of $3 \times 3\,\mathrm{mm}^2$ SiPMs in the detector while using higher granularity in J and K Tilemodules as proposed in layout scenario 2. Shown in fig. 7.18 is the expected SNR after $\mathcal{L}_{int} = 3600\,\mathrm{fb}^{-1}$ operating at an over-voltage of 2 V.

The exclusive use of $3 \times 3\,\mathrm{mm}^2$ SiPMs will increase the cost of the detector. Negotiations are ongoing to reduce the cost due to the bulk size of the order supporting a scenario like this.

The use of $3 \times 3\,\mathrm{mm}^2$ SiPMs will also trigger the current limits set primarily by the HGCROC on the Tilemodules if operated at 2 V over-voltage until the detector end-of-life. Section 7.3.6 shows the expected current at end-of-life if operated at 2 V over-voltage. However, lowering the over-voltage to about 1.65 V towards the end-of-life of the detector will prevent exceeding the current limit. The leakage current at end-of-life where the SiPMs are operated at an over-voltage of 1.65 V is shown in section 7.3.6.

Under this layout, similar to layout scenarios 2 and 3, only the B, J and K Tilemodules will require two high-voltage ALDOv2 chips and two HGCROCs. This is because the other

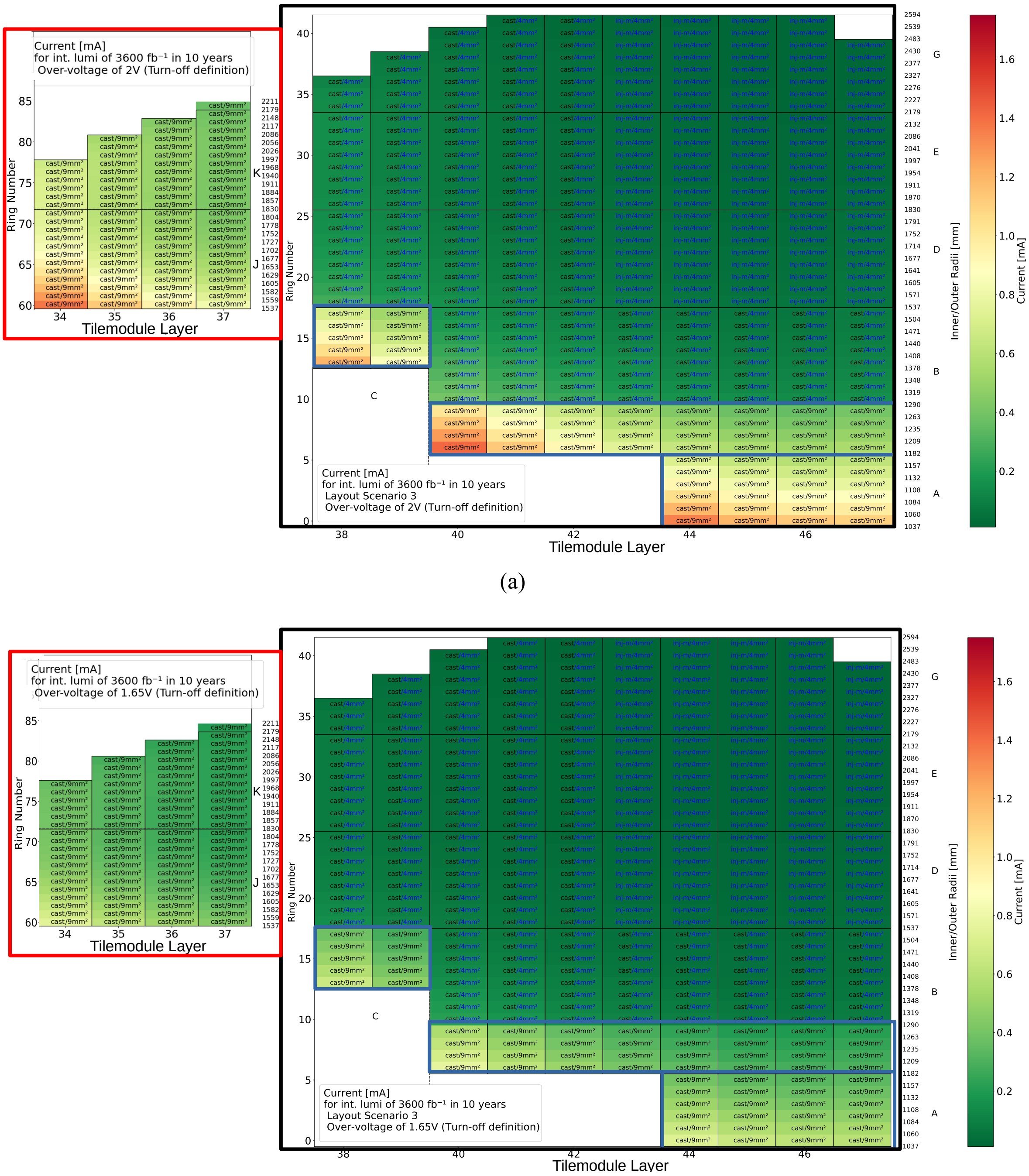

(a)

(b)

Figure 7.17: Leakage current expected from each SiPM-on-tile channel after an integrated luminosity of 3600 fb^{-1} over ten years employing layout scenario 3. (a) is if the SiPMs are operated at an over-voltage of 2 V. (b) is if the SiPMs are operated at an over-voltage of 1.65 V. The blue boxes show the areas where 3 × 3 mm² SiPMs replace 2 × 2 mm² SiPMs. The red box mark the area the granularity increased. The black box marks the area where the granularity was not changed. All these changes are with respect to the default scenario shown in fig. 7.8.

Tilemodules will be within the 50 mV current limit. This means that no modifications to the Tilemodule electronics are required apart from replacing the footprints of the 2 × 2 mm² SiPMs with 3 × 3 mm² SiPMs in comparison to scenarios 2 and 3. Therefore, the additional time and labour required for this change is minimal.

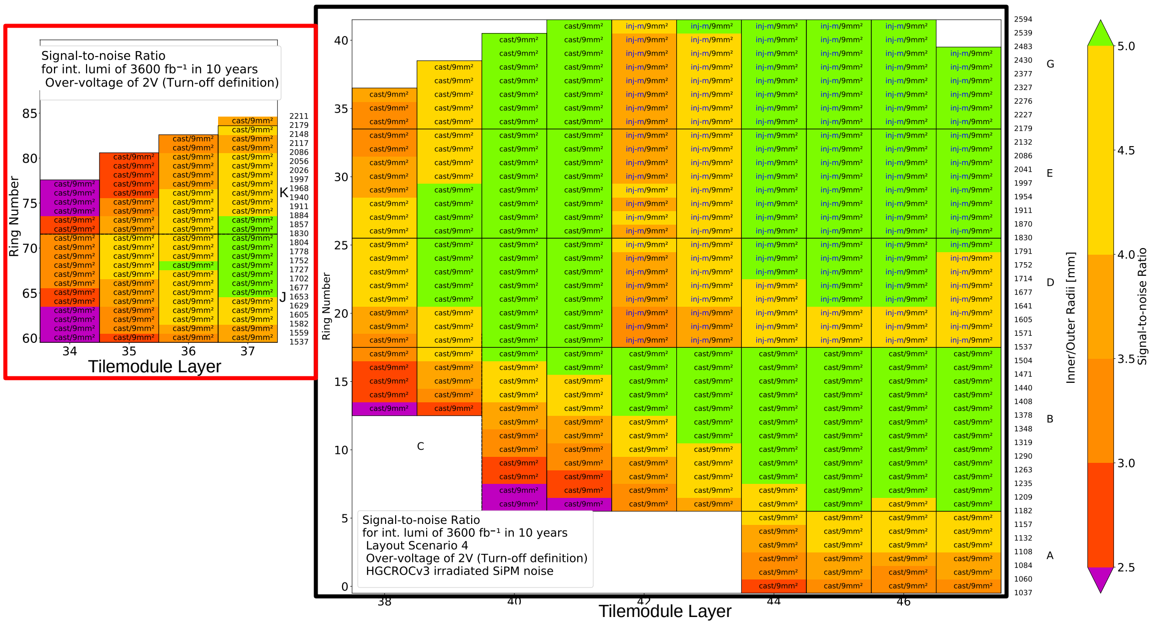

Figure 7.18: SNR from layout scenario 4 after an integrated luminosity of 3600 fb^{-1} over a 10-year period operating at an over-voltage of 2 V. All SiPMs used are 3 × 3 mm² in area. The red box mark the area the granularity increased. The black box marks the area where the granularity was not changed compared to the default scenario shown in fig. 7.8.

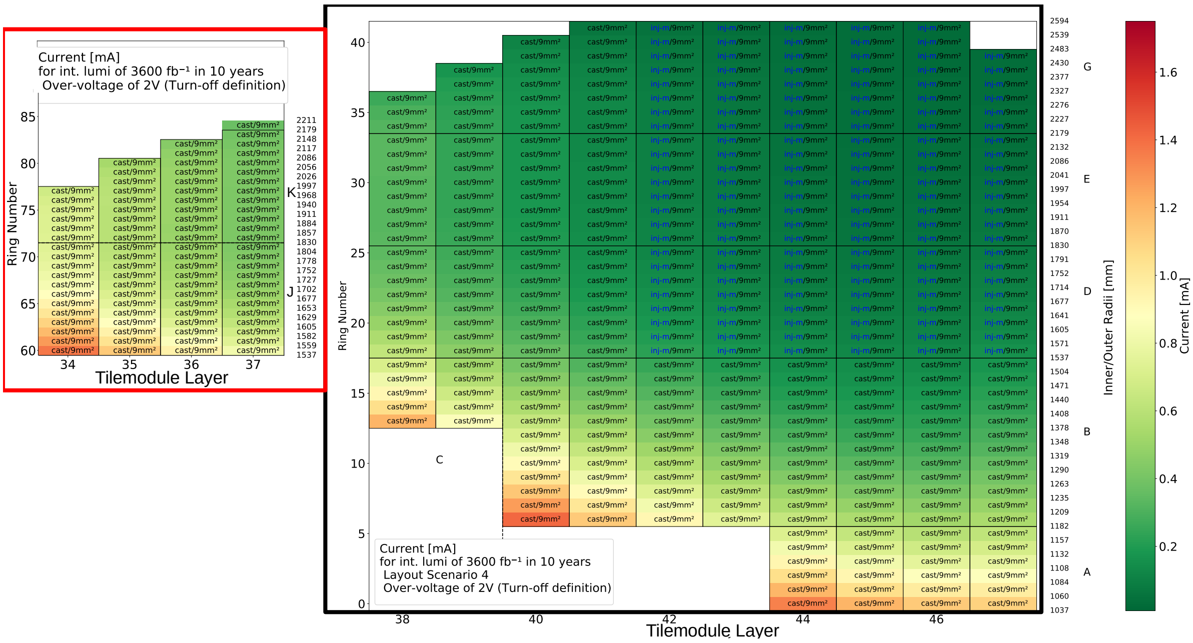

Figure 7.19: leakage current expected from each SiPM-on-tile channel after $\mathcal{L}_{int} = 3600\,\mathrm{fb}^{-1}$ over ten years employing layout scenario 4 if the SiPMs are operated at an over-voltage of 2 V. All SiPMs used are 3 × 3 mm² in area. The red box mark the area the granularity increased. The black box marks the area where the granularity was not changed compared to the default scenario shown in fig. 7.8.

Shown in fig. 7.21 is the expected SNR after $\mathcal{L}_{int} = 3600\,\mathrm{fb}^{-1}$ operating at an over-voltage of 1.65 V. Under these conditions, only layer 34 will consist of cells with SNR<3, with one

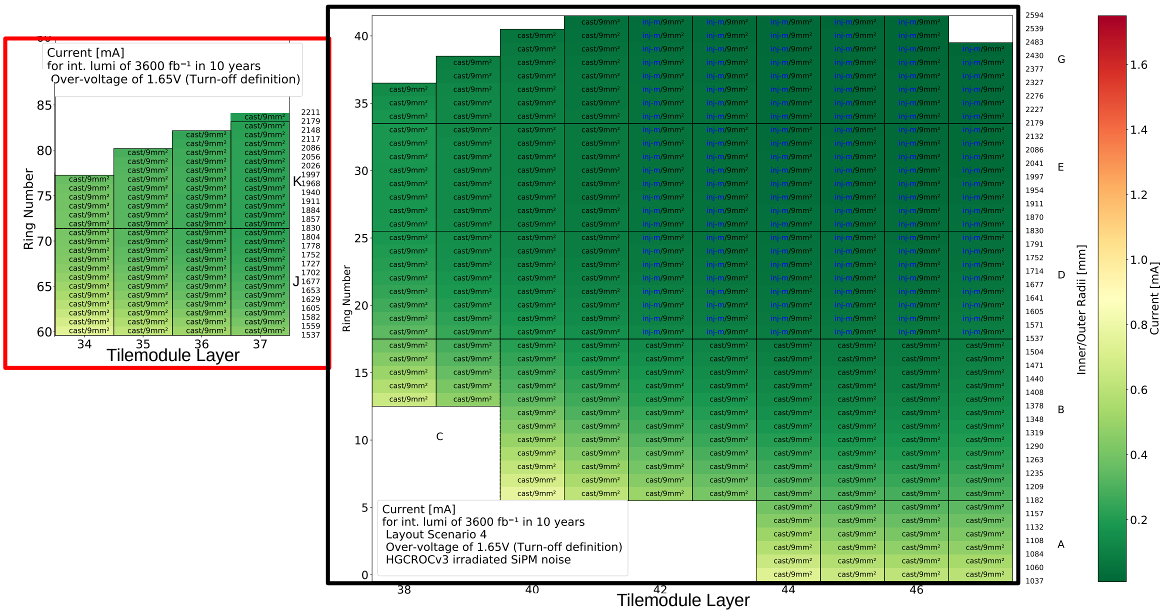

Figure 7.20: leakage current expected from each SiPM-on-tile channel after $\mathcal{L}_{int} = 3600\,\text{fb}^{-1}$ over ten years employing layout scenario 4 if the SiPMs are operated at an over-voltage of 1.65 V. All SiPMs used are 3 × 3 mm² in area. The red box mark the area the granularity increased. The black box marks the area where the granularity was not changed compared to the default scenario shown in fig. 7.8.

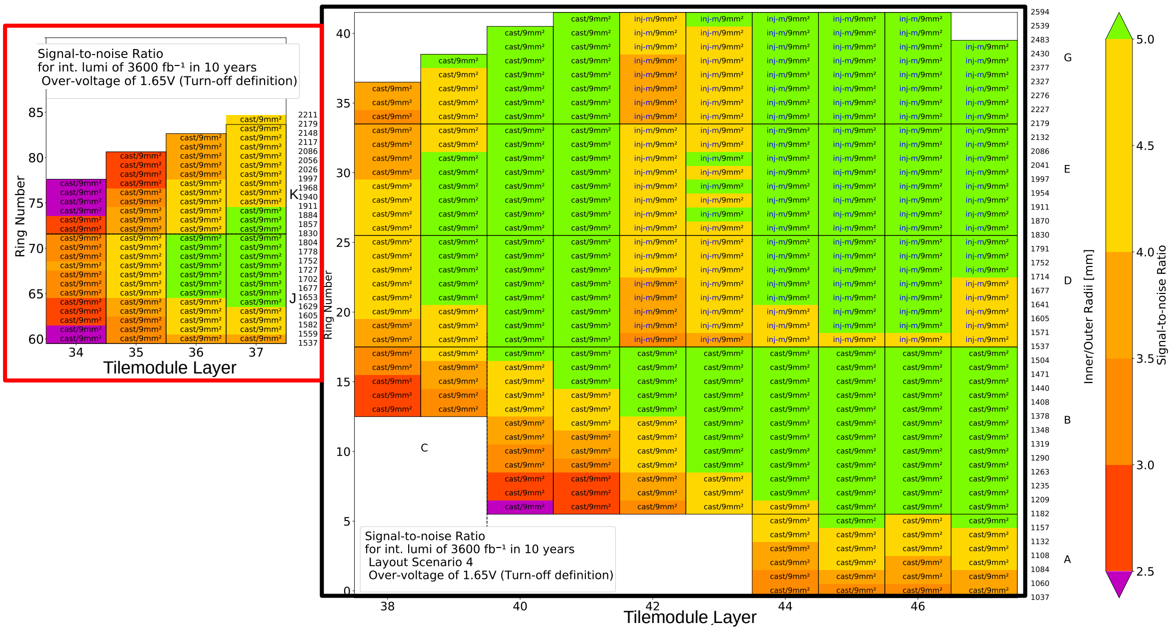

Figure 7.21: SNR from layout scenario 4 after an integrated luminosity of $3600\,\text{fb}^{-1}$ over a 10-year period operating at an over-voltage of 1.65 V. All SiPMs used are 3 × 3 mm² in area. The red box mark the area the granularity increased. The black box marks the area where the granularity was not changed compared to the default scenario shown in fig. 7.8.

more exception in layer 45. This layout produces the best SNR out of all the layouts discussed. However, this scenario will be prone to the same uncertainties due to temperature and over-voltage variations discussed previously.

7.4 Optimised, Realistic Final Layout and Configuration for Maximal SNR

In summary, taking all constraints, including current requirements, time, costs and labour constraints, into account, layout scenario 3 with SiPMs operated at an over-voltage of 1.65 V provides the most reasonable SNR after $\mathcal{L}_{int} = 3600\,\mathrm{fb}^{-1}$. In order to limit the uncertainties in breakdown voltage, it would be recommended to operate the detector at an over-voltage of 2 V or higher at the detector's start-of-life and decrease it down gradually over time to 1.65 V when the SNR drops below three. The current limits are reached by the most irradiated 3×3 mm² SiPMs.

Since the performance of the detector is quite good at the start-of-life, it would be recommended to run a few calibrations runs at much higher over-voltages (e.g., at 4 V over-voltage) to reduce the uncertainties due to breakdown voltage and temperature differences between SiPM-on-tiles. This would provide a solid baseline for calibration.

As mentioned in section 6.2, the irradiated SiPMs on HGCROCv3 have a 15 % elevated noise level in comparison to the exact SiPMs readout with HGCROCv2. If one assumes that this additional noise can be reduced, the SNR will improve by up to 15 %.

Finally, if the nominal $\mathcal{L}_{int} = 3000\,\mathrm{fb}^{-1}$ over the ten years of HL-LHC operation is not surpassed, this, in addition to the improved HGCROC noise will make the detector perform remarkably well under layout scenario 3 with only a few cells having an SNR<3 at end-of-life as shown in fig. 7.22. This will further improve if the over-voltage is reduced to 1.65 V over time.

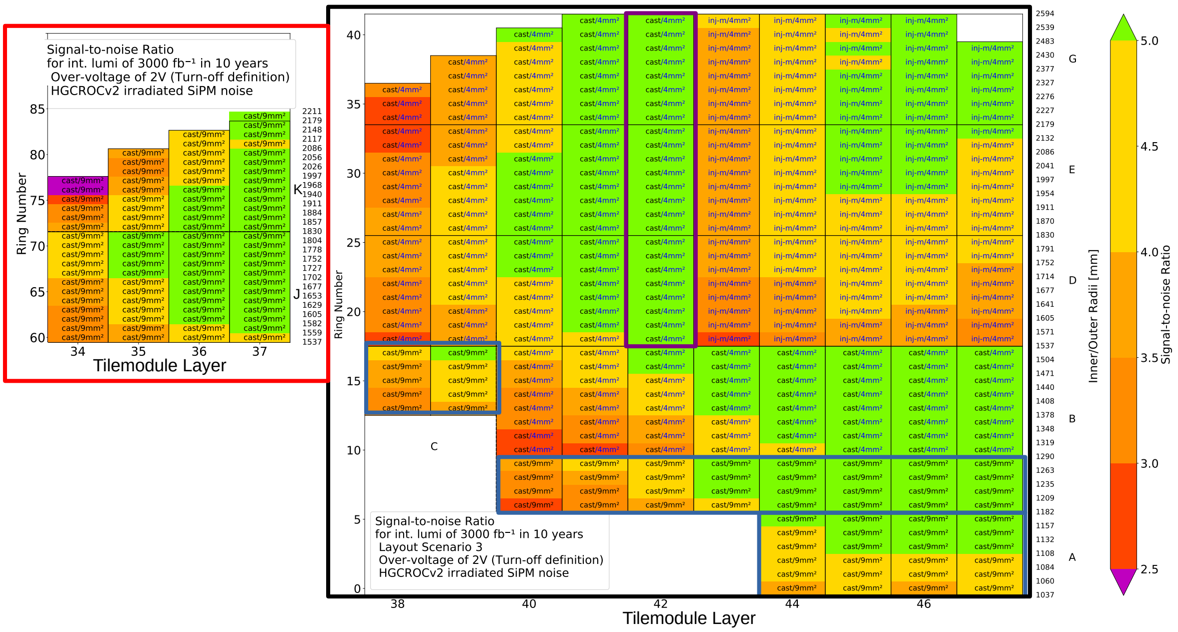

Figure 7.22: SNR after $\mathcal{L}_{int} = 3000\,\mathrm{fb}^{-1}$ over ten years operating at an over-voltage of 2 V using layout scenario 3 with the noise of irradiated SiPMs readout using HGCROCv2. The blue boxes show the areas where 3 × 3 mm² SiPMs replace 2 × 2 mm² SiPMs. The purple box shows the area where injection moulded tiles replace cast tiles. The red box mark the area where the granularity was increased. The black box marks the area where the granularity was not changed. All these changes are with respect to the default scenario shown in fig. 7.8.

Chapter 8

Conclusions and Outlook

The high-luminosity phase of the Large Hadron Collider (HL-LHC) will collide particles at unprecedented luminosities to probe the Standard Model with even higher precision. However, increasing the luminosity increases event pileup and radiation significantly. Therefore, many detectors, including the end-caps of the current CMS detector, will be replaced. A high granularity calorimeter comprising of highly granular silicon sensors (0.6 cm² and 1.2 cm² cell size) and scintillator tiles (4 cm² to 30 cm² areas) will replace the current CMS calorimeter end-caps for the HL-LHC phase. The area covered by the scintillators was chosen such that a signal-to-noise ratio (SNR)>3 can be maintained throughout the detector lifetime up to an integrated luminosity of 3000 fb^{-1}.

The scintillator section of the CMS HGCAL upgrade is based on the SiPM-on-tile technology, where a scintillator tile wrapped in a reflective foil is placed on a silicon photomultiplier (SiPM). The original layout of the Tilemodules holds up to 94 such SiPM-on-tile cells read out by up to two HGCROCs. The prime objective of this thesis was to measure the performance of such SiPM-on-tiles on Tilemodule prototypes and predict their SNR at the detector end-of-life.

The signal performance of the SiPM-on-tiles is measured in terms of light yield. The light yield is the most probable number of photons detected by the SiPM from minimum ionizing particles (MIPs) traversing the scintillator tile in the perpendicular direction. A methodology for obtaining light yields from SiPM-on-tiles on HGCAL Tilemodules was developed and presented in this thesis. This involved measuring the most probable charge deposition (MIP maximum) using 3 GeV electron beam at the DESY-II test beam facility. The SiPM gain was measured using the on-board low-intensity LED system under the same conditions, HGCROC settings and environment. The ratio of the two quantities calculates the light yield.

The light yield is independent of the on-board electronics. This was verified using many reproducibility studies, which involved remeasuring the same tiles and SiPMs on multiple Tilemodule prototypes and different HGCROC generations in the context of this thesis. Furthermore, beam tests at the CERN SPS with muons of 120 GeV energies validated the hypothesis that 3 GeV electrons produce signals very similar to MIPs. The light yield obtained from the Tilemodules at beam tests was consistent with those obtained using a ^{90}Sr source with different readout electronics, confirming that light yield is a purely optical observable.

However, due to this optical nature of light yield, the existence of a white paint around the SiPMs increased the light yield by 10 % compared to the those without this white paint. The white paint reflects the light back to the scintillator, which would otherwise pass through the

PCB, leading to more light losses. Therefore, it is recommended that all future Tilemodules, including the final production Tilemodules, incorporate the white paint around the SiPMs. The light yields from SiPM-on-tiles on Tilemodules that do not have this white paint have been increased by 10 % to compare with SiPM-on-tiles on Tilemodules, which has the white paint.

Analysis of the beam test results shows that the light yield scales linearly with increasing SiPM photosensitive area and inversely with the square root of the tile's area. Since light yield is proportional to the SiPM's photon detection efficiency (PDE), the PDE's relationship with over-voltage is used to rescale the light yield to an over-voltage (V_{over}) of choice.

Several generations of tiles were tested in beam tests held within the past four years in the context of this thesis. The best-cast and injection-moulded tiles were to be used in the final detector. The BC-412 cast tile machined in the US by North Illinois University (NIU) performs best and will be used in the final detector. However, due to geopolitical considerations, injection-moulded tiles will also be produced in the US. Nonetheless, the performance of the injection-moulded tiles produced at the Fermi National Accelerator Laboratory (FNAL) are within 10 % of the best measured injection-moulded tiles which were produced in Institute for High Energy Physics (IHEP), Russia. The best cast tiles perform more than two times better than the best injection-moulded tiles. However, cast tiles are more expensive and time-consuming to produce. Therefore, cast tiles will be limited to areas where a large radiation damage is expected, to facilitate an SNR>3 at the detector end-of-life.

A very similar methodology developed to acquire and analyse data from non-irradiated SiPMs was developed for irradiated SiPMs. As SiPMs irradiated to a neutron fluence of $2 \times 10^{12}\ \mathrm{n_{eq}/cm^2}$ operated at room temperature exhibit roughly the same leakage current as the SiPMs irradiated to the highest expected neutron fluence at detector end-of-life, a beam test was conducted at room temperature using devices irradiated to a neutron fluence of $2 \times 10^{12}\ \mathrm{n_{eq}/cm^2}$. The so-called relative-derivative method measured the breakdown voltages from these and non-irradiated devices. The measured breakdown voltages were then used to compare the light yields between the irradiated and non-irradiated SiPMs coupled to the same scintillator tiles. Both irradiated and non-irradiated SiPMs produced similar light yields under the assumption that the gain did not change at a neutron fluence of $2 \times 10^{12}\ \mathrm{n_{eq}/cm^2}$.

As the leakage current of SiPMs increases linearly with radiation fluence, and as the SiPM noise increases as a function of current, an increase in fluence increases the SiPM noise. The SiPM and electronic noise of irradiated SiPMs on Tilemodules were measured while simultaneously measuring the leakage current passing through the SiPM. These measurements were conducted using two setups developed in the context of this thesis. The first setup varied the leakage current by varying the temperature, and the second setup mimicked the leakage current by illuminating the SiPM with light. Results from both setups showed very similar behaviour between the current and SiPM noise. Furthermore, SiPMs of different sizes read out with an HGCROC of the same generation and similar irradiation levels showed similar noise-leakage current relationships.

However, SiPMs readout with HGCROCv3 reported a 15 % larger noise than the same SiPMs readout with HGCROCv2 for the same leakage current levels. The reasons for this are not well understood. The noise may return to the levels measured with the HGCROCv2 with the final HGCROC version. Furthermore, non-irradiated SiPMs also reported a 10 % higher noise than irradiated SiPMs for the same leakage current. The exact reason for the differences needs to be better understood, and further investigations may be necessary.

The final study estimated the signal-to-noise ratio at the end of the detector lifetime, starting with the default layout. This involved applying the light yield gathered from SiPM-on-tiles on Tilemodule prototypes, their associated noise at a given fluence and integrated luminosity, both measured and calculated within the context of this thesis. The light degradation due to scintillator radiation damage was also modelled using studies conducted for HGCAL scintillators. The estimations were calculated at an integrated luminosity of $3600\,\mathrm{fb}^{-1}$ to include a safety margin due to various uncertainties. Despite using the tiles having the best light yield, the increased noise and scintillator damage at higher radiation lead to a significant number of channels having an SNR<3 after an integrated luminosity of $3600\,\mathrm{fb}^{-1}$ especially in regions closest to the interaction point and the beampipe.

The solution proposed was to change the default layout. Out of all the proposed layout scenarios, the most cost-effective scenario which can be implemented to achieve an SNR>3 for most SiPM-on-tiles with minimal changes to the layout (labelled layout scenario 3) suggested the use of $3 \times 3\,\mathrm{mm}^2$ SiPMs on the most exposed Tilemodules, cast tiles in one additional layer and increased granularity in the front four layers with SiPM-on-tile technology. These changes improved the SNR in most layouts, but few cells still exhibit SNR<3. Furthermore, the most irradiated $3 \times 3\,\mathrm{mm}^2$ SiPMs also reach the HGCROC current limit if operated at an over-voltage of 2 V. Therefore, it was proposed to reduce the over-voltage towards the end of life to about 1.65 V as the SNR is expected to be the highest at this over-voltage. However, temperature variations and breakdown voltage deviations between SiPMs will result in larger percentage uncertainties at lower over-voltages, resulting in larger light yield fluctuations. Therefore, it is recommended to lower the over-voltage only towards the end of life.

The layout to produce the best SNR at end-of-life is a layout containing only $3 \times 3\,\mathrm{mm}^2$ SiPMs and higher granularity of the J and K Tilemodules (labelled layout scenario 4), also operated towards the end-of-life at 1.65 V. However, this layout could be more expensive.

The noise used for these measurements is HGCROCv3, meaning if the noise levels improved, even better SNR could be obtained. Therefore, maintaining the SNR extrapolation model to include the latest information is recommended. Implementing this model in a Monte-Carlo simulation for shower analysis will also allow determining key parameters such as the energy resolution and calorimeter response using realistic uncertainties.

The production of all components, including the PCBs, SiPMs, scintillators, electronics such as the HGCROCs and all other components to assemble the Tilemodules is scheduled to early 2024. These Tilemodules will be assembled at DESY and FNAL. Many test stands have already been developed for quality assurance of every component on the Tilemodule, including the ^{90}Sr-based setup discussed in this thesis. Assembly of the final detector will proceed after these tests, and the detector is scheduled to be lowered into the CMS cavern in August 2027.

The technology discussed here is also suitable for future electron-positron colliders. It was initially developed for linear colliders such as the ILC but will also be suitable for circular colliders such as the proposed electron-positron Future Circular Collider (FCC-ee). FCC-ee proposes to collide electrons and positrons at bunch crossing frequencies similar to those at the LHC. The detectors will face much lower radiation environments than LHC and, therefore will not need to be cooled down to $-30\,^{\circ}\mathrm{C}$. The main challenge will be achieving the energy resolution required for the precision physics program planned for an electron-positron collider. However, given the experience with prototypes such as the AHCAL designed for ILC and the new experience gained with HGCAL, this challenge can be accomplished before the lifetime of FCC-ee.

Appendix A

Determination of the Pedestal Mean Dependance on Leakage Current

The production of an avalanche in any SPAD in the SiPM will result in the discharge of that SPAD, producing a current through the SiPM. The number of SPADs undergoing avalanches determines the current level. This could be due to dark counts or due to the capture of photons by the SPADs. This is extensively discussed in section 2.4.2. The HGCROC samples the signals of the SiPMs. This means the current passing through the SiPM is proportional to the signal. This is a property of SiPMs used throughout this thesis.

This property can also estimate the leakage current level passing through the SiPMs. For SiPMs with negligibly small DCR, the leakage current flow is negligibly small, and a random trigger would measure the pedestal position determined by the readout electronics. In the presence of non-negligible DCR, the non-negligible leakage current flow will increase the pedestal level. Therefore, the pedestal mean can measure the leakage current passing through SiPMs. This chapter investigates this property in irradiated SiPMs on the Tilemodule prototype boards read by an HGCROC. This chapter will also investigate if this property can be used to measure the breakdown voltage of the SiPMs without requiring hardware adjustments to the Tilemodule. As HPK does not provide the breakdown voltages of individual SiPMs in the reel and since the breakdown voltage changes with irradiation, establishing the relationship between current and pedestal mean would allow the monitoring of breakdown voltage (under the relative derivative definition) of all SiPMs onboard in real-time during the operation of the HGCAL detector to reduce the variations in over-voltage between channels.

A.1 Methodology and Setup

The test setup used is the same as described in section 5.1.2. A Keithley 2000 series multimeter [94] was connected in parallel to the safety resistor. This voltage drop is used to measure the current passing through the SiPMs. The HGCROC parameters are left unchanged throughout the experiment, so the pedestal determined by the readout electronics will not change. The mean of the pedestal was obtained from 1000 events collected using a random trigger.

The tileboard was placed inside a climate chamber, and the pedestal mean, and leakage current were measured for irradiated SiPMs simultaneously while varying the temperatures. The bias voltage remains the same for all temperatures. Since the breakdown voltage is temperature-dependent, the over-voltage also varies from point to point. Similar measurements of pedestal mean, and leakage currents were also performed at multiple bias voltages supplied to the SiPMs.

A.2 Results and Discussion

Many SiPM channels produce results as shown in fig. A.1. The pedestal mean increases linearly with an increase in current. This gradient and intercept remain relatively invariant for different temperatures and over-voltages. The same linear relationship was also seen for non-irradiated SiPMs whose current was increased by varying the light intensity using an LED as described in section 6.1.2. However, the position of the intercept varies from HGCROC channel-to-channel and tileboard-to-tileboard. This quantity depends on the HGCROC parameters that determine the pedestal position.

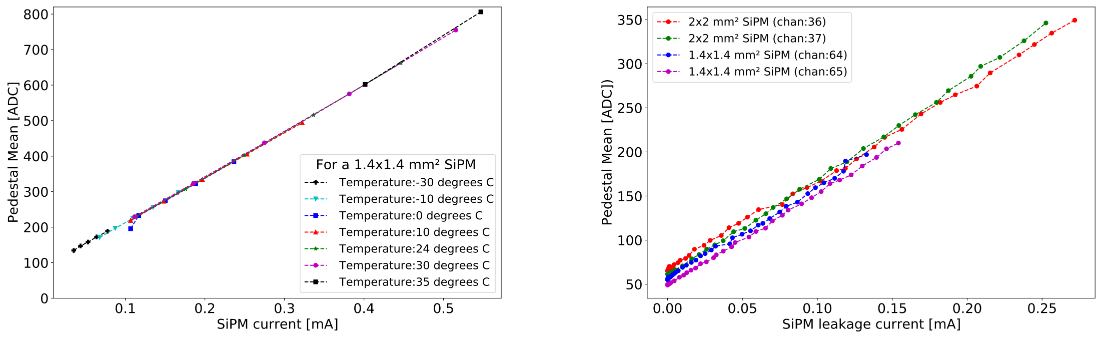

(a) (b)

Figure A.1: The relationship between pedestal mean and current passing through five irradiated SiPMs. (a) is the relationship for one channel at different temperatures at the same bias voltage supplied to the SiPM. (b) is the relationship for four different SiPMs of two different sizes.

However, few measurements show a non-linearity at very low SiPM currents, where the pedestal mean appears to increase much faster than the current passing through the SiPM as shown in fig. A.2. The reason for this inconsistency at low currents needs to be better understood.

Apart from the SiPM, the pedestal position heavily depends on the HGCROC parameters. The HGCROC have known issues stemming from pedestal fluctuations. One such observation is that the pedestal may fluctuate in one channel when a different channel has a high current passing through it: an electronically induced crosstalk [87].

A.3 Breakdown Voltage Determination using Pedestal Mean

As the pedestal mean increases linearly with the increase in current for some channels, the pedestal mean can be used to measure the breakdown voltage of these SiPMs. This section discusses a potential method to extract the breakdown voltage for these types of channels.

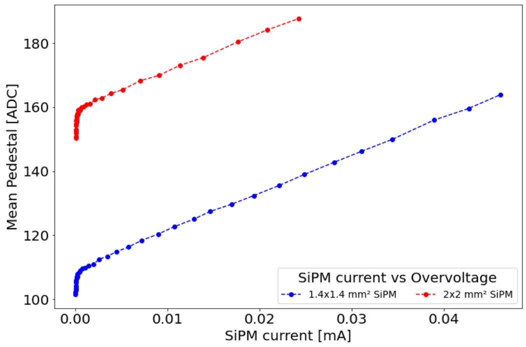

Figure A.2: The relationship between pedestal mean and current passing through two irradiated SiPMs at low leakage currents for two SiPMs of different sizes.

A.3.1 Methodology and Setup

Four irradiated SiPMs on a TBv1 tileboard were used for this experiment. The tileboard was placed inside a light-tight environment, and the breakdown voltage was determined by changing the voltage supplied to the SiPMs as described in section 5.1.2. Pedestal mean measurements were also conducted simultaneously alongside the current measurement. The relationship between the pedestal mean, and current is shown in fig. A.1(b). For the measurement of the breakdown voltage using the pedestal mean, a zero subtraction was performed on the pedestal data using the pedestal at the lowest bias voltage used as the reference pedestal mean value. As the breakdown voltage is roughly at 38 V, the bias voltage was varied between 37 V and 40 V.

A.3.2 Results and Discussion

The relationship between the SiPM current and the bias voltage is shown in fig. A.3(a) for the irradiated SiPMs, while the relationship between the pedestal mean and the bias voltage is shown in fig. A.3(b).

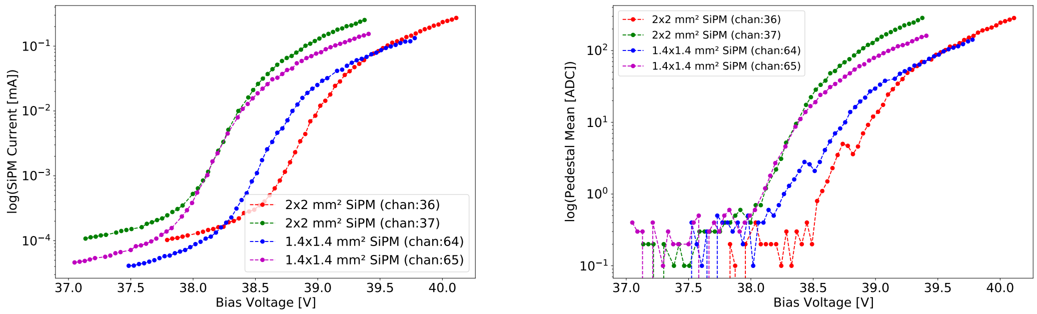

Figure A.3: (a) SiPM current and (b) pedestal mean vs bias voltage relationship for four different irradiated SiPMs of two different sizes on the same TBv2 tileboard.

The main difference between the current and pedestal mean measurement is that the current's resolution is much smaller than the resolution of the pedestal mean, which is limited by the

HGCROC ADC resolution. While it is possible to reproduce the current vs. bias voltage relationship at higher bias voltages, it is impossible to reproduce it below the SiPM breakdown voltage. Consequently, the relative derivative method cannot be used to extract the breakdown voltage of the SiPM using the pedestal mean instead of the current.

Nonetheless, as the pedestal mean vs. bias voltage curve reproduces the current vs. bias voltage curve at higher bias voltages, the four independent curves could be used first to estimate the fluctuation in breakdown voltages between channels. This could be done in two steps. As a first step, the bias voltage at which the pedestal means increases by 5 ADC counts with respect to the baseline is taken. This value is specific to this example and may not work for other channels. As a second step, one could draw a tangent using a linear fit, taking a few points above and below the anchor point mentioned above. If one could calculate the difference between the tangent and the actual value, the midpoint where the tangent and data agree can be obtained as the breakdown voltage. This is visualised in fig. A.4. The breakdown voltages are compared in table A.1.

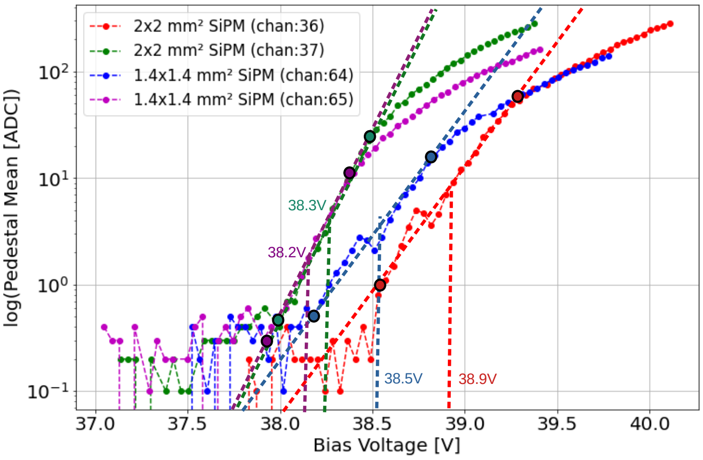

Figure A.4: measurement of the breakdown voltage using midpoint of the tangent in the area where the tangent lies on the pedestal vs voltage curve.

Table A.1: Differences between the breakdown voltages measured using the relative derivative method and the tangent method

Channel	Relative derivative breakdown voltage	Tangential breakdown voltage	Difference
Channel 36	38.90 V	38.9 V	0.0 V
Channel 37	38.28 V	38.3 V	0.0 V
Channel 64	38.59 V	38.5 V	0.1 V
Channel 36	38.20 V	38.2 V	0.0 V

This method is not precise due to the vague definition of where the tangent starts deviating from the tangent, especially at the lower bias voltages. This method is not consistent either. For example, although this method works well for channels 37 and 64, it may fail for channels 36 and 64 because of an unexplainable ’kink’ in the mid-region.

This method is also not reproducible for channels with non-linearity between current and pedestal mean at lower currents as shown in fig. A.5. Since the measurements are pedestal subtracted, this method is susceptible to the slightest fluctuations at lower currents and, therefore, proves to be ineffective.

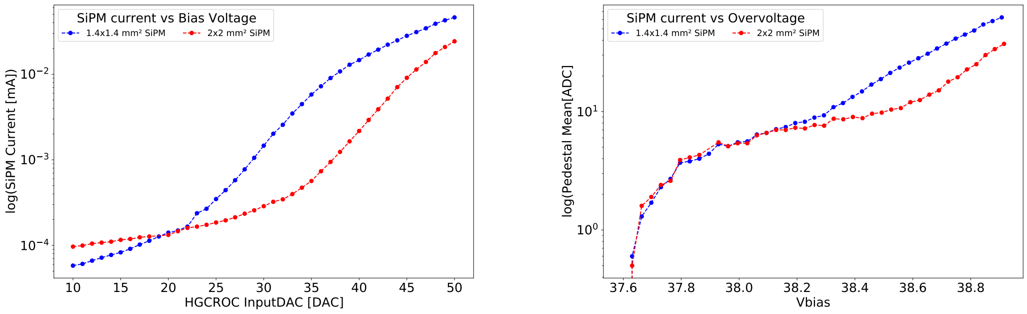

Figure A.5: (a) SiPM current and (b) pedestal mean vs bias voltage relationship for two different irradiated SiPMs of two different sizes on the same TBv1 tileboard. Both these channels showed a non-linearity at lower currents.

This non-linearity is effective in the pedestal below the breakdown voltage. One could exclude this region from the analysis by selecting the region where the pedestal increases linearly with the current. However, a typical tileboard will not have a method to determine the current. Therefore, determining the crossover point would only be possible by knowing the current. Due to this inconsistency in results, it is unclear if this method will work, and therefore, further studies may be necessary.

If one were to resolve this issue, it could improve the precision of the measurements as it would reduce the uncertainties due to the differences in breakdown voltages and improve the calorimeter response.

The bias voltage supplied to the SiPM can be varied in multiple ways. The most common way would be to vary the voltage supplied by the ALDOv2, as done in this experiment. The second method would be to vary the HGCROC's input DAC parameter. The ALDOv2 will supply the same bias voltage to all SiPMs globally in the final experiment. Therefore, the best method would be to vary the input DAC settings to measure the breakdown voltage and then set the input DAC settings per channel to bring them to the same over-voltage.

A measurable leakage current must pass through the SiPMs for this method to work. Since an external LED like the one used in this experiment cannot be used in the final HGCAL layout, this method works only with irradiated SiPMs. However, this is also where it is most needed. As the irradiation levels increase, the breakdown voltage of all the irradiated SiPMs will shift. Using this method, the shift in breakdown voltage can be monitored actively, and the voltage can be adjusted per channel.

For non-irradiated SiPMs, this method will not work due to the negligible amount of current passing through the SiPM. However, it might be possible to use the onboard LED system to do the job of the external LED. This is yet to be investigated and is outside the scope of this thesis.

Bibliography

[1] Joseph John Thomson. XL. Cathode rays. *The London, Edinburgh, and Dublin Philosophical Magazine and Journal of Science*, 44(269):293–316, 1897.

[2] Wilhelm Röntgen. Über eine neue Art von Strahlen. Vorläufige Mitteilung. *Aus den Sitzungsberichten der Würzburger Physik.-medic. Gesellschaft Würzburg*, page 137–147, 1895.

[3] Henri Becquerel. Sur les radiations émises par phosphorescence. *Comptes Rendus*, 122: 420–421, 1896.

[4] Charles Thomson Rees Wilson. On an expansion apparatus for making visible the tracks of ionising particles in gases and some results obtained by its use. *Proceedings of the Royal Society of London. Series A, Containing Papers of a Mathematical and Physical Character*, 87(595):277–292, September 1912. doi: 10.1098/rspa.1912.0081. URL https://doi.org/10.1098/rspa.1912.0081.

[5] Donald A. Glaser. Some Effects of Ionizing Radiation on the Formation of Bubbles in Liquids. *Phys. Rev.*, 87:665–665, Aug 1952. doi: 10.1103/PhysRev.87.665. URL https://link.aps.org/doi/10.1103/PhysRev.87.665.

[6] Georges Aad et al. Observation of a new particle in the search for the Standard Model Higgs boson with the ATLAS detector at the LHC. *Phys. Lett.*, B716:1–29, 2012. doi: 10.1016/j.physletb.2012.08.020.

[7] S. Chatrchyan et al. Observation of a new boson at a mass of 125 GeV with the CMS experiment at the LHC. *Phys. Lett.*, B716:30–61, 2012. doi: 10.1016/j.physletb.2012.08.021.

[8] CERN. Luminosity forecasts : HL-LHC proton-proton luminosity out to 2041 - impact of 19 weeks YETS, 2023. URL https://lhc-commissioning.web.cern.ch/schedule/HL-LHC-plots.htm.

[9] CERN HL-LHC. LHC/ HL-LHC Plan, 2023. URL https://hilumilhc.web.cern.ch/content/hl-lhc-project.

[10] CMS Collaboration. The Phase-2 Upgrade of the CMS Endcap Calorimeter. techreport, CERN, Geneva, 2017. URL http://cds.cern.ch/record/2293646.

[11] Felix Sefkow and Frank Simon. A highly granular SiPM-on-tile calorimeter prototype. *J. Phys. Conf. Ser.*, 1162(1):012012, 2019. doi: 10.1088/1742-6596/1162/1/012012.

[12] Ties Behnke, James E. Brau, Philip N. Burrows, Juan Fuster, Michael Peskin, Marcel Stanitzki, Yasuhiro Sugimoto, Sakue Yamada, and Hitoshi Yamamoto. The International Linear Collider Technical Design Report - Volume 4: Detectors, 2013.

[13] Omega Microelectronics. *HGCROC2/2A Datasheet*, 2019. URL https://edms.cern.ch/ui/file/2133536/1/HGCROC2_datasheet_v2.pdf.

[14] Omega Microelectronics. *HGCROC3 Datasheet*, 2021. URL https://edms.cern.ch/ui/file/2324379/1/HGCROC3_Spec_Working_Document_v2.0.pdf.

[15] R. Diener et al. The DESY II Test Beam Facility. *Nuclear Instruments and Methods in Physics Research Section A: Accelerators, Spectrometers, Detectors and Associated Equipment*, 922:265–286, 2019. ISSN 0168-9002. doi: https://doi.org/10.1016/j.nima.2018.11.133. URL https://www.sciencedirect.com/science/article/pii/S0168900218317868.

[16] B. Kronheim, A. Belloni, T. K. Edberg, S. C. Eno, C. Howe, C. Palmer, C. Papageorgakis, M. Paranjpe, and S. Sriram. Reduction of light output of plastic scintillator tiles during irradiation at cold temperatures and in low-oxygen environments, 2023.

[17] Cush. Standard model of elementary particles, 2019. URL https://commons.wikimedia.org/wiki/File:Standard_Model_of_Elementary_Particles.svg.

[18] D. P. Barber et al. Discovery of Three-Jet Events and a Test of Quantum Chromodynamics at PETRA Energies. *Phys. Rev. Lett.*, 43:830–833, Sep 1979. doi: 10.1103/PhysRevLett.43.830. URL https://link.aps.org/doi/10.1103/PhysRevLett.43.830.

[19] F. J. Hasert et al. Observation of Neutrino Like Interactions Without Muon Or Electron in the Gargamelle Neutrino Experiment. *Phys. Lett.*, B46:138–140, 1973. doi: 10.1016/0370-2693(73)90499-1. [,5.15(1973)].

[20] Mark Thomson. *Modern particle physics*. Cambridge University Press, New York, 2013. ISBN 978-1-107-03426-6. doi: 10.1017/CBO9781139525367.

[21] Itaru Shimizu. Search for majorana neutrinos, 2023.

[22] J.D. Cockcroft and E.T. Walton. Experiments with High Velocity Positive Ions.-(I) Further Developments in the Method of Obtaining High Velocity Positive Ions. *Proceedings of the royal society of London. Series A*, 830(136):619–630, 1932.

[23] Stanford National Accelerator Laboratory. Stanford National Accelerator Laboratory, 2023. URL https://www6.slac.stanford.edu/.

[24] International Linear Collider. International Linear Collider. website, 2023. URL https://linearcollider.org/.

[25] SuperKEKB. SuperKEKB Project. website, 2023. URL https://www-superkekb.kek.jp/.

[26] Fermi National Laboratory. Tevatron, 2023. URL https://www.fnal.gov/pub/tevatron/tevatron-accelerator.html.

[27] DESY. Deutsches Elektronen Synchrotron (DESY), 2023. URL `https://www.desy.de/index_eng.html`.

[28] Jenny Williams. CMS Particle Detection Summary, 2007. URL `https://twiki.cern.ch/twiki/bin/view/CMSPublic/WorkBookCMSExperiment`. Accessed: 2023-4-15.

[29] CMS Collaboration. Precision luminosity measurement in proton-proton collisions at $\sqrt{s}$= 13 TeV in 2015 and 2016 at CMS. *Eur. Phys. J. C*, 81(800), 2021. doi: 10.1140/epjc/s10052-021-09538-2. URL `https://doi.org/10.48550/arXiv.2104.01927`.

[30] Juliette Alimena et al. Searching for long-lived particles beyond the Standard Model at the Large Hadron Collider. *Journal of Physics G: Nuclear and Particle Physics*, 47 (9):090501, sep 2020. doi: 10.1088/1361-6471/ab4574. URL `https://doi.org/10.1088%2F1361-6471%2Fab4574`.

[31] Felix Kahlhoefer. Review of LHC dark matter searches. *International Journal of Modern Physics A*, 32(13):1730006, may 2017. doi: 10.1142/s0217751x1730006x. URL `https://doi.org/10.1142%2Fs0217751x1730006x`.

[32] M. J. Berger and S. M. Seltzer. Tables of Energy Losses and Ranges of Electrons and Positrons. In *Studies in Penetration of Charged Particles in Matter*, page 205, Jan 1964. URL `https://ntrs.nasa.gov/archive/nasa/casi.ntrs.nasa.gov/19650002905.pdf`.

[33] R. L. Workman et al. Review of Particle Physics. *PTEP*, 2022:083C01, 2022. doi: 10.1093/ptep/ptac097.

[34] R. Leo William. *Techniques for Nuclear and Particle Physics Experiments: A How-to Approach*. Springer, 1994. ISBN 3540572805.

[35] Pablo Sempere Roldan. Quality control and preparation of the PWO crystals for the electromagnetic calorimeter of CMS. *CERN-THESIS-2011-113*, 2011. URL `http://cds.cern.ch/record/1388922/files/CERN-THESIS-2011-113.pdf?version=1`.

[36] Tejinder S Virdee. Experimental techniques. *1998 European School on High-Energy Physics*, (CERN-OPEN-2000-261):347–419, 1999. doi: 10.5170/CERN-1999-004.347. URL `http://cds.cern.ch/record/454176`.

[37] Particle Physics Group. Atomic and Nuclear Properties of copper (Cu), 2019. URL `http://pdg.lbl.gov/2019/AtomicNuclearProperties/HTML/copper_Cu.html`.

[38] L. Landau. On the Energy Loss of Fast Particles by Ionization. *J. Phys.(USSR)*, 8:201–205, 1944.

[39] Christian Wolfgang Fabjan and F Gianotti. Calorimetry for Particle Physics. *Rev. Mod. Phys.*, 75:1243–1286, 2003. doi: 10.1103/RevModPhys.75.1243. URL `https://cds.cern.ch/record/692252`.

[40] ATLAS Collaboration. *ATLAS liquid-argon calorimeter: Technical Design Report*. Technical design report. ATLAS. CERN, Geneva, 1996. doi: 10.17181/CERN.FWRW.FOOQ. URL `https://cds.cern.ch/record/331061`.

[41] Louise Heelan. Performance of the ATLAS Tile Calorimeter. *Journal of Physics: Conference Series*, 623(1):012014, may 2015. doi: 10.1088/1742-6596/623/1/012014. URL `https://dx.doi.org/10.1088/1742-6596/623/1/012014`.

[42] Bayatian, G L and others. *CMS Physics: Technical Design Report Volume 1: Detector Performance and Software*. Technical design report. CMS. CERN, Geneva, 2006. URL `https://cds.cern.ch/record/922757`. There is an error on cover due to a technical problem for some items.

[43] Malinda de Silva. Evaluation of Scintillator Tiles and Silicon Photomultipliers for Highly Granular Calorimeters. Master's thesis, Technical University of Munich, 2019.

[44] Glenn F Knoll. *Radiation detection and measurement; 4th ed.* Wiley, New York, NY, 2010. URL `https://cds.cern.ch/record/1300754`.

[45] Luxium Solutions. Solid Plastic Scintillators : Organic, 2022. URL `https://www.crystals.saint-gobain.com/radiation-detection-scintillators/plastic-scintillators#`.

[46] Saint Gobain Crystals. *BC-400,BC-404,BC-408,BC-412,BC-416 Premium Plastic Scintillators datasheet*. Saint-Gobain crystals, 2018.

[47] Eljen Technology. *General Purpose Plastic Scintillator EJ-200, EJ-204, EJ-208, EJ-212*, 2021.

[48] Robert Todd. *Manufacturing Processes Reference Guide*. Industrial Press Inc., 1994. ISBN 0831102004.

[49] W. Busjan, K. Wick, and T. Zoufal. Shortlived Absorption Centers in Plastic Scintillators and Their Influence on the Fluorescence Light Yield. *Nuclear Instruments and Methods in Physics Research Section B: Beam Interactions with Materials and Atoms*, 152(1):89–104, 1999. ISSN 0168-583X. doi: https://doi.org/10.1016/S0168-583X(98)00974-4. URL `https://www.sciencedirect.com/science/article/pii/S0168583X98009744`.

[50] J. Bartos and J. Tino. Study of macroradical reactivity in polystyrene by means of ESR and stochastic models for diffusion-controlled reactions. *Chem. zvest*, 1982.

[51] A.M. Sirunyan et al. Measurements with silicon photomultipliers of dose-rate effects in the radiation damage of plastic scintillator tiles in the CMS hadron endcap calorimeter. *Journal of Instrumentation*, 15(06):P06009–P06009, jun 2020. doi: 10.1088/1748-0221/15/06/p06009. URL `https://doi.org/10.1088%2F1748-0221%2F15%2F06%2Fp06009`.

[52] Frank Simon. Silicon photomultipliers in particle and nuclear physics. *Nuclear Instruments and Methods in Physics Research Section A: Accelerators, Spectrometers, Detectors and Associated Equipment*, 926:85–100, May 2019. doi: 10.1016/j.nima.2018.11.042. URL `https://doi.org/10.1016/j.nima.2018.11.042`.

[53] Koei Yamamoto et al. Recent Development of MPPC at Hamamatsu for Photon Counting Applications. *Proceedings of the 5th International Workshop on New Photon-Detectors (PD18)*, 2018. doi: 10.7566/jpscp.27.011001. URL `https://journals.jps.jp/doi/abs/10.7566/JPSCP.27.011001`.

[54] A. Ghassemi et al. MPPC - Technical Note. Technical Note, Mar 2017. URL https://www.hamamatsu.com/resources/pdf/ssd/mppc_kapd9005e.pdf. Hamamatsu Photonics K.K.

[55] Hamamatsu Photonics K.K. *MPPC S14160 series specification sheet*. Hamamatsu Photonics K.K., August 2018.

[56] Martyna Grodzicka, Tomasz Szczęśniak, Marek Moszyński, Marek Szawłowski, and Krystian Grodzicki. New Method for Evaluating Effective Recovery Time and Single Photoelectron Response in Silicon Photomultipliers. *Nuclear Instruments and Methods in Physics Research Section A: Accelerators, Spectrometers, Detectors and Associated Equipment*, 783:58–64, May 2015. doi: 10.1016/j.nima.2015.01.074. URL https://doi.org/10.1016/j.nima.2015.01.074.

[57] Gunnar Lindström. Radiation Damage in Silicon Detectors. *Nuclear Instruments and Methods in Physics Research Section A: Accelerators, Spectrometers, Detectors and Associated Equipment*, 512(1):30–43, 2003. ISSN 0168-9002. doi: https://doi.org/10.1016/S0168-9002(03)01874-6. URL https://www.sciencedirect.com/science/article/pii/S0168900203018746. Proceedings of the 9th European Symposium on Semiconductor Detectors: New Developments on Radiation Detectors.

[58] E. Garutti and Yu. Musienko. Radiation Damage of SiPMs. *Nuclear Instruments and Methods in Physics Research Section A: Accelerators, Spectrometers, Detectors and Associated Equipment*, 926:69–84, 2019. ISSN 0168-9002. doi: https://doi.org/10.1016/j.nima.2018.10.191. URL https://www.sciencedirect.com/science/article/pii/S0168900218315055. Silicon Photomultipliers: Technology, Characterisation and Applications.

[59] Roland H. Haitz. Mechanisms Contributing to the Noise Pulse Rate of Avalanche Diodes. *Journal of Applied Physics*, 36(10), 1965. doi: 10.1063/1.1702936.

[60] Roberto Pagano et al. Dark Current in Silicon Photomultiplier Pixels: Data and Model. *IEEE Transactions on Electron Devices*, 59(9):2410–2416, 2012. doi: 10.1109/TED.2012.2205689.

[61] Giovanni Bonanno et al. Characterization Measurements Methodology and Instrumental Set-Up Optimization for New SiPM Detectors—Part I: Electrical Tests. *IEEE Sensors Journal*, 14(10):3557–3566, 2014. doi: 10.1109/JSEN.2014.2328621.

[62] Zhe Wu et al. Studies of Detector Cells for a Hadronic Calorimeter Based on Plastic Scintillators. *Radiation Detection Technology and Methods*, 2018.

[63] L.M.S. de Silva and F. Simon. Effects of Misalignment on Response Uniformity of SiPM-on-Tile Technology for Highly Granular Calorimeters. *Journal of Instrumentation*, 15(06):P06030, jun 2020. doi: 10.1088/1748-0221/15/06/P06030. URL https://dx.doi.org/10.1088/1748-0221/15/06/P06030.

[64] CMS Collaboration. The Phase-2 Upgrade of the CMS Tracker. techreport, CERN, Geneva, 2017. URL http://cds.cern.ch/record/2272264.

[65] CMS Collaboration. Technical proposal for a MIP timing detector in the CMS experiment Phase 2 upgrade. techreport, CERN, Geneva, 2017. URL http://cds.cern.ch/record/2296612.

[66] CMS Collaboration. The Phase-2 Upgrade of the CMS Barrel Calorimeters. techreport, CERN, Geneva, 2017. URL http://cds.cern.ch/record/2283187. This is the final version, approved by the LHCC.

[67] CMS Collaboration. The Phase-2 Upgrade of the CMS Muon Detectors. techreport, CERN, Geneva, 2017. URL http://cds.cern.ch/record/2283189. This is the final version, approved by the LHCC.

[68] The ATLAS Collaboration. The Phase-2 Upgrade of the CMS L1 Trigger Interim Technical Design Report. techreport, CERN, Geneva, 2017. URL http://cds.cern.ch/record/2283192. This is the CMS Interim TDR devoted to the upgrade of the CMS L1 trigger in view of the HL-LHC running, as approved by the LHCC.

[69] CMS Collaboration. The Phase-2 Upgrade of the CMS DAQ Interim Technical Design Report. techreport, CERN, Geneva, 2017. URL http://cds.cern.ch/record/2283193. This is the CMS Interim TDR devoted to the upgrade of the CMS DAQ in view of the HL-LHC running, as approved by the LHCC.

[70] David Barney. Overview slide of CE with main parameters, 2022. URL https://cms-docdb.cern.ch/cgi-bin/PublicDocDB/ShowDocument?docid=13251.

[71] 3M. *3M Enhanced Specular Reflector Films*, 2020. URL https://www.3m.com/3M/en_US/company-us/all-3m-products/~/Vikuiti-TM-Enhanced-Specular-Reflector-ESR-17-in-x-17-in-10-Shts-Kit/?N=5002385+3294396287&rt=rud.

[72] Hamamatsu Photonics K.K. *MPPC S14160-976x series specification sheet*, 2022.

[73] Hamamatsu Photonics K.K. *MPPC S16713 series specification sheet*, 2022.

[74] Mitch Wayne et al. Endcap Calorimeter: SiPM Production Readiness Review, 2023. URL https://indico.cern.ch/event/1227228/contributions/5163765/attachments/2563671/4419615/Endcap%20Calorimeter%20-%20PRR%20for%20SiPMs%20v4.pdf.

[75] Mathias Reinecke, Jeremy Mans, Ted Kolberg, Felix Sefkow, and Katja Krüger. CMS HGCAL – Scintillator detector's LV and BV powering requirements. Technical report, CMS Collaboration, 2023.

[76] Jeremiah Mans. Front end electronics of the HGCAL Scintillator section. Internal Communications, 2022.

[77] Paolo Carniti, Claudio Gotti, and Gianluigi Pessina. ALDO2, A Multi-function Rad-hard Linear Regulator for SiPM-based HEP Detectors. *Nucl. Instrum. Meth. A*, 1039:167028, 2022. doi: 10.1016/j.nima.2022.167028.

[78] CALICE and CMS Collaborations. Performance of the CMS High Granularity Calorimeter prototype to charged pion beams of 20-300 GeV/c. techreport, CALICE and CMS Collaborations, 2022. URL https://cds.cern.ch/record/2840846. Accepted for publication by JINST.

[79] J. Borg et al. SKIROC2_CMS an ASIC for testing CMS HGCAL. *Journal of Instrumentation*, 12(02):C02019, feb 2017. doi: 10.1088/1748-0221/12/02/C02019. URL https://dx.doi.org/10.1088/1748-0221/12/02/C02019.

[80] Xilinx, Inc. *KCU105 Board User Guide*, 2019.

[81] Mathias Reinecke. *Operation and Instruction Manual for the CMS HGCAL Tileboard Prototype1 (TB1)*, 2020.

[82] Mathias Reinecke. *Operation and Instruction Manual for the CMS HGCAL Tileboard2 and Tileboard3*, 2022.

[83] CERN. *FEAST - Radiation tolerant 10W Synchronous Step-Down Buck DC/DC converter*, 2018.

[84] Mathias Reinecke, Peter Goettlicher, and DESY-ZE. Floor plan of Tileboards TB1.2, TB1.3, TB2, TB2.1, TB3, MiniTB. Internal Communications, 2023.

[85] Arabella Martelli, Chris Seez, Pedro Silva, and Suho Kim. Study of HGCAL SiPM-tile intercalibration using Muons. techreport, CMS Experiment, 2022.

[86] Olin Pinto. *Shower Shapes in a Highly Granular SiPM-on-Tile Analog Hadron Calorimeter*. PhD thesis, University of Hamburg and Deutsches Elektronen-Synchrotron (DESY), 2022.

[87] Mathias Reinecke. ADC DNL from Internal Charge Injection of the HGCROC. Internal Communications, 2021.

[88] Phi Chau. *Optimierung von hochauflösenden Sampling-Kalorimetern mit szintillatorbasierter SiPM-Auslese*. PhD thesis, Johannes Gutenberg-Universität Mainz, Mainz, 2022.

[89] A. Kaminskiy et al. Tile Light YIeld Measurements at DESY, 2022. URL https://indico.cern.ch/event/1141893/contributions/4805447/attachments/2419708/4141540/LY_20220401.pdf.

[90] Daria Selivanova. Tile Quality Control (QC) Measurements : Measurements at DESY TAC, 2023. URL https://indico.cern.ch/event/1289034/contributions/5462470/attachments/2672431/4633063/HGCworkshop-jun23_tileQC.pdf.

[91] Yuri Musienko et al. Results on Pre-Series SiPMs. Internal Communications, 2021. URL https://indico.cern.ch/event/1200224/contributions/5046871/attachments/2508433/4310862/Results%20on%20preseries%20SiPMs_14.09.2022-corr.pdf.

[92] B Smodiš and L Snoj. The JSI TRIGA Mark II Reactor, Slovenia. In *History, Development and Future of TRIGA Research Reactors. Companion CD-ROM*. International Atomic Enegry Agency, 2016.

[93] Arjen Heering, Mitch Wayne, and Yuri Musienko. Irradiation of SiPMs at JSI, Ljubljana. Internal Communications, 2020.

[94] Keithley. *Keithley 2000 Series 6 1/2-Digit Multimeter*, 2000.

[95] Mitch Wayne et al. SiPM Qualification Plans and Needs. Internal Communications, 2020.

[96] Mathias Reinecke et al. SiPM Bias Voltage Generation and new LED system on Tileboard2, 2022. URL https://indico.cern.ch/event/1103724/contributions/4644457/attachments/2364456/4036970/TB2_BV_Reinecke_14Dec21.pdf.

[97] E. Garutti et al. Radiation hardness study using SiPMs with single-cell readout, 2021. URL https://doi.org/10.48550/arXiv.2111.00483.

[98] Carmen Villalba, Erika Garutti, and Jörn Schwandt. Performance of Neutron Irradiated SiPM for the CMS HGCAL. In *DPG SKuM 2021*, 2021. URL https://www.dpg-verhandlungen.de/year/2021/conference/dortmund/part/t/session/57/contribution/2.

[99] E. Garutti et al. Self-heating effect in Silicon-Photomultipliers. *Nuclear Instruments and Methods in Physics Research Section A: Accelerators, Spectrometers, Detectors and Associated Equipment*, 1039:167026, sep 2022. doi: 10.1016/j.nima.2022.167026. URL https://doi.org/10.1016%2Fj.nima.2022.167026.

[100] CMS HGCAL DPG Group. Dose and Radiation Constant Calculation, version 4. internal communication, 2022.

[101] Yuri Musienko. HGCAL 1.4x1.4 mm2 SiPM during LHC operation: Idark vs. time (annealing scenarios), 2021. URL https://indico.cern.ch/event/993641/contributions/4178426/attachments/2170515/3664508/HGCAL_2mm2-SiPM_Idark-vs-time_annealing_scenarios-corr-v2.pdf.

[102] Braden Kronheim. Signal Degeneration due to Temporary and Permanent Damage over Time at thw HGCAL, 2023. Internal Communications.

List of Figures

2.1 Elementary particles in Standard Model of particle physics [17] 5

2.2 Simplified scheme of the CMS detector at CERN including the electromagnetic and hadronic calorimeters [28]. 9

2.3 A cross-section of the CMS detector with the barrel marked in orange and end-cap region marked in purple. The red area marks the very forward calorimeter of the CMS. Taken and repurposed from [29]. 10

2.4 Vector Boson Fusion leading to the Higgs boson production. 12

2.5 (a) shows the stopping power of electrons and positrons per radiation length as a function of the particle energy. (b) shows the total photon cross sections as a function of photon energy for each type of interaction, showing the contributions of different processes. $\sigma_{\text{p.e.}}$ is the cross section for photoelectric effect, σ_{Rayleigh} for Rayleigh scattering, σ_{Compton} for Compton scattering, κ_{nuc} for pair production in nuclear field, κ_{e} for pair production in electron field and $\sigma_{\text{g.d.r.}}$ for photo-nuclear interactions. Both diagrams are for interactions in lead and taken from [33]. 14

2.6 An illustration of the development of an electromagnetic shower using the simple cascade model. X_0 is the radiation length. Taken from [35]. 15

2.7 Stopping power for positive muons traversing copper as a function of the muon momentum. The solid line shows the total stopping power and the dashed lines show the different contributions, including the stopping power via inelastic collisions and bremsstrahlung. Taken from [33]. 16

2.8 An illustration of the development of a hadronic shower. λ describes the mean distance a particle travels in a given material before undergoing inelastic interactions. Taken from [36]. 17

2.9 (a) shows the electronic energy deposit distribution for a 10 GeV muon traversing 1.7 mm of silicon. (b) shows the mean stopping power (dE/dx) described by the Bethe-Bloch equation and the most probable energy loss described by the Landau-Vavilov-Bichsel equation (Δ_p/x) shown as a function of muon energy traversing 1.7 mm of silicon. Silicon has a similar stopping power as a 3 mm of PVT-based scintillator. Taken from [33]. 19

2.10 Energy levels of organic molecules. S denotes the singlet state, and T denotes the triplet states. Red arrows mark electron movements, while blue arrows mark the emitted photons. Taken from [43] 23

2.11 (a) shows an image of Hamamatsu HDR-2 type SiPM with a 15 µm pitch while (b) shows an individual SPAD of a similar SiPM seen through a microscope taken from [53]. An optical trench separates each SPAD from the neighbouring SPADs in this generation of SiPMs. 26

2.12 The avalanche region within a silicon SPAD alongside the strength of its electric field. Taken from [54]. 26

2.13 A single photon spectrum (SPS) obtained from a S14160 series SiPM produced by Hamamatsu Photonics K.K. (HPK) operated at an over-voltage of 6 V. The SiPM was on a Tilemodule prototype produced for the CMS HGCAL upgrade. The charge was obtained by sampling the signal's peak and converted using an analog-to-digital converter (ADC) to a digital value. Each peak corresponds to the number of photons detected by the SiPM. 28

2.14 Photon Detection Efficiency dependence on (a) photon wavelength and (b) over-voltage for HPK S14160-1315PS, -3015PS, 1310PS and -3010PS HDR-2 SiPMs. (b) also shows the increase in SiPM gain and crosstalk with over-voltage. Taken from [55] 29

2.15 Measured dark count rate as a function of the discriminator threshold. Each blue vertical line corresponds to the mean amplitude of a SiPM signal due to the discharge of n microcells (in p.e. scale). The measurement of DCR was performed using an HPK S13360-1325PE SiPM at a V_{bias} of 55.0 V, taken from [43]. 30

2.16 The number of single photon avalanche photo-diode cells in a SiPM fired (N_{fired}) vs. the number of photo-electrons detected by a photomultiplier tube (N_{PMT}) as observed by Grodzicka et al. [56]. 32

2.17 Schematic of possible band gap defects in silicon, including in SiPMs. The red lines indicate the movement of electrons and the blue ones of holes. 34

2.18 SiPM-on-tiles produced for the CMS HGCAL scintillator section. (a) shows scintillator tiles with a central dimple, wrapped and unwrapped, mounted on a Tilemodule with SiPMs. (b) sketches the working principle of the SiPM-on-Tile. 35

3.1 Latest luminosity estimates during the operation of the HL-LHC between 2028 and 2042 for the CMS and ATLAS experiments. The blue line depicts the expected integrated luminosity collected with 15 weeks of year-end technical stops (YETS), while the purple line depicts the expected integrated luminosity collected with 19 weeks of YETS. Taken from [8]. 38

3.2 Schematic view of the CMS high granularity end-cap calorimeter. Taken from [70]. 39

3.3 Schematic cross-sections of the three different sections in the CMS end-cap: (a) the CE-E region consisting of silicon-based active layers and Pb/Cu-W/Cu absorber layers, (b) the CE-H silicon sensor section with stainless steel absorber layers, and (c) the CE-H mixed silicon/scintillator cassette with stainless steel absorber layers. Cu is used as the cooling plate. Taken from [10]. 40

3.4 CMS FLUKA study showing the area of the HGCAL showing the 1 MeV equivalent neutron fluence in silicon at the end of life. The scintillator section is limited to the area where the expected fluence is below 5×10^{13} $\mathrm{n_{eq}/cm^2}$. Taken from [10] 42

3.5 A D8 Tilemodule partially equipped with scintillators. 42

3.6 (a) shows the base layout of Tilemodule geometry to be used in the HGCAL. The alphabet letter symbolises the different types of Tilemodules, generally categorised by the distance to the beamline, while the number symbolises the number of rings the Tilemodule covers. The Tilemodules shown here cover a 10 ° sector. Thirty-six similar sectors (with minor variations) cover the scintillator section of a single end-cap. Two such end-caps exist in either direction of the beamline. (b) shows the top view of a 15 ° sector showing only the scintillator Tilemodules, taken and modified from [75]. The Tilemodules in (a) corresponds to the Tilemodules in (b) at the same radial position. 43

3.7 The front-end electronics system of the scintillator section includes the relevant modules on which they lie (Tilemodules, Wingboard and Motherboard). Taken from [76]. 45

3.8 Block diagram of the HGCROCv3. Taken from [14] 46

3.9 ADC, TOT and TOA variations with external charge injection via a pulse generator. The charge pulse was injected to a SiPM (channel 45) on a Tilemodule readout using an HGCROCv2. 48

3.10 Definitions of ADC, TOT and TOA for a typical SiPM pulse. 49

3.11 A Tilemodule in the typical setup with interconnection via Twinax cable to a DAQ FPGA module (KCU105). Taken from [81] 50

3.12 Block-diagram of the typical interconnection of a Tilemodule to the KCU105 FPGA module (DAQ). Taken from [81] 51

3.13 Tilemodule in the typical setup with interconnection via adapter board to a DAQ FPGA module (TB-Tester). The light cover to protect from the LED UV light is not shown. Taken from [81] 52

3.14 Block-diagram of the typical interconnection of Tilemodule, in this case to the TB-tester DAQ system. Taken from [82] 52

3.15 Front view and back view of a version 1, D8 Tilemodule prototype with the main sensors (SiPM, scintillator tiles, LED) and electronics (HGCROC readout chip, GBT-SCA) 54

3.16 Floor plan of the tileboard TB1.2 including the positions of the on-board electronics and SiPMs [84]. 55

3.17 Floor plan of the tileboard TB1.3 including the positions of the on-board electronics and SiPMs [84]. 55

3.18 Front view and back view of a typical 64-channel tileboard version 2 with the main sensors (SiPM, scintillator tiles, LED) and electronics (HGCROC readout chip, GBT-SCA, ALDO) 56

3.19 Floor plan of the tileboard TB2 including the positions of the on-board electronics and SiPMs [84]. 57

3.20 Front view and back view of a typical 64-channel tileboard version 3 with the main sensors (SiPM, scintillator tiles, LED) and electronics (HGCROC readout chip, GBT-SCA, ALDO) 57

3.21 Floor plan of the tileboard TB3 including the positions of the on-board electronics and SiPMs [84]. 58

3.22 (a) shows the floorplan of the mini-tileboard (MiniTB), which includes the HGCROCv3, GBT-SCA and the two temperature sensors (T1 and T2) [84]. (b) shows the mini-tileboard with the SiPM side up and two R18 tiles mounted. . . 58

4.1 DESY-II test beam facility layout. Taken from [15] 63

4.2 The basic setup of the Tilemodule and DAQ system used at beam tests conducted at DESY-II and CERN SPS test beam facilities 64

4.3 Photos of a beam test setup on the movable stage at DESY-II: (a) tileboard alongside the power supplies used for powering; (b) trigger scintillators used in addition to the tileboard. 65

4.4 The fraction of triggered events with no signal observed as a function of the beam position with respect to the stage holding the Tilemodule in place. The rough dimensions of the bare R2 tile used for the measurement are shown in red. 66

4.5 Sketch showing the interplay between the bias voltage, breakdown voltage and input DAC voltage. 66

4.6 Five events acquired with a 3 GeV electron beam using TB1.3 tileboard using the KCU105 DAQ. The six consecutive points sampled were used to reconstruct the SiPM pulse to extract the peak. 68

4.7 Distribution of SiPM pulse amplitudes from MIP-like events. A convoluted Landau-Gaussian function extracts the fit maximum. 69

4.8 Correlation between TOA acquired by the TDC in the HGCROC and the timing of the pulse maxima obtained using the template fit 69

4.9 Sketch visualises the interplay between TOA and the delay measured by the template fit method. The template fit calculates the delay at which the signal peak is sampled t while TOA is the time at which the signal crosses the TOA threshold. 70

4.10 Sketch showing the relationship between TrigTime, TOA and ADC based on the trigger and data signals. The sampling point of the ADC is depicted as dots. 71

4.11 Sampled ADC value vs. TrigTime of events measured by the TB-tester DAQ. The yellow band follows the peak of each bin on the x-axis. The pedestal is the continuous blue line at roughly 140 ADC across all three sampled data. 71

4.12 The histogram obtained using a 10-bin time interval at which the pulse from the SiPM-on-tile is at its peak. A Landau-Gaussian convoluted function is used to obtain the pulse amplitude. The corrected pulse amplitude is obtained after subtracting the pedestal value, also given in the plot. 72

4.13 Correlation between TOA acquired by the TDC in the HGCROC and the trigger timestamp of the TB-tester DAQ 73

4.14 MIP maxima obtained using template fit method and TrigTime method using the same TB2 Tilemodule and TB-tester DAQ system at the DESY beam test held in April 2022. The statistical errors of the measurement are negligibly small, and therefore, error bars are not visible. 74

4.15 A typical single photo-electron spectra obtained from a TB1.3 Tilemodule using a SiPM over voltage of 6 V and LED bias voltage of 5.9 V 75

4.16 The DNL effect in the conversion of charge to ADC scale by the HGCROC as observed at DESY [87]. (a) shows the DNL when just one channel is injected with a charge. (b) shows the DNL in the same channel when all channels are injected with charge. 76

4.17 (a) shows the raw SPS obtained from LED pulses are heavily affected by the differential non-linearity of the ADC of the HGCROC while (b) shows the SPS for the same channel after DNL reduction using multiple datasets with different pedestals 77

4.18 Single photo-electron spectra obtained across five different LED bias voltages for the same SiPM, keeping all other conditions constant. 78

4.19 SiPM gain vs. signal delay used for data acquisition for three selected channels on a TB1.2 tileboard of two different SiPM sizes. The vertical dotted lines show the delay at which the maximum SiPM gain is obtained for that respective channel. The error bars give the statistical errors of the gain measurement as described in section 4.3.2.4. 79

4.20 Variation of SiPM gain with over-voltage measured using channels on TB2 tileboard 80

4.21 Comparison of SiPM gains of two different SiPM sizes for Over-Voltage=4 V and conveyor gain=12. The 39 SiPMs shown here are on three tileboards (TB1.2, TB1.3 and TB2) read out using HGCROCv2. 81

4.22 SiPM gain vs. delay of pulse acquisition for two channels containing two different SiPM sizes on the MiniTB tileboard. The vertical dotted lines show the delay at which the pulse amplitude can be obtained for that respective channel. The error bars give the statistical errors of the gain measurement from the multi-Gaussian fit and average the gain obtained using different LED bias voltages. . 82

4.23 Flow chart showing the steps taken to obtain the final light yields adjusted to the needed over-voltage (V_{over}) and 25 °C temperature. 84

4.24 Photon detection efficiency vs. SiPM over-voltage plot. The data were obtained from the SiPM datasheet [72]. The PDE is fitted using a second-order polynomial. 85

4.25 Light yield derived to an over-voltage of 3 V using 2 V and 4 V data sets and eq. (4.17). The black dotted line plots the points at which the two different light yields are identical, while the grey area shades the area within a 5 % deviation of this black line. Error bars show the statistical uncertainties of the measurement. 86

4.26 Multiple light yields were measured for the same seven IHEP injection-moulded tiles over different beam tests and SiPMs and Tilemodules. (a) and (c) used TBv1 tileboards for over-voltages of 4 V and 2 V respectively, while (b) and (d) used TBv2 tileboards for over-voltages of 4 V and 2 V. The final uncertainties are given as a fraction of the mean light yields. Light yields from $1.4 \times 1.4\,\text{mm}^2$ SiPMs (shown by triangles) have been increased by a factor of 2.04 in order to be combined with $2 \times 2\,\text{mm}^2$ SiPM data (shown by circles). 87

4.27 MIP maxima obtained from different IHEP cast tiles of two different tile sizes. (a) is for the smallest tiles (to be used in ring R0 of the detector) of 22.50 mm tile edge length, and (b) is for tiles of 29.48 mm tile edge length (to be used in ring R12 of the detector). 88

4.28 Light yields measured for different conveyor gains for an over-voltage of 4 V compared with the light yield measured for a conveyor gain of 12. The black dotted line plots the points at which the two different light yields measured are identical, while the grey area shows the area within a 5 % deviation of this black line 89

4.29 The SiPM area on two generations of tileboards. (a) is from a TBv1 tileboard, while (b) is from a TBv2 tileboard. (c) shows the modified TBv2 tileboard with white stickers surrounding the SiPMs to recreate the white paint around SiPMs in TBv1 tileboards. 90

4.30 Change in light yields due to the effect of the white paint dot. (a) compares the light yield from identical IHEP-produced injection-moulded tiles placed on the same SiPM on a TB2 Tileboard before (yellow) and after (purple), adding the white paint dot. The same tiles are also placed on SiPMs on TBv1, which contains the white paint dot (green). (b) compares the light yields from cast tiles on TBv2 tileboards (yellow) and after (purple) adding the white paint dot. The green curve gives the light yield from TBv1 tileboards, which contains the white paint dot. 90

4.31 Light yields from IHEP cast tiles and IHEP version 1 injection-moulded tiles as observed for 4 V and 2 V over-voltages. The fit uses the relation light yield $= \frac{k}{\sqrt{\text{scintillator area}}}$. 91

4.32 MIP spectra rescaled to p.e. units using SiPM gains for two channels with the same scintillator placed on top. (a) is a channel with a $2 \times 2\,\text{mm}^2$, and (b) is a channel with a $3 \times 3\,\text{mm}^2$ SiPM. Both channels have the same IHEP v2 scintillator tile. Light yield of the $3 \times 3\,\text{mm}^2$ SiPM is 105.34 ± 1.04 p.e. and the light yield $2 \times 2\,\text{mm}^2$ SiPM is 46.1 ± 0.7 p.e.. 92

4.33 Light yields from all tiles measured at beam tests at a SiPM over-voltage of 4 V. (a) shows the light yields of all injection-moulded tiles. (b) shows the light yields of all cast tiles. The fit used the relation light yield $= \frac{k}{\sqrt{\text{scintillator area}}}$. Error bars give the statistical uncertainties of each light yield measurement. 93

4.34 Beam test setup used at SPS, CERN test beam facility. The setup is identical to that used at DESY. TB1.3 was used here with the KCU105 DAQ system. The beamline was shared with colleagues working on the silicon sensors needed for the HGCAL upgrade, with their setup placed in front of the Tilemodule, with the Tilemodule using the beam parasitically. The common trigger scintillator pair was used for both setups. (a) shows the tileboard and KCU DAQ system on the aluminium frame placed. (b) shows the position of the setup with respect to the stage and the silicon sensor setup. 95

4.35 Light yields measured at the DESY test beam facility with 3 GeV electrons in comparison with light yields measured at the CERN, SPS test beam facility with 120 GeV muons. 95

4.36 ^{90}Sr source-based light yield setup developed for quality control and assurance. (a) shows a sketch of the setup, and (b) shows the setup with the corresponding areas marked. Electrons from the source pass through the HGCAL tile (tile under test) and pass through the trigger tile, which triggers data taken from the SiPM under the HGCAL tile. Taken from [89]. 96

4.37 ratio of light yields measured by the ^{90}Sr setup (LY_{Sr90}) and light yield measured with tileboards at beam tests (LY_{TB}) for the same 89 FNAL tiles. 97

4.38 comparison of light yields of all cast tiles measured, including the NIU cast tile measured using the ^{90}Sr source-based setup. All light yields were scaled for the $2 \times 2\,\text{mm}^2$ SiPMs. The fit parameter for NIU cast tile $k = 3222 \pm 95\,\text{p.e.} \cdot \text{mm}$. 98

5.1 LED placed under the tileboard containing the SiPMs under test 102

5.2 Determination of $(V_{br}(\text{IV}))_{\text{non-irrad}}$ using the relative derivative method for the six non-irradiated SiPMs mounted on tileboard TB1.3. (a) shows the current passing through the SiPM in log scale vs voltage curves for four non-irradiated SiPMs while (b) shows the $\frac{1}{I} \cdot \frac{dI}{dV}$ vs voltage curves for the same SiPMs. The fit on (b) uses a Gaussian function with its mean used to determine $(V_{br}(\text{IV}))_{\text{non-irrad}}$. 102

5.3 Determination of $(V_{br}(\text{IV}))_{\text{irrad}}$ using the relative derivative method for the six irradiated SiPMs mounted on two tileboards. (a) are for the two SiPMs mounted on TB1.2. (b) are for the four SiPMs mounted on TB2.1. The fit on (b) uses a Gaussian function with its mean used to determine $(V_{br}(\text{IV}))_{\text{irrad}}$. 103

5.4 LED placed under the tileboard containing the SiPMs under test. The vertical orange lines roughly separate the SiPMs of different reels. Here, $V_{OP}(\text{HPK}) = V_{br}(\text{HPK}) + 2\,\text{V}$ and $\text{VB(CERN)} = V_{br}(\text{IV})_{\text{non-irrad}}$. Taken from [74]. 104

5.5 Bias voltages generated via the ALDOv2 BV chip steered via the GBT-SCA on a TBv2 tileboard as reported in [96]. (a) shows the variations for 5000 s (or 1 hr and 23 min), while (b) shows the short-period variations ($\sim$ min). 105

5.6 The determined relative-derivative breakdown voltage for the non-irradiated SiPMs on TB2.1. (a) shows the ln(I) vs. voltage curves for the SiPMs while (b) shows the $\frac{1}{I} \cdot \frac{dI}{dV}$ vs. voltage curves for them. The fit on (b) uses a Gaussian function with its mean used to determine $(V_{br}(\text{IV}))_{\text{non-irrad}}$. 106

5.7 Tileboard TB2.1 with irradiated SiPMs and non-irradiated SiPMs. The first data run configuration is shown in (a), where cast tiles from ISMA, Ukraine, were placed on the non-irradiated SiPMs (marked in red). As shown in (b), the same tiles were placed on the four irradiated SiPMs (marked in red) for the second data run. 107

5.8 histogram showing the pedestal events for the same SiPM shown in fig. 5.9 measured at approximately the same over-voltage 108

5.9 (a) shows the ADC vs. TrigTime spectra for one of the SiPMs irradiated to 2×10^{12} $\mathrm{n_{eq}/cm^2}$ fluence. An 8 ns TrigTime window around the peak (shown in red) is used to sample the signal peak. The resulting histogram is shown in (b), where a Landau-Gaussian function extracts the MIP maximum. 109

5.10 The standard deviations of the pedestal data obtained from irradiated SiPMs for different over-voltages are shown as circles. A linear fit estimates the standard deviation required to smear the MIP spectra obtained from non-irradiated SiPMs (shown as triangles). The over-voltage in terms of $V_{br}(TO)$ and $V_{br}(IV)$ are given in the two x axes. 110

5.11 comparison of light yields after smearing the spectra for non-irradiated SiPMs and the corresponding irradiated SiPMs with the same tile. A linear function shows the trend of the light yield increase with over-voltage. The over-voltage in terms of $V_{br}(TO)$ and $V_{br}(IV)$ are given in the two x axes. 111

5.12 SNR as a function of over-voltage for the four irradiated SiPMs. The over-voltage in terms of $V_{br}(TO)$ and $V_{br}(IV)$ are given in the two x axes. 112

5.13 Separation of the pedestal and MIP peaks for channel 37, which contains a 2×2 mm² SiPM irradiated to 2×10^{12} $\mathrm{n_{eq/cm^2}}$ fluence for over-voltages of roughly (a) 1.4 V, (b) 1.8 V, (c) 2.0 V and (d) 2.2 V. The blue curves are pedestal-contaminated MIP data estimated to have a contamination of about 40 %. The pink and red curves show a pure noise run and a data run with less than 2 % pedestal noise contamination. 113

5.14 Separation of the pedestal and MIP peaks for channel 36, which contains a 2×2 mm² SiPM irradiated to 2×10^{12} $\mathrm{n_{eq/cm^2}}$ fluence for over-voltages of roughly (a) 1.4 V, (b) 1.8 V, (c) 2.0 V and (d) 2.2 V. The blue curves are pedestal-contaminated MIP data estimated to have a contamination of about 50 %. The pink and red curves show a pure noise run and a data run with less than 2 % pedestal noise contamination. 114

5.15 MIP peaks obtained from a non-irradiated SiPM (channel 59 on TB2.1) measured by varying noise generated via a Gaussian smearing factor ((a) no smearing, (b) SNR=5, (c) SNR=3 and (d) SNR=2). The data were taken at an over-voltage of around 2 V with respect to the turn-off voltage for conveyor gain 12. A Landau-Gaussian fit is used to fit the MIP peak from which the MIP maximum is extracted for each case. 115

5.16 MIP efficiencies and noise occupancies were measured for four different non-irradiated channels as a function of the Gaussian smear factor (or SNR). A threshold at half the MIP maximum value calculates the MIP efficiencies and noise occupancies. 116

5.17 MIP efficiency as a function of noise occupancy plotted for channel 57 for different smear factors (or SNR). A threshold at half the MIP maximum value calculates the MIP efficiencies and noise occupancies. 116

6.1 Tileboard in climate chamber setup used for measuring the noise vs. leakage current relationship of irradiated SiPMs. 118

6.2 PT-1000 temperature sensors mounted close to an irradiated SiPM on TB1.2 . . 119

6.3 Variation of leakage current passing through the SiPM (a) and the noise of the SiPM and readout electronics (b) as a function of over-voltage for different temperatures and for an irradiated $1.4 \times 1.4\,\mathrm{mm}^2$ SiPM. Both plots share the same legend given in (b). 120

6.4 Noise vs. leakage current plot measured for the six irradiated SiPMs of two different SiPM sizes for an over-voltage of 2 V. Each noise and leakage current point for a given SiPM was measured at different temperatures ranging between $-30\,°\mathrm{C}$ and $45\,°\mathrm{C}$. A single fit is used for all channels. Uncertainties were derived from the linear fits used to extract noise and current. 121

6.5 The variation of the temperature difference measured via the climate chamber thermostat and the PT1000 on the ground plane as a function of the climate chamber temperature. 122

6.6 Comparison between the two measurement methods extracting the noise vs. leakage current relationship at the same over-voltage. (a) shows the comparison between the two measurements for the $1.4 \times 1.4\,\mathrm{mm}^2$ SiPM while (b) shows the comparison for the $2 \times 2\,\mathrm{mm}^2$ SiPM. The uncertainties for the data from the multi-temperature setup were derived from the linear fits used to extract noise and current. The uncertainties for the LED setup are due to uncertainties in over-voltage measurement. 124

6.7 The noise vs. leakage current variation for the same two irradiated SiPMs on TBv2 containing a HGCROCv2 and MiniTB containing a HGCROCv3 at an over-voltage of 2 V. Uncertainties were derived from the linear fits used to extract noise and current. 125

6.8 The noise vs. leakage current variation for non-irradiated SiPMs on TB3 and MiniTB at an over-voltage of 2 V. Both tileboards contain HGCROCv3 chips. Uncertainties were derived from the linear fits used to extract noise and current. 125

6.9 Comparison of noise vs. current relationships between four non-irradiated SiPMs and two irradiated SiPMs on MiniTB Tileboard operating at an over-voltage of 2 V. 127

6.10 Comparison of noise vs. current relationships between six non-irradiated SiPMs (four on MiniTB and two on TB3) and two irradiated SiPMs on MiniTB (both containing HGCROCv3 chips) operating at 2 V. Two fits are used for the non-irradiated and irradiated SiPMs separately. 129

6.11 The I-V curves from three SiPMs irradiated to $5 \times 10^{13}\,\mathrm{n_{eq}/cm^2}$ at $-30\,°\mathrm{C}$. Taken from [74]. VB here is the breakdown voltage of the SiPMs measured w.r.t. the IV-definition (V_{br}(IV)). The dark current measured here is the same as leakage current. 129

7.1 The tile positions in the scintillator section. The width of the tile w_n is measured along the tile centre, and the height of the tile h_n is measured along the radial direction. The distance from the centre of the detector to the centre of the tile is given by d_n. $\delta\phi$ gives the angle covered by a single tile. 133

7.2 (a) shows the absorption dose map and (b) shows the neutron fluence map for each ring and layer of the HGCAL SiPM-on-tile section for an integrated luminosity of 3000 fb^{-1}. Each cell contains eight SiPM-on-tile cells whose dose and fluence are assumed to be constant throughout the cell. 135

7.3 (a) shows the absorbed dose and (b) shows the neutron fluence as a function of integrated luminosity for a few selected channels of different Tilemodule sections. 136

7.4 (a) shows the PDE vs. over-voltage measured for HGCAL SiPMs as given in [74]. (b) compares the PDE curve measured by the collaboration with the curve measured by HPK. As the PDE measurement done within the CMS collaboration is a relative PDE curve, in order to compare the two curves, the HPK PDE measurement at an over-voltage of 4 V is used to rescale the curve measured by the CMS collaboration accordingly. 137

7.5 Signal degradation normalised to the initial signal over time due to temporary and permanent radiation damage. For tiles with 30 rad/hr dose rates and assuming an integrated luminosity of 300 fb^{-1} is delivered by LHC annually. Taken from [102]. 140

7.6 Default Tilemodule layout of the HGCAL scintillator section. Each cell consists of eight SiPM-on-tiles on a single layer and ring. Only NIU machined BC-412 cast tiles are assembled on the cells reading 'cast', and FNAL produced injection-moulded (batch 1) tiles on the cells reading 'inj-mld'. 142

7.7 SNR after an integrated luminosity of 3000 fb^{-1} received over a 10-year period. The red and purple cells indicate the areas where SNR<3 and SNR<2.5, respectively. 142

7.8 SNR with 20 % higher fluence and dose rates after an integrated luminosity of 3000 fb^{-1} over a 10-year period (equivalent to $\mathcal{L}_{int} = 3600\,\mathrm{fb}^{-1}$ collected over a 10-year period). The red and purple cells indicate the areas where SNR<3 and SNR<2.5, respectively. 143

7.9 SNR from layout scenario 1 after $\mathcal{L}_{int} = 3600\,\text{fb}^{-1}$ over a 10-year period. The blue boxes mark all the areas where 2×2 mm² SiPMs were replaced by 3×3 mm² SiPMs. The purple box marks where injection moulded tiles were replaced with cast tiles. 145

7.10 SNR for layout scenario 2 after an integrated luminosity of $3600\,\text{fb}^{-1}$ over a 10-year period. The red box marks all the areas where each area containing 2×2 SiPM-on-tile channels is replaced with 3×3 SiPM-on-tile channels. The black box marks the area which remains unchanged from layout 1. 146

7.11 SNR from Layout scenario 3 after an integrated luminosity of $3600\,\text{fb}^{-1}$ over a 10-year period. The red box marks areas with increased granularity. The black box marks the area where the granularity was not changed. The blue boxes show the areas where 3×3 mm² SiPMs replace 2×2 mm² SiPMs. The purple box shows the area where cast tiles replace injection moulded tiles. All these changes are with respect to the default scenario shown in fig. 7.8. 148

7.12 The floorplan of the B12 Tilemodule prototype (TBv3 generation tileboard). BV1 and BV2 are the two high-voltage lines of the first high-voltage ALDOv2 ASIC, and BV3 and BV4 are the two high-voltage lines of the second high-voltage ALDOv2 ASIC. The top eight rings are read out by the first HGCROC (ROC1), and the bottom four rings are read out by the second HGCROC (ROC2) [84]. 149

7.13 SNR from layout scenario 3 just after YETS, after $\mathcal{L}_{int} = 3600\,\text{fb}^{-1}$. The blue boxes show the areas where 3×3 mm² SiPMs replace 2×2 mm² SiPMs. The purple box shows the area where injection-moulded tiles replace cast tiles. The red box marks the area with increased granularity. The black box marks the area where the granularity was not changed. All these changes are with respect to the default scenario shown in fig. 7.8. 150

7.14 (a) shows the SNR as a function of $\mathcal{L}_{int}$ for the five worst performing SiPM-on-tile cells while (b) shows the noise as a function of $\mathcal{L}_{int}$ for the tile with the best SNR of each Tilemodule type. These numbers were generated for layout scenario 3, assuming the detector collects $\mathcal{L}_{int} = 3600\,\text{fb}^{-1}$ in 10 years. 151

7.15 SNR calculated for the same SiPM-on-tile cell using the PDE curves obtained from HPK and the CMS collaboration [74] as a function of over-voltage. The over-voltage relative to the turn-off definition is given as OV_TO, and the over-voltage relative to the relative-derivative definition is given as OV_IV. See section 2.4.2.8 for the difference between the two breakdown voltage definitions. The SNR is calculated for $\mathcal{L}_{int} = 3000\,\text{fb}^{-1}$ for layout scenario 1. 152

7.16 SNR operating at an over-voltage of 1.65 V employing layout scenario 3 after $\mathcal{L}_{int} = 3600\,\text{fb}^{-1}$ over a 10-year period. The blue boxes show the areas where 3×3 mm² SiPMs replace 2×2 mm² SiPMs. The purple box shows where injection moulded tiles replace cast tiles. The red box mark the area where the granularity was increased. The black box marks the area where the granularity was not changed. All these changes are with respect to the default scenario shown in fig. 7.8. 152

7.17 Leakage current expected from each SiPM-on-tile channel after an integrated luminosity of 3600 fb^{-1} over ten years employing layout scenario 3. (a) is if the SiPMs are operated at an over-voltage of 2 V. (b) is if the SiPMs are operated at an over-voltage of 1.65 V. The blue boxes show the areas where 3×3 mm² SiPMs replace 2×2 mm² SiPMs. The red box mark the area the granularity increased. The black box marks the area where the granularity was not changed. All these changes are with respect to the default scenario shown in fig. 7.8. . . 154

7.18 SNR from layout scenario 4 after an integrated luminosity of 3600 fb^{-1} over a 10-year period operating at an over-voltage of 2 V. All SiPMs used are 3×3 mm² in area. The red box mark the area the granularity increased. The black box marks the area where the granularity was not changed compared to the default scenario shown in fig. 7.8. 155

7.19 leakage current expected from each SiPM-on-tile channel after $\mathcal{L}_{int} = 3600\,\mathrm{fb}^{-1}$ over ten years employing layout scenario 4 if the SiPMs are operated at an over-voltage of 2 V. All SiPMs used are 3×3 mm² in area. The red box mark the area the granularity increased. The black box marks the area where the granularity was not changed compared to the default scenario shown in fig. 7.8. 155

7.20 leakage current expected from each SiPM-on-tile channel after $\mathcal{L}_{int} = 3600\,\mathrm{fb}^{-1}$ over ten years employing layout scenario 4 if the SiPMs are operated at an over-voltage of 1.65 V. All SiPMs used are 3×3 mm² in area. The red box mark the area the granularity increased. The black box marks the area where the granularity was not changed compared to the default scenario shown in fig. 7.8. 156

7.21 SNR from layout scenario 4 after an integrated luminosity of 3600 fb^{-1} over a 10-year period operating at an over-voltage of 1.65 V. All SiPMs used are 3×3 mm² in area. The red box mark the area the granularity increased. The black box marks the area where the granularity was not changed compared to the default scenario shown in fig. 7.8. 156

7.22 SNR after $\mathcal{L}_{int} = 3000\,\mathrm{fb}^{-1}$ over ten years operating at an over-voltage of 2 V using layout scenario 3 with the noise of irradiated SiPMs readout using HGCROCv2. The blue boxes show the areas where 3×3 mm² SiPMs replace 2×2 mm² SiPMs. The purple box shows the area where injection moulded tiles replace cast tiles. The red box mark the area where the granularity was increased. The black box marks the area where the granularity was not changed. All these changes are with respect to the default scenario shown in fig. 7.8. 158

A.1 The relationship between pedestal mean and current passing through five irradiated SiPMs. (a) is the relationship for one channel at different temperatures at the same bias voltage supplied to the SiPM. (b) is the relationship for four different SiPMs of two different sizes. 164

A.2 The relationship between pedestal mean and current passing through two irradiated SiPMs at low leakage currents for two SiPMs of different sizes. 165

A.3 (a) SiPM current and (b) pedestal mean vs bias voltage relationship for four different irradiated SiPMs of two different sizes on the same TBv2 tileboard. . 165

A.4 measurement of the breakdown voltage using midpoint of the tangent in the area where the tangent lies on the pedestal vs voltage curve. 166

A.5 (a) SiPM current and (b) pedestal mean vs bias voltage relationship for two different irradiated SiPMs of two different sizes on the same TBv1 tileboard. Both these channels showed a non-linearity at lower currents. 167

List of Tables

3.1 Differences between the two DAQ systems used with the tileboards 53

3.2 A summary of the different board generations developed over the years 59

4.1 Overview of all SiPMs used. All SiPMs were HDR-2 type SiPMs with custom-made radiation hard packaging. Two models were better used: HPK S14160-976x series used in TBv1 and TBv2 tileboards, and HPK S16713-xx used in TBv3 tileboards. Parameters quoted from [72, 73] 62

4.2 Overview of all scintillator tiles used. * Performance of FNAL cast tiles was quantified only using ^{90}Sr source-based setup explained later in this chapter. . 63

4.3 Overview of light yields measured for all IHEP injection moulded tiles. All values were measured or scaled for $2 \times 2\,\text{mm}^2$ operating at $V_{over} = 4\,\text{V}$. 93

4.4 Overview of light yields measured for all cast tiles. values were measured or scaled for $2 \times 2\,\text{mm}^2$ SiPMs operating at $V_{over} = 4\,\text{V}$ 94

5.1 Overview of $V_{br}(\text{IV})_{\text{non-irrad}}$ measured using LED based system and $V_{br}(\text{HPK})$ supplied by HPK for non-irradiated SiPMs on TB1.3 tileboard. 103

5.2 Overview of $V_{br}(\text{IV})_{\text{irrad}}$ measured using LED based system and $V_{br}(\text{HPK})$ supplied by HPK for non-irradiated SiPMs on TB1.2 and TB2.1 tileboard. 103

5.3 Overview of $V_{br}(\text{IV})_{\text{non-irrad}}$ measured using LED based systemfor non-irradiated SiPMs on TB2.1. 106

6.1 Overview of expected noise for different HGCROC generations for SiPM-on-tiles operating after a fluence of $5 \times 10^{13}\,\text{n}_{\text{eq}}/\text{cm}^2$ working at $V_{over} = 2\,\text{V}$ w.r.t. $(V_{br}(\text{TO}))_{\text{irrad}}$. The noise and current were calculated for $2 \times 2\,\text{mm}^2$ SiPMs using eq. (6.2). For other sizes, multiply the leakage current by the scaling factor of SiPM area and use eq. (6.4) to calculate the noise. 130

7.1 Values of constants needed to calculate the scintillator temporary damage per year assuming $\mathcal{L}_{int} = 300\,\text{fb}^{-1}$ per year was achieved [16]. 139

7.2 Overview of parameters used for the calculation of the SNR at an over-voltage $(V_{over}(\text{TO}) = 2\,\text{V})$. 141

7.3 Number of SiPMs, scintillator tiles and total area of scintillator material needed to produce the HGCAL scintillator section for both end-caps under the proposed layout scenarios. 148

A.1 Differences between the breakdown voltages measured using the relative derivative method and the tangent method 166

Acronyms

AHCAL Analog Hadronic Calorimeter

ALICE A Large Ion Collider Experiment

APDs avalanche photo-diodes

ATLAS A Toroidal LHC Apparatus

BSM beyond the standard model

bx bunch crossings

CALICE Calorimeter for Linear Collider Experiments

CE-E Electromagnetic End-Cap Calorimeter

CE-H Hadronic End-Cap Calorimeter

CMS Compact Muon Solenoid

CSCs cathode strip chambers

DAQ data acquisition

DCR Dark Count Rate

DNL differential non-linearity

DTs drift tubes

ECAL electromagnetic calorimeter

ESR Enhansed Specular Reflector

eV electron Volts

FCC-ee electron-positron Future Circular Collider

FNAL Fermi National Accelerator Laboratory

GBT-SCA Giga-Bit Transceiver - Slow Control Adapter

GEMs gas electron multipliers

HBU HCAL base unit

HCAL hadronic calorimeter

HGCAL High Granularity Calorimeter

HGCROC High Granularity Calorimeter Read-Out Chip

HGF Helmholtz Association

HL-LHC High Luminosity LHC

HLT High Level Trigger

IEL ionisation energy loss

IHEP Institute for High Energy Physics

ILC International Linear Collider

ISMA Institute for Scintillation Materials

L1 Level 1

L1A Level 1 Accept

LED light emitting diode

LHC Large Hadron Collider

LHCb Large Hadron Collider beauty

LINAC linear accelerator

LpGBT Low Power GigaBit Transceiver

MiniTB mini tileboard

MIPs minimum ionizing particles

MPPCs Multi-Pixel Photon Counters

MPV most probable value

NIEL non-ionisation energy loss

NIU North Illinois University

p.e. photo-electron

PDE photon detection efficiency

PKA primary knock-on atom

PMTs photomultiplier tubes

Sp$\bar{p}$S Proton-Antiproton Collider

QCD Quantum Chromodynamics

QED Quantum Electrodynamics

RF cavities radio frequency cavities

RPCs resistive plate chambers

SiPMs silicon photomultipliers

SNR signal-to-noise ratio

SPADs Single-Photon Avalanche Diodes

SPS single photon spectrum

SPS facility Super Proton Synchrotron facility

SUSY Supersymmetry

TBv1 Tileboard version 1

TBv2 Tileboard version 2

TBv3 Tileboard version 3

TDC time-to-digital converter

TDR Technical Design Report

TOA time-of-arrival

TOT time-over-threshold

UMN University of Minnesota

VBF Vector Boson Fusion

YETS year-end technical stops

Z Atomic number

Acknowledgements

Let me take this opportunity to thank and dedicate this thesis to a few exceptional individuals who helped me throughout my studies.

First and foremost, I would like to thank my supervisor, Felix Sefkow. Your excellent supervision and continuous guidance throughout the past three and a half years have influenced my career as a budding young physicist. I learned so much about physics, calorimetry and project management by watching you plan and execute the project within all the constraints. Thank you for giving me this opportunity to complete my doctoral studies in your group.

Next, I would like to give a special thanks to my second supervisor, Katja Krüger. Despite your busy schedule, you took time every day to come and discuss the progress, failures, ideas and outcomes. I will never forget the countless beam tests we organised and took part in. Thanks to you, not only have I learnt so much about calorimetry and particle physics in general, but I have also learnt so much about how to design an experiment, gather data, analyse them and finally present them.

I want to thank Mathias Reinecke and Ole Bach, with whom I worked closely these past three and a half years. Your friendliness and helpful feedback have immensely helped me throughout my doctoral journey. Especially to you, Mathias, who made it a point to help me with my setup whenever I have an idea and want to test it. I remember back in 2020, when I first joined the group, and we were all in lockdown; you used to turn my setup on and off daily so I could work remotely. Without you, this research would not have begun.

I want to thank Norbert Herrmann for his friendly willingness to act as the second referee of this thesis. I would also like to thank Moritz Guthoff, my mentor at DESY, for the support you gave me in mentoring. Thank you very much to Andrea Schrader, who undertook all our administration tasks, for being so kind! I also wish you a very happy retirement!

To my fellow colleagues present and past in the DESY FTX group: Daniel, Eldwan, Remi, Vladimir, Olin, Yasser, Jakob, Swathi, Engin, Timo, Antoine, Jia-Hao, Daria, Uli, Annabel, Yee, David, Ivo, Julie, Bohdan, John, Bryan, Cameron, Tanguy, Jennifer, Felix, Antonios, Peter, Sascha, Thomas, Thorsten, Anatolii, Konrad, Arianna, Dohun, Lennart, Adrian, Oliver, Frank, Ralf, Marcel, Jenny to name a few. Thank you for making my life at DESY so enjoyable. The conversations over lunch and coffee breaks, the weekly Friday night dinners, and the occasional game nights have been memories I will never forget!

To my colleagues at the DESY CMS: Gabriele, Matthias K., Lovisa, Jeremi, Juliette, and Freya. Thank you so much for all the help throughout my time at DESY. To the members of the CMS HGCAL and CALICE AHCAL collaborations, Konrad, Anna, Jiri, Jose, Michael, Fabian, and so many others. To Hans-Christian and his group at KIP in Heidelberg. To my supervisor during my master's study: Frank. Thank you so much for the support over the years!

To DESY, especially DESY-II testbeam coordinators, the testbeam group, the DESY electronics lab, and administrative and clerical staff. Thank you all so much for the support during my time at DESY. Similarly, I would like to thank the Department of Physics at Heidelberg University and the Heidelberg Graduate School for Physics (HGSFP) staff. Despite never being present at Heidelberg physically, you always succeeded in helping me via email. Thank you very much!

I would also like to thank Antoine, Mathias R, Matthias K, Daniel, Sanjana and Katja, who proofread my thesis. Thank you for your time and effort. Some of you spent your weekends reading and correcting my thesis. I am sorry that I gave you so much extra work. Thank you again!

I would also like to thank my parents, two sisters, my brother-in-law and niece. Your support means so much to me. Thank you so much for being there for me!

I thank my friends here in Hamburg, especially Thisal, Dashanka, Shashini, Maria, Charlie, Yuka, and Sanjana. The travels we did together in Barcelona, Lecce, Sri Lanka, the days we spent cooking and chatting at Thisal's old place, watching Eurovision and betting on who wins have all been truly memorable.

Finally, I would like to thank Sanjana Nair in an extraordinary way. You are my pillar of strength, my partner in crime. You helped me get through particularly rough days during my research. Thank you for being here for me! You will always be my plus one!